Structure of Hydrated Ions and Cyanide Complexes by X-Ray Absorption Spectroscopy

Farideh Jalilehvand

ROYAL
INSTITUTE OF
TECHNOLOGY

Doctoral Thesis
Department of Chemistry
STOCKHOLM 2000

Doctoral Dissertation 2000
Department of Chemistry
Inorganic Chemistry
Royal Institute of Technology
S-100 44 STOCKHOLM
Sweden

ISBN 91-7170-561-9
TRITA – OOK- 1058

Printed in Sweden by Kista Snabbtryck AB

The cover picture is adapted from: *Anal. Chem.* **1988**, *60*, 1225A, with permission.

To my Parents

If we knew what we were doing - it would not be research, would it ?"
Albert Einstein

List of Papers

This thesis comprises the present summary and the following articles, which are referred to in the text by their Roman numerals:

Paper I. *The Hydration of the Calcium Ion. An EXAFS, Large Angle X-Ray Scattering and Molecular Dynamics Simulation Study*
F. Jalilehvand, D. Spångberg, P. Lindqvist-Reis, K. Hermansson, I. Persson, and M. Sandström
Submitted to *J. Amer. Chem. Soc.* **2000**

Paper II. *Structure of the Aqua Ions and Fluoride Complexes of Uranium(IV) and Thorium(IV) in Aqueous Solution an EXAFS Study*
H. Moll, M. A. Denecke, F. Jalilehvand, M. Sandström, and I. Grenthe
Inorg. Chem. **1999**, *38*, 1795-1799 (Reproduced with permission from Inorganic Chemistry. Copyright 1999 American Chemical Society)

Paper III. *Structure of the Heterobimetallic Cyano Compound $TlPt(CN)_5$ in the Solid State by X-Ray Powder Diffraction, EXAFS and Vibrational Spectroscopy*
F. Jalilehvand, L. Eriksson, J. Glaser, M. Maliarik, J. Mink, M. Sandström, and I. Tóth
In manuscript

Paper IV. *Structure Studies of Heterobimetallic Cyano Complexes with a Direct Platinum-Thallium Bond in Aqueous Solution by EXAFS and Vibrational Spectroscopy*
F. Jalilehvand, J. Glaser, M. Maliarik, J. Mink, I. Persson, P. Persson, M. Sandström, and I. Tóth
In manuscript

Paper V. *Structure Studies of the Dimeric Bis{pentacyanoplatinate(III)}(Pt—Pt) and Monomeric Pentacyanoplatinum(IV) Complexes by EXAFS and Vibrational Spectroscopy, and X-Ray Crystallography*
F. Jalilehvand,[a] A. Ilyuhin, M. Maliarik, M. Sandström, and J. Glaser
In manuscript

Abstract

The present thesis contains an overview of the use of x-ray absorption fine-structure spectroscopy (XAFS) and large-angle x-ray scattering (LAXS) techniques for structure determination, in particular for solutions, with a number of applications. For the structure of the hydrated calcium(II) ion in CaX_2 (X= Cl, Br, I, ClO_4) in aqueous solution, the XAFS and LAXS studies show a broad and asymmetric distribution of Ca-O bond distances centered at 2.46(2) Å with a probable hydration number of eight, and a second coordination sphere, Ca···O_{II} at 4.58(5) Å. For the hydrated halide ions the LAXS results gave the distances Cl···O 3.25(1) Å, Br···O 3.36(1) Å and I···O 3.61(1) Å. Molecular dynamics (MD) simulations were used to calculate theoretical Ca K-edge XAFS spectra and thermal displacement parameters from the MD snapshots.

XAFS studies gave the M-O bond distances 2.42(1) and 2.45(1) Å for the hydrated U^{4+} and Th^{4+} ions, and the M-O [M-F] distances 2.45 [2.10] Å for UF^{3+} and 2.48 [2.14] Å for ThF^{3+} in aqueous solution, respectively. For all four hydrated species, the most likely total coordination number was found to be 10 ± 1.

The crystal structure of the solid compound $TlPt(CN)_5$ has been determined by combining the results from x-ray powder diffraction (XRD), XAFS and vibrational spectroscopy. The XRD data show the tetragonal space group P4/*nmm* (No. 129) with $a = 7.647(3)$, $c = 8.049(3)$ Å, $Z = 2$, and a structure comprising $TlPt(CN)_5$ entities linked together in linear -Tl-NC-$Pt(CN)_4$-Tl- chains. A three-dimensional network is formed by the cyano ligands of the platinum atom forming bridges to the neighboring thallium atoms. The Pt-Tl bond distance was found to be 2.627(2) Å. The local structure around the metal ions was described by means of XAFS data measured at both the Pt L_{III} and Tl L_{III} edges. For the data treatment the most important multiple scattering (MS) pathways were included. Vibrational spectra were recorded by Raman and infrared absorption spectroscopy, showing strong coupling, in particular of the Pt-Tl bond stretching mode. Assignments were made using factor group theory, and had to be based on a structural unit larger than the crystallographic unit cell. The structure of three related heterobimetallic complexes, $[(NC)_5Pt\text{-}Tl(CN)_n]^{n-}$, n = 1 - 3, were studied in aqueous solution by means of XAFS and vibrational spectroscopy. The short Pt-Tl bond distances, 2.598(3), 2.618(4), and 2.638(4) Å, increase with the number of cyano ligands on the thallium atom, n = 1, 2, and 3, respectively. A comparison with the thallium(III)-cyano complexes $[Tl^{III}(CN)_n]^{3-n}$, n = 1-3, shows the Tl-C bond distances to be longer in the $[(NC)_5Pt\text{-}Tl(CN)_n]^{n-}$ complexes for the same coordination number. For the dimeric platinum(III) complex $[Pt_2(CN)_{10}]^{4-}$ in aqueous solution XAFS studies showed a non-supported Pt-Pt bond, 2.729(3) Å, between two $Pt(CN)_5$ groups. In $[Pt(CN)_5X]^{n-}$ complexes the mean Pt-C bond distance of the pentacyanoplatinum groups was found to increase with increasing donor ability of the ligand X = H_2O, OH, I and $Pt(CN)_5$. The crystal structures of the compounds $Tl_2[Pt(CN)_5(OH)]$ and $K_2[Pt(CN)_5I]\cdot 0.6H_2O$ were determined by single crystal x-ray diffraction techniques.

Keywords: calcium, uranium, thorium, platinum, thallium, hydration, fluoride, halide, metal-metal bond, bimetallic, cyanide, cyano complexes, EXAFS, Raman, IR, normal coordinate analysis, x-ray diffraction, molecular dynamics.

Contents

List of abbreviations

CCD	Charge Coupled Device
DFT	Density Functional Theory
EXAFS	Extended X-ray Absorption Fine Structure
FT	Fourier Transform
HOMO	Highest Occupied Molecular Orbital
IR	Infrared absorption
LAXS	Large Angle X-ray Scattering
LUMO	Lowest Occupied Molecular Orbital
MD	Molecular Dynamics
MO	Molecular Orbital
NEXAFS	Near-Edge X-ray Absorption Fine Structure
PRDF	Pseudo Radial Distribution Function
RDF	Radial Distribution Function
Rtc	Real time clock
XAFS	X-ray Absorption Fine Structure
XANES	X-ray Absorption Near Edge Structure
XAS	X-ray Absorption Spectroscopy
XPD	X-ray Powder Diffraction
XRD	X-Ray Diffraction
YAG	Yttrium Aluminium Garnet

Index

Introduction

Progress in science is often closely connected to the development of new technology or improved instrumentation for experimental measurements. Chemistry is a science based on experimental observations of matter and its changes. The results of such observations are interpreted in terms of models with varying degree of sophistication. The progress of technology has allowed a rapid development of the experimental techniques, which allow new systems to be studied and new information to be obtained.

In many cases the development and refinement of the theory and methods of interpretation follow after the technological progress. This is a consequence of the wish and need to extract as much reliable information as possible out of the experimental data, which could be obtained after the construction of new instruments or measuring techniques.

The development of the x-ray absorption fine structure (XAFS) technique for structure determination is such a case. Several examples are given in the present thesis on how this method has been used in different combinations with other techniques, to give information on chemical problems which were not previously possible to obtain.

Hydrated metal ions with first hydration spheres showing disorder and asymmetry, have become possible to study by the XAFS technique. For the biochemically important calcium ion an XAFS study has been performed, in combination with large angle x-ray scattering (LAXS) and molecular dynamics (MD) simulation (see Section *4.1*). The hydration and fluoride complex formation of the uranium(IV) and thorium(IV) ions are of interest as model for other actinide(IV) ions and the results are useful in particular for chemical considerations in connection with the handling and storage of nuclear waste from power plants. The large size in combination with high charge give high coordination numbers, and an investigation has been made with the new XAFS technique. Likewise, excessive multiple scattering has become possible to handle with new XAFS theory and programs, which has allowed the study of a number of cyanide complexes with heavy metals. Such complexes show interesting bonding properties, which have been investigated by normal coordinate analyses of their vibrational spectra. For a crystalline powder, $TlPt(CN)_5$, the crystal structure, as well as the local structure and bonding around both the Pt and Tl atoms, could be determined using a combination of x-ray powder diffraction, XAFS and vibrational spectroscopic techniques.

The main experimental techniques used for the current investigations have been discussed in this thesis. They represent different aspects of the progress in the development of experimental methods. The first method described here (Section *1*), is the X-ray Absorption Fine Structure spectroscopy (XAFS). The basic principles have been known since the 1930s by a theory of Kronig explaining the oscillatory fine structure in an x-ray absorption spectrum, which may extend for hundreds of electron volts after an x-ray absorption edge.[1] When synchrotron radiation became more easily available for x-ray absorption experiments in the 1970s, it was realised that XAFS could become a powerful method for determining the local structure around the absorbing atoms in a sample, providing information which was not accessible otherwise, *e.g.* for bio-inorganic and amorphous systems, solids as well as solutions.[2-4] Great efforts were then made to develop the scattering theory of the ejected photoelectrons, and the data treatment methods. Recently, the technique has become a well-developed and mature tool for structural studies.[4,5]

The large angle x-ray scattering (LAXS) technique (Section *2*), provides a somewhat different example of the development of a method for structure studies. The technique is experimentally simple, and is based on powder diffraction instrumentation developed more than 40 years ago.[6,7] Computer programs were written about 30 years ago based on the existing theory.[8] Neither the experimental technique, nor the theory or data treatment, has progressed much further since then, mainly because of the limited field of application. Nevertheless, the LAXS technique is quite useful for understanding the local structure in amorphous samples, e.g. for first and second hydration shells of metal ions in aqueous solutions. The information provided with this method is in some respects complimentary to that from the XAFS measurements for solutions and amorphous phases.[6] For example, more information can be obtained of outer-shell coordination around metal ions when the LAXS technique is used. One drawback is, however, that high concentration of the metal ion is required for LAXS measurements in order to make the metal-ligand contributions more prominent than those from the solvent. This is due to the fact that in a LAXS experiment all distances between pairs of atoms in a sample contribute to the x-ray scattering, in contrast to the XAFS method where only the interactions around the absorbing atom are probed by the backscattering of the ejected photoelectron.

Vibrational spectroscopy (Section *3*) is another technique, which strongly benefits from the technological progress. Both for infrared (IR) absorption spectroscopy and Raman scattering the instrumentation has reached a high degree of sophistication allowing

extremely sensitive and rapid measurements.[9] In particular, Raman spectroscopy has been revolutionised by the use of lasers as a source of radiation, and by the introduction of the Fourier transform technique, which was since the 1970s already well established for the IR absorption spectroscopy. Another breakthrough occurred when the extremely sensitive CCD detectors were developed (originally for video cameras) and applied for the use in Raman microscopes.[10]

Vibrational spectra are often used in a qualitative way to identify substances and characteristic groups. Finger-print techniques and group frequencies are then used to recognise a specific pattern of the vibrational transition energies.[9,11] Molecular vibrations are also sensitive and useful for comparisons of changes in the bond character in different complexes. However, in order to make detailed interpretations of the chemical bonding, analyses accounting for all possible vibrational modes and their interactions in the molecules, should be performed. This can be achieved by a so-called *normal coordinate analysis*, which in general is a complicated task. Even though the theory is well established, its application requires great care, since there are always more unknown force constants than the experimentally observed vibrational frequencies.[11,12] Correlations and approximations have to be introduced for the force constants and the interactions of the vibrational modes in a molecular system, with careful consideration of the validity of the model. In the present study, normal coordinate analyses have been used to get information of the metal-metal bond and the metal-cyanide bonding in a series of Pt-Tl cyano complexes.

A detailed description of the x-ray absorption fine structure spectroscopic (XAFS) technique and the data treatment methods used, is given in Section *1*. Brief accounts of the LAXS and vibrational spectroscopic methods used, follow in Sections *2* and *3* of this thesis.

Experimental methods

1. X-ray absorption spectroscopy, XAS

1.1 Absorption of x-rays in matter. Electromagnetic radiation in the x-ray region, about 0.1 to 50 Å, is a most powerful probe in the structural characterization of matter. Soon after the discovery of x-rays in 1895 by Wilhelm Röntgen, intensive studies on the interaction of x-rays with different materials started. The oscillating electric field of the electromagnetic radiation interacts with the electrons bound in an atom. Either the radiation will be scattered by these electrons, or absorbed and excite the electrons. It was found that a narrow parallel monochromatic x-ray beam of intensity I_0 passing through a sample of thickness x will get a reduced intensity I according to the expression:

$$\ln (I_0 / I) = \mu x \qquad (1)$$

where μ is the *linear absorption coefficient*, which depends on the types of atoms and the density ρ of the material. It is more convenient to use the *mass absorption coefficient* (μ/ρ),[♦] which is a measure of the photoelectric absorption (neglecting scattering processes), and is independent of the physical state of the absorbing elements of the sample. This gives the mass absorption law:

$$I(\lambda) / I_0(\lambda) = \exp[-(\mu/\rho)\, \rho x]$$

where the mass absorption coefficient (μ/ρ) of the absorber decreases within the x-ray range with decreasing wavelength λ, except at certain energies where the absorption increases drastically, and gives rise to an *absorption edge*.[♣] Figure 1a shows the sudden increases in the x-ray absorption of a thin foil of platinum metal with decreasing photon wavelength.[6] Each such *edge* occurs when the energy of the incident photons is just sufficient to cause excitation of a core electron of the absorbing atom to a continuum state, *i.e.* to produce a *photoelectron*.[13] Thus, the energies of the absorbed radiation at these edges correspond to the binding energies of electrons in the K, L, M, etc, shells of the absorbing elements. In Sommerfeld´s notation the absorption edges are labeled in the order of increasing energy, K, L_I, L_{II}, L_{III}, M_I,…., corresponding to the excitation of an electron from the 1s ($^2S_{½}$), 2s ($^2S_{½}$), 2p ($^2P_{½}$), 2p ($^2P_{3/2}$), 3s ($^2S_{½}$), …, orbitals (states), respectively.[14]

♦ Tabulated *e.g.* in *International Tables of Crystallography*, Volume C, Ed. A.J.C. Wilson, Kluwer Academic Publishers, Dordrecht, 1995

♣ Beyond each absorption edge the mass absorption coefficient is approximately proportional to $Z^4\lambda^3$. With increasing atomic number Z, the absorption coefficient increases. For a given Z, decreasing λ (increasing energy) leads to decreasing absorption coefficient.[15a]

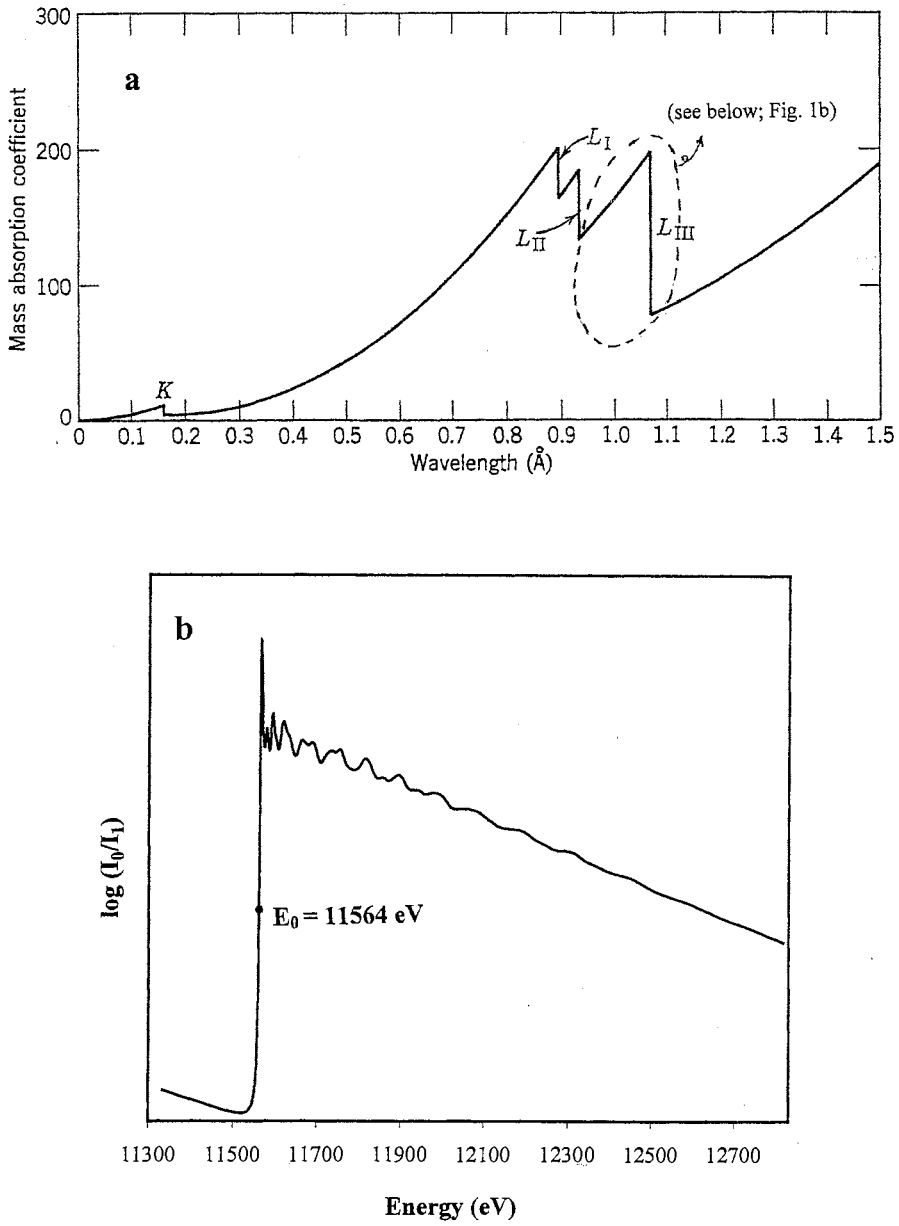

Figure 1. a) Plot of the mass absorption coefficient for platinum *vs.* wavelength, showing positions of the *K* and *L* absorption edges (ref. 6); b) X-ray absorption spectrum of platinum metal over the range 11.3 to 12.8 keV, showing the Pt L_{III}- edge and XAFS oscillations. The tabulated threshold energy value is E_0 = 11564 eV. Note that the wavelength and energy scales are in opposite directions.

The threshold energy of the absorption edge, is the energy when the photoelectron is released. This E_0 value is normally taken as corresponding to the first inflection point on the low energy side of the edge (see Section *1.4.3*). For calibrations of the energy scale in XAS measurements, often a Cu-foil with a peak at 8980.3 eV on the Cu *K-edge*, is used (see Figure 2a).[16a]

The high-energy side of the absorption edge is found to have a fine structure, which can be related to structural properties of the material. This phenomenon, nowadays referred to as *X-ray Absorption Fine Structure (XAFS),* has been known for a long time,[1] but its usefulness was not fully recognized until much later by the work by Stern et al.[17] This became the starting point of a remarkable development, to make synchrotron-based *X-ray Absorption Spectroscopy (XAS)* a very powerful and versatile structural probe for studying the local structure around most elements of the periodic table (except the lightest ones).[4]

1.2 Absorption edge structure

1.2.1 Electronic transitions and photoelectron production. The following cases can be distinguished for a sample irradiated by x-rays of increasing energy E, close to an absorption edge (threshold energy E_0) of the absorbing atom:[14]

- For $E < E_0$, the *pre-edge* region (Figure 2b), the probability for x-ray absorption is low, except for electronic transitions within the atom to unfilled or partially filled energy levels, which can give rise to sharp pre-peaks before the edge (Figure 2c).
- For $E \approx E_0$, the *edge* region, electronic transitions occur with high probability to unoccupied bound states or continuum states.
- For $E > E_0$, the *near-edge* and *EXAFS* regions, electronic transitions occur to continuum states, and photoelectrons are ejected with the kinetic energy $E_k = E - E_0$.

The wavelength of the ejected photoelectron (from an 1s orbital for the Cu K edge, and a 2p orbital for the Pt L_{III} edge) is given by de Broglie´s expression:

$$\lambda_e = \frac{h}{m_e v} = \frac{h}{P} = \frac{h}{[2m_e (E-E_0)]^{1/2}} \qquad (2)$$

where m_e is the mass of an electron, E is the energy of the incident photon, and E_0 (the threshold energy) is the minimum energy which is sufficient to liberate a core electron.

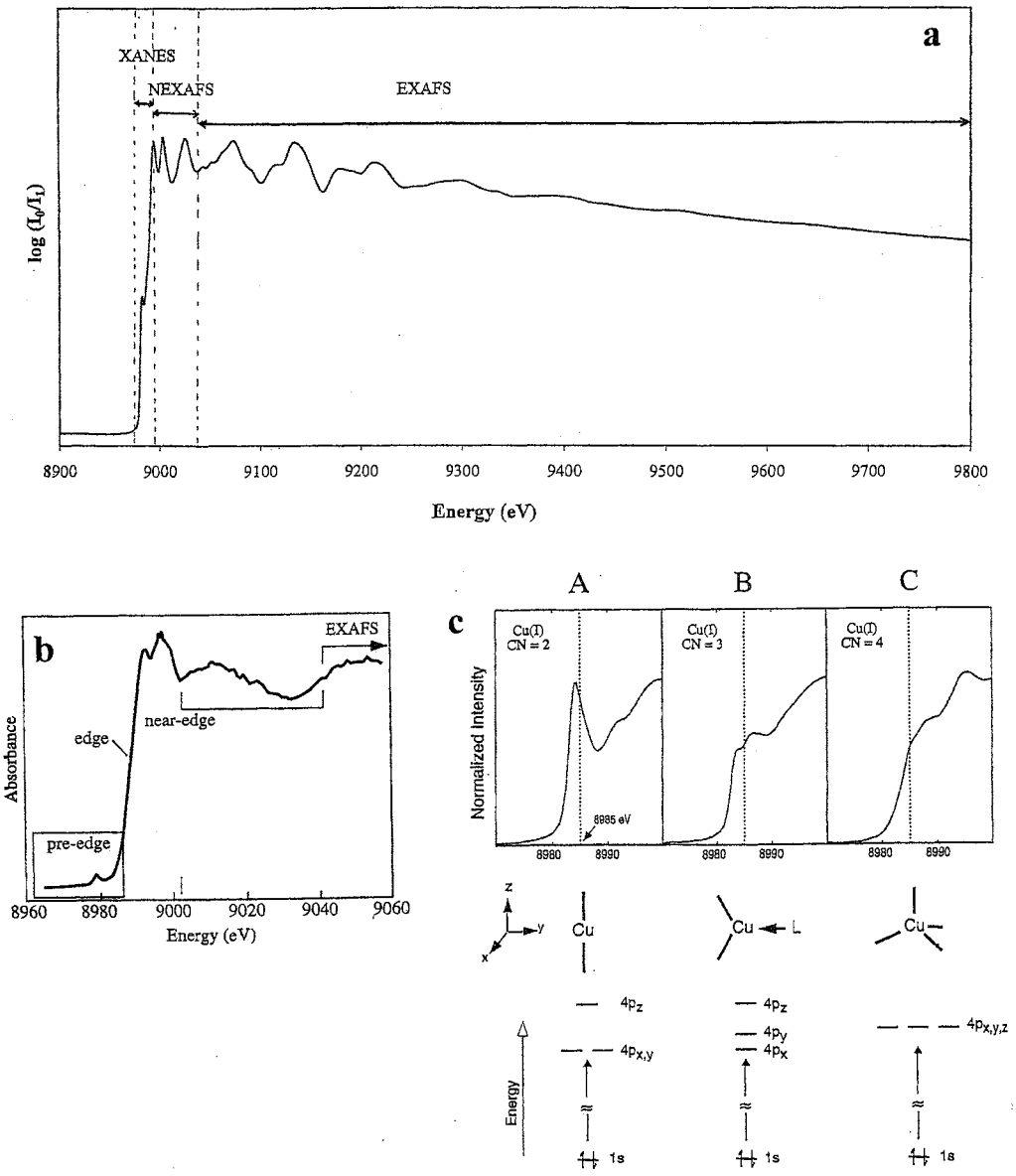

Figure 2. a) K-edge x-ray absorption spectrum of Cu metal, showing the XANES, NEXAFS and EXAFS regions. Note the edge-peak at 8980.3 eV corresponding to an electronic transition in the XANES region. b) K-edge spectrum of a $[CuCl_4]^{3-}$ complex showing a pre-edge feature, and the start of the EXAFS region (ref. 4b). c) Pre-edge features corresponding to 1s-4p electronic transitions within copper(I) complexes with different geometry: (**A**) linear two-coordinate, (**B**) three-coordinate, and (**C**) four-coordinate distorted tetrahedral (ref. 4b).

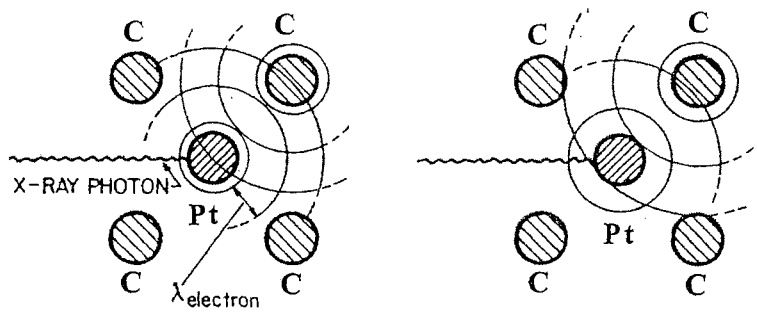

Figure 3. Schematic representation of the backscattering of platinum L_{III} edge photoelectron waves by nearest neighbor carbon atoms in a planar $[Pt(CN)_4]^{2-}$ complex at two different energies of the incident x-ray photons. Constructive (left) and destructive (right) interference between the outgoing and backscattered photoelectron waves give rise to the EXAFS oscillation.

The outgoing photoelectron wave can be backscattered from the surrounding atoms. As the kinetic energy of ejected photoelectron increases (*i.e.* its wavelength decreases), the outgoing and the backscattered photoelectron wave will interfere. This interference will induce variations in the electron density of the absorbing atom, which depend on the energy of the ejected photoelectron. Constructive interference will increase the electron density and increase the probability of the photon to be absorbed. Therefore, a change in interference from destructive (minimum in the absorption) to constructive (maximum in the absorption) will give rise to the oscillations in the absorption observed after the edge.[4] No XAFS oscillations are observed for a monoatomic gas, since there are no close neighbors for backscattering.[13] Figure 3 shows a schematic illustration of this effect for a platinum atom surrounded by carbon atoms in a square-planar coordination figure.

1.2.2 Absorption edge regions: XANES, NEXAFS, EXAFS. The absorption spectrum at an absorption edge has traditionally been divided into two major regions (XANES and EXAFS), where the EXAFS region refers to the oscillatory structure in the x-ray absorption coefficient starting at an energy about 50 eV higher than the threshold energy E_0.[2] In recent years important progress in curved-wave and multiple scattering theory has been made and implemented in the data analysis (*e.g.*, in the GNXAS and FEFF programs),[4,5,18] which now allows further structural information to be extracted by including the near-edge part of the XANES region in the analyses. Following the suggestion by Rehr et al.,[5] based on the new advancements in the data treatment, it seems more practical to divide the absorption spectrum in the following way (see Figure 2a):

1. XANES. The first region contains the *X-ray Absorption Near Edge Structure, XANES,* within about ± 10 eV of the main absorption edge. Traditionally, XANES also included the NEXAFS region (see below). The theoretical description of the features in this edge region is still not fully developed and it has been suggested that *atomic-XAFS* should be included for a full description (see Section *1.4.5*).[5]

Before the edge (*pre-edge* region) there are a series of features due to electronic transitions from a core level (1s, 2s, etc.) to unoccupied or partially occupied energy levels (*cf.* Figure 2c).[4b,14,19a] On top of the absorption edge there is frequently a sharp and intense so-called "white" line (see Figure 1b). This is due to transitions of the core electron to unoccupied energy levels near the continuum; since these energy levels are closely spaced, the probability of absorption will increase. The pre-edge features can give information on coordination geometry, which affects the energy levels in the valence shell, as shown for some Cu(I) complexes in Figure 2c.

The edge position is influenced by the oxidation state of the absorbing atom. A change of one unit in oxidation state makes a significant change in the energy of the electronic transitions, which can give a shift of several electron volt in the position of the edge.[19a] The change in ionization energy with oxidation state is mostly affecting the potential energy of the electron, which is due to contributions from the coulombic interactions between the electrons and the nuclei.[19a] At a higher oxidation state the attraction between the core electrons and the nucleus will increase, since the removal of valence electrons to some extent reduces the shielding of the core electrons from the nucleus. This will shift the edge features to higher energies, *e.g.* the vanadium absorption edge in a series of vanadium oxides shifts to higher values by about 2.5 eV for each unit increase in oxidation number. For L_{III} edges of lanthanides, corresponding shifts of 6-8 eV per unit increase in oxidation number have been reported.[19a]

2. NEXAFS. The *Near-Edge X-ray Absorption Fine Structure* region, extends from a few eV to about 50 eV above the edge (Figure 2a). This region often contains intense spectral features, which are due to scattering of photoelectrons ejected with relatively low kinetic energy.[5] Multiple scattering, mostly dominated by contributions from scattering pathways between the atoms of the first shell around the absorber, is prominent in this region. In addition, relatively long pathways involving tightly bonded atoms beyond the first shell can give significant contributions (see Figure 4b), even for complexes in solution.

Thus, the edge structure in the XANES and NEXAFS regions is sensitive to the geometrical arrangement of the atoms surrounding the absorber, and can give useful structural information. The features can *e.g.* serve as a fingerprint for the structural arrangement of atoms in a group or complex, and pre-edge transition energies can be reproduced by *ab-initio* calculations.[4b] However, even well beyond the threshold energy, the atomic background absorption $\mu_0(E)$ may exhibit white lines, resonances and jumps due to multi-electron transitions. Further improvements in the theoretical description are still needed for quantitative edge calculations.

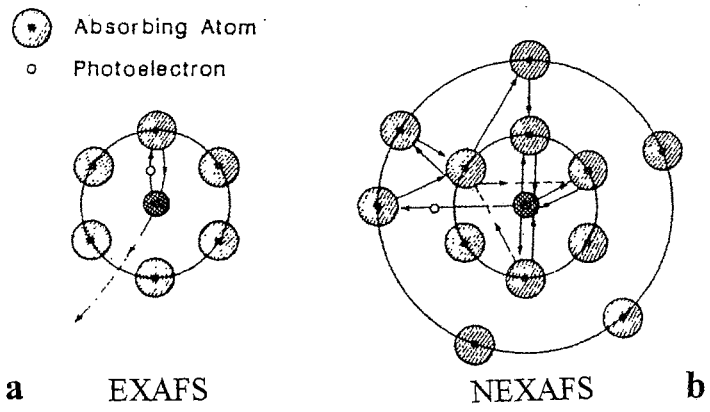

Figure 4. Schematic illustration of: a) single backscattering (SS) process dominating in the EXAFS region, and b) multiple scattering (MS) process, prominent in the NEXAFS region (ref. 13).

3. EXAFS. The third region, which extends from energies about 50 eV up to more than 1000 eV higher than the edge, is the *Extended X-ray Absorption Fine Structure* (EXAFS) region, and will be treated in more detail below. The EXAFS region is characterized by weak oscillations of low frequency, arising from backscattering of photoelectrons of high kinetic energy, mostly in single backscattering processes (Figure 4a). Previously, the analysis of EXAFS was largely restricted to the first coordination shell, giving information about the distance from the absorber to its near neighbors. However, this has dramatically changed in recent years due to the development of efficient computer codes, describing curved-wave scattering theory combined with high-order multiple scattering, which allows us to describe the EXAFS functions by calculations based on theoretical models for all kinds of systems.[5,20]

1.2.3 X-ray Absorption Fine Structure, XAFS. With the use of high-order multiple scattering theory implemented into the FEFF codes, these theoretical calculations can now extend into or describe the NEXAFS region, allowing a unified treatment of the EXAFS and NEXAFS regions. Therefore, the need to separate the EXAFS and NEXAFS regions has become less strict, and a common name *X-ray Absorption Fine Structure* (XAFS) is often used nowadays for these regions together, and also for this entire technique of structure determination. The development in theory, data treatment, and experimental techniques, in particular the modern synchrotron radiation sources, now makes the XAFS technique competitive with, and complementary to, high precision structural methods such as x-ray diffraction. For some complexes (*e.g.* bio-inorganic) and disordered materials, XAFS is the superior method for local structural determinations.[4] The multiple scattering calculations permit more definitive conclusions concerning distances and disorder, even beyond the first shell.

1.2.4 Lifetime of the Core Hole. When a photoelectron is ejected from the core level, an inner-shell vacancy "*core hole*" is created in the absorber. This excited state of the absorber atom has a finite lifetime, before it relaxes via different relaxation mechanisms, such as producing Auger electrons (for light elements), or emission of fluorescence photons (for heavy elements); *cf.* Figure 7b.[15b]

The time scale for this electronic excitation (the photoelectron ejection) depends on the time, which the incident photon takes to travel the diameter d of the inner shell. For example, the K-shell diameter d_K for oxygen can be approximated from $d_K \approx (2a_o / Z)$ to be

~0.13 Å (a_0 = Bohr radius; Z = atomic number). With c = $3 \cdot 10^{18}$ Å/s and d_K ~0.1 Å, we can estimate that the excitation takes place in about 10^{-17} to 10^{-18} seconds for oxygen.[21a]

The EXAFS oscillations are a result of the backscattering of the ejected photoelectron from the neighboring atoms. This is correlated to the probability that the photoelectron can return to the core hole. Thus, for this process the life time of the core hole is important, and can be estimated using the Heisenberg uncertainty principle: $\tau_h \cdot \Gamma \cong \hbar = 6.6 \cdot 10^{-16}$, where τ_h is the core hole lifetime (s) and Γ is the hole-state width (eV). The estimated hole-state widths Γ for the K and L_{III} shells are shown in Figure 5.[21a] For example, in the case of Pt L_{III}-edge, Γ is 5.31 eV (Appendix C, Reference 19). Therefore, the lifetime of its core hole is $\tau_h \sim 1.2 \cdot 10^{-16}$ s.

We can also calculate the time τ that a photoelectron takes for travelling the distance between the absorber and neighboring atom, *r*, and for going back to the core hole:

τ = (traveling distance)/ speed = $2r / v$

The speed v depends on the kinetic energy of the photoelectron, $E_k = E - E_0$. Since $E_k = \frac{1}{2}mv^2$, then $v = (2E_k / m)^{1/2}$. This can be expressed as a function of the photoelectron wave-vector* $k = [2mE_k]^{1/2} / \hbar$ (see Section *1.4.4*). Thus, $k = m / \hbar$, or, $v = \hbar k / m$, which gives the traveling time:

$\tau = 2mr / (k\hbar)$

For example, when $r \approx 2$ Å and $E_k = 60$ eV ($k \approx 4$ Å^{-1}), the traveling time for the photoelectron is about $\tau \approx 2.5 \cdot 10^{-17}$ sec, an order of magnitude shorter than the lifetime for core hole (in the case of Pt L_{III} edge, $\tau_h \sim 1.2 \cdot 10^{-16}$ sec). In practice, for the energy range corresponding to the EXAFS region $4 \leq k \leq 16$ Å^{-1}, the photoelectron basically sees the central atom with a core hole.[15b] If E_k is smaller and the photoelectron has low kinetic energy (low *k*-value), the traveling time τ is longer and becomes comparable with the lifetime of the core hole, τ_h, which reduces the amplitude of the EXAFS oscillation and makes the peaks in the XANES region broader (see Mean free path factor, Section *1.5.5*)

* *k* is the scattering variable.

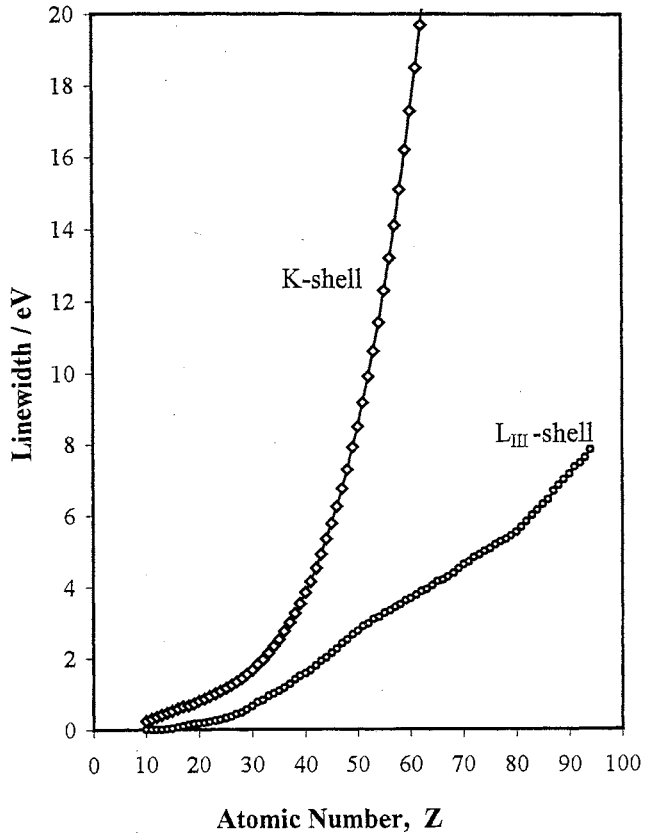

Figure 5. Natural core hole-state widths for K and L_{III} atomic energy levels (ref. 19, Appendix C)

1.3 Synchrotron-based XAFS.[22] X-ray absorption fine-structure (XAFS) spectroscopy can in principle be applied for almost all elements of the periodic table (see Table 1). In practice, however, there are a number of restrictions for the collection of useful data. The EXAFS oscillations are weak, and the information content depends on how wide the data-range is, which can be obtained with sufficient signal to noise ratio (see Section *1.7*). Dilute samples, such as metalloproteins, and light absorber elements (ligand atoms, and also calcium in the present study) require intense radiation, and are only possible to study with the use of synchrotrons as x-ray sources.[4]

1.3.1 Synchrotrons as x-ray sources. For producing synchrotron radiation, charged particles (electrons or positrons) which have been accelerated in a linear accelerator and have a speed close to that of light, are injected into a storage ring under high vacuum. The storage ring is not circular; it consists of curved sections (with small diameter 5-10 cm) joined with straight parts. Magnetic fields from strong magnets around the ring (bending magnets) force the electrons to follow the ring in the curved sections. When the high energy particles (3 GeV in SSRL) hit the curved parts, they lose part of their energy as *synchrotron radiation* which is emitted tangential to these curved sections. A radio frequency (*rf*) cavity in the ring occasionally "kick" the particles and increase their kinetic energy (Figure 6c).

The wavelength of the synchrotron radiation can be tuned by changing the magnetic field, *e.g.* with wigglers or undulators consisting of an array of dipole magnets, giving a continuous energy range from infrared to hard x-rays. The possibility to change the wavelength and also, the high brilliance of this radiation (number of photons per volume unit) allow many experiments which otherwise would be very difficult. XAFS spectroscopy has been developed, and is nowadays almost exclusively done by using x-ray radiation emitted from synchrotrons.

Starting from the early 80´s, the 2nd generation of synchrotron sources were built, which were exclusively designed for the production of "synchrotron light" for research purposes. It was then realized that insertion elements, such as wigglers and undulators, drastically improved the properties of the radiation, *e.g.* increased the brilliance (number of photons per volume unit) by several magnitudes. A wiggler also shifts the intensity maximum of the synchrotron flux to shorter wavelengths, which is useful for XAFS spectroscopy of most elements (Figure 6b). During the 90´s the 3rd generation of synchrotron sources were constructed, which are based on these insertion elements (Figure 6a).[16b,19b]

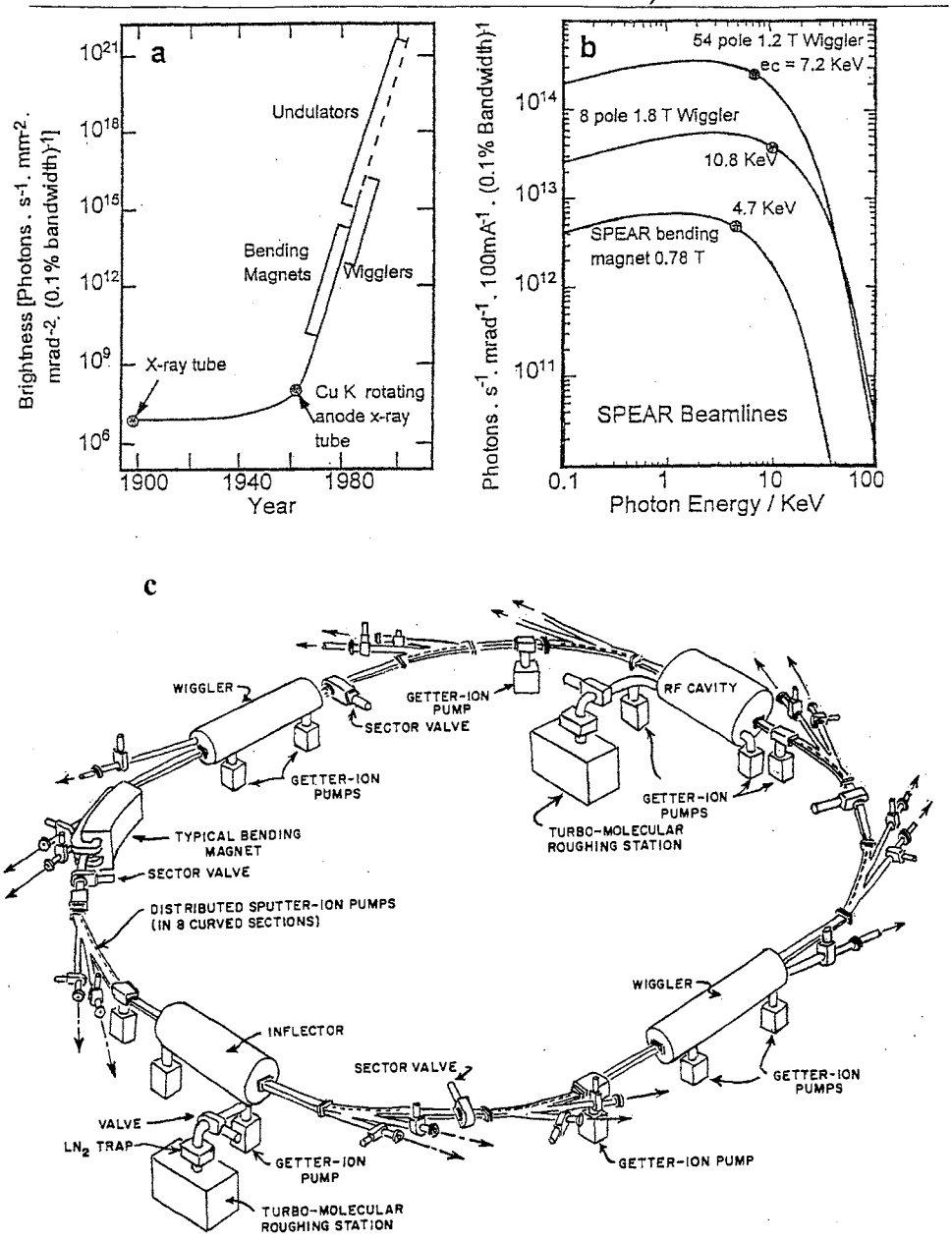

Figure 6. a) The development of x-ray sources. Bending magnets, wigglers and undulators have an increasing number of dipoles for bending the electron beam, which creates x-rays. The energy range from an undulator is smaller than that from a wiggler, and is less suited for scanning XAS spectra. b) Characteristic synchrotron spectra from the SSRL source SPEAR operated at 3 GeV (ref. 23). c) Schematic view of an electron-storage ring (Brookhaven National Laboratory) designed as a source of synchrotron radiation, showing one bending magnet and wigglers (ref. Winick, H.; Doniach, S; *Synchrotron Radiation Research*, Plenum Press, 1980, p.31, reproduced by permission).

There are a number of important advantages using synchrotrons as x-ray sources:

(1) An EXAFS experiment typically requires scanning an x-ray energy range of about 1000 eV. This is achieved by rotation of selected monochromator crystals (mostly Si or Ge) in special arrangements (see Section *1.8.1*).[19c]

(2) A high x-ray flux is required in an XAS experiment in order to obtain high signal-to-noise data during a reasonable length of time for the data collection (in the order of 30 minutes per scan), in particular for dilute samples of the absorbing element. Synchrotron sources give x-rays of much higher brilliance and five or more orders of magnitude greater flux than conventional laboratory x-ray sources (see Figure 6a).

(3) The high stability required in flux, energy, and beam position for an XAS experiment can be achieved with a synchrotron x-ray source.[19b,22]

1.3.2 Availability of absorption edges.[22] When planning an experiment, a synchrotron beamline with a suitable flux distribution for the energy range of the absorbing element should be chosen. Nowadays, synchrotron beamlines are well equipped for experiments using relatively hard x-rays ($\lambda < 5$ Å).

K-edge spectra show low absorption probability (*cf.* Figure 1a), but high fluorescence yield for each photon absorbed (*cf.* Figure 7c), although the fluorescence yield goes down for lighter elements (0.17 for Ca and only 0.0058 for O, *cf.* Figure 7d). K-edge measurements are only possible for elements with $Z \leq 53$, because for higher K-edge energies, the synchrotron flux becomes too low (*cf.* Figure 6b). Moreover, for heavier elements, the hole-state width (Γ) of the K-shell becomes quite large, resulting in short lifetime of the core hole, τ_h (see Figure 5; p.12). A shorter core hole lifetime τ_h, will give broader peaks in the XANES region (*cf.* Section *1.2.4*).[15a]

Elements with K-edge energies lower than about 2500 eV, including C (284 eV), N (410 eV), O (543 eV), F (697 eV), Na (1071 eV), Mg (1303 eV), Al (1559 eV), Si (1839 eV), and P (2149 eV), require soft x-ray vacuum beamlines at synchrotron sources and the experiment is technically much more difficult than with hard x-rays in air. The reason is that x-rays softer than about 2500 eV (5 Å) are strongly absorbed by air and by the Be windows (transparent for x-rays) which are necessary to keep the ultra high vacuum (UHV $< 10^{-9}$ torr) within the electron storage ring of the synchrotron. Despite these difficulties in such measurements, K-edge spectra of light elements can give valuable information on the chemical bonding, by comparing the peaks in the edge region with *ab initio* calculated electronic transition energies.

For the heavy elements the triple L-edge spectra are in an accessible energy range. The fluorescence yield is relatively low, although increasing with increasing atomic number, 0.33 for Pt (11.56 keV) and 0.49 for U (17.17 keV), *cf.* Figure 7c. The edge jump generally increases in the order $L_{III} > L_{II} > L_I$ which makes the L_{III} edge the most sensitive one (see Figure 1a). However, for elements with relatively low L-edge absorption energies, the L_{III} and L_{II} edges can be rather close, which limits the useable data range. For example, for Ba the synchrotron flux is too low at the K-edge (37.44 keV or 0.331 Å), and the usable *k*-range between the L_{III} and L_{II} edges at 5.24 and 5.62 keV, respectively, is only up to $k_{max} \approx 9$ Å^{-1}. The values of the K and L absorption edges for all elements in the periodic table are given in Table 1.

M edge spectra occur at lower energies and are more complex (five edges), and are seldom used for XAS studies. Even for the heaviest elements the L edges can be used, *e.g.* the U L_{III} edge at 17.17 keV (0.722 Å) is still in a convenient range for EXAFS measurements.[22]

1.3.3 Usefulness and limitations of XAS. The main advantage of synchrotron based x-ray absorption spectroscopy (XAS), as compared to diffraction techniques, is its ability to probe the local structure around almost any specific element in the periodic table (except the lightest). The technique can be used for absorbing atoms in any aggregation state (solid, liquid, or gas), in all kinds of environment: crystalline solids, glasses, amorphous phases, liquids and solutions. With optimal experimental conditions, XAFS studies can be made at trace levels (< 1000 ppm), which is useful *e.g.* for studies of metal complexes on surfaces, catalysts, metal sites in bio-inorganic samples, etc.[4]

The local structure can be probed up to 5-6 Å around the absorbing central atom, but requires that multiple scattering effects are taken into account in the data analysis. Due to the general reduction of the XAFS amplitude for longer distances and weakly coordinated atoms (see Section *1.5*), the inner-shell distances are more easily detected and can be determined with higher accuracy than outer shell distances.[4] The edge structure in the XANES region contains peaks corresponding to electronic transitions, which are sensitive to the electronic structure of the absorber and its chemical bonding. Together with analyses of the multiple scattering in the NEXAFS region, this also yields information about the coordination geometry.

X-ray Absorption Edge Periodic Table of the Elements

Z Symbol	1 H																2 He
L3																	
L2																	
L1																	24.6
K	16																
Z Symbol	3 Li	4 Be											5 B	6 C	7 N	8 O	9 F	10 Ne
L3																		21.6
L2																		21.7
L1																		48.5
K	54.7	111.5											188	284.2	409.9	543.1	696.7	870.2
Z Symbol	11 Na	12 Mg											13 Al	14 Si	15 P	16 S	17 Cl	18 Ar
L3	30.5	49.2											72.5	99.2	135	162.5	200	248.4
L2	30.5	49.6											72.9	99.8	136	163.6	202	250.6
L1	63.5	88.6											117.8	149.7	189	230.9	270	326.3
K	1070.8	1303.0											1559.0	1839	2149	2472	2833	3205.9
Z Symbol	19 K	20 Ca	21 Sc	22 Ti	23 V	24 Cr	25 Mn	26 Fe	27 Co	28 Ni	29 Cu	30 Zn	31 Ga	32 Ge	33 As	34 Se	35 Br	36 Kr
L3	294.6	346.2	398.7	453.8	512.1	574.1	638.7	706.8	778.1	852.7	932.5	1021.8	1116.4	1217.6	1323.6	1433.9	1550.0	1678.4
L2	297.3	349.7	403.6	461.2	519.8	583.8	649.9	719.9	793.3	870.0	952.3	1044.9	1143.2	1248.1	1359.1	1474.3	1596.0	1730.9
L1	378.6	438.4	498.0	560.9	626.7	695.7	769.1	844.6	925.1	1008.6	1096.7	1196.2	1299.0	1414.6	1527.0	1652.0	1782.0	1921.0
K	3608.4	4038.5	4492	4966	5465	5989	6539	7111.8	7709.0	8333.0	8980.3	9659	10367	11103	11867	12658	13474	14326
Z Symbol	37 Rb	38 Sr	39 Y	40 Zr	41 Nb	42 Mo	43 Tc	44 Ru	45 Rh	46 Pd	47 Ag	48 Cd	49 In	50 Sn	51 Sb	52 Te	53 I	54 Xe
L3	1804	1940	2080	2223	2371	2520	2677	2838	3004	3173	3351	3538	3730	3929	4132	4341	4557	4782
L2	1864	2007	2156	2307	2465	2625	2793	2967	3146	3330	3524	3727	3938	4156	4380	4612	4852	5104
L1	2065	2216	2379	2532	2698	2866	3049	3224	3412	3604	3806	4018	4238	4465	4698	4939	5188	5453
K	15200	16105	17038	17998	18986	20003.9	21044	22117	23220	24350	25514	26711	27940	29200	30491	31814	33169	34561
Z Symbol	55 Cs	56 Ba	57 La	72 Hf	73 Ta	74 W	75 Re	76 Os	77 Ir	78 Pt	79 Au	80 Hg	81 Tl	82 Pb	83 Bi	84 Po	85 At	86 Rn
L3	5012	5247	5483	9561	9881	10207	10535	10871	11215	11564	11919	12284	12658	13055	13419	13814	14214	14619
L2	5359	5624	5891	10739	11136	11544	11959	12385	12824	13273	13734	14209	14698	15200	15711	16244	16785	17337
L1	5714	5989	6266	11271	11682	12100	12527	12968	13419	13880	14353	14839	15347	15861	16388	16939	17493	18049
K	35985	37441	38925	65351	67416	69525	71676	73871	76111	78395	80725	83102	85530	88005	90526	93105	95730	98404
Z Symbol	87 Fr	88 Ra	89 Ac															
L3	15031	15444	15871															
L2	17907	18484	19083															
L1	18639	19237	19840															
K	101137	103922	106755															

Z Symbol	58 Ce	59 Pr	60 Nd	61 Pm	62 Sm	63 Eu	64 Gd	65 Tb	66 Dy	67 Ho	68 Er	69 Tm	70 Yb	71 Lu
L3	5723	5964	6208	6459	6716	6977	7243	7514	7790	8071	8358	8648	8944	9244
L2	6164	6440	6722	7013	7312	7617	7930	8252	8581	8918	9264	9617	9978	10349
L1	6548	6835	7126	7428	7737	8052	8376	8708	9046	9394	9715	10116	10486	10870
K	40443	41991	43569	45184	46834	48519	50239	51996	53789	55618	57486	59390	61332	63314
Z Symbol	90 Th	91 Pa	92 U	93 Np	94 Pu	95 Am	96 Cm	97 Bk	98 Cf	99 Es	100 Fm	101 Md	102 No	103 Lw
L3	16300	16733	17166	17606.2	18053	18504.1								
L2	19693	20314	20948		22258									
L1	20472	21105	21757		23102									
K	109651	112601	115606		121760									

* X-ray binding energies for the elements are given in electron volts. X-ray wavelength (Å) = 12398.4/eV

Data from Center for X-ray Optics X-ray Data Booklet, PUB-490 Rev, LBL, Berkeley, CA.

Graham N. George, SSRL May 1993

Table 1. X-ray absorption edge periodic table of the elements (G. Graham, SSRL, 1993)

The XAFS region gives average interatomic distances and information on the number and chemical identities of near neighbors.[22] However, XAFS provides essentially no information on long-range order in a solid, because of the many multiple scattering paths which are possible outside the near-neighbor distances.[5] Even for the well-defined distances corresponding to the hydrogen bonded second hydration shells around highly charged ions in aqueous solution, multiple scattering within the first hydration shell dominates over the single back-scattering path from the oxygen atoms of the second hydration sphere.[24] In addition, there is a strong reduction of the amplitude of the XAFS function for long distances,[4] which often makes large angle x-ray diffraction the more suitable method for outer shell distances for amorphous phases, (see Section *2.1*).[22,24]

The usefulness of XAFS as a technique for structural analysis depends on accurate knowledge of the phase shifts and scattering amplitudes in the XAFS formula (see Section *1.5.1* and *1.5.2*). The *ab initio* theoretical calculations of these parameters by means of the FEFF program, allow inner shell distances to be determined with an accuracy of about ±0.01 Å and in favorable cases coordination numbers within ± 10 % (normally not better than about 25%, *cf.* Section *1.7*).[5,20]

1.3.4 Principles for measurement of x-ray absorption spectra. Figure 7a gives a schematic overview of the events occurring when irradiating a sample. The incident x-ray beam has the energy E (eV), wavelength λ and intensity I_0. For a sample of thickness x (cm) and density ρ (g.cm^{-3}) the transmitted intensity I is given by equation (1):

$$I = I_0 \exp(-\mu x)$$

where μ is the *linear absorption coefficient* (cm^{-1}) for the sample. Often the *mass absorption coefficient* (μ/ρ) (cm^2·g^{-1}) is used, which is roughly independent of the physical state of the material and is approximately additive to give the linear absorption of the sample:

$$\mu = \rho \sum f_i (\mu/\rho)_i \qquad (3)$$

in which f_i is the mass fraction of the element i with the mass absorption coefficient $(\mu/\rho)_i$. The EXAFS function, $\chi(E)$, is defined as the modulation in the absorbance, *i.e.*:

$$\chi(E) = \frac{[\mu(E) - \mu_0(E)]}{\mu_0(E)} \qquad (4)$$

where $\mu(E)$ is the measured absorbance while $\mu_0(E)$ is the "atomic background absorption" (absorption for the isolated atom in the field of its neighbors, without specific interactions).[18]

Two commonly used experimental detection methods for XAS studies are based on measurements of: 1) *transmission*, or 2) *fluorescence*. The transmission method is used typically for samples with high concentrations (> 2 wt %) of the absorber, and measures the direct absorption by the sample. In the fluorescence method the absorption is measured indirectly by detection of the fluorescent x-rays emitted when the core hole is filled. The intensity of the x-ray fluorescence is proportional to the number of absorbed photons, but it is competing with other processes, *e.g.* emission of *Auger electrons*. When the core hole is filled, the released energy can alternatively be used to eject Auger electrons, usually from the same shell (see Figure 7b). Therefore, the yield for emitting fluorescent x-rays varies considerably (between 0 to 1), and is higher for heavier elements, see Figure 7c,d.

An illustration of the experimental arrangements required for two types of XAS experiments is shown in Figure 8. The setup for a fluorescence detection experiment, using a *Lytle* detector, differ from a transmission experiment only in the placement of the second ion chamber, *i.e.* the *Lytle* detector (Figure 9), and in the orientation of the sample. The fluorescence is measured from the front of the sample and is used for samples with low concentrations of the absorber (< 2 wt %) and/or high matrix absorption. This method is also used for very small samples.

1.3.5 Transmission XAS measurements. In the transmission experiment, the sample is aligned perpendicular to the x-ray beam, with the second detector placed behind it.[22] In order to avoid errors in the measurements of the EXAFS amplitudes, it is important to choose a suitable thickness x of the sample. The optimum sample thickness depends on the energy of the absorption edge for the element being measured. Statistically, the optimum S/N value is obtained when $\ln(I_0 / I) = \Delta\mu \cdot x = 2.6$ (*i.e.* $^{10}\log (I_0 / I) = 1.1$) over the absorption edge ($\Delta\mu$ is the edge step). However, the amplitude of the absorption signal can be reduced by a number of experimental factors, such as leakage through an inhomogeneous solid sample (pinholes and particle size), fluorescence from the sample, harmonics and detector efficiency with variations in wavelength, etc. These factors decrease with decreasing sample thickness. Empirically, it has been found that for a well-conducted experiment, an edge step of $\Delta\mu \cdot x < 1.5$ should give errors in the amplitude of less than 5%.

The most commonly used detectors for transmission measurements are gas-filled ion chambers. The choice of gas or gas mixture depends on the energy of the beam and the desired amount of absorption of the incident beam.[13]

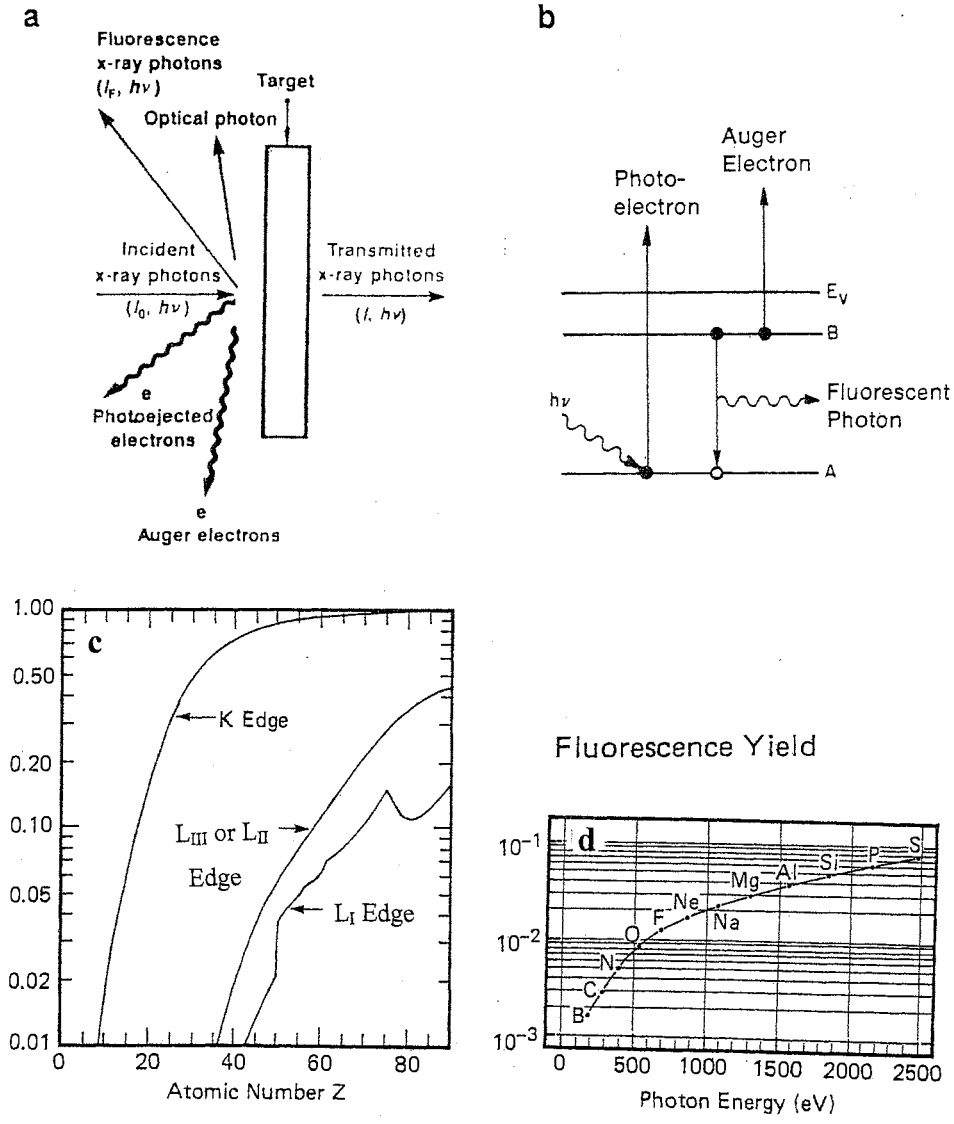

Figure 7. a,b) X-ray absorption of an incoming beam with intensity I_0 by a sample. Primary effect: attenuation of transmitted beam to intensity I and generation of photoelectrons. Secondary effects when filling the core hole: fluorescent x-rays and Auger electrons (ref. 13). c) Yield of fluorescent x-rays after exciting K and L shells, as a function of atomic number Z. d) Fluorescence yield of light elements after exciting the K-shell (ref. 21b).

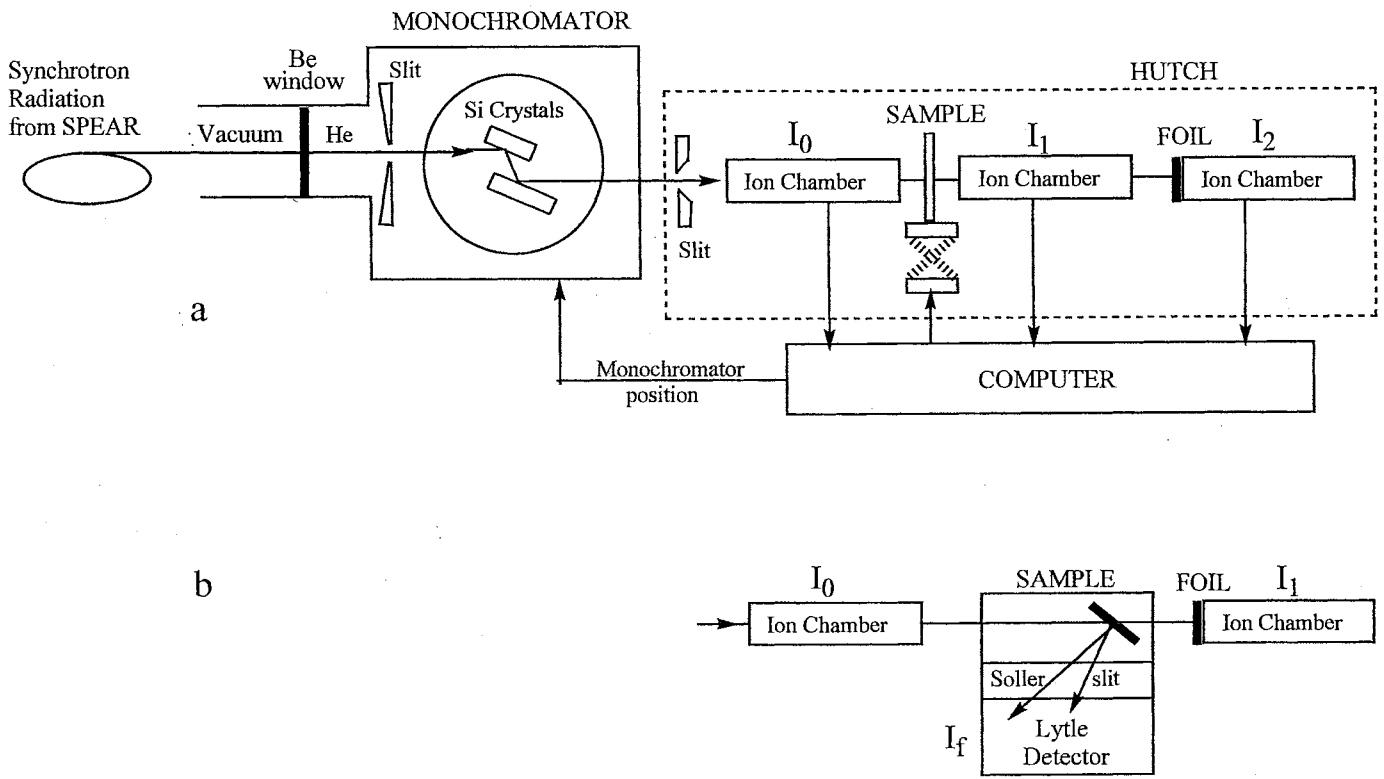

Figure 8. Experimental arrangements for XAS measurements: a) Transmission setup (side view) with a metal foil for calibration of the energy scale; b) Fluorescence measurement (top view) with a Lytle detector; See Section *1.8.2* (adapted from ref. 25).

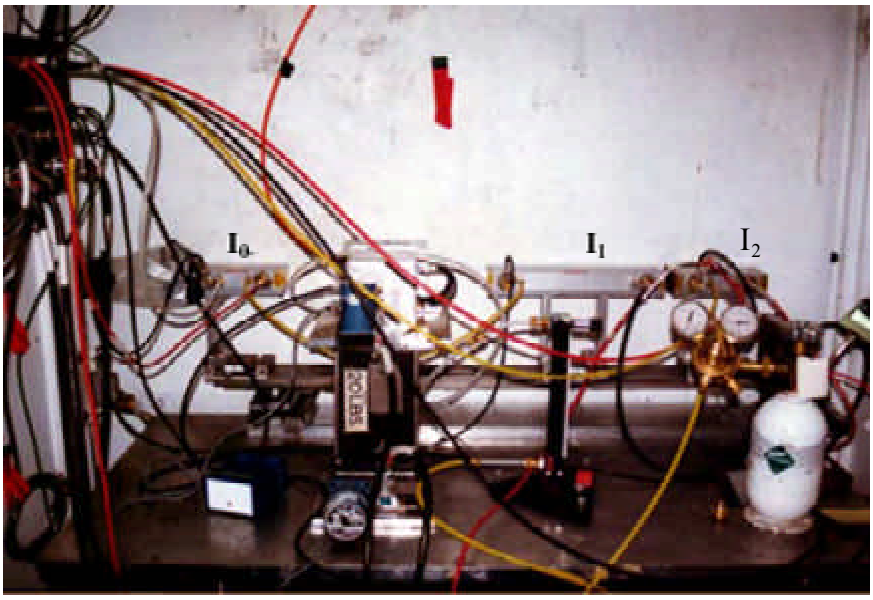

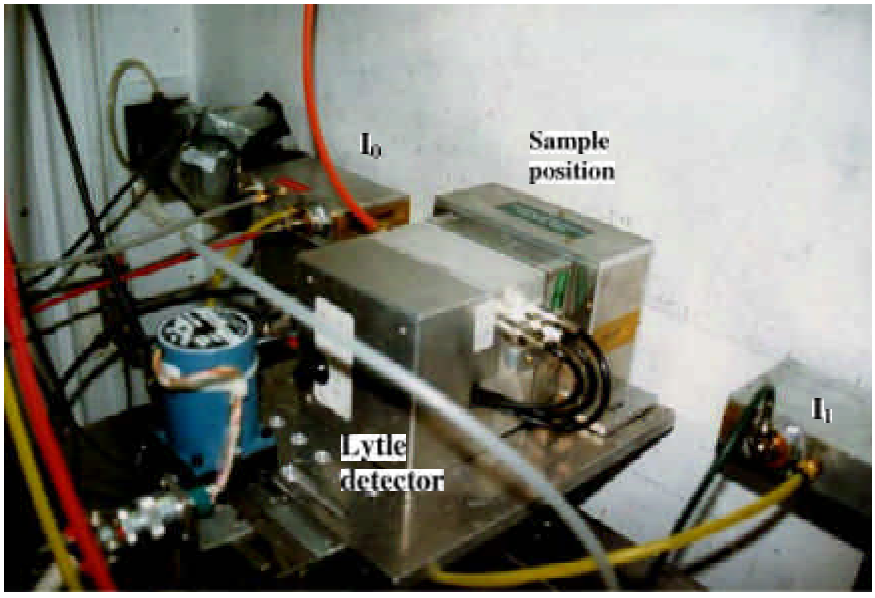

Figure 9. Experimental arrangement for an XAS measurement in fluorescence mode, using the Lytle detector. The ion chambers are marked I_0 and I_1.(Beam line 4-1; SSRL)

In the same way as for optical absorption spectroscopy, the intensity I_0 of the incident beam and the intensity I_1 of the transmitted beam, are measured. The first ion chamber is filled with a gas mixture, which absorbs up to 20 % of the incident beam. The second ion chamber placed after the sample measures the intensity of the transmitted beam, and is filled with a gas mixture chosen to absorb about 20-40 % of the beam. Between the second and a third ion chamber a reference sample, often a metal foil, is placed to enable an internal calibration of the energy scale (Figure 8a). The third ion chamber is filled with a gas-mixture absorbing most of the remaining beam.

The gases N_2, Ne, Ar (in increasing order of absorbance), and mixtures of these gases with He are commonly used in these ion chambers (Figure 10).[13] The densities, absorption edge energies, and absorption coefficients for these gases are listed in Table 6 (see Section *1.8.3*).

Transmission measurements can be used for XAFS studies of absorbers with Z > 16-20 at high concentrations (> 2 wt %). For absorbers with edge energies in the range 2000 to 4000 eV, absorption of the x-rays by air becomes significant, and He gas is generally used in the beam path and the sample chamber. At these low energies, self absorption in the sample can become a serious problem and very thin samples may be required.[13,16c]

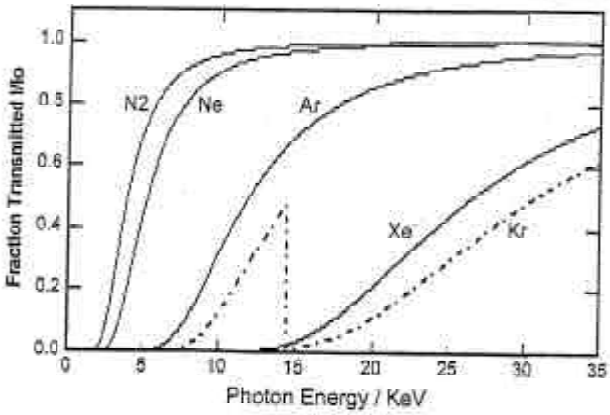

Figure 10. Detector gases: Fraction of transmission *vs.* energy for common ion chamber detector gases at atmospheric pressure and 10 cm path length. Note that it is preferable to use Kr (with K-edge at 14326 eV), instead of the more expensive Xe, in the energy range above 15 keV (ref. 23).

Another type of problem may originate from the absorption process in the sample. When a photoelectron is ejected, a core hole is created for a short time in the absorbing atom (Figure 7b). The process of filling the core hole gives fluorescent x-ray photons of characteristic energy, typically a K_α line of the absorbing element for a K-edge experiment, but also softer x-rays and Auger electrons. Thus, the sample becomes a secondary source emitting fluorescent radiation in all directions. If the sample is placed too close to the ion chambers I_0 or I_1 (see Figure 8a), a considerable amount of the fluorescent photons from the sample may enter the ion chambers. Two different effects are possible:

1) In the ion chamber I_1 this will add to the intensity of the transmitted photons (I_1) and cause an apparent decrease in the measured absorption, $\log(I_0/I_1)$, which is not easy to notice since the fluorescence signal is proportional to the absorption, (I_f/ I_0).[16c]
2) In the ion chamber I_0, an added fluorescence signal may cause oscillatory variations in the curve (I_0 / rtc) *vs.* energy. This is a sign that the fluorescence from the sample is strong and will distort the measured absorption. Such an addition of the fluorescence signal to the ion chamber I_0 will look like an increase in the measured absorption and therefore, it will increase the apparent amplitude of the EXAFS signal (this is probably one reason for high amplitude reduction factors in the data treatment, see Section *1.5.4*).

A simple way to reduce the effect of fluorescence from the sample is to increase the distance from the sample to the detectors.[16c]

1.3.6 Fluorescence XAS measurements: The absorption of an x-ray photon from the incident beam results in photoelectron ejection, which creates a core-hole in the K or L shell of the absorber. When the core-hole is filled by an electron from the next shell (Figure 7b) another photon is created with an energy corresponding to the K_α or L_α emission lines of the absorbing atom. The intensity of this emitted fluorescent x-ray, I_f, is directly proportional to the amount of absorbed x-rays in the sample, and (I_f / I_0) is thus proportional to μ. However, there are a number of complications to consider:

- Other competing processes in the absorber, such as multiple electron excitation and Auger effects (Figure 7b), reduce the fluorescence yield.
- K_α or L_α emission lines are also excited from the other elements in the sample which creates a background.
- Scattering of the incident x-ray beam by the sample, which can be divided into two categories:

1) elastic scattering (diffraction) of x-ray photons by tightly bound atomic electrons without energy (or wavelength) change;

2) inelastic (Compton) scattering of x-ray photons interacting with loosely bound electrons. Compton radiation has a slightly longer wavelength, which depends on the scattering angle 2θ (*cf.* Figure 29 and 30, Section *1.8.2*). The increase in wavelength is approximately given by the expression:

$$\Delta\lambda = (h/m_e c)\,(1-\cos 2\theta) \qquad (5)$$

where $(h/m_e c) = 0.02426$ Å. The intensity of the Compton scattering increases with increasing Z (the number of loosely bound electrons).[15a]

For a proper measurement based on the fluorescence of a characteristic emission line of the absorber in the sample, it is important to reduce the background level of radiation from the sample. This can be done by the use of an energy-dispersive detector for selecting the appropriate wavelength range. By means of a semiconductor, *e.g.*, germanium-diode detector, satisfactory discrimination of the fluorescence signal from the background noise can be achieved. However, such detectors have a limited count rate and work best for samples with weak signals. The Lytle detector is another special type of ion chamber, designed to enhance the fluorescence signal by means of x-ray filters and a Soller slit (Figure 28). More detailed considerations about the Lytle detector and the requirements for how to select x-ray filters are given in Section *1.8.2*.

Fluorescence XAS measurements are mostly used for dilute samples, with low concentration of the absorber, such as bio-inorganic samples. For first row transition elements, concentrations as low as 1000 ppm or 0.001 M in an aqueous solution can be studied.[13]

Conversely, samples with high total absorption, causing difficulties in transmission measurements, or with low K-edge energies (*e.g.* calcium) can also yield better results in fluorescence mode than in transmission.

Dilute samples can be thick, but concentrated samples should be thin to avoid *self-absorption* (absorption of fluorescence radiation by the sample itself), which reduces the intensity of the fluorescent x-rays, I_f , leaving the sample. In such cases, the amplitude reduction factor, S_0^2, sometimes obtains very low values. For a fluorescence measurements it is important to use the same experimental setup for all samples, since the background intensity partly will depend on the geometrical arrangement of the sample and detector.

Figure 11 shows both transmission and fluorescence Pt L_{III}-edge absorption spectra of a 0.1 M $PtTl(CN)_7$ solution, measured simultaneously. A Lytle detector was used for the fluorescence measurement. The increasing background in a fluorescence experiment is due to the fact that the absorption of x-rays generally decreases when the energy increases *(cf.* footnote p. 4 and Figure 1). Then the incident x-ray beam will penetrate deeper and increase the effective volume of the sample and more of the produced fluorescent x-rays can reach the detector.[15a]

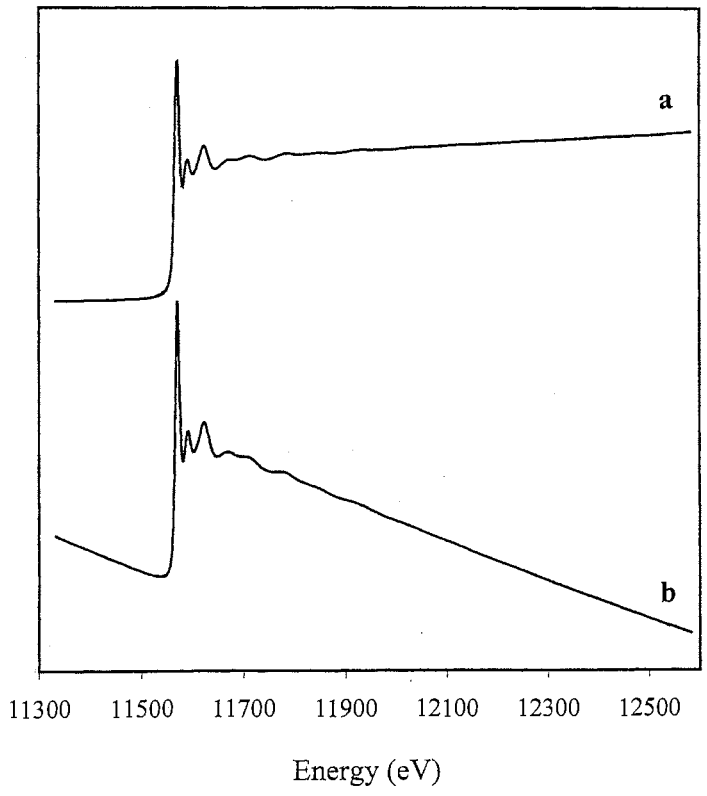

Figure 11. Pt L_{III}-edge absorption spectra for 0.1 M $[PtTl(CN)_7]^{2-}$ aqueous solution in the range 11.3 to 12.6 keV. a) fluorescence measurement with Lytle detector; b) transmission.

1.4 Extraction of the EXAFS modulation. The x-ray absorption fine structure oscillations or the XAFS function, $\chi(E)$, is defined as the modulation in the absorbance, *i.e.*:

$$\chi(E) = \frac{[\mu(E) - \mu_0(E)]}{\mu_0(E)} \qquad (6)$$

where μ is the measured absorbance while μ_0 is the absorbance of the isolated atom. The steps required for extraction of this experimental XAFS function include the following:

- pre-edge background removal
- normalization
- energy calibration and conversion to *k*-space
- spline fitting and isolation of fine-structure oscillations

There are several program systems available for these standard procedures which all assume μ_0 to be a smooth monotonically decreasing function, notably EXAFSPAK[26] and WinXAS.[27] In this work all the procedures for extraction of EXAFS oscillation and data refinement was done using the WinXAS program, while the preliminary energy calibration and averaging procedures of the raw data were performed with the EXAFSPAK program.

1.4.1 General background correction:[13] The experimental absorption spectrum must be corrected for the effects of other atoms in the sample and other electron shells of the absorbing atom, and also for instrumental effects or absorption in the sample cell windows, etc. Ideally, only the specific absorption of the atom chosen for study should remain for EXAFS analysis. For transmission data there is for example the semi-empirical expression by Victoreen,[15a] which in principle gives a good approximation of the expected shape of the variation of the background absorption for the absorbing atom.

The differences or non-linearity in the ion chamber response, contamination by higher order harmonics, etc, will add non-ideal terms depending on the experimental setup to the measured background absorption.[16d] Therefore, an empirical removal of the background absorption is mostly made. Normally, a smooth polynominal (linear or quadratic) function is fitted by least-squares methods to the pre-edge region of the spectrum (with lower energy than the edge). The fit values are then subtracted from the raw data (*cf.* Figure 13a). The background in a fluorescence experiment normally shows a tendency to increase, opposite to that of the absorption in transmission (Figure 11); since the fluorescence from the sample increases with increasing energy (see p.27). A linear polynomial is usually sufficient for an empirical background subtraction for fluorescence data.[16d]

1.4.2 Normalization: In many experiments, the exact concentration of the absorbing atom and the sample thickness are not precisely known. In the beam path, between the detectors I_0 and I_1, there are also cell windows, Mylar films, etc., and also the other elements in the sample. This causes the observed signals to be multiplied by energy dependent absorption factors.[14]

A normalization procedure is used to put the EXAFS on a proper amplitude scale. After pre-edge background correction, the EXAFS energy region is next fit by a similar procedure and extrapolated to lower energies over the edge. The difference between this extrapolation and the background-corrected spectrum at the edge is the *step height* or *edge step* (Figure 13b). This edge step is proportional to the total amount of the absorbing element in the sample.[13] The data are then divided by the size of the edge step, to normalize the EXAFS to a unit edge, which compensates for uncertainties in the concentration and sample thickness.[14]

1.4.3 Threshold energy E_0: In order to correlate the XAFS oscillation to the kinetic energy of the photoelectron, the threshold energy E_0 is required, *i.e.* the minimum energy required for the photoelectron ejection. This value is used in the scattering formulas, converting the energy of the incident beam E to the scattering variable k by means of the relation: $k = \{0.2625(E - E_0)\}^{½}$

In the version 8 of the FEFF program, the E_0 value corresponds to the Fermi energy, which should correspond to the inflection point of the edge, *i.e.* the first maximum in the 1st derivative of the XAFS edge. However, *there is no simple way to experimentally determine E_0 from the spectrum or edge structure.*[20a] E_0 is known to be influenced by chemical effects such as oxidation state, covalency in the chemical bonds, etc.[15c]

1.4.4 Conversion to k-space: At this stage, the energy scale is changed from eV to the *photoelectron wavenumber* or *wave vector*, k ($Å^{-1}$), (see Figure 13c).

Kinetic energy of the photoelectron : $E - E_0 = ½\ m_e v^2 = \dfrac{(m_e v)^2}{2m_e} = \dfrac{P^2}{2m_e}$

photoelectron momentum = $\hbar . k$

k = wave vector = $\dfrac{2\pi}{\lambda_e}$ = photoelectron wavenumber

$$\Rightarrow \quad E - E_0 = \frac{\hbar^2 k^2}{2m_e} \qquad k = \sqrt{\frac{2m_e(E - E_0)}{\hbar^2}} = \left\{0.2625\,(E - E_0)\right\}^{½} \qquad (7)$$

Therefore, when the energy E corresponds to the threshold energy, E_0, then $k = 0$.

In the above formulas, λ_e = wavelength, v = velocity, m_e = mass and P = momentum of the photoelectron, and h is Planck's constant.

In the early stages of data treatment, we can estimate a value for the threshold energy, E_0', using the 1st and 2nd derivatives of the spectrum to find the first inflection point. The true E_0 value can be obtained by refining a shift parameter ΔE_0, for which: $E_0 = E_0' + \Delta E_0$ (see Section *1.7.3*). The effect of this correction of the estimated threshold energy is to shift the *k*-scale, which affects the distance obtained in the data analysis (see Section *1.7*). The corrected *k*-scale is given by:[15b]

$$k_{corr} = [k'^2 - (\Delta E_0 \cdot 2m_e/\hbar^2)]^{1/2} \quad (8)$$

where m_e is the electron mass and k' corresponds to the estimated threshold energy, E_0'.

1.4.5 Spline "atomic background" removal: At this stage it is convenient to express the variation in the total absorption coefficient $\mu(k)$ as the isolated atom absorption $\mu_0(k)$ times a *k*-dependent factor, $\chi(k)$:

$$\mu(k) = \mu_0(k)\{1 + \chi(k)\} \quad (9)$$

The factor $\chi(k)$ then represents the fractional change (modulation) in the absorption coefficient induced by neighboring atoms, and contains structural information. This $\chi(k)$ factor is a measure of the x-ray absorption fine structure (XAFS) oscillations. Thus, the definition of XAFS, $\chi(k)$, is:

$$\chi(k) = \frac{[\mu(k) - \mu_0(k)]}{\mu_0(k)} \quad (10)$$

The crucial function is $\mu_0(k)$, the "*atomic background absorption*", which corresponds to the (hypotetical) absorption for an "isolated" atom at the same energy, usually described by the "muffin-tin" potential approximation.[5,18]

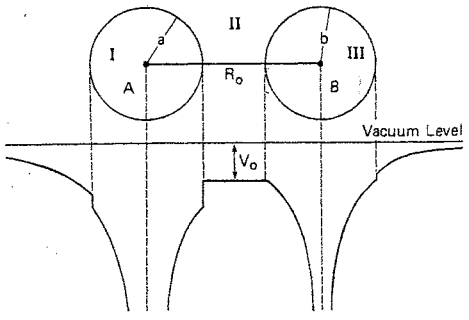

Scheme 1. In the "muffin-tin potential" approximation, the atoms are described with spherically symmetric potential functions sharply increasing toward the atomic centre, each located inside a "muffin-tin" sphere (regions I and III). The potential between the spheres (region II) is constant.[21]

The difference $\mu(k) - \mu_0(k)$ thus represents the experimental x-ray fine structure oscillations. The amplitude of the oscillations becomes smaller at high k-values due to the general decrease in absorption with increasing energy (see footnote in page 4). Division by $\mu_0(k)$, which is proportional to the number of atoms per unit volume, normalizes the XAFS data to a per atom basis, and compensates for the general k-dependence of the absorption.

Even though $\mu_0(k)$ can not be measured experimentally, we must determine the $\mu_0(k)$ function well enough to obtain the structure-dependent XAFS function in sufficiently good approximation for evaluation of structural information by model fitting. The $\mu_0(k)$ function is normally assumed to be a smoothly varying function, but in later versions of the *ab initio* based FEFF code, theoretical calculations can be performed, which show that $\mu_0(k)$ can have some oscillatory structure, so-called *atomic-XAFS*.[5] It has been suggested that the atomic-XAFS oscillations can be largely responsible for the spurious peaks often observed at about half the near-neighbor distance in the Fourier transforms of XAFS data.[5,18]

In the present programs for extracting the EXAFS oscillation according to equation (10), the $\mu_0(k)$ function in EXAFS region (after the pre-edge background correction, Section *1.4.1*) is normally approximated by a numerically determined smooth curve, $\mu_{spline}(k)$, which is a slowly varying function fitted to the experimental data.[29] Therefore, the experimental XAFS function, $\chi(k)$, is not a directly measured quantity but depends on the approximation introduced for the $\mu_0(k)$ function.

For normalizing the extracted oscillation, it is often convenient to use $\mu_{spline}(k)$ as an approximation for $\mu_0(k)$:

$$\chi(k) = \frac{[\mu_{data}(k) - \mu_{spline}(k)]}{\mu_{spline}(k)} \qquad (11)$$

However, in some cases there are non-linear contributions to the background, in particular for the fluorescence data, which makes $\mu_{spline}(k)$ a poor approximation of $\mu_0(k)$ at high k-values for the normalization (see Figure 12a). It is clear that using μ_{spline} as an approximation of $\mu_0(k)$ for the fluorescence data will introduce an error in the amplitude of the calculated $\chi(k)$ function. In such a case, it can be better to use a theoretical approximation, for example according to the Victoreen formula,[30] which is an option in the EXAFSPAK program (see Figure 12b). The Victoreen polynominal is a semi-empirical expression for the "fall off" of the absorption coefficient of the absorbing element between the absorption edges with decreasing wavelength, λ (*cf.* Figure 1a). The Victoreen approximation of the absorption coefficient, μ_{vic}, is given by: [26] $\mu_{vic} = C_{vic}\,\lambda^3 - D_{vic}\,\lambda^4$,

where the x-ray wavelength is given by: λ (Å) = (hc/E) = 12398.4 / E (eV), and C_{vic} and D_{vic} are tabulated Victoreen coefficients for a particular edge and element. When μ_{vic} is used, the oscillatory part of the x-ray absorption, the EXAFS function, is calculated by:

$$\chi(k) = \frac{[\mu_{data}(k) - \mu_{spline}(k)]}{\mu_{vic}(k)} \qquad (12)$$

By using the Victoreen polynominal we can make sure that background problems with the data (in particular common for fluorescence data) or inadequate pre-edge background subtraction do not distort the amplitude of the EXAFS data. Figure 13 gives an example of the extraction of the XAFS function, using the WinXAS program.

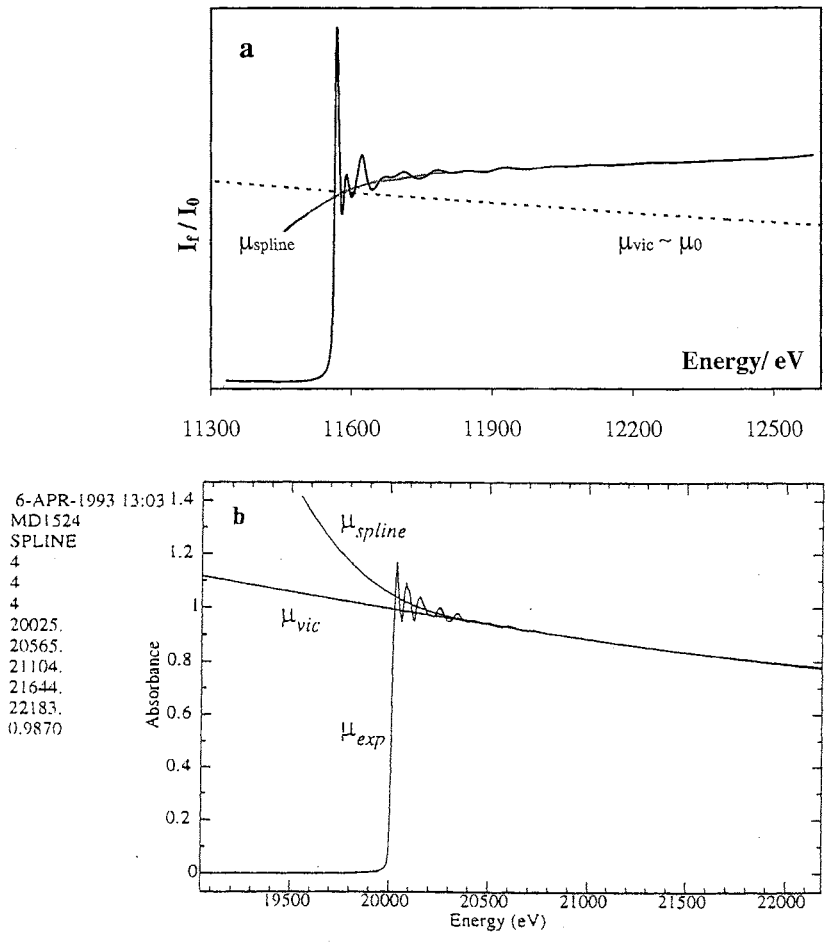

Figure 12. a) Pt L_{III} edge fluorescence data (corrected for pre-edge background) for 0.1 M solution of a $[PtTl(CN)_7]^{2-}$ complex. In comparison with μ_{spline}, the μ_{vic} function better represents the general "fall-off" of the atomic background absorption (μ_0) with increasing energy (see the text); b) Transmission data showing that in this case μ_{spline} can be a good approximation to μ_{vic} and μ_0 (example from the EXAFSPAK manual).

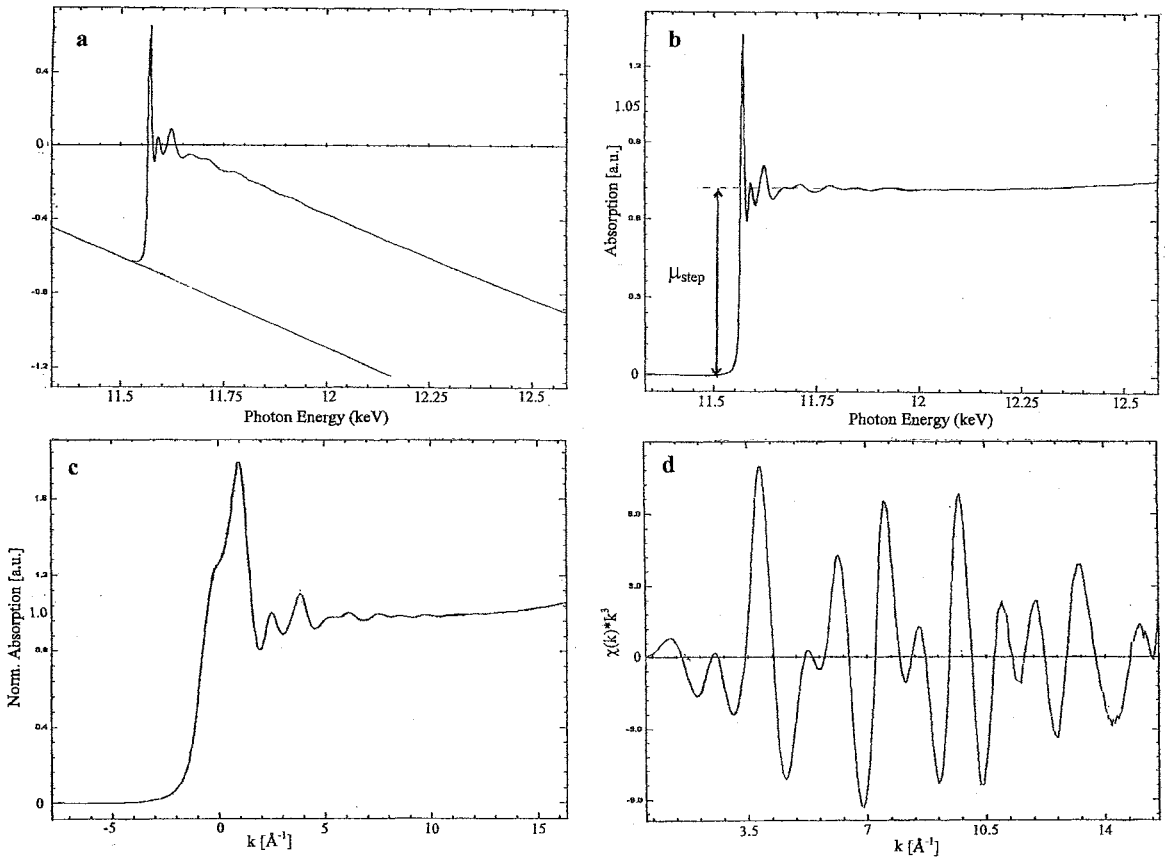

Figure 13. Extraction of EXAFS oscillation for Pt-L_{III} edge transmission data for 0.1 M $[PtTl(CN)_7]^{2-}$ aqueous solution. a) fit of linear pre-edge background; b) background subtraction; c) conversion of energy scale to *k*-space after edge-step normalization; d) k^3-weighted EXAFS oscillation after spline removal.

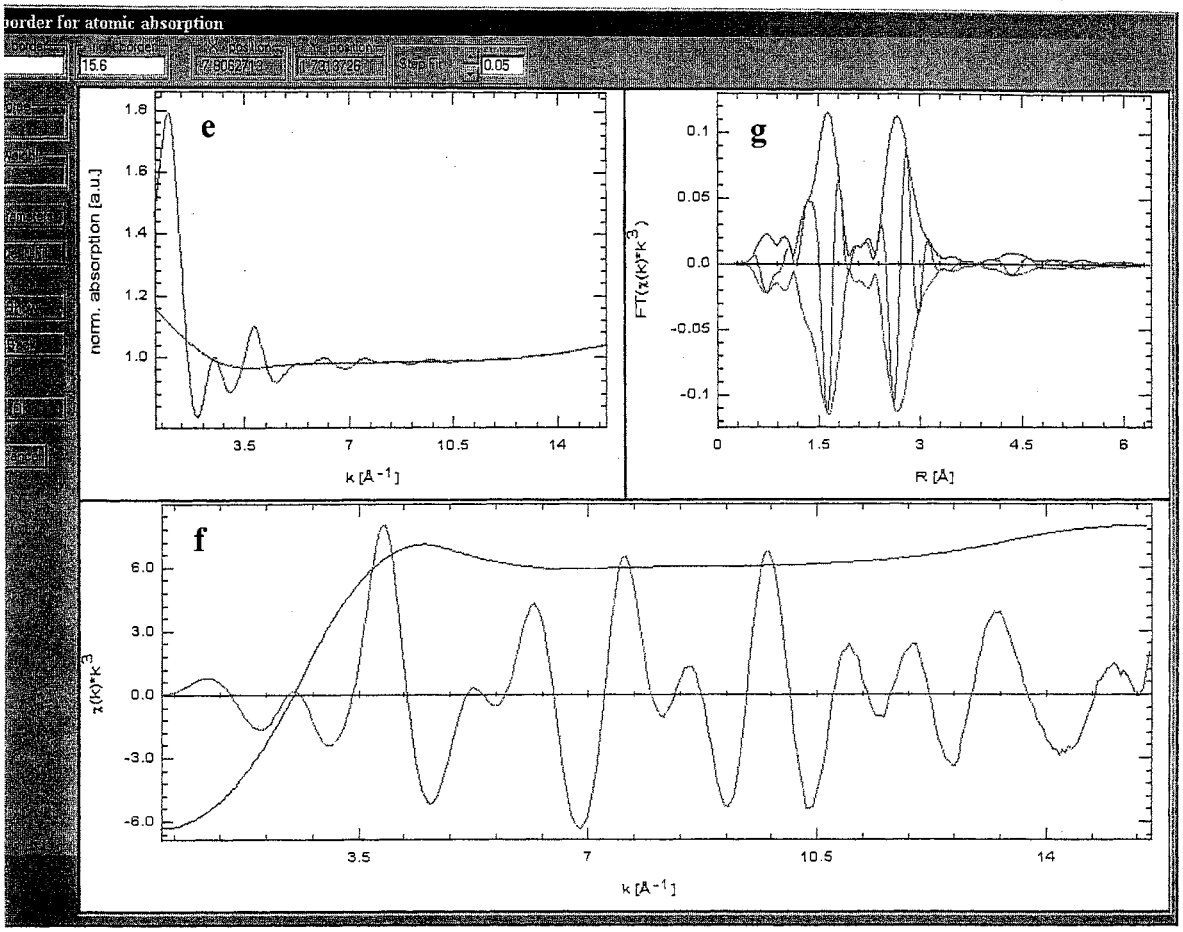

Figure 13-cont. Detailed spline-fitting procedure for the Pt L_{III} edge spectrum of the $[PtTl(CN)_7]^{2-}$ complex in aqueous solution: e) spline-fitting on the curve in Figure 13**c** in the k range 0.5-15.6 Å^{-1} using 8 spline points and k^3-weighting; f) extracted k^3-weighted EXAFS oscillation as in **d**. The first derivative of the spline is shown by the smooth curve; g) preliminary Fourier-transform (no window function, full k range) of the EXAFS oscillation in **f**.

1.5 EXAFS equation. The scattering process of the photoelectron can be modelled at different levels of scattering theory. The XAFS oscillation, $\chi_i(k)$, is the sum of modified sine waves with different frequency and phase from each backscattering coordination shell *j*, around the central atom *i*, and can be written in the general form:

$$\chi_i(k) = \sum_j A_j(k) \sin[\Psi_{ij}(k)] \qquad (13)$$

where $A_j(k)$ is the total backscattering amplitude of the *j*th shell of backscattering atoms and $\Psi_{ij}(k)$ is the corresponding total phase function.[29] Both the amplitude and phase functions contain structural information. In order to extract this information, we need a structural model with parameters, which can be adjusted to improve the fit between the experimental data and a calculated XAFS function.

The early development of the scattering theory can be found in the book by Teo,[2] and by Stern.[16e,17] The curved wave scattering theory including contributions from multiple scattering, as developed by Rehr and co-workers,[5,17] can be written in a form analogous to the standard XAFS equation:

$$\chi_i(k) = \sum_j \frac{N_j . S_0^2(k)}{k.R_j^2} \left| f_{eff}(k) \right|_j .\exp(-2k^2\sigma_j^2).\exp[-2R_j / \Lambda(k)].\sin[2kR_j + \phi_{ij}(k)] \qquad (14)$$

in which:

N_j = Number of backscatterers in the *j*th shell

R_j = Distance between the central atom *i* and the backscatterers in the *j*th shell in single-backscattering (for multiple scattering, half of the total path length, $R_j = R_{tot} / 2$)

$S_0^2(k)$ = Amplitude reduction factor due to multiple excitations, etc.

$f_{eff}(k)$ = Effective amplitude function for each scattering path

$\exp [-2\sigma_j^2 k^2]$ = Debye-Waller factor in the harmonic approximation

σ_j = Debye-Waller parameter accounting for thermal and configurational disorder

$\Lambda(k)$ = Photoelectron mean free path

$\exp [-2R_j / \Lambda(k)]$ = Mean free path factor

$[2kR_j + \phi_{ij}(k)]$ = Total phase = $\Psi_{ij}(k)$

$\phi_{ij}(k)$ = Phase shift due to the coulomb potential of the central atom *i* and of the backscattering atom *j*

Figure 14 shows the effect of distance and coordination number on phase and amplitude (respectively) of an XAFS spectrum.

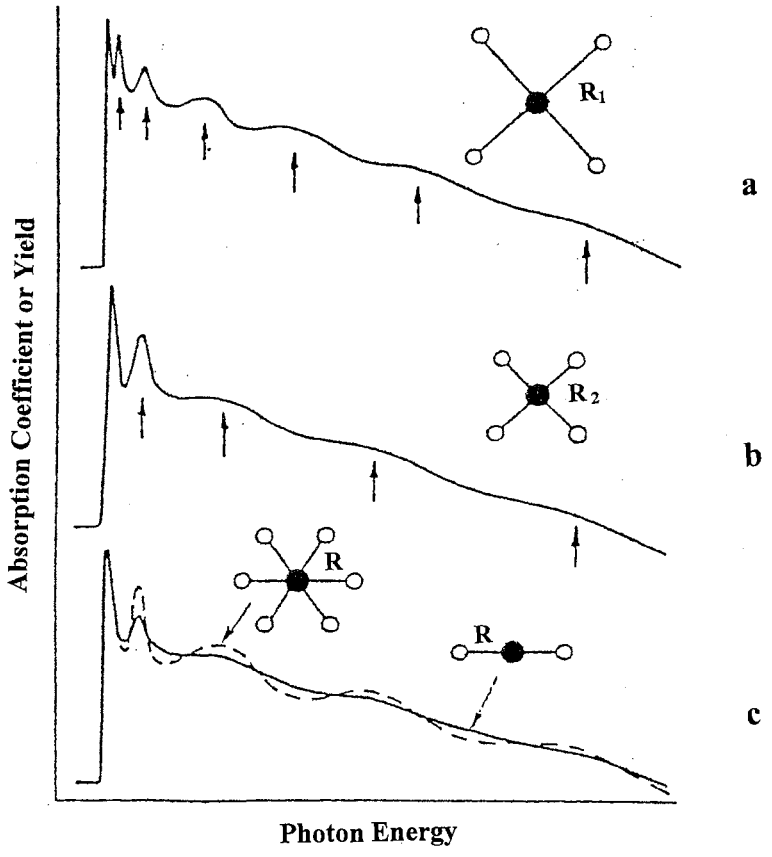

Figure 14. Comparisons of EXAFS frequency and amplitude for: a) long absorber-backscatterer distance resulting in high frequency oscillations, b) short distance resulting in low frequency oscillations, and c) amplitude differences by different numbers of nearest-neighbors around the absorber (ref 13).

1.5.1 Phase: In order to find the total phase of the backscattered photoelectron wave, $\Psi_{ij}(k)$, we have to consider firstly, the length of the pathway the photoelectron travels and secondly, the phase shifts it will undergo at the scattering process.

The photoelectron has a wavelength λ_e, given by its kinetic energy E_k (= E - E_0). In a single backscattering process, the distance from the absorber to the backscatterer in shell *j* and then back to the absorber atom is $2R_j$. The number of wavelengths that the photoelectron travels is then $(2R_j / \lambda_e)$. This causes a phase difference of the outgoing and incoming waves at the absorber, given by $[2\pi\cdot(2R_j / \lambda_e)]$. Since $k = 2\pi / \lambda_e$, this part of the phase change becomes $2kR_j$.

If this was the only contribution to the phase, then the XAFS oscillations for single backscattering would be directly connected to the interatomic distances, R_j. However, there is another part, $\phi_{ij}(k)$, which arises from the interaction of the photoelectron with the coulomb potentials of the scattering atomic pair, *ij*. The absorbing atom *i* creates a *k*-dependent phase shift both on the outgoing and the incoming (backscattered) waves, $2\delta_i$, which varies with the nature of the absorbing atom. In addition, the potential of the backscattering atom *j*, also causes a phase shift, $\delta_j(k)$, which is smaller for light atoms. The sum of the phase shift is then: $\phi_{ij}(k) = 2\delta_i(k) + \delta_j(k)$.

Figure 15 a and b show $2\delta_i(k)$ and $\delta_j(k)$ functions calculated by the FEFF program,[33] for Pt as absorber with different backscatterers. The phase shift function (δ_j) shows more features at low *k* values for the heavy backscatterers. These features are related to the features in the corresponding amplitude functions in Figure 16. In Figure 15c, the reason for the sharp feature in the Pt-Pt 2.7 Å phase shift curve is a scattering resonance, which can occur between the photoelectron and electronic shells of the backscatterer.[15d]

Previously, it was normal practice to derive an experimental value of $\phi_{ij}(k)$ from standard compounds which have similar backscattering conditions for the absorber/ scatterer pair *ij*, as the unknown sample. Nowadays, with the event of the *ab initio* FEFF program, in which efficient and accurate approximations for the scattering potentials are used,[5,20] a theoretically calculated phase shift function $\phi_{ij}(k)$ of high quality can be obtained and is normally used.

When the experimental EXAFS function is Fourier-transformed directly, a "Pseudo Radial Distribution Function" (PRDF) is obtained (see Section *1.6*), in which the peak positions are shifted about 0.5 Å below the true distance, R_j. This is a consequence of not including the phase shift terms, $\phi_{ij}(k)$, in the Fourier transformation. In the model fitting,

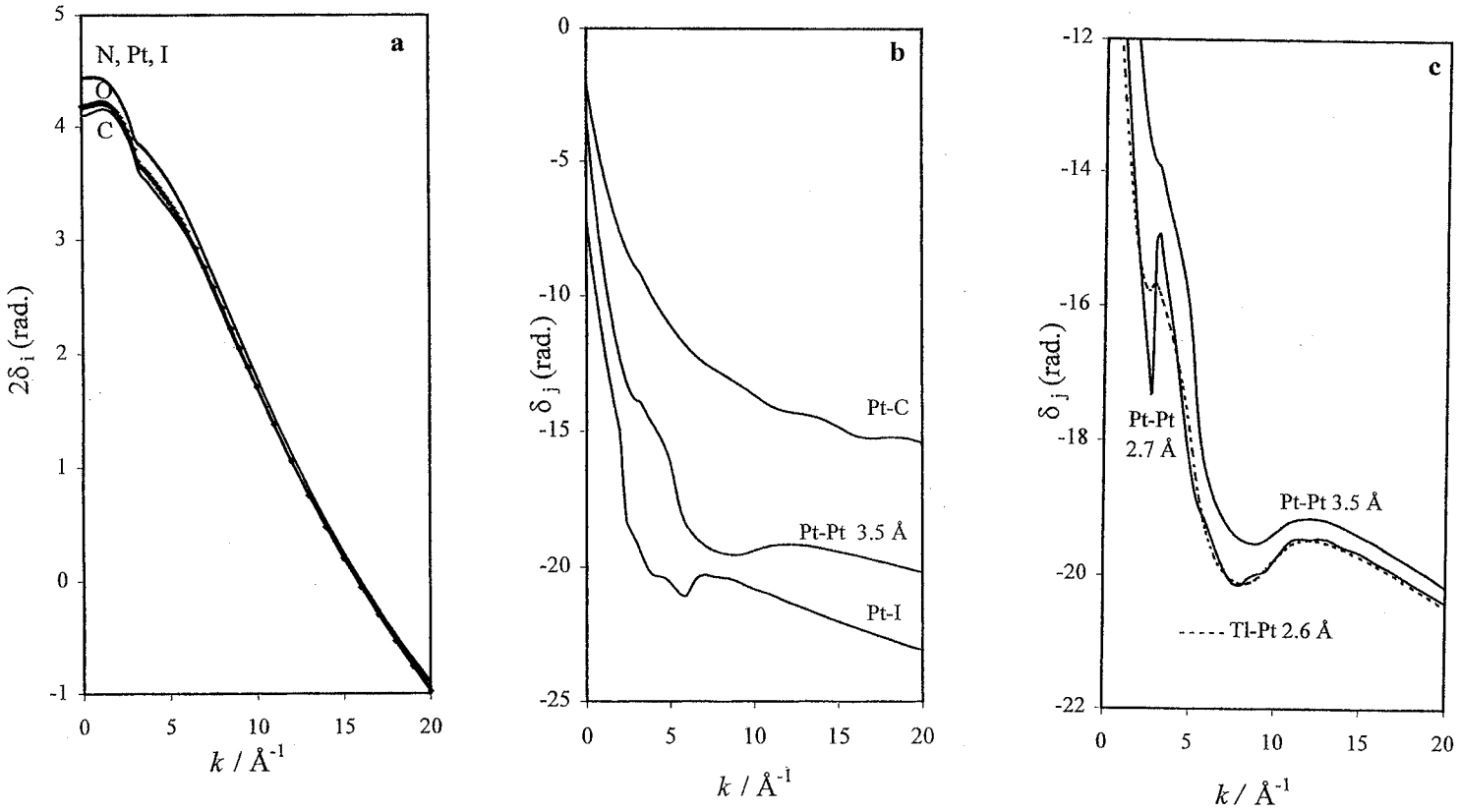

Figure 15. Phase shifts of the photoelectron wave calculated by the FEFF7 program for Pt as absorber. a) Central atom phase shift ($2\delta_i$), showing that differences in the chemical surrounding has little influence on $2\delta_i$. The backscatterers are C (Pt-C 1.99 Å), O (Pt-O 2.05Å), I (Pt-I 2.6 Å), Pt (Pt-Pt 2.6 Å) and N (Pt-N 3.15 Å); b,c) Phase shift at the backscatterers (δ_j). In **c**, a scattering resonance at $k \sim 3$ Å^{-1} can be observed for the Pt-Pt 2.7 Å curve. For the similar Tl-Pt 2.63 Å (Tl as absorber), and the Pt-Pt 3.5 Å curves, this resonance is damped.

the calculated $\phi_{ij}(k)$ function is subtracted from the total phase $\Psi_{ij}(k)$ of the backscattering shell j, in order to obtain accurate distances from the $2kR_j$ portion of the $\Psi_{ij}(k)$ function.

1.5.2 Effective amplitude function $f_{eff}(k)$: In the plane-wave approximation, the curvature of the spherical wave and the size of the backscattering atom is neglected.[16e] The backscattering amplitude function $F_j(k)$ will then depend only on the nature of the backscattering atom, and not on the type of absorber.[2] The modern curved wave scattering theory uses an effective backscattering amplitude, $f_{eff}(k,R)$, which depends on the chemical surrounding and makes it slightly R-dependent.[20a] The $f_{eff}(k)$ function can be obtained from the FEFF program which is based on *ab initio* calculations,[5,20,21] using R-values from an assumed model structure.[32] With this calculated $f_{eff}(k)$, a theoretical $\chi(k)$ function can be obtained (eqn. 14) and compared with the experimental XAFS data in order to improve the model (at this stage, minor distance dependence can be ignored). Then by using the refined model, another set of FEFF calculations can be performed which results in new $f_{eff}(k)$ functions for the final fitting.

Calculated $f_{eff}(k)$ amplitude functions for several investigated species in Paper III-V, with Pt as absorber and a number of different backscatterer atoms are shown in Figure 16. For light backscatterers, the amplitude function has its largest value at low k-values and decreases for $k \geq 3$ Å^{-1}. Therefore, the lightest backscattering atoms contribute little to the scattering in the EXAFS region, and hydrogen atoms can not be detected by the XAFS method. The maximum of the amplitude function in the EXAFS region moves to higher k-values with increasing atomic number.

For heavy elements, the amplitude function has a more complex shape (with peaks and valleys) due to the resonances in the scattering process. The effect is more prominent at low k-values when the energy of the ejected photoelectron is low, and the photoelectron is mainly backscattered by the valence electrons of the backscatterer.[15d] In Figure 16, such features are evident for Pt, Tl and I as backscatterers, even in the EXAFS region.

The amplitude function to some extent depends on the distance and also the electronic structure of the valence shell of the backscatterer, as can be seen from two top curves in Figure 16. The Pt-Pt interaction at 3.5 Å in the linear chain $Pt(CN)_4^{2-}$---$Pt(CN)_4^{2-}$--- in $K_2[Pt^{II}(CN)_4].3H_2O$ gives the curve at the top, while the curve below results from the Pt-Pt interaction at 2.7 Å in the $[(NC)_5Pt^{III}$-$Pt^{III}(CN)_5]^{4-}$ complex. The resonance effects are seen to be more pronounced in the latter case.

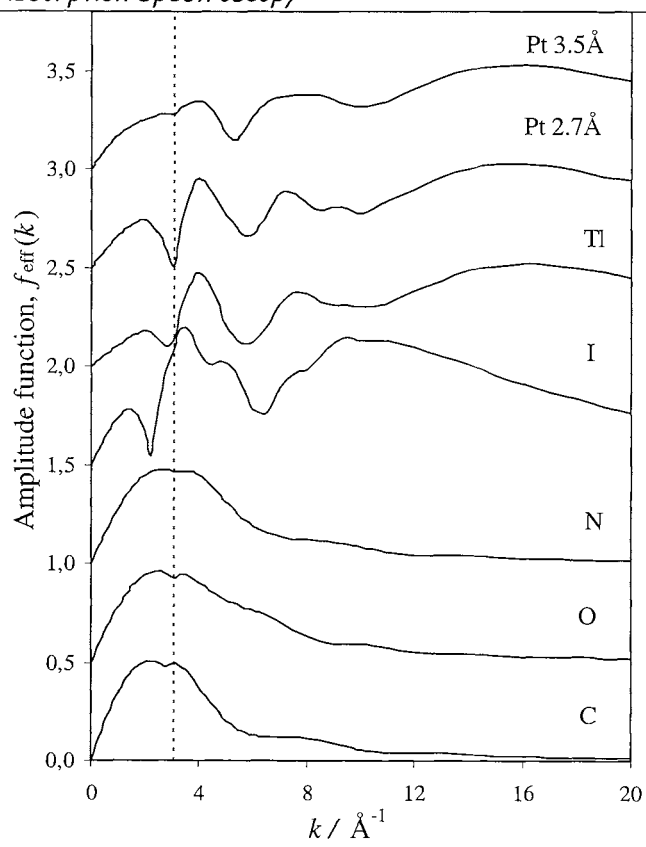

Figure 16. Calculated $f_{eff}(k)$ amplitude functions for a number of backscatterer atoms. Heavy backscatterers have their maximum amplitude at high k-values.[15d] The Pt-Pt interaction at 3.5 Å in the linear chain $Pt(CN)_4^{2-}\cdots Pt(CN)_4^{2-}\cdots$ in $K_2[Pt^{II}(CN)_4]\cdot 3H_2O$ gives the curve at the top, while the curve below results from the Pt-Pt interaction at 2.7 Å in the $[(NC)_5Pt^{III}\text{-}Pt^{III}(CN)_5]^{4-}$ complex. The dashed line indicates the start of the EXAFS k-range, $k > 3$ Å^{-1}.

In Figure 17, it can be seen that the overall shape of the XAFS function (the *envelope*; dashed line) is controlled by the shape of the amplitude function, especially when a k^n weighting scheme is employed. This influence of $f_{eff}(k)$ on the shape of the total backscattering amplitude, $A_j(k)$, (eqn. 13) allows the detection and determination of heavy backscatterers in the presence of the light scatterers. This is exemplified by the Pt-C and Pt-I contributions to the k^3-weighted XAFS function for the $[PtI(CN)_5]^{2-}$ complex (Figure 18). However, such a separation of the interactions is possible only if the backscatterers have significantly different atomic numbers. Other terms in the XAFS expression: the Debye-Waller factor, $\exp[-2\sigma_j^2k^2]$, and the mean free path term, $\exp[-2R_j / \Lambda(k)]$ will also modify the shape of the total amplitude curve $A_j(k)$ (Figure 17).

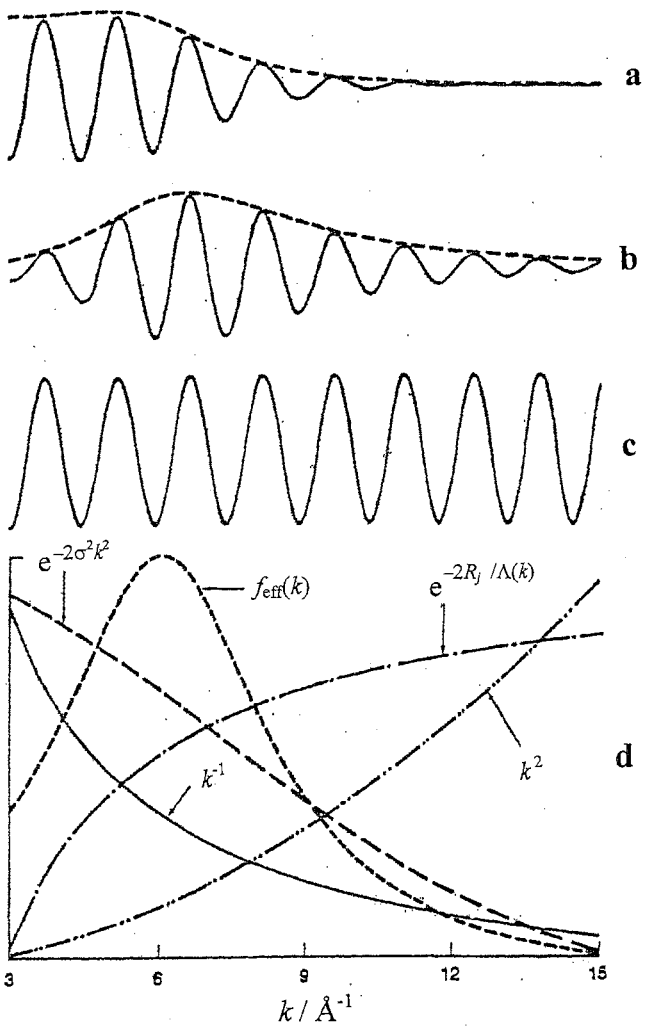

Figure 17. Schematic illustration of the influence of different terms in the amplitude function $A_j(k)$ (eqn. 13, 14), for the first coordination shell of a transition metal. a) $\chi(k)$ and envelope $A(k)$; b) $k^3 \cdot \chi(k)$ and $k^3 \cdot A(k)$; c) oscillatory part, sin $[2kR_j + \phi_{ij}(k)]$; and d) amplitude terms (for $S_0^2 = 1.0$ and constant N); backscattering amplitude, $f_{eff}(k)$; Debye-Waller term, exp $(-2\sigma^2k^2)$; mean free path factor, exp $[-2R_j / \Lambda(k)]$; plots of $1/k$ and k^2 functions (ref. 29).

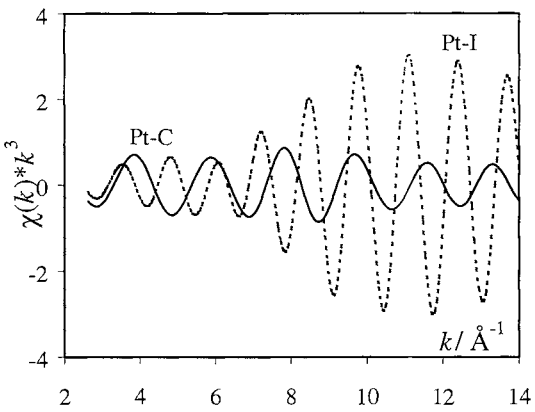

Figure 18. Theoretical $\chi(k)*k^3$ functions for one Pt-C (2.00 Å; $\sigma^2 = 0.002$ Å^2; solid line) and one Pt-I (2.66 Å; $\sigma^2 = 0.003$ Å^2; dashed line) contribution in the $[PtI(CN)_5]^{2-}$ complex, calculated by means of the FEFF7 program. The large differences in phase and amplitude makes it easy to differentiate between iodide and cyanide carbon atoms as ligands in the model fitting to the experimental EXAFS function.

1.5.3 k-*weighting:* There is a general reduction of the XAFS amplitude because of its $1/k$ dependence (*cf.* eqn 14), and the fall-off of the back-scattering amplitude function $f_{eff}(k)$ at high k-values, in particular for light backscattering atoms (Figure 16b). Also for backscattering paths with a large Debye-Waller factor, the amplitude will be reduced at high k-values.[4a] Therefore, the XAFS function, $\chi(k)$, is usually k^3-weighted for the distance determinations involving light backscatterers. In the case of heavy atoms, for which the maximum in the amplitude function $f_{eff}(k)$ appears at high k-values (see Figure 16b), k^1 or k^2 weighting schemes may be required in order to balance the contributions from different types of backscatterers.

1.5.4 Amplitude reduction factor $S_0^2(k)$*:* Usually the calculated $\chi(k)$ function has higher amplitude than the experimental XAFS data. This intensity reduction of the experimental data is mostly due to inelastic losses. One part comes from the inelastic losses within the central atom during the ejection of the photoelectron (an intrinsic process), another from the excitation of the neighboring environment (extrinsic losses). The first part is described by multiplying the calculated $\chi(k)$ by an amplitude reduction factor, $S_0^2(k)$, the second is accounted for by the mean free path factor, $\exp[-2R_j / \Lambda(k)]$ (Section *1.5.5*).

Normally, the amplitude reduction factor is connected to multiple excitations of other electrons in the absorber, leading to shake-up (excitation to a bound state) or shake-off (excitation to the continuum) processes of the outer electrons (Figure 19). This usually requires the excess (kinetic) energy of the photoelectron ($E_k = E - E_0$) to be several times of the binding energy of the outer electrons. After such an excitation process, the photoelectron will have a kinetic energy less than ($E - E_0$), and its EXAFS contribution will be shifted in energy and may have a different phase. Therefore, these contributions do not add coherently, resulting in a loss in the total EXAFS amplitude.

Photoelectrons with low kinetic energy (low k-values) are not involved in such multiple excitation processes, and therefore at low k-values: $S_0^2(k) \approx 1$. Theoretical calculations show that for high energies ($k > 7$ Å^{-1}), $S_0^2(k)$ is almost independent of k with a value mostly between 0.7 to 0.8. [15c,16e,31] Therefore, $S_0^2(k)$ can be treated as a *scale factor* (independent of k) in the data analysis, especially when using high k-weighting.

The $S_0^2(k)$ factor is the only factor directly related to the central absorber atom, which significantly affects the EXAFS amplitude. However, due to interference between intrinsic and extrinsic processes, an approximate cancellation of the effects may occur and typical values are $S_0^2 \approx 0.85 - 1.1$ from experimental measurements.[15c,16d 20a] In our refinements of platinum and thallium cyano complexes with known coordination numbers (Papers III-V), the S_0^2 values varied between 0.9 to 1.25.

Beside the inelastic losses, there are also experimental factors affecting the S_0^2, which should be considered. In a transmission measurement on a hexahydrated indium(III) ion in an alum salt an abnormally high value, $S_0^2 = 1.9$, has been obtained.[24] This was clearly due to strong fluorescence coming from the sample to the I_0 ion chamber, which appeared as an oscillation when intensity from (I_0 / rtc) was plotted *vs.* energy. On the other hand, in fluorescence measurements of highly absorbing samples, low values of S_0^2 (~0.4) were

obtained for the solid Ca compounds (Paper I). The reason is *self-absorption*, *i.e.*, the fluorescent radiation is absorbed by the sample itself and this reduces the emitted intensity, I_f, leaving the sample (see Section *1.3.6*). The self-absorption effect is reduced if thin samples can be used.

By means of calibrations with a proper model compound, reliable S_0^2 values can be obtained for the experimental conditions used. This is useful in order to get good accuracy (down to ± 10 %) in the determination of the number of backscatterers in a shell, N_j (see Section *1.7.6*).

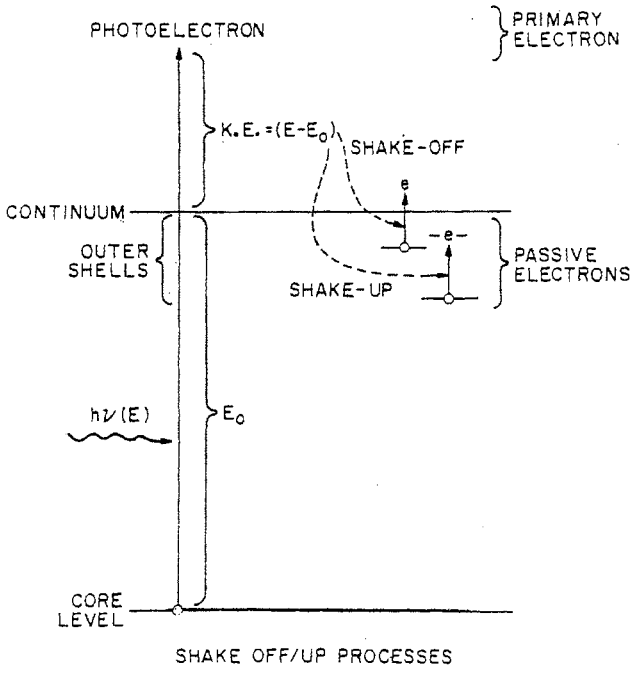

Figure 19. Shake-up and shake-off processes within the absorber, which correspond to excitation and ionization, respectively, caused by the excess energy, E - E_0, of the photoelectron. These processes are important for E - E_0 > 200 eV (k > 7 Å^{-1}), which is much larger than the binding energies of the electrons in the outer shells, ~60 eV, (ref. 15c).

1.5.5 Mean free path factor, exp[-2R$_j$ / Λ(k)]: The interference between the outgoing photoelectron wave with the backscattered wave requires coherence with a well-defined phase difference. There is a finite lifetime after which the photoelectron loses this coherence, which is determined by: 1) the lifetime of the core hole, 2) interactions between the photoelectron and weakly bound electrons of backscatterers. The average time for the photoelectron to lose coherence, τ, has contributions from the actual travel time before inelastic electron-electron occurs, and also from the core hole lifetime. An average distance, which the photoelectron can travel before losing its coherence with its initial state, is simply given by $\Lambda = \tau \cdot v$, where Λ is the photoelectron *mean free path* and v is its velocity: $v = \hbar k / m_e$.[16e]

The reduction of XAFS amplitude by these extrinsic inelastic losses is approximately accounted for by the *mean free path factor*, exp[-2R$_j$ / Λ(k)]. This exponential factor describes the *probability* that the photoelectron travels to the backscattering atom and returns to the absorber, without inelastic scattering taking place or the core hole being filled. Thus, the weakly bonded valence electrons of the backscatterers and the chemical environment around the absorber will influence the inelastic scattering process.[15c,16e]

For the analyses of the EXAFS data, the energy dependence of Λ(k) must be evaluated explicitly. Previously, it was usually estimated from *universal curves* for different types of material, using tabulated coefficients to generate a Λ(k) function.[15c,♣] By means of the FEFF program direct calculations of Λ(k) are made for each absorber in the XAFS analyses. In Figure 20a calculated Λ(k) values are shown for the Pt L$_{III}$ edge for several of the molecular species studied in Paper III-V. Only small differences occur due to the different surroundings of the absorber, and the type of backscatterer (C, O, I, Pt, Tl) had no influence on the Λ(k) values for the same complex. However, the Λ(k) values in Figure 20b, obtained for Ca, Pt and U as absorbers, show substantial differences. For Ca, the mean free path length Λ(k) increases rapidly with increasing energy of the photoelectron.

In these figures, the minimum value of Λ (*i.e.* the shortest photoelectron mean free path) about 5 Å, corresponds to the energy when it is easiest to excite loosely bound

---

♣ The mean free path Λ(k) of the photoelectron can be estimated from a semi-empirical equation:

$\Lambda(k) = \frac{1}{\eta}\left[\left[\frac{\xi}{k}\right] + k^n\right]$ in which η and ξ are tabulated values,[15c] and $k = (0.2625(E-E_0))^{1/2}$,

giving a *universal curve* of Λ *vs.* kinetic energy, $E_k = E - E_0$. For $k > 5$Å^{-1}, this formula reduces to:

$\Lambda(k) = k^n / \eta$

electrons in the backscattering atoms, and occurs at about k = 2.5 Å^{-1} for Ca, and k = 4 - 5 Å^{-1} for the heavy atoms.

Theoretical curves of the mean free path factor, exp[-2R$_j$ / $\Lambda(k)$], corresponding to the calculated $\Lambda(k)$ for the complexes in Figure 20a and b, are given in Figure 20c and d. This factor, exp[-2R$_j$ / $\Lambda(k)$], has its smallest values in the k-range 3-6 Å^{-1}. Figure 20c shows the distance dependence of the factor for the different backscatterers in Pt-complexes. Figure 20d shows that for different absorbers there are significant differences between the mean free path factors, even for similar R$_j$ distances.

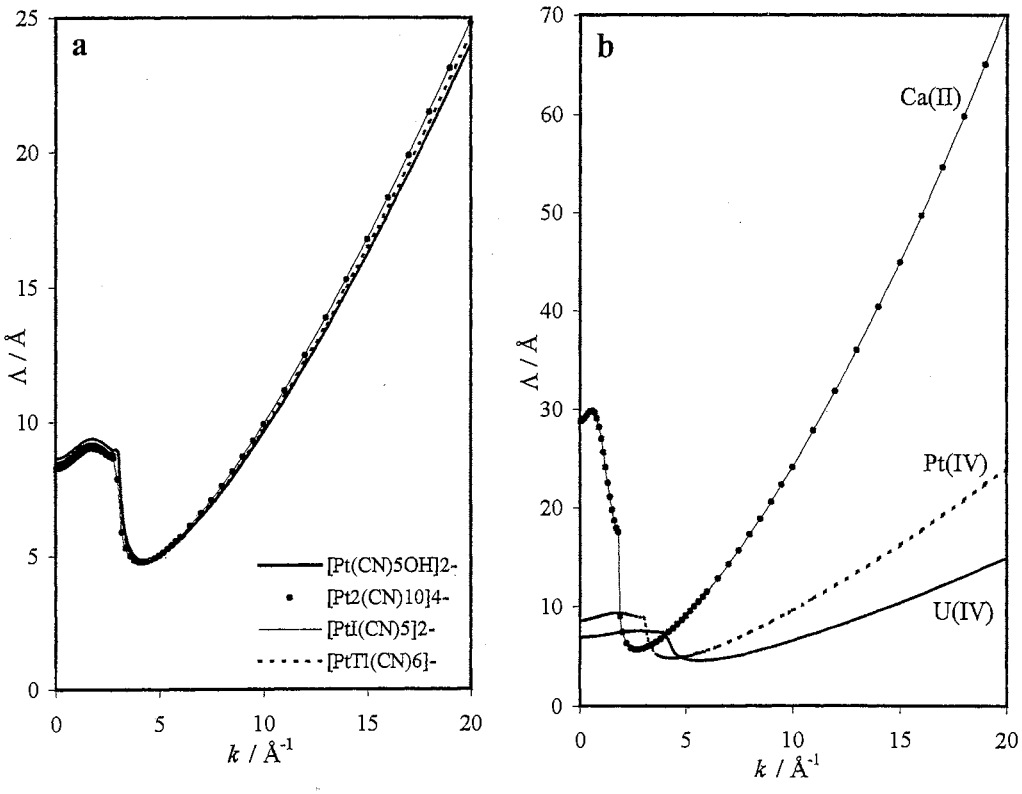

Figure 20. Mean free path $\Lambda(k)$, calculated by the FEFF7 program: a) For Pt as absorber, showing very little difference between mean free path values for complexes with different backscatterers; b) For Ca(II), Pt(IV) and U(IV) as absorber in $Ca(aq)^{2+}$, $[Pt(OH)(CN)_5]^{2-}$ and $U(Aq)^{4+}$, respectively, showing $\Lambda(k)$ to be strongly dependent on the absorbing atom.

In Figures 20c and d, the probability of coherent interference, *i.e.* the value of the mean free path factor, is between 0.35 - 0.9 in the EXAFS k-range (3 - 15 $Å^{-1}$) with a minimum between k = 2.5 - 5 $Å^{-1}$. The damping of the contributions to the EXAFS function by this factor is therefore greatest at low k-values. Therefore, it is difficult to detect the contribution of outer-shell distances in EXAFS, because of:

1) the high damping effect of the mean free path factor at low k-values (*cf.* Figure 17d),
2) the higher Debye-Waller factors, exp $(-2\sigma_j^2 k^2)$, for long distances which damp out their contributions at high k-values, and
3) the inverse distance dependence $(1/R^2)$ of the $\chi(k)$ function in eqn. (14).

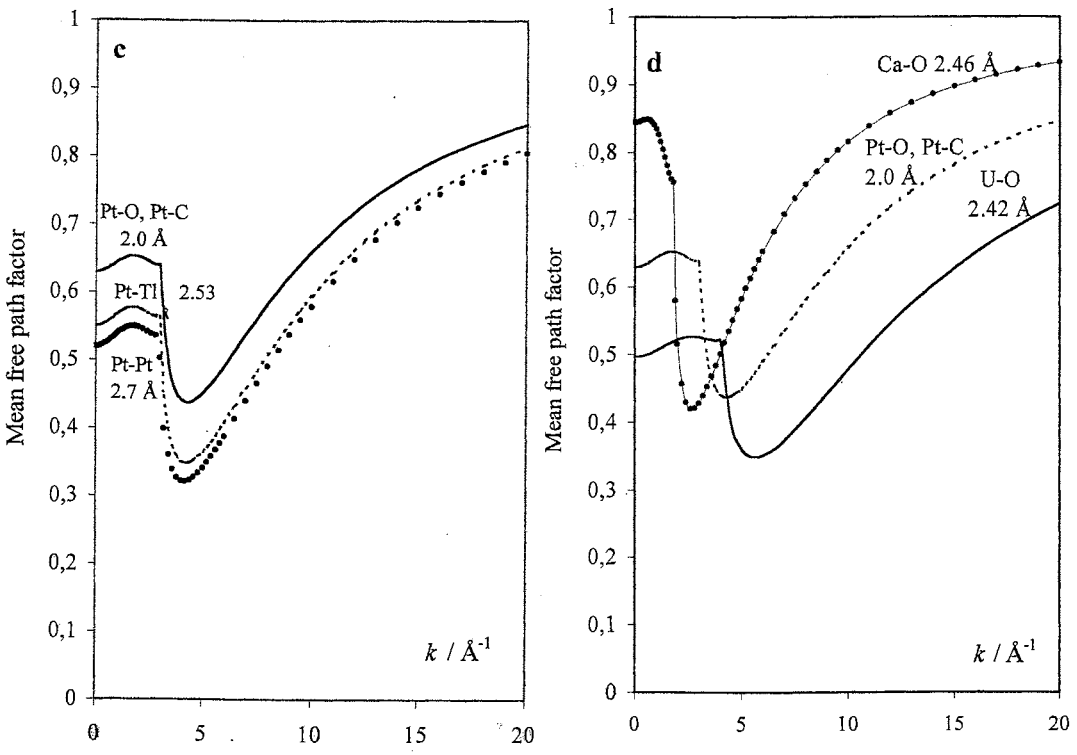

Figure 20 -cont. c, d) The mean free path factors, exp $[-2R_j/\Lambda(k)]$, which have a damping effect on the XAFS amplitude (particularly at low k-values) due to inelastic losses, calculated for the corresponding $\Lambda(k)$ values in **a** and **b**.

1.5.6 Debye-Waller factor, exp (-2$\sigma_j^2 k^2$): If the backscatterers in a shell are disordered with slightly different distances R_j, the EXAFS oscillations from that shell will be reduced in amplitude especially at high *k*-values, because the back-scatterered contributions will be slightly out of phase. The scattering process in EXAFS has a time scale of 10^{-15} - 10^{-16} s (see Section *1.2.4*), which is shorter than that of a molecular vibration, typically 10^{-13} s. Therefore, for a specific *k*-value, the $\chi(k)$ function represents the average of the contributions from all distances R_j between the absorber and backscattering atoms in one molecular species. An overall average on many such species will describe the distribution of the interatomic distances to the backscatterers in a shell, both due to *vibrational* (thermal) disorder and *configurational* disorder.

Vibrational disorder. The vibrational movements of bonded atoms will give rise to a distribution of scattering path lengths over a range, corresponding to the change in interatomic distances. A small difference in path length gives a phase shift in the individual contributions to the total $\chi(k)$ function, which at high *k*-values is large enough to reduce its amplitude. For a Gaussian distribution (the harmonic approximation of a vibration) of the distances between the absorber and the backscattering atoms in a shell, the intensity reduction is described by a Debye-Waller factor, $\exp[-2\sigma^2_{vibr} k^2]$. The disorder parameter, σ^2_{vibr}, is the mean-square deviation from the average distance R_0, or more generally (for multiple scattering), half of the path length (Figure 21a).[15c,16f] In the harmonic approximation the vibrational contribution is given by:

$$\sigma^2_{vibr} = [h / 8\pi^2 m_r \nu] \coth [h\nu / 2k_B T] \qquad (15)$$

where m_r is the reduced mass*, T is the temperature in K, k_B is Boltzmann´s constant, and ν is the vibrational frequency. When carrying out EXAFS studies of atoms with weak bonds (low vibrational frequency), it may be necessary to cool the sample in order to reduce σ_{vibr}, the root-mean-square *(r.m.s.)* deviation, for a less severe damping of the EXAFS function at high *k*-values. A high value of σ_{vibr} can reduce the S/N ratio for the corresponding EXAFS contribution which limits the usable *k*-range.

Configurational disorder. In addition to the vibrational disorder, "static" or "configurational" disorder can sometimes increase the distribution of the distances in a shell of backscatterers. For example, the coordination around a metal ion in the solid state

* $m_r = \dfrac{m_A . m_B}{m_A + m_B}$

can be influenced by packing effects resulting in a lower site symmetry than for a free complex. The differences in the coordination distances R_j will then give rise to a *static* disorder in the solid. A similar *configurational* disorder occurs for weakly coordinated shells in solution or amorphous phases, for irregular coordination geometries which can be found in complexes with high coordination number (such as hydrated Ca^{2+} and U^{4+} ions in Papers I & II), and for complexes with Jahn-Teller distortions.

Configurational disorders can be *symmetric* (*e.g.* Jahn-Teller distortions for Cu^{2+} ions) or *asymmetric*. For *N* discrete bonds of the same type *symmetrically* distributed in a coordination shell *j*, the additional contribution due to the configurational disorder parameter, σ_{conf}, is given by:

$$\sigma^2_{conf} = \sum_{j=1}^{N} \frac{(R_j - R_0)^2}{N} \qquad (16)$$

where R_0 is the average distance. If the total distribution of the distances can be considered to have a Gaussian shape, a disorder parameter, $\sigma^2_{disorder} = \sigma^2_{vibr} + \sigma^2_{conf}$, describing the width of the distribution, can then be used in a Debye-Waller factor, $\exp[-2\sigma^2_{disorder}k^2]$. The damping effect of typical Debye-Waller factor on the XAFS amplitude (especially at high *k*-values) is shown in Figure 21b.

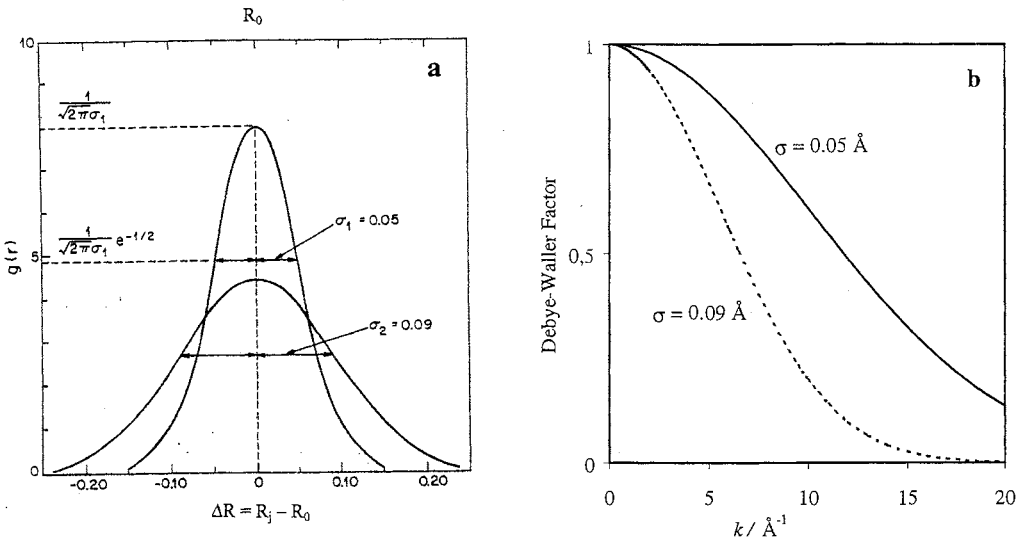

Figure 21. a) Two normalized Gaussian pair distribution functions with different half-widths: $\sigma_1 = 0.05$ Å, $\sigma_2 = 0.09$ Å (ref. 15c); b) corresponding Debye-Waller factors, $\exp(-2\sigma^2k^2)$.

1.5.7 Asymmetric distribution of distances in a shell:[16f]

Temperature effect. At room temperature about 99% of all molecular vibrations are in the ground state, which means that the harmonic approximation can be applied. At high temperatures, the amplitude of the bond stretching and its vibrational movement increases, corresponding to a population increase of higher vibrational states. Moreover, because of the asymmetry of the potential energy function (the anharmonicity), the distribution of the distances becomes *asymmetric*. Therefore, the increase in the atomic movement will enhance the damping of the EXAFS amplitude, and the asymmetry will give a phase shift especially at high *k*.

For temperatures higher than 300 K, the reduced EXAFS amplitude and the phase shift at high *k*-values can have a negative effect on the resolution and accuracy in the determination of interatomic distances and coordination numbers.[13] On the other hand, if the sample temperature is decreased, the reduced vibrational motion will cause an increase in the EXAFS amplitude up to three times at liquid nitrogen temperatures.[4] In addition, the usable *k*-range (with sufficient S/N ratio) for EXAFS oscillations can be extended to a higher *k*-values, which increases the resolution.

Asymmetry in configurational disorder. Usually, large configurational disorders or anharmonic thermal vibrations may cause considerable extent of asymmetry in the distribution of distances R_j in a shell, which can be described by an asymmetric pair distribution function. Large asymmetry effects can give drastic reduction of the EXAFS amplitude (which can make problems in the determination of the coordination number), and the mean distance will shift from that obtained when the simple Gaussian distribution model is applied.[16f] It can be shown that the effect on the EXAFS expression is not only to introduce an amplitude modification factor, but also a more easily detected *k*-dependent contribution to the phase shift.[15c]

To summarize, the distribution of distances in a shell of backscatterers due to thermal and configurational effects, causes a partial cancellation of the EXAFS amplitude at high *k*-values when the contributions from all individual configurations are added together. This damping effect on the EXAFS spectrum for a symmetric disorder is given by a Debye-Waller factor, $\exp[-2\sigma_j^2 k^2]$ (see Section *1.5.6*), in the EXAFS expression:

$$\chi_i(k) = \sum_j A_j(k) \sin[2kR_j + \phi_{ij}(k)]$$

where: $A_j(k) = \frac{N_j S_0^2(k)}{kR_j^2} |f_{eff}(k)|_j \exp(-2k^2\sigma^2_j) \exp[-2R_j / \Lambda(k)]$ (17)

For asymmetrical disorder, however, a more general expression should be used:

where $P(r_j)$ is the pair distribution function and $P(r_j)dr_j$ is the probability of finding the

$$\chi_i(k) = \sum_j S_o^2(k) |f_{eff}(k)|_j \int_o^\infty P(r_j) \frac{e^{-2r_j/\Lambda(k)}}{k r_j^2} \sin[2kr_j + \phi_{ij}(k)]\, dr_j \quad (18)$$

atom j in the range r_j to $(r_j + dr_j)$. An asymmetrical distribution will affect not only the amplitude but also the phase of the $\chi(k)$ function, and thus influence the distance determinations. We can replace $P(r_j)$ by the effective distribution function $P(r_j, \frac{1}{\Lambda})$, which incorporates the smoothly varying EXAFS amplitude:

$$P(r_j, \frac{1}{\Lambda}) = P(r_j) \frac{e^{-2r_j/\Lambda(k)}}{r_j^2}$$

A cumulant expansion of the probability function $P(r_j, \frac{1}{\Lambda})$ can be used in order to separate these effects. For a single shell containing N atoms of the same type j, the amplitude-determining terms can be written as:

$$\ln\left[\frac{k\chi(k)}{N S_o^2(k) |f_{eff}(k)|}\right] = C_0 - C_2 \frac{(2k)^2}{2!} + C_4 \frac{(2k)^4}{4!} + \cdots \quad (19)$$

while the total phase in equation (13) is given by:

$$\Psi_{ij} = 2k\bar{R} + \phi_{ij}(k) - \frac{(2k)^3}{3!} C_3 + \frac{(2k)^5}{5!} C_5 + \cdots \quad (20)$$

where: $\bar{R} = \frac{\int P(r, 1/\Lambda) r dr}{\int P(r, 1/\Lambda)\, dr}$

Here, "cumulant averages" C_n over the distribution are used for a systematic expansion.[16f] For $\bar{R}$ chosen as the centroid (mean distance) of the asymmetrical distribution, then $C_1 = 0$, and when the distribution is normalized: $C_0 = 0$. Thus, only the even cumulants of the effective distribution give corrections to the Debye-Waller factor. Including the first correction term, the Debye-Waller factor becomes $\exp(-2\sigma^2 k^2 + \frac{2}{3} C_4 k^4)$, where $C_2 = \sigma^2$.

The odd cumulants will contribute only to the XAFS phase, and therefore influence the determination of the distance. The following expression is used in the WinXAS program for the XAFS model function:[27]

$$\chi_i(k) = \sum \frac{N_j S_o^2 |f_{eff}(k)|}{k R_j^2} \exp(-2k^2\sigma_j^2) \exp(\frac{-2R_j}{\Lambda(k)}) \exp(\frac{2}{3}\sigma_j'' k^4) \sin[2kR_j + \phi_{ij}(k) - \frac{4}{3}\sigma_j' k^3] \quad (21)$$

where the backscattering amplitude $f_{eff}(k)$, the phase shift $\phi_{ij}(k)$, and the photoelectron mean free path $\Lambda(k)$, are taken from the FEFF output file *feffnnnn.dat* for the *j*th scattering path.[20] Coordination number N (or amplitude reduction factor S_0^2), distance R, disorder parameter σ_j, are free running parameters in the refinement (as well as the optional 3rd and 4th cumulants σ'_j and σ''_j, respectively).

Figure 22a shows the EXAFS of the Ca^{2+}(aq) ion fitted with a model function assuming a Gaussian distribution of Ca-O distances. However, since the distribution of distances is slightly asymmetric in the first shell, this gives rise to a deviation in the phase shift at high k-values. When the third cumulant σ' is included in the model function, a much better fit is obtained (Figure 22b).

Sometimes it is difficult to observe the phase shift deviation due to limitations of the data range or quality, such as the closeness of other x-ray absorption edges, monochromator crystal glitches, low signal-to-noise ratio, presence of other neighboring atoms and transform artifacts, which restrict analyses of the high k-region and hide the effects of asymmetry.

For strongly asymmetric distributions, the difference in phase may cause a substantial shift of the mean distance R_0 (obtained when fitting a Gaussian distribution) from the centroid distance $\overline{R}$ of the asymmetric distribution, 0.1 Å or more.[14b] When applied in the data analysis of the hydrated Ca^{2+} and U^{4+} ions in solution, the mean M-O distance shifted upwards with more than 0.02 Å.

However, care must be taken to ensure the results are reliable. There is strong correlation between the distance R, cumulant σ' and threshold energy, all affecting the phase of $\chi(k)$ function. For example, a small change on ΔE_0 shift during the refinement, will change the distance R obtained (see Section *1.7.3*). Therefore, in order to obtain accurate value for R, it is important to have a correct ΔE_0 value.

Consider an aqueous solution of $Cr(aq)^{3+}$ ion, which has a symmetric distribution of Cr-O distances. A solid Cr-hydrate can be used as standard compound. In both cases, the Gaussian model can be applied and the ΔE_0 obtained for the standard compound can be used for the data refinement of the solution.[24]

In the case of the $Ca(aq)^{2+}$ solution with an asymmetric distribution of the Ca-O distances, however, we can fit the data with a model based on the cumulant expansion. A

standard solid compound (*e.g.* CaO or $Ca(OH)_2$) with a symmetrical distribution of distances can be used to obtain ΔE_0, using a Gaussian model for the data treatment. If the cumulant expansion model gives a good description of the asymmetry for the solution, and if we assume that the threshold energy for the solution is close to that of the standard compound, then we can use the obtained ΔE_0 value for analyzing the solution data.

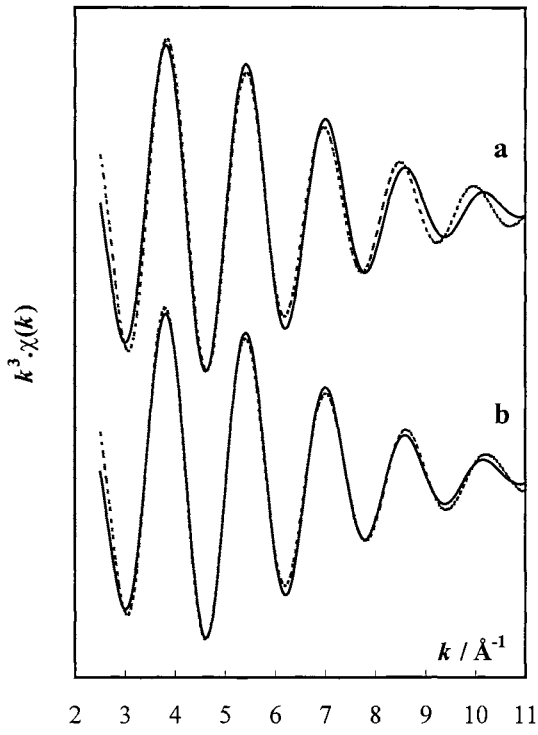

Figure 22. Ca K-edge EXAFS data for the $Ca(aq)^{2+}$ ion with hydration number 8 (solid line). Data fitting (dashed line) with a model: a) assuming Gausssian distribution of the Ca-O distances; b) introducing the third cumulant, σ', to account for the asymmetry.

1.5.8 Multiple scattering: The single-scattering (SS) term, corresponding to the scattering pathway from the absorbing atom to the nearest neighbour and back, $2R_j$, is commonly used to determine near-neighbor distances. However, the ejected photoelectron can be scattered by more than one atom before returning to the absorber. Then multiple scattering (MS) effects occur, which modify both the amplitude and the phase of the photoelectron wave. Multiple scattering pathways are always longer than the single backscattering paths from the nearest neighbours, and are particularly important in the low-k XAFS region.[2,4]

Although it has long been recognized that multiple scattering (MS) terms are generally needed to describe the structure beyond the nearest neighbor distance, there has been considerable controversy about how to describe the nature and the extent of multiple scattering in XAFS. In the EXAFS equation, multiple scattering pathways can be treated in the same way as the single-scattering terms by using a path-by-path approach. This became possible by using curved wave scattering theory, *ab initio* calculations of the slightly R-dependent effective backscattering amplitudes $f_{eff}(k,R)$, and computing the mean-free-path loss terms (see Section *1.7.1*).[20]

Figure 23 shows typical scattering pathways for a three-atom Pt-C-N configuration, with Pt as absorber. The pathway of the single Pt-C or Pt-N backscattering (SS) has two "legs": toward and back from the C or N atoms, which is denoted $n_{leg} = 2$. The multiple scattering Pt-C-N pathway then has $n_{leg} = 3$, and Pt-C-N-C $n_{leg} = 4$. It is well known that the strength of the MS effects depends on the angle of the atomic configuration. In Figure 23, this is shown for the linear Pt-C-N configuration to give several times higher amplitude for the 3-leg and 4-leg pathways than for the single Pt-N backscattering. However, when the deviation from linearity for Pt-C-N (angle α) is more than 55°, the MS amplitude becomes smaller than that of single Pt-N backscattering.

For a linear configuration, as for Pt-C-N in Figure 23, the strong forward scattering from the intermediate C atom to the N atom gives a significant amplitude enhancement in the MS process, the so-called "*focusing effect*". This forward scattering is sensitive to the chemical bonding and electron configuration of the intermediate atom, since both its core and valence electrons are involved. A single backscattering process, however, (*e.g.* Pt-N) only involves the core electrons of the neighboring atom.

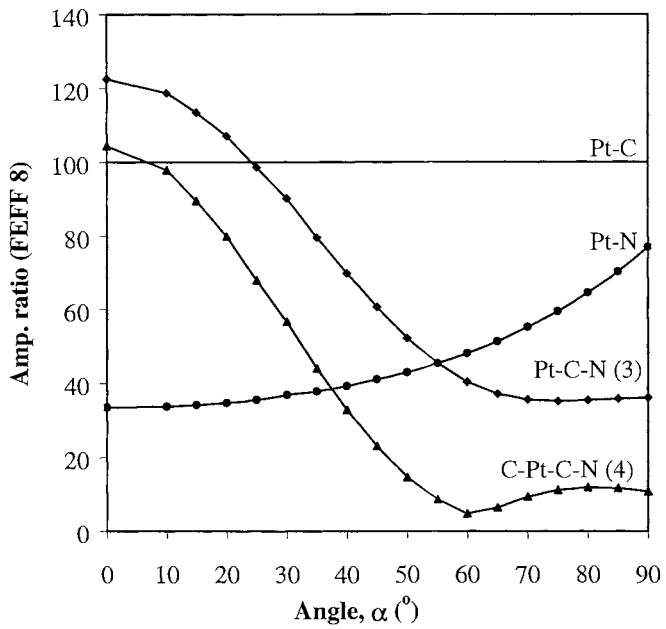

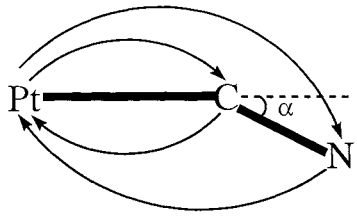

Single scattering
Pt-C ; Pt-N

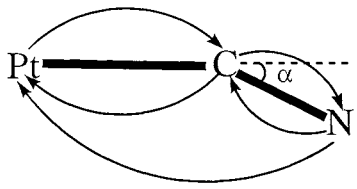

Multiple scattering
Pt-C-N (n_{leg} = 3); C-Pt-C-N (n_{leg} = 4)

Figure 23. Multiple scattering. Importance of focusing effect for a three-atom system, Pt-C-N. The contribution of different scattering paths *vs.* deviation from linearity (angle α) has been calculated using the FEFF8 program for a global $\sigma^2 = 0.005$ Å^2.

1.6 Fourier-transform. The XAFS function can be written as a sum of modified sine waves corresponding to different backscattering shells, *j*:

$$k^n \chi_i(k) = k^{n-1} \sum_j A_j(k) \sin [2kR_j + \phi_{ij}(k)] \qquad (14)$$

A Fourier-transform (FT) is useful for separating these frequency functions and converting them to corresponding peaks in *r*-space, with the aim to extract the interatomic distances, R_j, between the absorber and the backscatterers.[34]

$$\mathbf{FT}\ [k^n.\chi(k)] = \frac{1}{\sqrt{2}} \int_{k_{min}}^{k_{max}} k^n.\chi(k).W(k)\ .\ e^{2ikR} dk \qquad (22)$$

W(k) is a window function which minimizes the ripples due to termination effects in the FT integral at the finite limits k_{min} and k_{max} (see below).[13]

The Fourier-transform converts the XAFS function from *k*-space (or frequency space) to *r*-space (distance or real space) and produces a "Pseudo Radial Distribution Function" (PRDF), in which the peak positions are related to (but do not directly give) the average absorber-backscatterer distances, because of the phase shift, $\phi_{ij}(k)$.

In the preliminary Fourier-transforms the phase shift parameter, $\phi_{ij}(k)$, is normally omitted from the sinusodical term for simplicity. Therefore, Fourier-transforms uncorrected for phase shift, give peaks in the transform which are shifted by a distance α_j relative to the correct distances (α = 0.2 - 0.5 Å). The phase shift correction is normally applied during the fitting procedure.[13]

The width of the *k*-space window ($k_{min} \rightarrow k_{max}$) for the Fourier-transform affects the width of the peaks in the PRDF. A shorter *k*-range gives broader peaks, and therefore, a decrease in the effective resolution between similar distances, ΔR (see Section *1.7.5*).[34] For two shells of backscatterers with similar atomic number, the effective *k*-range, Δk, is related to the resolution limit by:

$$\Delta R = \frac{\pi}{2\Delta k} \qquad (23)$$

For high resolution, as large a window (in *k* space) as possible should be used. However, it is often not possible to use a lower *k* limit than $k_{min} \approx 3$ Å^{-1}, in order to avoid the increasing multiple scattering contributions at lower energies.

Qualitatively, the PRDF gives an informative picture of the local environment surrounding the central atom, but not quantitative structural information.[29] Beside the coordination number and the amplitude reduction factor, there are several *k*-dependent factors which affect the amplitude of the $\chi(k)$, such as the Debye-Waller factor, the mean-

free path factor and also the effective amplitude function, $f_{eff}(k)$. When the $\chi(k)$ function is Fourier-transformed, these k-dependent factors interfere with each other so that the peak area in PRDF can not be used as a direct measure of the coordination number. In that respect the PRDF is similar to a radial distribution function obtained by x-ray diffraction (see Section 2).[14]

However, each peak in the PRDF corresponds to a contribution to the $\chi(k)$ function from one or more shells of backscatterers. A large peak in the PRDF corresponds to large amplitude in the corresponding EXAFS oscillation. In order to obtain accurate structural information these oscillations should be analyzed by model calculations in k-space. The PRDF is useful for selecting the important backscattering paths and building the model function. An important tool in the analysis of the data is to select a specific peak or range in r-space by means of Fourier filtering, and backtransform it into k-space (see Section *1.6.2*).

1.6.1 Window function: If the data are weighted so that their amplitude is approximately constant over the observed k-range, then an abrupt drop to zero will occur outside this range in the Fourier-transform procedure. This sudden change in amplitude of the data causes "ringing" in r-space, that is, on both sides of each transformed peak, side lobes appear which may interfere with peaks from other shells and make it difficult to isolate separate shells. Selecting the k-region for the FT by cutting the $\chi(k)$ at a zero value of the oscillations has a similar effect (contrary to popular belief!).[14]

A window function, W(k), is often used to reduce truncation effects, by making the oscillations in the spectrum smoothly approach zero at k_{min} and k_{max} (rather than dropping abruptly). This will efficiently suppress the side lobes, but makes the main part of each peak in the PRDF slightly broader.[14] The window function can be selected in many ways for this purpose. A smooth window function facilitates Fourier filtering, but too much damping of the $\chi(k)$ oscillations should be avoided since the increasing width of the peaks may cause loss of information.

Figure 24 shows a k^3-weighted spectrum modified by a Bessel window function, so that the weighted EXAFS data rise smoothly from a small value at the low k-side and fall smoothly on the high k-side, giving a clean peak in the Fourier-transform.[16e]

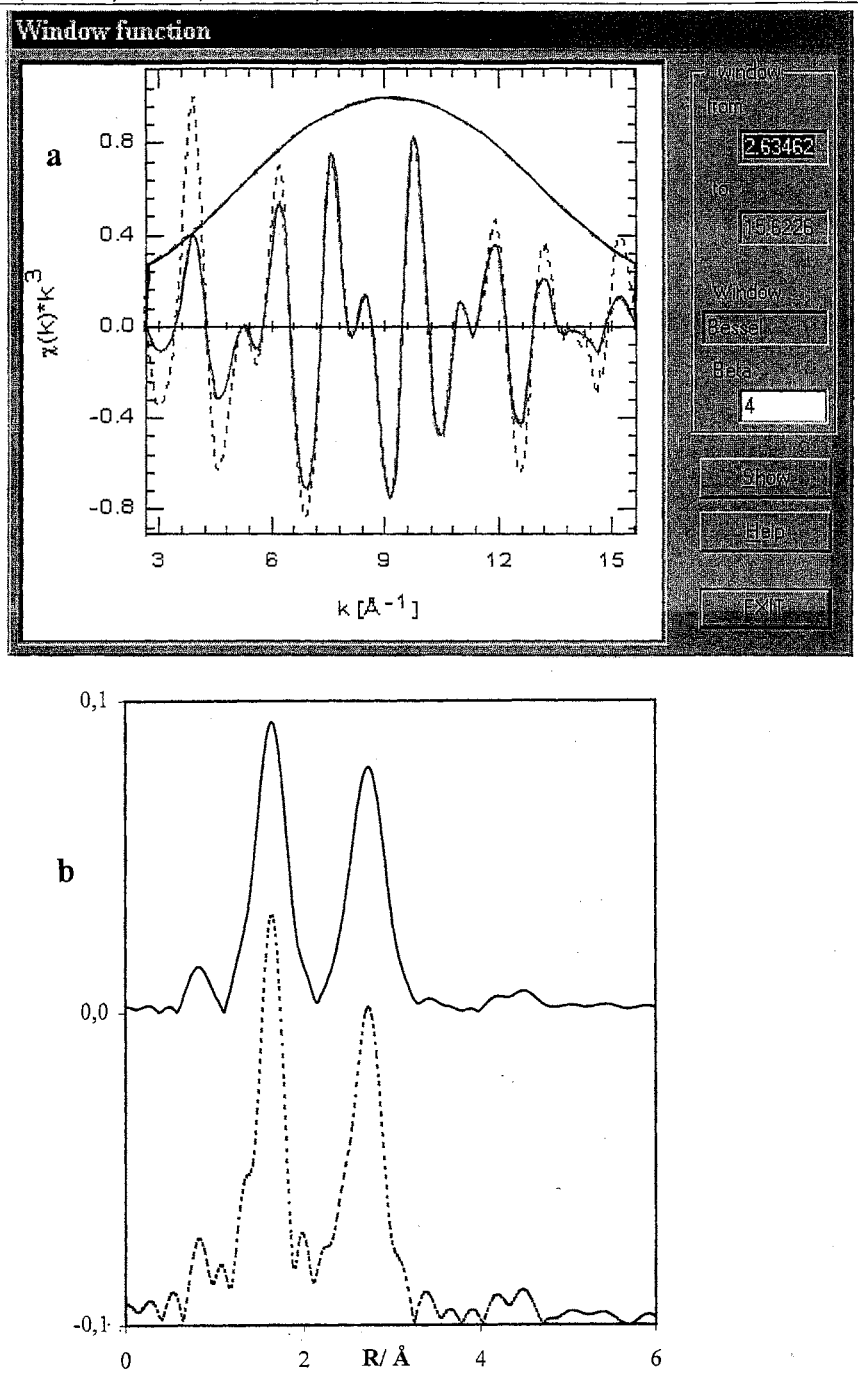

Figure 24. a) A Bessel type window function (smooth curve) applied on the k^3-weighted EXAFS data (Pt L_{III}-edge $K_2Pt(CN)_4 \cdot 3H_2O$; dashes) reduces the amplitude at the transform limits k_{min} and k_{max} (solid line). b) Fourier-transforms of the above data with (solid line) and without (dashes) window function.

1.6.2 Fourier filtering: The Pseudo Radial Distribution Function (PRDF) is a useful way to visualize the structural information, but more detailed structural results must be obtained by analyzing the EXAFS data in *k*-space.[29] An important application of the Fourier technique is Fourier-filtering. In this procedure, a particular region of a Fourier-transform, frequently a single shell of backscatterers, is back-transformed to *k*-space, and the resulting isolated EXAFS oscillation, $\chi_f(k)$, is used for further analysis.[15e] Figure 25 illustrates the selection of a back-transform window for Fourier filtering by the bars(1-2) surrounding the peak for the first shell of backscatterers. The corresponding $k^3 \cdot \chi_f(k)$ oscillation is then analyzed by fitting a calculated model function describing the selected range in *r*-space, in order to obtain structural information such as nearest neighbor distance, coordination number, Debye-Waller factors (indicative of the degree of the vibrational and configurational disorder), and the types of nearest neighbors.[29]

This Fourier-filtering procedure allows the main features in the PRDF to be analyzed separately, by eliminating features in the PRDF which are not described in the applied model function. Spurious peaks at low *r*-values, which originate from low-frequency oscillations in the $\chi(k)$ function due to problems in the spline or background elimination, can be removed. Multiple scattering contributions, which always occur at *r*-values higher than those for backscattering from the first coordination shell, and which may be difficult to account for in a model function, can be eliminated on the high *r*-side.

It is important to use a range which is wide enough around the peak in *r*-space for the back-transformation. The narrower the window, the more perfectly sine-like the oscillations in the filtered $\chi_f(k)$ function becomes. If the entire peak can be included in the *r*-space window, the distortion by the Fourier-filtering is minimal. However, if shoulders and side-lobes of the peak (including truncation ripples) must be excluded, because other peaks are too close, there will be some distortion of the *k*-space data. To make these effects similar for the standard and an unknown compound, one should choose the same width of the *r*-space window (the position can differ).[14] Different steps for extracting the oscillation of a single shell, from the treatment and corrections of the raw data to Fourier-filtering, is shown in Figure 25.[12]

1.7 Curve fitting analysis. The data analysis always involves some form of curve fitting of a model function to the experimental data.[15e] Such a model function is usually based on an assumed structure, from which separate backscattering paths can be extracted.

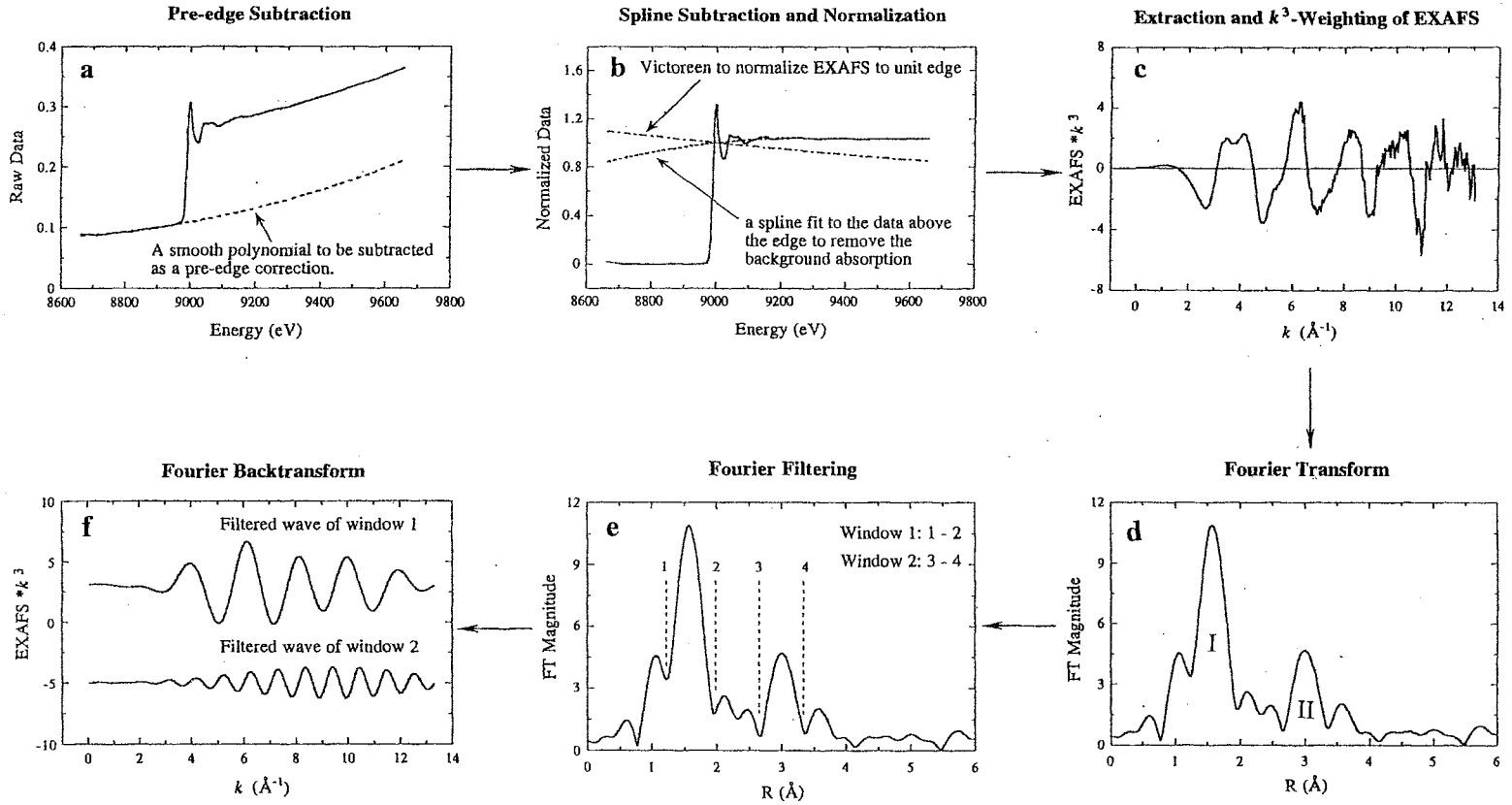

Figure 25. Steps in the analysis of an EXAFS spectrum: a) Pre-edge correction by subtracting a smooth polynominal; b) Normalization and atomic background correction by spline removal; c) Extraction and k^3-weighting of EXAFS function; d) Fourier-transform of **c** resulting in a pseudo-radial distribution function (PRDF). The two major peaks in the PRDF correspond to first and second neighbor distances around the absorber; e) Fourier filter windows for filtering the two major peaks are defined by the R_1-R_2 and R_3-R_4.regions; f) Back Fourier transform of the peaks in **e** over the filter ranges, showing their individual contributions to the χ(k) function (ref. 4a). (*Reproduced by permission*).

After Fourier-filtering, the theoretical model function used to describe the filtered $k^n\chi_f(k)$ oscillation, is constructed using eqn. (14). Backscattering amplitudes and atomic phase shifts are obtained from *ab initio* based FEFF calculations for the selected pathways from the assumed structure.[29] The values of various parameters in the theoretically simulated model function are adjusted (by least-squares fitting) until an acceptable fit with the experimental function is achieved.[13] In the final step, when the model is extended to include and describe all significant contributions in the experimental spectrum, fitting to the raw (unfiltered) $\chi(k)$ data can be performed.

1.7.1 Program systems for data analysis.

The FEFF program:[20] The present version, FEFF8, of the program allows *e.g.* calculations of phase shifts, effective scattering amplitudes ($|$ f_eff $|$ from which FEFF gets its name) for possible single and multiple scattering pathways using curved wave scattering theory, for XAFS and XANES spectra.[33] The atomic background absorption μ_0, which is normally assumed to be a smooth monotonically decreasing function with increasing energy, was recently shown to have structure in the NEXAFS region.[5] For accurate evaluation of XANES and XAFS spectra such variations can be of importance, and improved background calculations have been introduced in the later FEFF program codes.[20]

Rehr et al. have devised a strategy for multiple scattering (MS) calculations that greatly speeds up their path-by-path approach.[19] Their method includes mean-free-path inelastic loss terms and Debye-Waller factors for each individual MS pathway.[5] In this formalism the contribution from each individual multiple scattering path p can be described in an expression analogous to the standard XAFS equation:

$$\chi_p(k) = \frac{\left|f_{eff}(k,R)\right|_p}{kR_p^2} S_0^2(k).\ \exp(-2k^2\sigma_p^2)\ \exp[-2R_p / \Lambda(k)]\ \sin[2kR_p + \delta_p(k)] \qquad (24)$$

Here $f_{eff}(k,R)$ is the effective curved wave scattering amplitude, $\delta_p(k)$ is the phase shift for the path p, $\Lambda(k)$ is the inelastic mean free path for the photoelectron, R_p is half of the total backscattering pathway $R_p = R_{path}/2$, σ_p is the root-mean-square displacement (the Debye-Waller parameter) of the path R_p, and S_0^2 is the amplitude reduction factor which accounts for *e.g.* multiple electron excitation effects.[18]

The important backscattering pathways appear as peaks in the *r*-space Fourier-transform (PRDF) of the experimental $\chi(k)$ function (see Section *1.6*). By Fourier-filtering

and back-transformation procedures, we can select an *r*-range for analysis and ignore the contributions outside this range. All the significant contributions, including multiple scattering, should be accounted for in the model fitting of the selected *r*-range.

For an assumed structural model, the FEFF program can calculate the contributions from all possible pathways in this *r*-range. Since it is not obvious which of the MS paths that can be ignored in the model, Rehr et al. have developed efficient path filters to discard the insignificant ones. This allows accurate calculations to be carried out of the remaining important paths, normally for the Debye-Waller parameter $\sigma_p = 0$.

A model function, describing the filtered $\chi_f(k)$ function, is then constructed by including the Debye-Waller factors for the most important paths. The parameters for each path can be adjusted individually, but care must be taken to introduce appropriate constraints not to exceed the meaningful number of adjustable parameters.

The calculation is automated and done sequentially in different steps: [33]

- The scattering potentials, phase shifts, dipole matrix elements and absolute energies are calculated.
- The possible scattering paths for the cluster are described.
- The effective scattering amplitudes and other XAFS parameters are calculated for each scattering path.
- The XAFS contributions from selected paths can be combined to obtain a complete XAFS model function

ATOMS for crystal structures.[32] For crystal structures the ATOMS program is available to simplify the input to FEFF. ATOMS runs from an input file called atoms.inp, which contains the crystallographic information of a crystal structure. The output of ATOMS which contains a list of atomic coordinates for that crystal structure, is in fact a text file that can serve as the input file for FEFF; named *feff.inp*.[32]

EXAFSPAK. Several independent program packages allow analyses of XAFS data with the use of FEFF files of phase and amplitude data. These include for example, EXAFSPAK,[26] an analysis package developed at Stanford Synchrotron Radiation Laboratory (SSRL), which runs under UNIX. In the current studies, this program has been used for all preliminary data treatment, calibrations and averaging procedures.

WinXAS is a software package running under MS-Windows for PC-computers.[27] It contains some useful features: easy-to-use graphics, all necessary numerical functions for

conventional XAS data reduction including a complete FEFF interface, smoothing, glitch removal, etc. For the least-squares refinements of model functions, multiple scattering pathways including constraints of the refined parameters, and descriptions of asymmetric distributions of distances in a shell by means of third and fourth order cumulants, can be introduced. These features have been very useful for most of the analyses in the Papers I-V of asymmetric distributions and multiple scattering contributions.

1.7.2 Amplitude and phase shift transferability: Previously, EXAFS data analyses of a structurally unknown sample were based on backscattering amplitude and phase functions extracted from the same absorber-backscatterer pair in a well-characterized standard compound. For this extraction, Fourier-filtering of the corresponding peak in the PRDF from the standard compound was made to isolate the $\chi_f(k)$ contribution.

Approximate phase shift $\phi_{ij}(k)$ and amplitude $F_j(k)$ functions for these backscattering atoms, parameterized in simple analytical forms, allowed an initial theoretical XAFS model function to be calculated.[15e] The parameters of the actual amplitude and phase functions were then refined by fitting this model function to the experimental $\chi_f(k)$ contribution for the standard compound, keeping the known values for distance R_j and coordination number N_j fixed. Once the amplitude and phase functions for a given absorber - backscatterer pair had been obtained empirically in this way, the unknown could be analyzed.[13]

Even though this procedure removed some contributions from instrumental effects and approximations in the theoretical model functions, the method had severe limitations. It was restricted to single-scattering analyses of the EXAFS data, and required a suitable standard compound to account for the effects from the chemical environment of the backscattering shell on the amplitude and phase functions. Also, truncation effects in the Fourier-filtering procedure for the standard compound could affect the derived parameters. Another serious drawback was that the Debye-Waller factors of the unknown could only be determined relative to those of the standard compound.

Nowadays, *ab initio* calculations (with the FEFF codes) of effective back-scattering amplitudes, $f_{eff}(k,R)$, and phase shifts, $\phi_{ij}(k)$, give superior results for the determination of accurate distances R_j, and evaluation of structural disorder, etc. The parameters of structural model used to generate the theoretical XAFS spectrum are refined in a curve-fitting procedure. In the preliminary structural refinements, one can assume that the

effective $f_{eff}(k,R)$ values from curved wave theory are insensitive to small variations in near-neighbor distances R, *i.e.* not strongly dependent on chemical effects. Therefore, in this stage a simple model can be used for the FEFF calculations. However, for the best accuracy in the final stage, $f_{eff}(k,R)$ and $\phi_{ij}(k)$ parameters from a theoretical *ab initio* calculation on the complete structural model should be used.

The phase shift $\phi_{ij}(k)$ from theoretical calculations is subtracted from the total phase shift of the unknown, yielding an accurate R_j value from the $2kR_j$ portion of the XAFS equation (14). The inelastic scattering loss factor, $\exp[-2R_j/\Lambda(k)]$, is obtained with sufficient accuracy from the FEFF calculations. However, as discussed above (Section *1.5.4*), the amplitude reduction factor $S_0^2(k)$ can be uncertain to ± 20% or more, giving low accuracy in the number of atoms in each shell. Therefore, it is still useful to experimentally determine the amplitude reduction factor, S_0^2, for a closely related standard compound with known coordination number. The use of a known S_0^2 value leads to better accuracy in the determination of the coordination number, and also the Debye-Waller parameters of the *j*th shell in related unknown compound, especially for disordered complexes.

1.7.3 Non-linear least-squares curve fitting: Usually most systems contain multiple shells of backscatterers, and require non-linear curve-fitting techniques in order to extract the structural information. For this purpose, the EXAFS is calculated for a proposed structure, which is then modified to improve the agreement between the calculated and the experimental data. The calculations are based on varying the parameters R_j, N_j, and σ_j^2 in eqn. (14); in which the amplitude and phase shift functions $f_{eff}(k)$ and $\phi_{ij}(k)$ normally are calculated theoretically for each scattering shell.[15e]

The XAFS equation is a linear function of the coordination number N (and S_0^2), but it is a non-linear function of the distance and disorder parameters, R_j and σ_j. Thus, the fitting problem is a non-linear one, and many local minima in the sum of squares function may exist. For this reason, it is important to try several different starting points in the minimization procedure [14]

The least-squares fitting procedure minimizes the variance S expressed as:[13]

$$S = \sum_i (\chi_i^E - \chi_i)^2 \qquad (25)$$

χ_i^E = experimental data

χ_i = calculated EXAFS using eqn. (14)

which gives the parameter values for the best fit.[14] The number of parameters which can be refined independently (N_{idp}= degrees of freedom) is limited and can be expressed by:

$$N_{idp} = (2\Delta r \cdot \Delta k/\pi)+2$$

where Δr is the back-Fourier transform range in Å and Δk is the k-range in $Å^{-1}$.[4] For a k-range of about 13 $Å^{-1}$ and a Δr of 1.0 Å (often the first shell in the Fourier-transform), the number of degrees of freedom is about 10, which means that it is possible to fit up to 10 independent parameters.

For each shell of atoms around an absorber we can refine the interatomic distance R, coordination number N, and a disorder parameter σ^2. Also ΔE_0 can be refined as a common parameter for adjusting the k-scale (see Section *1.4.3*). When we extend the Δr-range in the Fourier-filtering, we include additional scattering shells and the number of parameters increases rapidly. At the same time the degrees of freedom N_{idp} increases. However, the number of parameters which can be refined simultaneously, must often be restricted not to exceed N_{idp}, *i.e.* the parameters must be fixed or constrained to each other. Usually, in order to reduce the number of parameters, the N (and S_0^2) parameters can be fixed at a known (or likely) number, and σ^2 varied.[15e]

When there are strong chemical bonds around the absorber, the electron density of the absorber is not uniform in all directions (as assumed in "muffin-tin potential" theory). This could be accounted for by using separate ΔE_0 shifts for different scattering paths.[18b] However, normally only a common ΔE_0 value is used.

There are always strong correlations between some of the parameters, *e.g.* between the number of distances N and the Debye-Waller parameter σ^2, both of which affect the amplitude. The correlation between the distance R and ΔE_0 [the correction to the estimated threshold energy, see Section *1.4.3*)], affects the phase within a shell of the model function, $\chi(k)$. If E_0 increases 2-3 eV, the R_j value increases about 0.01 Å; thus this correlation may introduce a *systematic error* in the determination of the distance.[4] Independent refinements of the R and ΔE_0 parameters may work well in order to minimize this type of error, if the data quality is good enough (low S/N ratio, wide k-range). Also, when a careful calibration of the energy scale has been made (*e.g.* simultaneous measurement on a metal foil to establish its E_0 value) the ΔE_0 shift, due to chemical effects in the investigated compound, can be determined by FEFF8 calculations to within ±1 eV.[28]

Fixing ΔE_0 to a value obtained for a standard compound should be done with caution. In the case of Ca K-edge EXAFS measurements in Paper I, it was difficult to calibrate the

energy scale (no Ca foil available!). We then evaluated an E_0-value from a measurement on solids with known Ca-O distances (assuming chemical transferability), and used this E_0-value for the hydrated ion in aqueous solution. The estimated uncertainty in E_0, ± 1 eV, corresponds to about ± 0.02 Å in the determination of the distance.

1.7.4 Standard Deviation and Goodness of Fit:

Standard deviations. The fit errors or "estimated standard deviations" in the WinXAS program are calculated from the covariance matrix of the Levenberg-Marquard least-squares algorithm.[27] To calculate this matrix and, hence, meaningful errors in the XAFS parameters, an "experimental error" is needed that reflects the overall error in the XAFS data. However, such an experimental error is difficult to estimate unambiguously. In the WinXAS program, the *statistical* standard deviation is estimated from the noise at high *k*-values of the zero-weighted $\chi(k)$ function. Glitches at high *k*-values can increase the apparent estimated error.

However, the experimental error is more than just data noise; it also includes *systematic errors* in the experiment, in the data reduction procedure, extraction of phases and amplitudes or theoretical calculations. In fact, the accuracy of the EXAFS parameters are determined mainly by the systematic errors and correlation effects, which are much more difficult to estimate. In Reference 4, it is outlined how multidimensional contour plots in parameter space can be used for analyzing correlation effects and statistical uncertainties.

In order to estimate the actual errors, one can examine how much a change in a specific fitting variable, *e.g.* ΔE_0, will change the desired parameters, *e.g.* R_j, for a particular noise level of the experimental data.

Model fitting indicators. As for 'goodness of fit' values, the *Residual* value given in the WinXAS program does not depend on the experimental error, but only reflects the deviation of the theoretical XAFS curve from the experimental one. The $(chi)^2$ (or χ^2) indicator is, on the other hand, calculated from the squared difference between theory and experiment divided by the experimental error. Residuals and χ^2 are calculated from:in

$$(\text{chi})^2 \text{ (minimized parameter in fit)}: \quad \chi^2 = \frac{1}{\sigma^2} \cdot \sum_{i=1}^{N} [\, y_{exp}(i) - y_{theo}(i) \,]^2 \qquad (26)$$

$$\text{Residual [\%]} = \frac{\sum_{i=1}^{N} [\, y_{exp}(i) - y_{theo}(i) \,]}{\sum_{i=1}^{N} [y_{exp}(i)]} \qquad (27)$$

which y_{exp} and y_{theo} are the experimental and theoretical data points, N the number of data points and σ is an estimate of the experimental error.

To summarize, the error in the parameters obtained in the least squares fitting procedure is estimated from the noise in the data. However, several sources of systematic errors are also present. It is useful to estimate the actual errors by analyzing the data at different conditions, *i.e.* different k-weighting and k-ranges, comparisons of r-space and k-space refinements, and by independent model fitting for experimental data from different scans of the same sample, etc.

1.7.5 Resolution and accuracy of interatomic bond distances: [22] In an EXAFS experiment, the resolution of the interatomic distances in a Fourier transform is related to the data range which can be used in the analysis (not the data range scanned, which may include regions at high k-values with no observable EXAFS). For example, assume that the useable data in an EXAFS scan is up to 1000 eV above the edge. The maximum k-value is then approximately $k = [0.2625(E-E_0)]^{½} = (0.2625*1000)^{½} = 16$ Å^{-1}, and the maximum k-range is 0-16 Å^{-1}. If the k-range 0-3 Å^{-1} is excluded due to overlap with the NEXAFS (when multiple scattering is not included in the model), we have a useful Δk range of 13 Å^{-1}. The resolution for two shells of similar backscatterers, which is given by $\Delta R = \pi /(2\Delta k)$, then becomes 0.12 Å. The distances must then differ by at least this much, or more for noisy data, to be resolved in the FT.

If the back-scattering shells have rather similar distances to the absorber (in the above example, $\Delta r < 0.12$ Å) but are very different in amplitude and phase functions, it can still be possible to resolve their EXAFS contribution in k-space using non-linear least squares curve fitting methods. This was the case for the separation of the Tl-N (2.50 Å) and Tl-Pt (2.63 Å) distances in Tl L_{III} edge EXAFS for the solid compound $TlPt(CN)_5$, Paper III.

Comparing distances from EXAFS and Crystallography.

The scattering phenomenon is on the femtosecond time scale, or faster.[16e] So, with this technique it is possible to take a snapshot picture of the position of atom A (absorber) relative to B (backscatterer), even for a vibrating A-B bond (the vibrational time scale is about 10^{-12} - 10^{-13} s). At each energy or k-value, the contribution of the backscatterer B to the EXAFS function, $\chi_{AB}(k)$, is the sum of all individual contributions from A-B pairs of atoms. When the photoelectron kinetic energy is varied over the k-range, this provides an *average of the exact A-B separations* (for all AB pairs); *cf.* Scheme 2. The movement

along the bond distance is related to the root-mean-square displacement parameter σ in the Debye-Waller factor term (Section *1.5.6*).

From crystal structures an *average distance between the separately determined mean positions of atoms* in a lattice, is calculated. Therefore, bond distances obtained from crystal structures for atoms with a strong bond to the absorber, always suffer from apparent shortening due to thermal motion effects.[35] Since the largest vibrational amplitudes always are perpendicular to the bond direction, as can be seen from the thermal ellipsoids in a crystal structure determination, the distance between the mean *positions* of the two atoms will appear shorter than their mean *separation* (Scheme 2). At room temperature the apparent shortening of the bond distance may account to 0.01-0.03 Å, considerably greater than all other errors in a well-determined crystal structure.[35]

A correction for this systematic error requires information about the movements of both the absorber A and backscatterer B, and the correlation due to their bonding interaction. A crystal structure determination provides no information about this correlated movement. However, "riding motion" correction is sometimes used for strong bonds, assuming a lighter ligand atom B to ride on (or follow) the motion of the heavier atom A.[35]

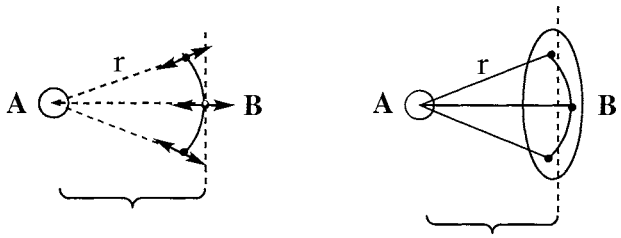

Scheme 2

As a consequence, carefully determined EXAFS bond distances can be more accurate than high precision values from crystal structures. For example, the M-O bond lengths of the hexahydrated $[Ga(H_2O)_6]^{3+}$ and $[In(H_2O)_6]^{3+}$ ions from EXAFS measurements were obtained as 1.957(2) and 2.122(2) Å, respectively, while single crystal x-ray diffraction data gave somewhat shorter mean values, 1.944(3) and 2.112(4) Å, respectively.[24]

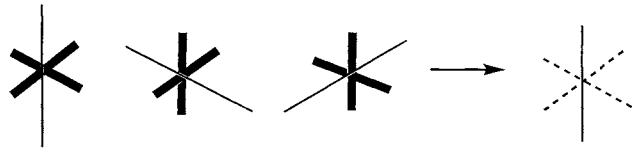

When there is positional disorder in the crystal structure, and/or too high symmetry of the crystal lattice is used, much larger differences can occur. For example, the $[Cu(en)_3](SO_4)$ complex appears at room temperature to have six equivalent Cu-N bonds of 2.15 Å. However, the EXAFS shows the local structure around the copper ion to have four short Cu-N bonds at 2.04 Å and two long Cu-N bonds at 2.28 Å.[36] The d^9 electronic configuration of Cu(II) cause a Jahn-Teller elongation of the octahedral coordination. At room temperature, the orientation of this elongation changes along the different axes (see below), so-called *dynamic* Jahn-Teller effect. XRD gives the average position of each atom and therefore, all bond distances appear to be equal.[36]

1.7.6 Coordination number accuracy:[22] The accuracy in the determination of the number of back-scatterers in a shell is sometimes given to be as low as ± 25%.[4] Part of this lack of accuracy is due to the determination of the amplitude reduction factor, S_0^2, which is connected to intensity losses due to multiple excitations (see Section *1.5.4*). Theoretical values of this factor often are about 0.7-0.8.[16e] However, for standard compounds (with known coordination number) the experimental values are sometimes even higher than unity. In some cases this can be related to fluorescence effects from the sample (*Note:* check the intensity of the I_0 monitor for sine-like variations from sample fluorescence).

An important source of error in the XAFS amplitude function can originate from the background removal (spline) procedure, in particular for low-Z absorber atoms with strong decay of the background absorption.[18b] It is important to use a proper approximation for μ_0 for normalizing the EXAFS oscillation (see Section *1.4.5*). Fluorescence measurements often give such normalization errors because of the apparent increase in the background absorption (see Section *1.3.6*).

However, for carefully conducted experiments, under similar conditions for the sample and a good standard compound with known coordination number, an experimental determination of the amplitude reduction factor, S_0^2, can be made. The use of such an experimentally determined scale factor can give an accuracy better than ± 10% in the number of backscatterers in a shell, as was found in a study of hydrated yttrium(III) ions.[37]

Another way of obtaining information on the coordination geometry, can be made with the use of standard compounds. The XANES spectra for different types of coordination geometries often have distinctly different pre-edge features corresponding to electronic transitions within the absorber (see Figure 2c). Also in the NEXAFS region, the

features due to multiple scattering are dependent on the coordination geometry and can be used for qualitative comparisons. In a study of the hydration of Y^{3+} in aqueous solution, the EXAFS spectra of a number of crystalline standard compounds have been compared with that of the solution.[37] From the near-edge structure, octahedral geometry (six-coordination) could be excluded for the hydrated ions in solution. Theoretical calculations of the edge structure in XANES region, *e.g.* by means of the FEFF program, can also be useful to distinguish between different coordination geometries (*cf.* Figure 2).

A comparison between bond distances of different known coordination numbers is often very useful. In the study of the calcium hydration (Paper I), the strongest evidence for the hydration number eight comes from correlations between the Ca-O bond distances and different coordination numbers.

1.7.7 EXAFS curve-fitting summary: [34]

Model parameters	*Comments*
R – Interatomic distance	- accuracy ± 0.01 Å for careful E_0 calibrations and well-defined coordination shells
N – Coordination number	- accuracy ± 25% (± 10% with proper standard compound)
σ^2 – Debye Waller parameter	- typical range: $0.0015 \leq \sigma^2 \leq 0.0080$ Å^2
ΔE_0 – Energy scale offset	- correction of estimated threshold energy E_0 (at which $k = 0$)

Restrictions

Resolution of distances in PDRF	- $\Delta R = \pi/(2\Delta k)$; Δk = k-range
No. of independent parameters	- $N_{idp} = (2\Delta k \Delta r/\pi) + 2$; Δr = Fourier-filtering r-range

Correlations

Amplitude of $\chi(k)$	- N correlates strongly with σ^2 and is proportional to the amplitude reduction factor S_0^2
Phase of $\chi(k)$	- R correlates strongly with ΔE_0

1.8 Technical Points in XAS measurements

1.8.1 Monochromators and rejection of higher order harmonics. The basic monochromator system for synchrotron XAS studies contains two parallel crystals, each cut parallel to the same (*hkl*) plane. The first crystal is used for monochromatization of the incident beam. The energy scale of the outgoing beam is then determined by rotating the crystal to change the incident angle θ. The second crystal is used to keep the outgoing beam parallel to the incident one.

According to Bragg's law ($2d_{hkl} \sin\theta = n\lambda$)*, lattice planes with smaller d_{hkl} spacing are favorable in order to obtain shorter wavelengths. In our experiments at SSRL, we have used two-crystal monochromators, at higher energy Si(220) with $2d_{hkl}$-spacing 3.840 Å, and at lower energy Si(111) with $2d_{hkl}$-spacing 6.271 Å. The energy resolution (ΔE/E) of the Si(111) monochromator is lower (*cf.* Figure 26 and Table 2).[19c]

Detuning. Synchrotron radiation may simultaneously satisfy the Bragg condition for multiple orders of diffraction, $2d_{hkl} \sin\theta = n\lambda$, ($n > 1$). However, x-rays corresponding to higher order harmonics, $n = 2, 3, \ldots$ have energies that may interfere with data collection, and should be removed. Higher order harmonics are hardly absorbed in the sample but can contribute to the intensity in both the I_0 and I_1 ion chambers, depending on the absorption of the gas in the ion chamber, *cf.* Figure 10.[16g] With the double-crystal monochromator arrangement, harmonics in the beam transmitted through the monochromator (giving the intensity I_0) can be reduced by slightly tilting the second crystal from the parallel alignment.[13] The intensity of higher orders of diffraction will then decrease much more than the fundamental ($n = 1$ in Bragg's law). This so-called *detuning* procedure is performed by rotating the second monochromator crystal slightly off the Bragg angle θ, by means of the force from a piezo-electric crystal.[22]

To measure the amount of detuning required for a certain energy range, a sample or foil (of the element being investigated) with strong fluorescence is placed in front of the Lytle detector. The monochromator is then set to a lower energy than that of the absorption edge of the element. Thereby, most of the fluorescence emitted from the sample should result from the harmonics in the beam, which will have high enough energy to eject photoelectrons. Before collecting data, it should be checked that the detuning is enough for the entire scan range.

* λ is the wavelength and θ is the Bragg angle.

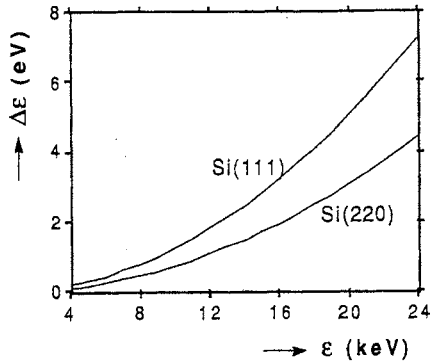

Figure 26. Typical energy resolution of a synchrotron x-ray beam diffracted by Si(111) and Si(220) single crystals, showing that at high energies, Si(220) gives better resolution (ref. 19c).

Table 2. Properties of some reflecting planes of silicon and germanium crystals (ref. 14)

	h	*k*	*l*	*2d (Å)*	*ΔE / E*
Si	1	1	1	6.2708	1.3×10^{-4}
	2	2	0	3.8400	5.6×10^{-5}
	4	0	0	2.7154	2.3×10^{-5}
Ge	1	1	1	6.5328	3.4×10^{-4}
	2	2	0	4.0004	1.5×10^{-4}

Table 3. Detuning data for uranium (ref. 25)

% Detuned at 17100 eV	$\mathbf{I_0}$	$\mathbf{I_f}$	$\mathbf{I_f / I_0}$
0 %	2.5	0.844	0.34
5 %	2.38	0.818	0.34
10 %	2.25	0.759	0.34
15 %	2.13	0.695	0.33
20 %	2.00	0.624	0.31
25 %	1.88	0.568	0.30
30 %	1.75	0.510	0.29
35 %	1.63	0.458	0.28
40 %	1.50	0.390	0.26
45 %	1.38	0.364	0.26
50 %	1.25	0.320	0.26

Practical procedure.[25] Create a table like Table 3 with the following columns: percent detuned, I_0, I_f, and I_f/I_0. Record the values for I_0 and I_f in the rows and begin with the monochromator without detuning, 5% (of I_0) detuned, 10% (of I_0) detuned, and so on. Then plot the ratio I_f/I_0 as a function of percent detuning. When the ratio of I_f/I_0 approaches a constant value, the desired amount of detuning has been achieved.

As an example of the procedure for detuning, consider the actual detuning data collected for uranium at beamline 4-3 of SSRL shown in Table 3 and Figure 27. The ratio I_f/I_0 becomes constant at 40%. Therefore, the optimal detuning is 40%.

Once the amount of detuning is determined, the direction of detuning must also be determined: whether to detune up or down in piezo voltage. The direction of detuning can effect the severity of "*glitches*" (*i.e.* sudden intensity variations in I_0) in the data. Detuning in one direction may reduce or even eliminate glitches, which are present when tuned in the other direction. Therefore, a sample should be tested with a scan once with the monochromator tuned in one direction and then once in the other. Qualitative comparison will then yield the best direction to detune.

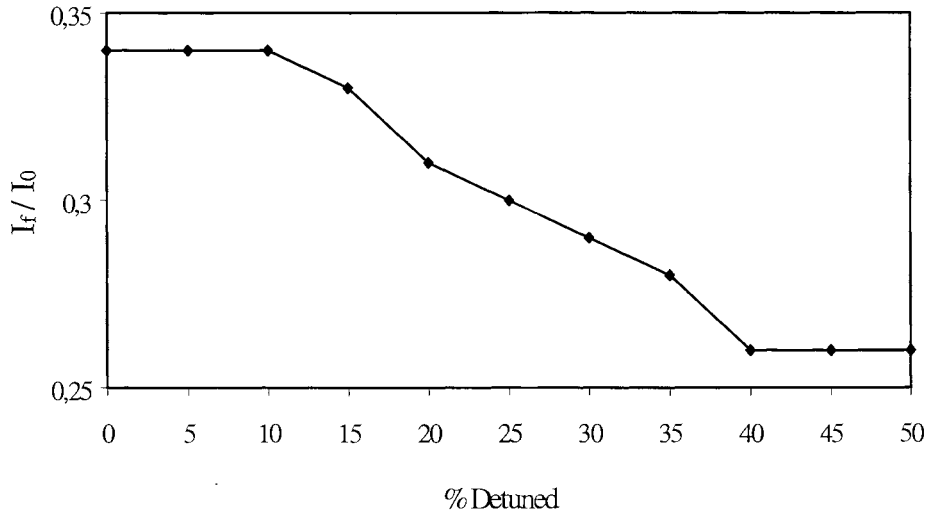

Figure 27. Detuning graph for uranium using Table 3 (ref. 25)

1.8.2 Lytle detector.[25] The Lytle detector provides a simple way of measuring the fluorescent x-rays emitted from a sample (see Figures 8 and 9). Typically, the Lytle detector is used for samples having more than 0.1% of the metal ion of interest. For more dilute samples, it is often necessary to use the more sensitive germanium detector. The advantages of the Lytle detector are that it collects the fluorescence for a much larger solid angle and its much higher count rates than for germanium detectors.

When using a Lytle detector, the sample should normally be positioned such that the angle between the incident beam and the measured fluorescent radiation is equal to 45°, which minimizes elastic scattering into the detector and maximizes the fluorescence signal from the sample (see Figures 9 & 28). The gas in the ion chamber of the Lytle detector should absorb 90-95% of the fluorescence radiation passing into the Lytle chamber. In general, nitrogen can be used for x-ray energies below 3 keV, argon between 3-7 keV, and krypton (or heavier gases) for energies above 7 keV (see Figure 10).[25]

With the fluorescent method of detection, one of the major concerns is noise, generated by the Compton scattering and the elastic scattering from the sample. X-ray filters may be used to reduce the scattering radiation that enters the detector, and the choice of a proper x-ray filter is an important consideration.

When selecting a filter, the K-edge (or L-edge) energy of the filter should be such that it absorbs much of the elastic plus Compton radiation scattered by the sample, while simultaneously transmitting the desired fluorescent K_α radiation. For elements from titanium (Ti) to ruthenium (Ru) with atomic number Z, it is preferable to select an x-ray filter containing the element with atomic number (Z-1), *i.e.* one unit less than the measured element (Figure 29). Beyond Ru, either Z-1 or Z-2 elements may be used. However, if the L-edge of a sample is to be measured, it may be difficult to find an element that satisfies the Z-1 or Z-2 condition for the filter. For example, consider an uranium sample, whose L_α, Compton, and elastic peaks are illustrated in Figure 30. The elements satisfying the Z-1 or Z-2 conditions are protactinium and thorium, both of which are unavailable to use as filter elements. Therefore, the periodic table must be searched to find a suitable element that is available, *i.e.* with a K-edge energy that will absorb the Compton and elastic radiation from the uranium sample. In this case strontium is an excellent candidate, with a K-edge energy that will absorb much of the radiation scattered towards the detector.[25]

For the fluorescence measurements on $[PtTl(CN)_7]^{2-}$ complex (Paper IV), a Ga filter was used (see Table 4).

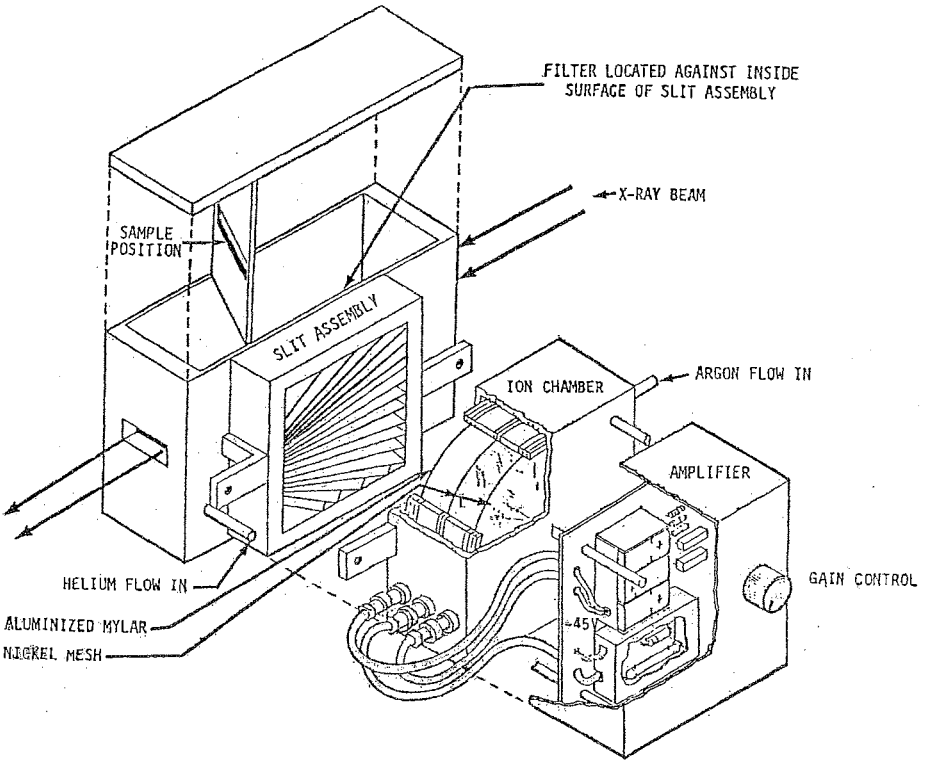

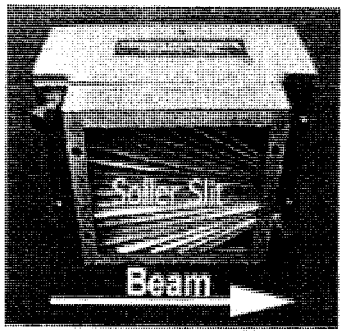

Figure 28. Lytle detector showing the position of the Soller Slit (ref. 25).

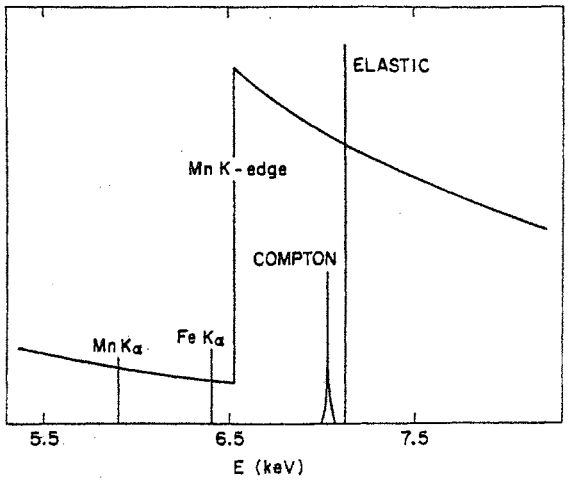

Figure 29. A manganese (Z= 25) filter is useful for background suppression in a Fe K-edge fluorescence experiment (Z=26). The sample is irradiated with a beam with energy $h\nu_0$, which can produce Fe K_α fluorescence. The incident beam is also scattered elastically (without energy loss), and inelastically (Compton scattering with lower energy). When these three types of radiation go through the Mn-filter, the Fe K_α line which has lower energy than the Mn K-edge, can pass through the filter without too much absorption. However, another contribution to the background arises from the Mn K_α fluorescence, produced by absorption of the elastic and Compton scattering in the Mn filter. (Note: $h\nu_0$ varies over the XAFS scan range)

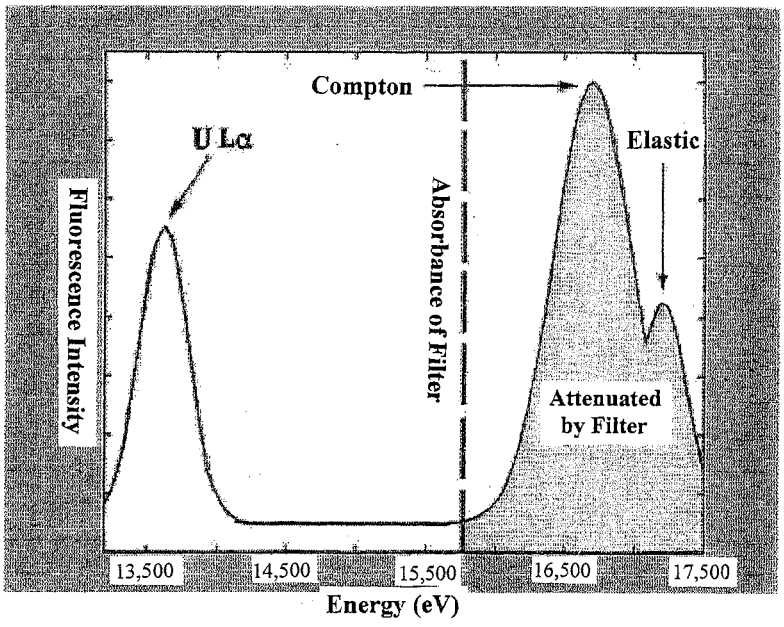

Figure 30. Uranium L_α, Compton, and elastic scattering peaks (ref. 25).

One consideration when choosing a filter is its thickness. In a Lytle detector, x-ray filters with an attenuation of 3 to 6 absorption lengths,* are often used. For dilute samples, it is often preferable to use a filter of 3 absorption lengths, and for more concentrated samples, 6 absorption lengths. However, filters with different absorption lengths should be tested in order to find the optimal one. Included is a table of selected elements to illustrate this (Table 5).

1.8.3 Properties of useful gases for XAS measurements. The densities, absorption edge energies, and absorption coefficients for some useful gases are listed in Table 6. In this table, the ratios of the beam transmitted for ion chambers of length 15 cm and 30 cm are also given for different energy ranges. These ratios can be calculated using the following expression:

$$\textit{Ratio of the beam transmitted} = I_1 / I_0 = e^{-\mu \rho L} \qquad (28)$$

where I_0 is the photon flux of the incident beam, I_1 is the photon flux of the transmitted beam, μ is the mass absorption coefficient (cm^2/g), ρ is the density of the gas (g/cm^3), and L is the length of the gas chamber (cm).

Table 4. Examples of appropriate filter materials for various edges (ref. 14) [a]

Element	E_K (eV)	E_F (eV)	Filter	E_{filter} (eV)	R
V	5465	4952	Ti	4965	6.5
Fe	7112	6403	Mn	6540	6.6
Cu	8979	8047	Ni	8333	5.5
Br	13474	11923	Se	12658	4.2
Mo	19999	17478	Zr	17998	4.5
Ca	4038	3691	In- L_{III}	3730	3.2
Pt- L_{III}	11564	9441	Ga	10367	4.4

[a] The elastically scattered background can be estimated from the factor R, which is the ratio of the absorption coefficient for elastic scattering to the absorption coefficient for the fluorescence radiation, at an energy of 200 eV above the edge. For the background due to Compton scattering, R is slightly larger. E_K and E_F are the K-edge and fluorescence energies, respectively, and E_{filter} is the filter edge energy.

* One absorption length is defined as: $x = 1/\mu$; therefore for 3 absorption lengths, $I / I_0 = \exp(-3) = 0.05$ which means that 5% of the radiation is transmitted.

Table 5. Selected filter information (ref. 25)

Element	Density (g/cm^3)	Mass Absorption Coefficient Below and Above K-edge (cm^2/g)	Thickness for 3 Absorption Lengths (microns)	Transmission Below and Above Edge for 3 Absorption Lengths I / I_0	Transmission Below and Above Edge for 6 Absorption Lengths I / I_0
Ti	4.54	93	9.6	0.665	0.445
		685		0.050	0.0025
V	6.11	77	8.0	0.686	0.47
		612		0.05	0.0025
Cr	7.19	74	9.4	0.606	0.367
		445		0.05	0.0025
Mn	7.42	64	9.4	0.641	0.410
		431		0.05	0.0025
Fe	7.86	60	9.6	0.635	0.404
		397		0.05	0.0025
Co	8.90	54	8.1	0.667	0.459
		416		0.05	0.0025
Ni	8.9	47	11.6	0.614	0.378
		290		0.05	0.0025
Cu	8.94	41	12.0	0.644	0.415
		280		0.05	0.0025
Zn	7.14	36	15.0	0.680	0.462
		280		0.05	0.0025
Ga	5.9	31	22.0	0.669	0.447
		231		0.05	0.0025
Ge	5.32	30	26.8	0.651	0.424
		210		0.05	0.0025

Table 6. Useful gases, densities, absorption coefficient, and ratios of transmission (ref. 25)

Gas (Density g/cm^3) (Absorption Edge eV)	**Energy Range (keV)**	**μ** (cm^2 / g)	**I_1 / I_0** (L = 15 cm)	**I_1 / I_0** (L = 30 cm)
Helium	2	6.317	0.98	0.97
(1.78×10^{-4})	3	1.561	1.0	1.0
(24.6)	5	0.2611	1.0	1.0
	8	0.04951	1.0	1.0
	10	0.02241	1.0	1.0
	15	0.00530	1.0	1.0
	20	0.001919	1.0	1.0
	30	0.0004558	1.0	1.0
Nitrogen	2	493	9.7×10^{-5}	9.4×10^{-9}
(1.25×10^{-3})	3	148.2	0.062	0.0039
(401.6)	5	30.66	0.56	0.32
	8	6.853	0.88	0.77
	10	3.324	0.94	0.88
	15	0.8793	0.98	0.97
	20	0.3396	0.99	0.99
	30	0.0884	1.0	1.0
Neon	2	1258	4.2×10^{-8}	1.8×10^{-15}
(9.0×10^{-4})	3	405.6	0.0042	1.8×10^{-5}
(866.9)	5	91.06	0.29	0.086
	8	21.81	0.74	0.55
	10	10.90	0.86	0.75
	15	3.037	0.96	0.92
	20	1.213	0.98	0.97
	30	0.3294	1.0	0.99
Argon	2	513.5	1.1×10^{-6}	1.2×10^{-12}
(1.78×10^{-3})	3	167.4	0.011	1.3×10^{-4}
(3202)	5	438.6	8.2×10^{-6}	6.8×10^{-11}
	8	120.2	0.040	0.0016
	10	63.38	0.18	0.034
	15	19.14	0.60	0.36
	20	8.01	0.81	0.65
	30	2.295	0.94	0.88
Krypton	2	3870	5.3×10^{-95}	2.8×10^{-189}
(3.74×10^{-3})	3	1359	7.8×10^{-34}	6.1×10^{-67}
(K-edge = 14.3	5	348.9	3.2×10^{-9}	1.0×10^{-17}
L_I = 1921.0	8	95.92	0.0046	2.1×10^{-5}
L_{II} = 1727.2	10	51.26	0.0056	0.0031
L_{III} = 1674.9)	15	115.2	0.0016	2.4×10^{-6}
	20	54.84	0.046	0.0021
	30	18.13	0.36	0.13

1.8.4 Sample cells. Liquids and solutions are normally inserted between two cell-windows, separated by a spacer (Figure 31). The window material must be carefully selected (see below). It is important to have homogeneous samples in order to obtain quantitative estimates of EXAFS amplitudes.

Solid samples must often be diluted and distributed homogeneously in an inert and low-absorbing matrix, such as boron nitride, BN. A good transmission XAFS sample must be uniform, with the compound of interest ground to small size (typically less than x = 0.01 mm).[16c] The solid powder mixture is normally held in a metal frame (*e.g.*, Al)* or teflon frame, between Mylar tape windows.

1.8.5 Cell window materials. Figure 32 shows the transmittance through various window materials, which can be polymers, metals, glasses or ceramics.[23] Polymer films can often be used. For example, 6 μm polypropylene, is very transparent but not gas-tight (in particular for He). On the other hand, polyimide (Kapton) in 8 μm thickness is much stronger and can be used up to a temperature of 250-320° C. Mylar films (~ 10 μm) and adhesive Mylar tapes are useful for almost all (except very low) energy ranges.

Metal foils, *e.g.* Be, Al and Ti, can be used as window material for high energy x-rays. Be is very transparent and chemically inert. Al is reasonably transparent but not very strong and melts at 600° C. Ti is a good choice for a large fluorescence window, and can be exposed to corrosive environment, very high temperature and pressure up to ≈10 psi. Ceramics suitable for windows include boron nitride (BN) and quartz (SiO_2). For liquid cells with thin spacers, planar windows are important for a well-defined path length though the sample<. In the high-energy range, we could use ultra thin glass windows (~35 μm) for this purpose.[38] The absorption in the glass windows becomes significant at energies lower than ~8 keV (Figure 33). Note, that this type of glass contains about 5% Zn, and therefore is not suitable for Zn (and Cu) samples.

* If other metals are used, watch out for disturbing fluorescence

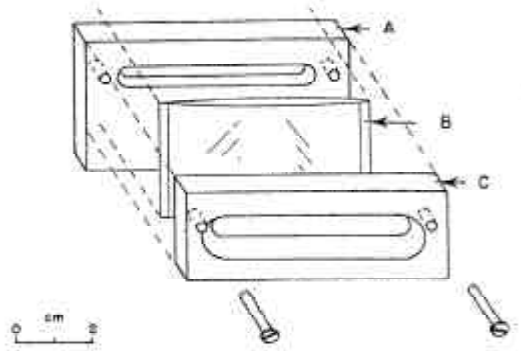

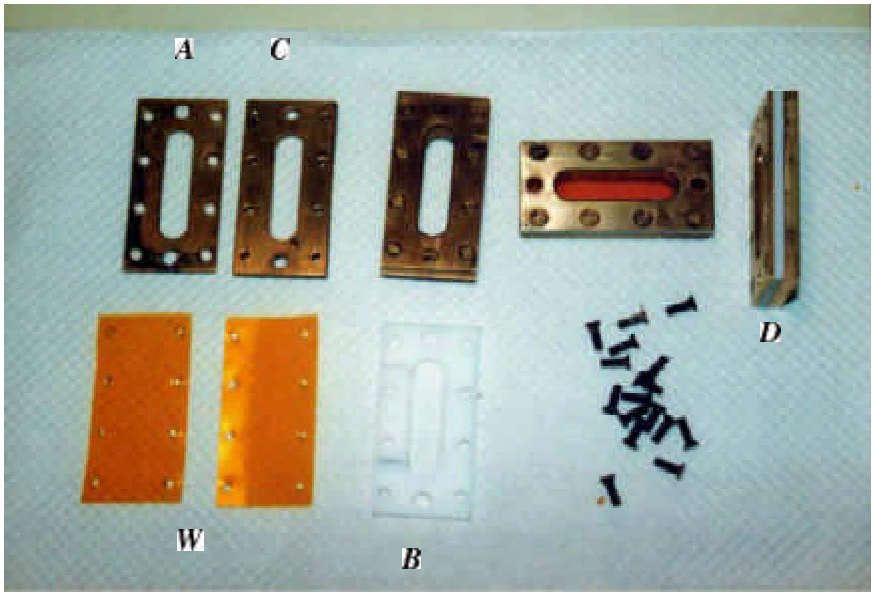

Figure 31. An example of an adjustable liquid sample cell for absorption measurements. Windows (***W***: Mylar, Polypropylene, Kapton films or glass) are placed on each side of the teflon spacer (***B***) and are clamped between the frames ***A*** and ***C***. The assembled cell is shown at the right hand corner, ***D***.

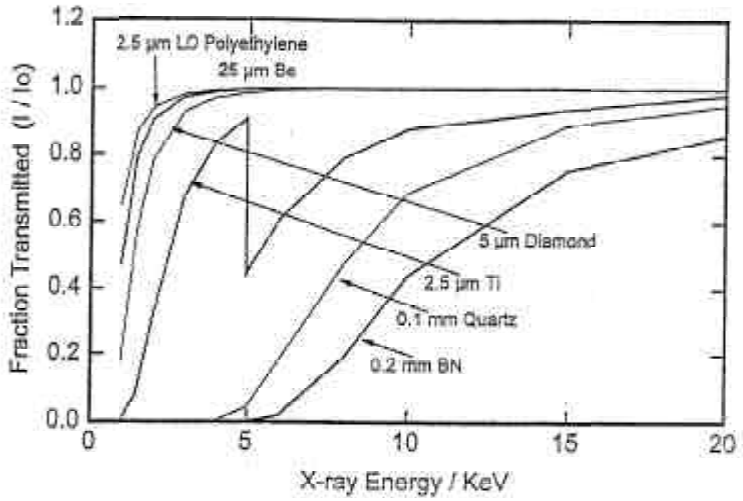

Figure 32. Fraction of transmission *vs.* energy through various commercially available window materials(ref. 23). The Ti K edge occurs at 4966 keV.

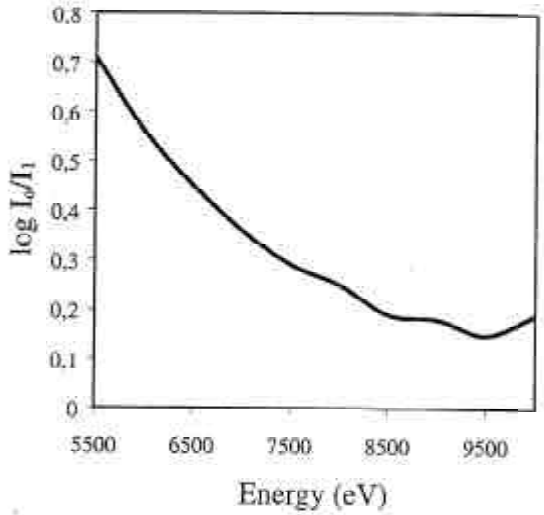

Figure 33. Energy dependence of the absorption of the ultra-thin glass windows (2x35 µm) used for liquid cells. Glass composition: 65% SiO_2, 8% B_2O_3, 4% Al_2O_3, 14% $Na_2O + K_2O$, 1% CaO, 3% TiO_2 and 5% ZnO (ref.38).

2. Large Angle X-ray Scattering (LAXS)

2.1 Structural information by diffraction methods and EXAFS on amorphous samples.
Diffraction methods and EXAFS are the generally available techniques for studying the structure of liquids and solutions. In the liquid phase the molecules are in random positions, but there is a short-range preferred orientation of one molecule toward its neighbors. Compared to crystalline compounds with ordered three-dimensional arrangements, the diffraction patterns of liquids are weak and diffuse. Therefore, the description of the structure of a liquid or solution from the diffraction data cannot be as detailed and unique as for a crystal.

A radial distribution curve for a polyatomic molecule in liquid phase has an intramolecular part (which is the same as its gas phase curve) and an intermolecular part, which contains all types of contacts between the molecules. Therefore, it can be difficult to extract the information from an experimentally obtained radial distribution curve for a liquid, because of possible overlap between the inter- and intramolecular parts. The situation is even more complicated for a solution, because of the many solvent molecules, which contribute to the total scattering pattern!

EXAFS has in this respect a major advantage over x-ray diffraction methods for studying amorphous phases: we can choose a specific element as central atom and obtain curves representing the distribution of neighboring atoms around this element.

Neutron diffraction can, in special cases, give a similar distribution curve from a difference between the distribution curves of two identical solutions with isotopic substitution of one element, *e.g* calcium. Because the neutron scattering factors are different for the two calcium isotopes, only the interactions involving calcium will remain in the difference curve, as in the study of calcium hydration by Enderby, Neilson *et al.*.[39,40]

Another difference between LAXS and EXAFS is the contributions from outer coordination shells. These shells, which are more distant from the central atom, often have higher disorder (higher Debye-Waller factors) than the first, more tightly coordinated shell. They give oscillations with higher frequency than that of the first shell (because of the larger R_j value), which die more rapidly at high k (or s)[♣] values, because of the higher Debye-Waller factor. For EXAFS there is an additional $1/R^2$ damping factor; *cf.* eqn. (14) in the intensity function $\chi(k)$, while the structure-dependent intensity function for LAXS

[♣] s is the scattering variable in the LAXS method: $s = 4\pi\lambda^{-1}\sin\theta$

contains an 1/R factor, see *e.g.* eqn. (34). Therefore, the contributions of the outer shell oscillations are most prominent at low values of the scattering variable, s in LAXS and k in EXAFS. However, at low k-values the EXAFS oscillation is also damped by the mean free path factor, $\exp[(2R_j / \Lambda(k)]$ (see Section *1.5.5*). Thus, the contributions of the outer shells become more damped for the EXAFS data, both at low and high k-values, than for LAXS.

An additional complication for EXAFS studies of outer coordination shells is the multiple scattering within the first coordination shell. The length of multiple scattering pathways within this shell can severely overlap *e.g.* with distances from the central atom to the second shell.[24] For LAXS, multiple scattering has a diffuse character without distinct pathways and focusing effects.[41] X-ray photons already scattered by an atom, can be scattered once more in the sample, before reaching the detector. The ratio of this secondary scattering to the primary intensity is usually small, and can normally be neglected. Only for solutions with low absorption ($\mu < \sim 10$ cm^{-1}) there is need to consider a correction for this effect. The LAXS method is therefore much better suited for the study of *e.g.* second hydration spheres around metal ions (*cf.* Figure 36a). However, high concentration is required to make the interactions with the metal ion prominent enough, because in LAXS all atoms in the sample contribute to the scattered structure-dependent intensity. Both methods can provide structural information of the first hydration shell with similar accuracy. The EXAFS method can be applied for samples with absorber atoms at much lower concentrations because only those interactions involving the absorbing atom will contribute. In Figure 34, the results of EXAFS and LAXS measurements on a $CaCl_2$ aqueous solution are compared both in k- (or s-) space and r-space.

2.2 The radial distribution function and Molecular Dynamics simulations. For a liquid, the distance between the scattering centers is not fixed (except within molecular species). A function, $g_{mn}(r)$, can be used to define the probability of finding an atom of type n at a distance r from the atom of type m. This function is called the *pair distribution function*, which is defined such that the probability of finding atoms of type n in a spherical shell of radius r and thickness dr around atom m is $4\pi r^2 g_{mn}(r)\mathrm{d}r$. The number of atoms of type n ($\boldsymbol{n}_{mn}$) in this spherical shell is:[40]

$$\mathrm{d}\boldsymbol{n}_{mn} = \frac{\boldsymbol{n}_n}{V} 4\pi r^2 g_{mn}(r)\mathrm{d}r \qquad (29)$$

where $\boldsymbol{n}_n/V$ is the *average number density*, *i.e.* the number of atoms of type n in the unit volume V.

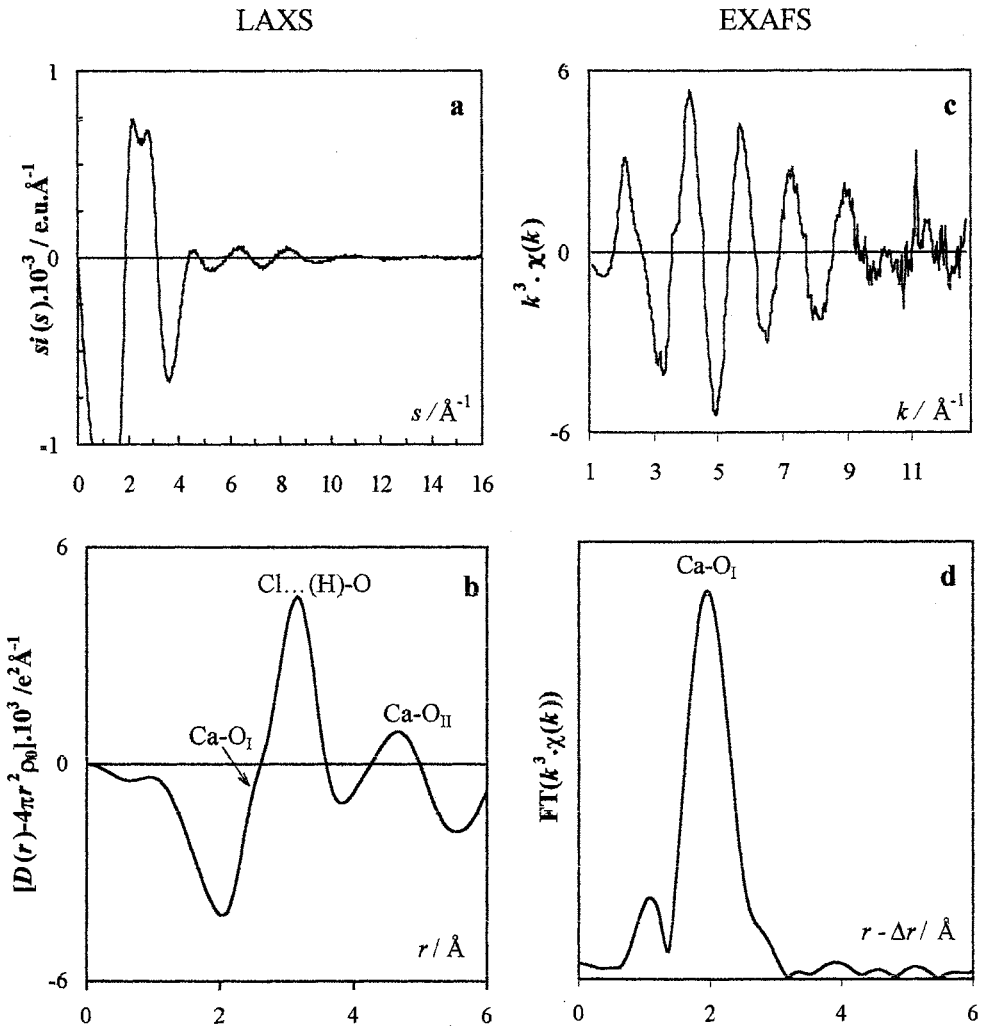

Figure 34. LAXS and Ca K-edge EXAFS measurements on a $CaCl_2$(aq) solution. a) LAXS; *s*-weighted structure-dependent intensity data; b) Fourier-transform of **a**; c) k^3-weighted EXAFS raw data, and d) Fourier-transform of **c**, not corrected for the phase-shift.

The hydrated metal ion can often be considered as an aqua complex, $[M(OH_2)_n]^{p+}$,[42] for which we would like to know the hydration number, *i.e.* the number of water oxygen atoms, $\boldsymbol{n}_{MO}$, arranged around the atom M. In the case when we have a well-defined hydration shell around a metal ion in solution, the $g_{MO}(r)$ function typically has a sharp maximum at a distance r_{MO}, corresponding to the sum of the ionic radii of the metal ion and the oxygen atom.[43] Then the hydration number, $\boldsymbol{n}_{MO}$, can be obtained as:[40]

$$\boldsymbol{n}_{MO} = \int_0^{r_d} 4\pi\rho_{oxygen}\, g_{MO}(r) r^2 dr = \int_0^{r_d} 4\pi\rho_{MO}(r) r^2 dr \qquad (30)$$

where ρ_{oxygen} ($= \boldsymbol{n}_O/V = \text{const.}$) is the *average number density* of oxygen atoms, $\rho_{MO}(r)$ is the *number density function* showing the variation of the number of oxygen atoms with distance r (around the metal ion M), and r_d is the first minimum after the MO peak.

Molecular Dynamics (MD) simulations, using potential functions for the interactions between ion M and the water molecule, can directly give the $g_{MO}(r)$ function. Eqn. (30), then gives a calculated hydration number, as shown in Figure 35, where different potential functions for the Ca-O_w interaction results in hydration numbers between 8 and 10.

By the Large Angle X-ray Scattering (LAXS) method we can not directly get the $g_{MO}(r)$ or number density $\rho_{MO}(r)$ functions, rather we get a modified number density function, $\rho(r)$, including all interactions, from which the M-O distance and hydration number can be obtained by model fitting, see Section *2.3*. In the combined LAXS and MD study of the hydration of the calcium ion in Paper I, the experimental results were used to evaluate the appropriate potential for calculating the radial distribution function.

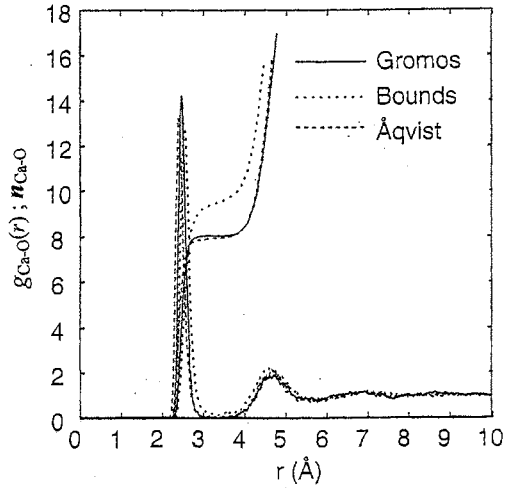

Figure 35. Molecular Dynamics (MD) simulation of the pair distribution function, $g_{Ca\text{-}O}(r)$, showing the probability to find water oxygen atoms around the calcium ions. Three different sets of potential functions have been used, giving differences in the coordination numbers, $\boldsymbol{n}_{Ca\text{-}O}$.

2.3 LAXS Theory. X-rays are scattered by the electrons in the atoms, and the intensity of the scattering depends on the number of electrons within the atom. Since the electrons are distributed over the atom, the interference between the scattering from individual electrons reduces the intensity at high scattering angles, 2θ. This is expressed by the x-ray atomic scattering factor, $f(s)$, which decreases with increasing s-value ($s = 4\pi\lambda^{-1}\sin\theta$).[41,44]

In the LAXS method, all atoms in the system contribute to the scattered intensity. For an isotropic and amorphous sample the total coherently scattered x-ray intensity (in electron units), $I(s)$, scattered from a sample is given by the Debye scattering equation:[45]

$$I(s) = \sum_m \sum_n [f_m(s) f_n(s) \cdot \sin(sr_{mn})/(sr_{mn})] \qquad (31)$$

where r_{mn} is the distance between two atoms m and n at the scattering event. The summations run over all atoms in the sample.

The scattering from each specific type of atom m (= n)*, regardless of its surrounding, has an intensity proportional to $f_m^2(s)$.[41] The total structure-*in*dependent intensity from all atoms in the sample is then $\sum_m f_m^2(s)$. For m≠n, if $\sum_m f_m^2(s)$ is subtracted from the total intensity, the structure-*dependent* part of the intensity remains, which is due to the interference between the waves scattered from different atoms, m and n, in the sample:

$$I(s) - \sum_m f_m^2(s) = \sum_{\substack{m \\ m \neq n}} \sum_n [f_m(s) f_n(s) \cdot \sin(s \cdot r_{mn})/(s \cdot r_{mn})] \qquad (32)$$

Assume that based on the stoichiometric composition of the sample, its volume is divided into N "stoichiometric" units of volume V, in each of which there is a stoichiometric number of atoms. The structure-dependent intensity from this unit of volume can be calculated, assuming one atom at a time in the unit volume V as reference atom, *m*, and all its neighbors within the total sample volume (NV) as *n*:*

$$i(s) = I(s)/N - \sum f_m^2(s) = \sum_m^V \sum_n^{NV} f_m f_n \sin(sr_{mn})/(sr_{mn}) \qquad (33)$$

The intensity $i(s)$ represents the structure-dependent part of the scattered intensity from the unit volume. The summation $\sum_n^{NV}$ is made over all atoms n in the sample volume (NV) and

* When $r_{mn} \rightarrow 0$, then $\sin(sr_{mn})/(sr_{mn}) \rightarrow 1$ in eqn. (31)

* There can be different types of atoms *n*, *e.g.*, *n* = Ca , Cl, O, ... in a $Ca(aq)^{2+}$ solution.

$\sum_{m}^{V}$ over all atoms (m) in the unit volume, V. The number of neighboring atoms n around a reference atom m (within V) is distance dependent for small r-values, but soon approaches the average number density ρ_0. Therefore a number density function, $\rho_{mn}(r)$, can be introduced which gives the number of atoms n per unit volume V at a distance r from the reference atom m. In a spherical shell of radius r and thickness dr from this atom m, the number of n atoms is $4\pi r^2\rho_{mn}(r)dr$. The sum $\sum_{n}^{NV}$ over the sample volume NV can then be replaced by an integral:

$$i(s) = \sum_{m}^{V} f_m \int^{NV} f_n \, 4\pi r^2 \rho_{mn}(r) \frac{\sin(sr)}{sr} dr \qquad (34)$$

By introducing (adding and subtracting) the average number density ρ_0 of neighboring atoms n per unit volume, the integral can be rewritten as:

$$i(s) = \sum_{m}^{V} f_m \int^{NV} f_n \, 4\pi r^2 \{\rho_{mn}(r) - \rho_0\} \frac{\sin(sr)}{sr} dr + \sum_{m}^{V} f_m \int^{NV} f_n \, 4\pi r^2 \rho_0 \frac{\sin(sr)}{sr} dr$$

The last term represents the small-angle scattering by an object of the same shape as the sample, but with uniform electron density. This scattering, which occurs at s-values lower than those used in LAXS measurements, can be neglected. The remaining expression is:[41]

$$i(s) = \sum_{m}^{V} f_m \int^{NV} f_n \, 4\pi r^2 \{\rho_{mn}(r) - \rho_0\} \frac{\sin(sr)}{sr} dr \qquad (35)$$

or $$i(s) = \sum_{m}^{V} f_m \int^{NV} f_n \, 4\pi r^2 \rho_0 \{g_{mn}(r) - 1\} \frac{\sin(sr)}{sr} dr \qquad (36)$$

where $g_{mn}(r) = [\rho_{mn}(r)/\rho_0]$ is the *mn pair distribution function* of atoms of type n around m; eqn. (30).

System with one type of atom. For simplicity, consider a one-component system, where we have only one reference atom in the unit volume ($m = 1$). If we multiply both sides of the equation with a "sharpening factor", $f^2(s=0)/f^2(s)$ [or $Z^2/f^2(s)$], the intensity function $i(s)Z^2/f^2(s)$ becomes the same as if the electrons had been concentrated in the nucleus of the atom (the same situation as in neutron scattering):

$$s \cdot i(s)Z^2/f^2(s) = \int^{NV} 4\pi r \rho_0 Z^2 [g(r) - 1] \sin(sr) dr \qquad (37)$$

This can be directly inverted by means of a sine Fourier transform[@], which gives:

$$r\rho_0 Z^2 [g(r) - 1] = rZ^2[\rho(r)-\rho_0] = \frac{1}{2\pi^2}\int_0^\infty [si(s)Z^2 / f^2(s)]\sin(rs)ds \qquad (38)$$

and when the equation is multiplied by $4\pi r$, then:

$$4\pi r^2\rho'_0 \cdot g(r) = 4\pi r^2\rho'_0 + \frac{2r}{\pi}\int_0^\infty [si(s)Z^2 / f^2(s)]\sin(rs)ds \qquad (39)$$

where $\rho'_0 = \rho_0 Z^2$. Thus, in the simple case with only one type of atom, the *electronic radial pair distribution function*, $4\pi r^2\rho'_0 \cdot g(r)$, can be obtained from a Fourier transform and directly connected to the structure-dependent intensity function, $i(s)$, which can be obtained from an experimental measurement.

System with many types of atoms. For such a system, eqn. (36) can be rewritten as:

$$i(s) = \sum_m^V \int^{NV} f_m(s) f_n(s) 4\pi r^2 \{\rho_{mn}(r)-\rho_0\} \frac{\sin(sr)}{sr} dr$$

In this case, we cannot completely eliminate the s-dependence of the $f(s)$ factors from the right side of the equation simply by multiplying with a "*sharpening factor*", $Z^2/f^2(s)$,[*] as we did in eqn. (37), because the scattering factors $f_n(s)$, have a somewhat different s-dependence for different elements. Nevertheless, multiplication by a sharpening factor, $Z^2 / f^2(s)$, with a function $f(s)$ of similar shape as the scattering factors $f_n(s)$, still will compensate for most of the s-dependence of the products $[f_m(s)f_n(s)]$. Often the $f(s)$ function is chosen as the scattering factor function for a reference atom, *e.g.* the metal ion for which we are studying the solvation. This sharpens the peaks and makes it easier to interpret the result in r-space, which is obtained after Fourier-transforming the experimental $i(s)$ function, weighted by s.

Since the experimentally accessible s-range typically is between 0.3 – 16 $Å^{-1}$, the integration in the Fourier transform has the cut-off limits s_{min} and s_{max}. Multiplying the $s \cdot i(s)$ function with the sharpening factor, $Z^2/f^2(s)$, increases the amplitude of the $s \cdot i(s)$ oscillation at the cut-off limit s_{max} of the Fourier integral, which gives termination effects

[@] The relations between Fourier transformed functions of the present type are (Ref. 41):

$$i(s) = 4\pi\int_0^\infty f(r)\sin(sr)dr \quad \text{and} \quad f(r) = \frac{1}{2\pi^2}\int_0^\infty i(s)\sin(rs)ds$$

[*] The sharpening factor, $Z^2/f^2(s)$ is in fact $f^2(s=0)/f^2(s)$, where at $s = 0$ (or $\theta = 0$) the atomic scattering factor $f(0)$ is equal to the number of electrons in the atom (neglecting anomalous dispersion corrections).[41,44]

in the Fourier-transformation. In order to reduce such effects, a so-called damping or *convergence factor,* $\exp(-b \cdot s^2)$, is applied (b has normally a value about 0.008). The effect is to reduce or remove the spurious ripples around the peaks in the Fourier transform, but also broadens the peaks by convoluting the peak shapes with a Gaussian function, which decreases the resolution.

$$s \cdot i(s) \cdot Z^2 \frac{\exp(-bs^2)}{f^2(s)} = \sum_m^V \int^{NV} Z^2 \cdot \frac{f_m(s) f_n(s)}{f^2(s)} \exp(-bs^2)\, 4\pi r\{\rho_{mn}(r) - \rho_0\} \sin(sr) dr$$

or $$s \cdot i(s) \cdot M(s) = \sum_m^V \int^{NV} f_m(s) f_n(s) \cdot M(s) \cdot 4\pi r\{\rho_{mn}(r) - \rho_0\} \sin(sr) dr \qquad (40)$$

where $M(s) = Z^2 \frac{\exp(-bs^2)}{f^2(s)}$ is called a "modification" function.

Now a Fourier-transformation can be performed on the modified structure-dependent intensity function, $s \cdot i(s) \cdot M(s)$, which can be derived from experimental measurements on a system with several types of atoms.

$$r[\rho(r) - \rho_0] = \frac{1}{2\pi^2} \int_{S\min}^{S\max} s \cdot i(s) \cdot M(s) \cdot \sin(sr)\, ds$$

When multiplying the equation by $4\pi r$, a modified *electronic radial distribution function* (RDF) is obtained:

$$4\pi r^2 \rho(r) = 4\pi r^2 \rho_0 + \frac{2r}{\pi} \int_{S\min}^{S\max} s \cdot i(s) \cdot M(s) \cdot \sin(sr)\, ds$$

which often is written

$$D(r) = 4\pi r^2 \rho_0 + \frac{2r}{\pi} \int_{S\min}^{S\max} s \cdot i(s) \cdot M(s) \cdot \sin(sr)\, ds \qquad (41)$$

$\rho(r)$ can be thought as mean of the modified electronic number density functions, while ρ_0 is the modified average electronic number density.

Structure information from the $D(r)$ *function.* The $\rho(r)$ function is no longer directly related to the number density functions $\rho_{mn}(r)$ in eqn. (40), since the factors $f_m(s)f_n(s)M(s)$ are different for each $\rho_{mn}(r)$ function. Therefore, they become dependent (convoluted) of each other in the Fourier transformation procedure. This makes the interpretation of the structural information less straightforward in the modified electronic radial distribution function, $D(r)$, which is the Fourier sine-transform of $s \cdot i(s) \cdot M(s)$. For example, it is not

possible to use eqn. (30) to directly integrate a peak in the $D(r)$ function, in order to get the hydration number. However, with the use of model functions, the experimental structure-dependent intensity function can be analyzed, both in k- and r-space. Let us now outline how this can be done, in order to extract the desired structural information for a solution.

Often the modified electronic radial distribution is visualized by plotting the difference $D(r) - 4\pi r^2 \rho_0$, in order to bring out the long-range variations around the mean value $4\pi r^2 \rho_0$. It can be shown,[41] that the $D(r)$ function can be written as a sum of pair functions, $P_{mn}(r)/r_{mn}$, which are independent (not convoluted) of each other:

$$D(r) = \frac{2r}{\pi} \sum_{m}^{V} \sum_{n}^{NV} [\boldsymbol{n}_m P_{mn}(r)/r_{mn}] \qquad (42)$$

where $\boldsymbol{n}_m$ is the number of atoms m in the unit volume V, and $P_{nm}(r)$ is defined as:

$$P_{mn}(r) = \int_{S\,min}^{S\,max} f_m(s) f_n(s) \sin(sr_{mn}) \cdot M(s) \cdot \sin(sr) ds \qquad (43)$$

The expression for the pair functions $P_{mn}(r)$ contain the atomic scattering factors, $f(s)$, which are nearly proportional to the number of electrons in the atoms. Thus, interactions involving heavy atoms in high concentration will be dominant, and give rise to peak shapes in the $D(r)$ function. The positions of these peaks represent the interatomic distances r_{mn} in the sample. By making use of known ionic sizes,[43] and intramolecular distances from crystal structures, it is usually possible from the peak positions and sizes in the $D(r)$ function to identify the atoms involved in corresponding interactions within structural units in the solution. For quantitative analyses, however, model calculations are performed to obtain the intensity contributions and the modified peak shapes of these interatomic interactions, which then can be fitted to the $i(s)$ and $D(r)$ curves.[46]

The procedure is similar to the XAFS data treatment, for which the effective scattering amplitudes, $f_{eff}(k)$, are k-dependent, in addition to other k-dependent factors affecting the amplitude, see Section *1.5*. An additional complication for XAFS is caused by the phase-shift at the back-scattering process, which shifts the peak positions in the pseudo-radial distribution function that is obtained by Fourier transformation of the $\chi(k)$ oscillations, Section *1.6*. Although the peak heights have some relation with the amplitudes of the $i(s)$ and $\chi(k)$ functions in the LAXS and XAFS techniques, respectively, the convolution of their s or k dependent factors in the Fourier transforms makes the peak areas unreliable as a direct measure of the coordination numbers.[41]

2.4 Model calculations and data analyses. For the purpose of model calculations, it is convenient to describe the investigated solution as consisting of molecular species or structural units. The bond lengths and intramolecular distances between the atoms p and q in a structural unit are then described by their mean values, r_{pq}. A symmetric deviation from the mean values, *e.g.* by thermal vibrations, can be described with a Debye-Waller factor, $\exp(-l_{pq}^2 s^2/2)$ in a harmonic approximation of the vibrational motion.[41] If the same notation is used as for EXAFS, the DW factor can be written as $\exp(-2\sigma_{pq}^2 s^2)$, where σ is the root-mean-square (*r.m.s*) displacement from the mean distance, r_{pq}. The structure-dependent intensity contribution from each type of structural unit is then given by:

$$i_{calc}(s) = \Sigma_p \Sigma_q f_p(s) f_q(s) \cdot \exp(-l_{pq}^2 s^2/2) \cdot \sin(s r_{pq})/(s r_{pq}) \qquad (44)$$

where l_{pq} ($= 2\sigma$) is the *r.m.s* of displacement *range* around the mean distance r_{pq}.

Anomalous dispersion effects, which occur close to absorption edges, can change the scattering amplitude for the atomic scattering factors $f(s)$ by $\Delta f'$, and also induce a phase shift described by a $\Delta f''$ term.[41,44] These anomalous dispersion correction terms, $\Delta f'$ and $\Delta f''$, which are independent of s, should be included when necessary. This gives

$$i_{calc}(s) = \Sigma_p \Sigma_q [f'_p(s) f'_q(s) + \Delta f''_p \Delta f''_q] \cdot \exp(-l_{pq}^2 s^2/2) \cdot \sin(s r_{pq})/(s r_{pq}) \qquad (45)$$

where the real part of the anomalous dispersion correction, $\Delta f'$, has been subtracted from the atomic scattering factor, giving $f'_p(s) = f_p(s) - \Delta f'$. The sums in eqns. (44) and (45) are taken over the different atoms p and q, with $p \neq q$, within the structural units in a stoichiometric unit volume, V (normally chosen to contain one metal atom)*.[46]

It is convenient to divide the interactions within a molecular species into a sum of specific atom pair interactions, each multiplied with the frequency factor $\boldsymbol{n}_{pq}$. For a specific interaction, *e.g.* the Ca-O bond, the calculated intensity contribution is then controlled by three main parameters: the distance r_{MO}, the frequency factor or hydration number $\boldsymbol{n}_{MO}$, and the Debye-Waller parameter, l_{MO}:[46]

$$i_{MO,calc}(s) = \boldsymbol{n}_{MO} f_M(s) f_O(s) \cdot \exp(-l^2_{MO} \cdot s^2/2) \cdot \sin(s r_{MO})/(s r_{MO}) \qquad (46)$$

Model fitting in s-*space.* For a full model description of the experimental structure-dependent intensity function, contributions should also be included from interactions between non-bonded atoms without well-defined separations, *i.e.* for any interatomic

* For example, for $Ca(ClO_4)_2$ aqueous solution, there are several structural units in a unit volume V, such as: a hydrated Ca^{2+} ion , two hydrated $(ClO_4)^-$ ions, and hydrogen bonded water molecules.

distance within the solution. Sometimes, such long non-bonded interactions are modeled as an even electron distribution surrounding the molecular species.[8,46] In the pair interaction model function this could be thought of as a large number of pair interactions with high values of the DW parameters (corresponding to large variations about the mean distances). Therefore, the corresponding intensity contributions are rapidly damped in *s*-space, and contribute significantly only for low *s*-values. At high *s*-values, and after weighting the $i(s)$ function with s, these contributions can be neglected, normally for $s > 3 - 4$ Å^{-1} (Figure 36c). In such a case, the high *s*-section of the $s \cdot i(s)$ function can be analyzed by fitting the experimentally derived $s \cdot i(s)$ curve to a calculated model function, $s \cdot i_{calc}(s)$, in which only well-defined mean interactions (with low Debye-Waller factors) in the structural units are included.[24] Non-linear least-squares fitting of the $s \cdot i(s)$ functions is then normally performed by varying the parameters of the main well-defined atomic pair interactions of the $s \cdot i_{calc}(s)$ contributions, in order to improve the fit to the experimental $s \cdot i(s)$ function.

Before this fitting procedure, the $i(s)$ function can be corrected for alignment errors giving rise to low frequency oscillations. Spurious peaks at low *r*-values (below about 1 Å) in the $D(r)$ function are then removed by means of a Fourier back-transformation procedure.[7] Often the number of free running parameters must be restricted in the refinements, in particular because of correlation between the frequency factor $\boldsymbol{n}$ and the Debye-Waller parameter l.

For the calcium halide solutions studied in Paper I, the structural parameters for the Ca-O_I bonds, and the $X^- \cdots O_w$ and $O_w \cdots O_w$ hydrogen bonded interactions, were included in the model and least squares refinements were performed by means of the STEPLR program.[47]

Model fitting in r-*space.* The individual intensity contributions for the different types of pair interactions (eqns 44 or 45) can be Fourier-transformed separately (eqn 47), with the same transform conditions (same modification function and *s*-range as for the $D(r)$ curve; eqn. 41). This gives modified pair functions, $\boldsymbol{P}'_{pq}(r)/r_{pq}$, including only the well-defined interactions described by the models for the structural units.

$$\boldsymbol{P}'_{pq}(r)/r_{pq} = \int_{s\,min}^{s\,max} si_{calc}(s)\, M(s)\, \sin(sr)\mathrm{d}s \qquad (47)$$

From eqn. (44), the $s \cdot i_{calc}(s)$ can be replaced:

$$\boldsymbol{P}'_{pq}(r)/r_{pq} = \int_{s\,min}^{s\,max} [f_p(s)f_q(s)\exp(-l_{pq}^2 s^2/2)\frac{\sin(sr_{pq})}{r_{pq}}]\,M(s)\sin(sr)ds \qquad (48)$$

Figures 36a and 36b show the *r*-space fitting for a $CaCl_2$(aq) solution with the modified pair functions for the hydrated Ca^{2+} and Cl^- ions at the top. The peak shapes obtained for these interatomic interactions are symmetrically broadened due to the exponential Debye-Waller factor, $\exp(-l_{pq}^2 s^2/2)$, and also due to the exponential convergence factor, $\exp(-bs^2)$, in the modification function, *M(s)* (*cf.* eqn. 40), which has the same form as the DW factor.

The peak shapes for these modified pair functions are then subtracted from the experimentally obtained $D(r) - 4\pi r^2 \rho_0$ curves. If the model describes all well-defined interactions within the structural units of the solution, the peaks in the $D(r) - 4\pi r^2 \rho_0$ curve should be explained by the model function. In a difference only a smooth curve should remain with broad features corresponding to intermolecular interactions which are not included in the model. It should, however, be emphasized that it is not possible to obtain a unique three-dimensional structural model based only on the evaluation of LAXS data, and that additional information always is necessary to reduce ambiguities in the interpretation.

Figure 36b compares the model function [(dashed line) as the sum of the modified pair functions in 36a] with the distribution function, $D(r) - 4\pi r^2 \rho_0$ (solid line). The dash-dotted line shows the difference.

Also the less well-defined or long distance intermolecular interactions, which are visible as broad peaks at high *r*-values in the $D(r) - 4\pi r^2 \rho_0$ curves, are often of interest, *e.g.* the second sphere interactions around the calcium ion. Such interactions give too small contributions at high *s*-values to the experimental *i(s)* function, to allow refinements of their structural parameters by fitting with a calculated model $s \cdot i_{calc}(s)$ curve in *s*-space. Therefore, modelling of the second sphere interactions for the calcium solution was made in *r*-space by fitting Fourier-transformed peak shapes to the $D(r) - 4\pi r^2 \rho_0$ function, and by adjusting the structural parameters of the corresponding intensity contributions (eqn. 44) within reasonable limits.

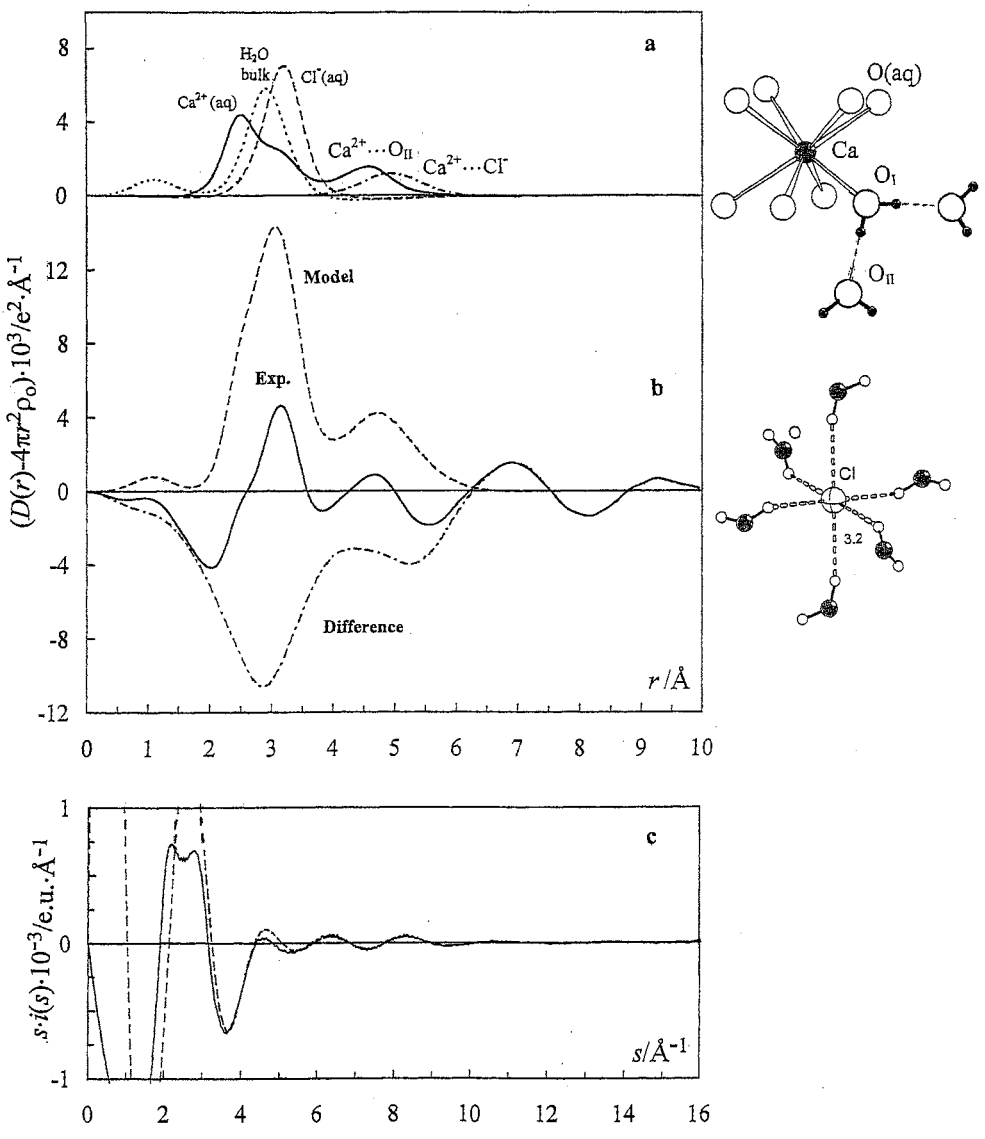

Figure 36. LAXS radial distributions (RDF) for a 2 M $CaCl_2$ solution. a) Separate model peak shapes: the $[Ca(OH_2)_8]^{2+}$ ion with the first (Ca-O_I) and second (Ca-O_{II}) hydration sphere including the O_I-O_I interactions (solid line), the hydrated chloride ion (dashed line), and O···O interactions in bulk water (dotted line). The dash-dotted line shows the contributions from two chloride ions in the second coordination sphere of calcium (~5 Å). b) Experimental RDF: $D(r)-4\pi r^2 \rho_0$ (solid line); sum of model peak shapes in **a** (dashed line); difference: Exp.– Model (dash-dotted line). c) LAXS s-weighted structure-dependent intensity functions $s \cdot i(s)$ (solid line); model $s \cdot i_{calc}(s)$ (dashed line).

2.5 Experimental procedures and preliminary data treatment. The data collection was performed by means of a θ-θ diffractometer, where 2θ is the scattering angle (Figure 37).[6b] A line focus of an Mo-Kα x-ray tube was used to illuminate the free surface of the solution with radiation of wavelength λ = 0.7107 Å. A Soller slit reduced sideways divergence of the beam, and a slit assembly defined the opening angle of the primary and scattered beam. The scattered x-ray intensity was measured in the symmetrical parafocusing θ-θ geometry of Bragg-Brentano type, which is normal for a powder diffractometer.[6b] A ground and bent single-crystal LiF monochromator focussed the diffracted beam on a scintillation detector. The intensity data were collected at 450 discrete θ-values for $1 < \theta < 65^{o}$. When expressing the intensity data as a function of the scattering variable $s = 4\pi(\sin\theta)/\lambda$, this corresponds to an s-range of 0.3 - 16.0 $Å^{-1}$.

In order to obtain the coherently scattered total intensity function, $I(s)$, appropriate corrections for instrumental and sample-dependent effects are applied on the experimental intensity, $I_{exp}(s)$. Corrections are made for the zero count rate of the detector, polarization in the sample and monochromator, and the amount of Compton scattering passing the monochromator.[6b,24,46] If the solution has low absorption, corrections for angle-dependent absorption effects and multiple scattering,[41] should be applied on the $I_{exp}(s)$ intensities.[8,46] Because the structure-dependent intensity $i(s)$ approaches zero for high s values, scaling of the $I_{exp}(s)$ function to the calculated structure-independent intensity $\sum_{p} f_p^2(s)$ for a chosen stoichiometric unit of volume V, (normally containing one metal atom) can be used for normalization of $I_{exp}(s)$ to electron units (= $I(s)/V$). When the anomalous dispersion corrections are included, the structure-dependent intensity is obtained from $i(s) = I(s) - \Sigma_p (f_p^2 + \Delta f''_p{}^2)$. All corrections and handling of the experimental data are made with the KURVLR program.[8]

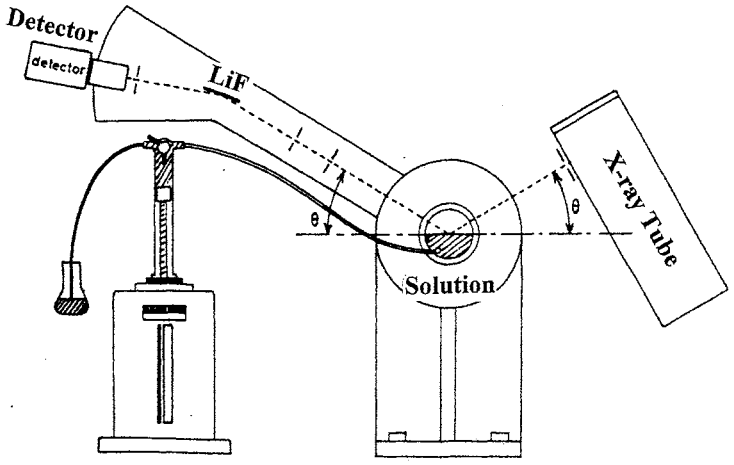

Figure 37. X-ray scattering (LAXS) measured in the parafocusing Bragg-Brentano geometry of a θ-θ diffractometer from the surface of a solution. A focusing single crystal LiF monochromator is placed before the detector (refs. 7, 46).

3. Vibrational Spectroscopy

3.1 Molecular vibrations. The origin of a molecular vibration is the chemical bond formed between the atoms, which gives rise to a returning force when an atom is displaced from the equilibrium position. Because the frequency of a vibration depends on the forces between the atoms and on the atomic masses, careful analyses of the vibrational spectra can give important information on the coordination and molecular structure.

For simple harmonic motion with symmetric displacements the returning force is proportional to the displacement of the atom. The corresponding force constant is a measure of the curvature at the bottom of the potential energy function (Figure 38), and need not in general to be directly correlated to the bond strength.[11a] However, for related compounds shifts in the vibrational frequencies provide sensitive probes for small changes in the bond strength and molecular symmetry, and vibrational spectra can be used qualitatively to identify molecular species in solution. For a solid the vibrational spectrum often becomes more complex due to deviations from the ideal symmetry, coupling of the modes, and collective motions within the crystal lattice (see below).[11a]

It is often found that similar groups of atoms in different compounds have similar *group frequencies*, which means that the vibrations of a particular group of atoms can be assumed to be relatively independent of those of the rest of the molecule. This is so for the cyano complexes in the present studies, for which the CN stretching frequency is a sensitive indicator of the type of bonding to a metal atom.[11b] However, generally all atoms are taking part in the normal vibrations of the molecule, and for a careful analysis of the bonding in a group of atoms, the influence of the motion of its neighbors should also be accounted for.

A free molecule with N atoms has $3N$ degrees of freedom associated with the motions of its atoms (movements in x, y, z directions). Collective motions (*i.e.* movement of the entire molecule) are translations and rotations in three directions each, (two rotations if linear). The motions remaining for the atoms within a molecule are vibrations, in which the atoms move periodically toward and away from one another. The number of so called *normal vibrational modes* of a molecule composed of N atoms is then $3N$-6 (or $3N$-5 if linear). All these forms of motion are ways for the molecule to store energy in quantified form. The energies of the vibrational transitions depend on the arrangement of the atoms in space and by the forces between the atoms and their masses. An excited normal vibration (in the harmonic approximation) still has the *same frequency of the atomic motions but increased amplitude.*

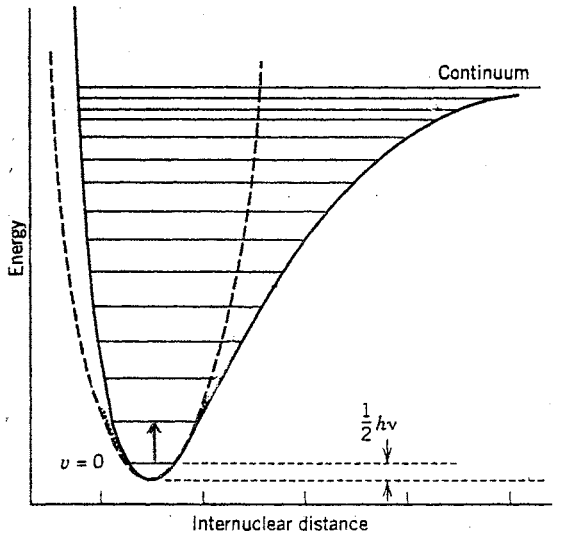

Figure 38. Potential energy curve (solid line) for a stretching vibration of the bond between two atoms. The dashed parabolic curve represents the harmonic approximation.

3.2 Normal Coordinate Analysis. The frequency of the normal vibration is determined by the kinetic and potential energies of the atoms in the molecule. The kinetic energy is given by the masses of the atoms and their geometrical arrangement. The potential energy is connected to the interactions between the atoms and is described in terms of force constants. When light with exactly the same frequency as the vibrational oscillation is absorbed and excites a vibrational mode, only the amplitude of its oscillation increases.

Thus, the $3N$-6 normal vibrational frequencies and their corresponding eigenvectors describing the motion, can be calculated by solving Newton´s equations of motion if the masses of all atoms, the geometry of the molecule and the force constants (together called the force field) are all known. One problem in normal coordinate analysis is that the force field is not known in advance and that the number of force constants always exceeds the number of normal vibrations. Initial values of the force constants are normally adapted from group frequencies or small molecules with similar bonding features, and adjusted to minimize the discrepancy between calculated and experimental frequencies. The large number of possible parameter combinations prevents a unique solution, and additional

information of the system is often necessary for a reliable assignment of the experimental frequencies. If the agreement is satisfactory this particular set of force constants is adopted as a representation of the potential energy of the system, which then contain valuable information about the nature of the interatomic forces in the system.[11a] The principles of the Wilson´s **GF** matrix method, which is used for the calculation of the vibrational frequencies, can be found elsewhere.[9,11a]

Normal coordinate analyses, taking all experimentally observed vibrations into account, have been performed for the cyano complexes in Papers III and IV. The force constants have been evaluated, and used for discussions of the chemical bonding in the molecular species.

3.3 Measurement methods: IR & Raman spectroscopy.

3.3.1 Principles of the effects. By combining results from infrared (IR) and Raman spectroscopic methods, complementary information about the vibrational modes of a compound can be obtained. In infrared absorption spectroscopy, photons with energies corresponding to the excitation of certain molecular vibrations are absorbed in the sample, and the reduced transmittance of the infrared light at those frequencies is measured.[9] Such resonance absorption of IR radiation requires that the vibrational movement of the atoms creates an oscillating electric dipole moment (by changing its direction or amplitude), which can couple to the electric field of electromagnetic radiation, if it is oscillating with the same frequency.

In Raman spectroscopy, most of the incident light (usually visible or near infrared monochromatic laser light) is scattered without frequency change, which is called *Rayleigh* scattering. However, a small fraction ($\sim 10^{-6}$) of the scattered light *changes its frequency* to a higher or a lower value. This is the *Raman* scattering, and the extent of the frequency change corresponds to the energy difference between two vibrational states of the molecule.

Raman scattering originates due to different mechanism than the direct absorption in IR. In a Raman spectroscopic experiment intense high frequency laser light is required. The oscillating electric field of the incident radiation interacts with the deformable electron cloud of the molecule, and induces an oscillating electric dipole moment of the same frequency ν_0. The oscillating dipole moment is proportional to the polarizability of the molecule and gives rise to Rayleigh scattering in all directions without frequency change.

On top of this, a molecular vibration can change the polarizability of the molecule and induce an additional oscillating dipole moment with the same frequency as the vibration, ν_{vib}. Excitation of this molecular vibration can then occur when it absorbs (or releases) energy with the same frequency as the vibration from (or to) the incident light, which then gets the frequency components $\nu_0 \pm \nu_{vib}$ as well as ν_0.[10]

Thus, the Raman scattering has a frequency lower (Stokes' lines) or higher (anti-Stokes' lines) than the frequency of the incident light by an amount corresponding to a vibrational transition. At normal conditions, the Stokes' lines are the more intense and used for Raman spectroscopy (Figure 39).

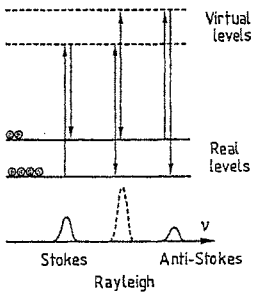

Figure 39. Raman scattering.

3.3.2 Selection rules for spectral activity. Simple symmetry arguments applied on the molecule by means of Group theory can be used to show which of the vibrational modes will be active in IR absorption and/or Raman scattering, or neither. This is done by firstly determining the point group of the molecule. Then the normal vibrations of the molecule are assigned to their respective irreducible representation (or symmetry species) in the corresponding character table. The character table then shows if the symmetry of normal vibration will induce a change in the dipole moment (IR-activity) or a change in the polarizability (Raman activity). This means that the excitation of such a normal vibration can be observed in an IR or Raman spectrum, if the probability for the vibrational transition (its intensity in the spectrum) is high enough.

IR-activity. For a vibration to be infrared active, there must be a change in the x, y or z component of the *dipole moment* vector associated with the vibration (*any molecular vibration that results in a change of the dipole moment is infrared active*). The selection rule can be formulated: *A vibration will be infrared active if its normal mode belongs to the*

same symmetry species as the x, y and z vectors in the character table of the point group of the molecular species.

Raman activity. For a vibration to be Raman active, the *polarizability* must change during the vibration. The dipole induced by the electric field is proportional to the polarizability, which is described by *the polarizability tensor* with quadratic terms. The selection rule can be formulated: *A vibration will be Raman active if its normal mode belongs to the same symmetry species as the quadratic functions of x, y, and z, in the character table of the molecular species* (look for x^2, y^2, z^2, xy, xz, yz, or combinations such as x^2-y^2, in the character table).

Rule of Mutual Exclusion. For centrosymmetric molecules these symmetry rules lead to a very useful Rule of Mutual Exclusion: *If a molecule has a center of symmetry, IR and Raman active vibrational modes are mutually exclusive; if a vibration is IR active, it cannot be Raman active, and vice versa. None of the IR and Raman bands can coincide.*

In general, the activity or intensity of vibrational transitions measured by these two modes of spectroscopy is complementary.

3.4 Molecular crystals. In a crystal, molecules or ionic molecular species can pack together in a regular manner with much weaker intermolecular interactions than the intramolecular bonds. A molecular species will occupy a site in the crystal lattice, which often has lower site symmetry than the point group symmetry for the free molecule, because of the packing effects in the solid compound. This may shift the vibrational transition energies, but a more easily visible effect is the splitting of degenerate molecular vibrational bands, because of the symmetry reduction; a *static* effect.

Another effect of the packing in a crystal is that the vibrations of a number of neighboring identical oscillators may couple with each other, which can further split the vibrational bands, a *dynamic* effect.[11a,48]

An illustration is given in Figure 40, which shows the Raman spectra in the C-N stretching region of the $[Fe(CN)_6]^{4-}$ ion in its potassium and sodium salts, $K_4[Fe(CN)_6]$ and $Na_4[Fe(CN)_6]$. Note that some of the bands are shifted above 2080 cm^{-1}, which is the wavenumber of the ν(C-N) band for the free cyanide ion in solution. In most cases the internal ligand frequencies decrease when a ligand coordinates. For cyanides, however, the σ-donation from the carbon atom to the metal ion removes electrons from a weakly antibonding (5σ) orbital, and therefore tends to raise the C-N frequency.[11b]

The different splittings of the frequencies in the two spectra in Figure 40 show that vibrational interactions occur between the $[Fe(CN)_6]^{4-}$ complexes in the crystal. However, care must be taken in such comparisons since such dynamic splittings can easily be confused with splittings induced by static effects due to reduced molecular symmetry. The general way in which solid-state splittings may originate from dynamic effects is illustrated in Figure 41, in which it is shown how four single vibrators in a unit cell can interact to give four coupled vibrations. If the coupling is strong enough, the four vibrations may appear as separate bands in a vibrational spectrum.[48]

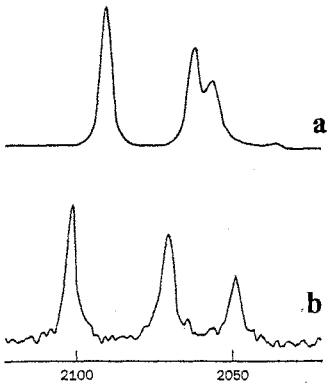

Figure 40. The Raman spectra of C-N stretching vibrations for crystalline samples of:
a) $K_4[Fe(CN)_6]$ and b) $Na_4[Fe(CN)_6]$, showing coupling of the C-N vibrations. The highest frequency bands in both spectra is the totally symmetric stretching mode (A_{1g}), and the lower two bands belong to the E_g mode, which is split due to the coupling with the interacting C-N oscillators in neighboring complexes.(ref. 48, reproduced with permission)

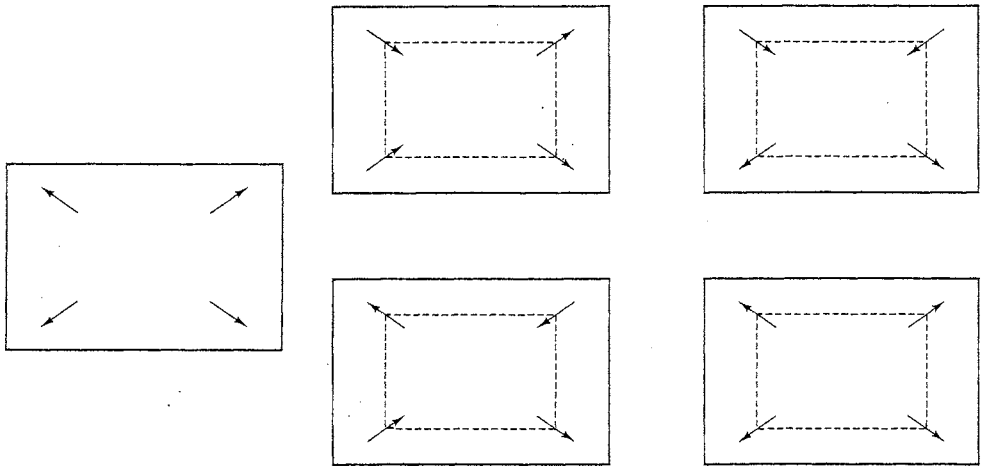

Figure 41. Unit cell of a crystal containing four molecules (left). The arrows represent stretching vibrations of each molecule, which can couple together to give four types of unit cell vibrations (right). The coupling between the individual vibrations is represented by the dashed-lines (ref. 48).

3.5 Vibrational spectra for the solid $TlPt(CN)_5$ compound. Such splittings of vibrational frequencies are evident in the spectrum of the solid $TlPt(CN)_5$ compound (Figure 42), treated in Paper III. In this compound the crystal structure and EXAFS results indicate that there is only one type of Pt-Tl bond (Figure 43), and thus only one Pt-Tl stretching vibration should be expected in the Raman and in the IR spectra. Nevertheless, in the Raman spectrum of this compound there are two double peaks which can be assigned to Pt-Tl stretching vibrations, *i.e.* four intense bands at 151, 164 and 195, 211 cm^{-1}, and two IR absorption bands at 150 and 194 cm^{-1} (*cf.* Figure 42b). All these bands are typical for a strong metal-metal bond, because of their low wavenumbers corresponding to the heavy atoms involved, and their high intensity.[11c] They are also close to the single, strong and polarized Raman bands at 163.7, 162.6 and 159.1 cm^{-1}, observed for the Pt-Tl bond in the three complexes $[(NC)_5Pt\text{-}Tl(CN)_n]^{n-}$ (n = 1, 2 and 3), in aqueous solution, respectively (Paper IV). The vibrational spectra of the solid $TlPt(CN)_5$ compound show a large number of bands (Table 7 and Figure 42) with good resolution, which allow a closer analysis of the type of splitting.

X-ray powder diffraction data were collected and interpreted to show that the compound crystallizes in the space group P4/*nmm* (No. 129), which corresponds to the crystallographic point group D_{4h}^7 in the Schönflies notation (the superscript 7 only gives the order of the D_{4h} groups listed in the *International Tables of Crystallography*).[44] There are two formula units (Z = 2) in the tetragonal unit cell with a = 7.647(3), c = 8.049(3) Å. The site symmetry of the Pt-atom is C_{4v} (4*mm* in the Hermann-Mauguin notation).[44]

For an isolated $TlPt(CN)_5$ molecule with 12 atoms in the point group C_{4v}, an analysis by group theory shows that 30 molecular vibrations with symmetry species $7A_1 + A_2 + 4B_1 + 2B_2 + 8E$ (where the E species correspond to doubly degenerate modes) would be expected. If only the isolated $Pt(CN)_5$ group is considered in C_{4v} symmetry, the symmetry species of the Pt-C and C-N stretching vibrations are $2A_1 + B_1 + E$, which all are Raman active, but only A_1 and E are IR active. Based on this assumption of the symmetry, we can expect 4 Raman bands and 3 coincident IR bands in the C-N stretching region, which is about 2150 to 2240 cm^{-1}, and a similar number of bands in the Pt-C stretching region from about 410 to 500 cm^{-1}.[11b]

In a solid compound the site symmetry is frequently lower than the point group symmetry for an isolated group, and then the degenerate modes may split their frequencies.

However, the crystal structure indicates that the site symmetry is the same as the point group symmetry for the isolated groups of the $TlPt(CN)_5$ compound.

Another type of splitting occurs if there is strong enough interaction between the molecules in the unit cell. Then all vibrations may split, which in a case with Z = 2, in principle would mean a doubling of the number of vibrations.[11a,49]

In the present case, the short distances in the linear -N2-C2-Pt-Tl-N2-C2-Pt- chain result in strong interaction between the atoms. Also, there are bridging cyano groups connecting different chains (Figure 43). Thus, a factor group analysis should be made to determine the expected number and activity of the vibrational modes.[50]

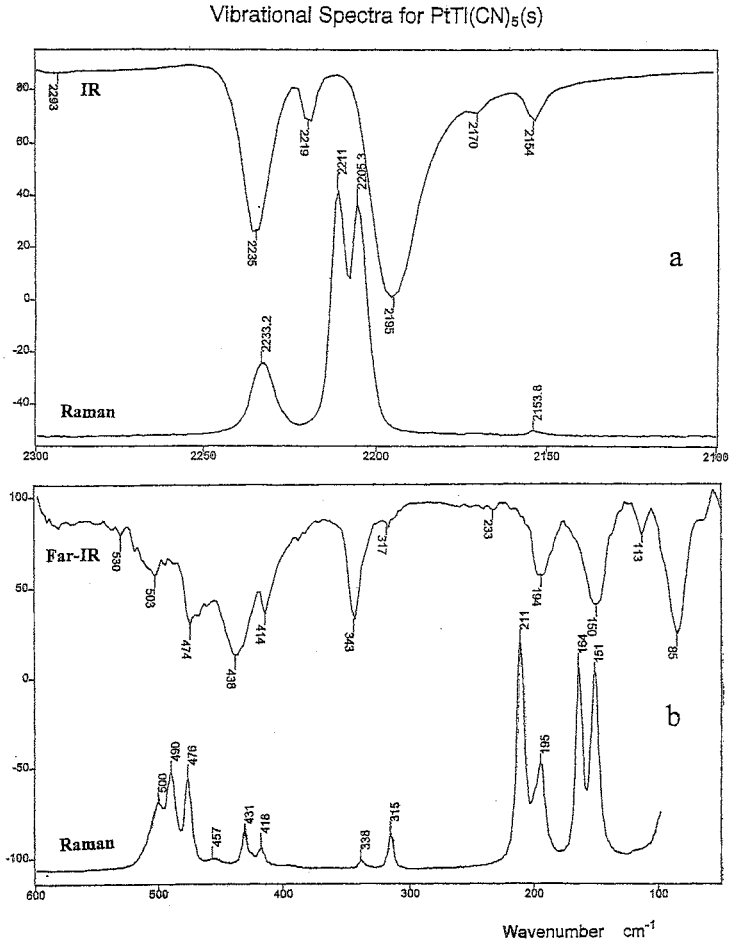

Figure 42. Raman and IR absorption spectra of the solid $TlPt(CN)_5$. a) Cyanide stretching region. b) Low-frequency region. The metal-metal stretching bands are between 150- 211 cm^{-1}. The point group symmetry of the space group requires that the dynamic splitting of the vibrational modes is correlated to the factor group symmetry D_{4h} (refs. 49, 50).

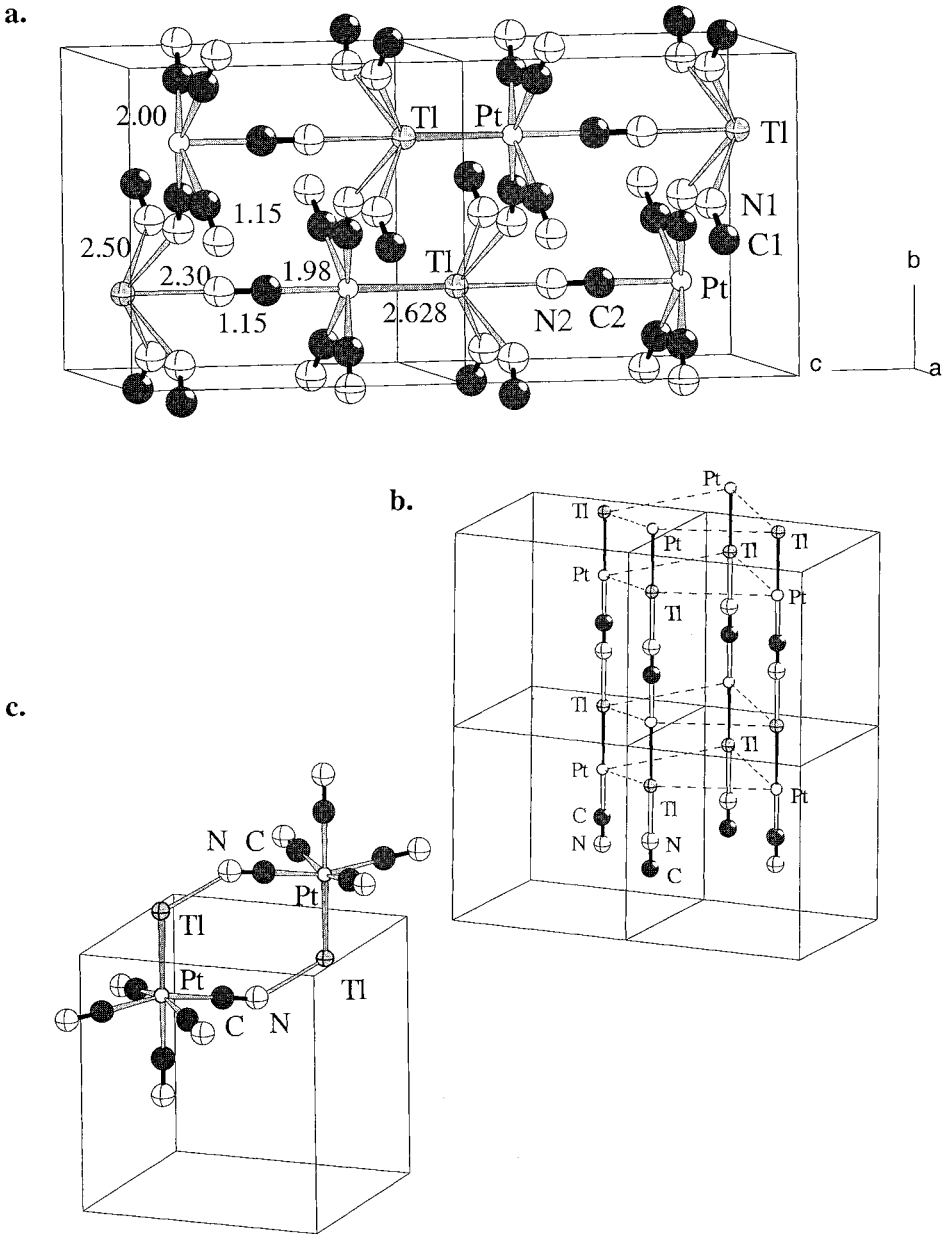

Figure 43. a) Two unit cells of the $TlPt(CN)_5$ solid compound. The proposed structural model is based on combined results from powder diffraction and EXAFS data (distances in Å). The linear -N2-C2-Pt-Tl-N2-C2-Pt- chains along the *c*-axis are connected by bridging cyano (C1-N1) groups; b) The eight formula units (Z = 8) used to describe the interaction between the linear chains (bridging cyano ligands not shown). c) The two centrosymmetrically related $TlPt(CN)_5$ entities, each with site symmetry C_{4v}.

Table 7. Assignment of the solid state infrared absorption and Raman spectra of the $TlPt(CN)_5$ compound, with crystallographic point group symmetry D_{4h}^7, after factor group analysis (see text).

The intensity of a band is indicated by the abbreviations: s strong, m medium, w weak, v very.

Infrared (cm^{-1})	*Raman (cm^{-1})*	*Symmetry species for D_{4h}^7*	*Description*
2235 s		A_{2u}	CN stretchings (axial)
	2233 s	A_{1g}	
2219 w		A_{2u}	CN stretchings (equatorial)
	2210vs	A_{1g}	
	2205 vs	E_g	
2195 vs		E_u	
2170 w (*2167*)[a]		(E_u)	$C^{15}N$ stretching (equatorial)
2154 w (*2153*)[a]		(E_u)	^{13}CN stretching (equatorial)
	2153 w	B_{1g}	
503 vw		A_{2u}	PtC stretchings (axial)
	500 w	A_{1g}	
	490 m	E_g	PtCN linear bending (axial)
	476 m		
474 w		E_u	
	457	E_g	PtC stretchings (equatorial)
438 vw		E_u	
	431 w	B_{1g}	
	418 w	A_{1g}	
411 vw		A_{2u}	
	398 vw	E_g, B_{1g}	PtCN linear bending (equatorial)
343 vw		A_{2u}, E_u	
	338 w	A_{1g}, B_{2g}	
317 vw		E_u	
	315 w	E_g	
	211 s	A_{1g}	Pt-Tl stretchings
	195 m	B_{1g}	
194 w		A_{2u}	
	164 s, 151 s	E_g[b]	
150 m		E_u	

[a] Calculated frequencies for the isotopic species (*within brackets*)

[b] Splitted possibly by lowered site symmetry (see text).

The number of interacting molecular units to be used in the factor group analysis is the number of formula units in the Bravais cell, which is the same as the crystallographic unit cell for a primitive type of lattice (P).[49,50] In our case the number of formula units in the Bravais cell is then $Z' = 2$, the same as in the crystallographic cell. The correlation method can be used for the factor group analysis, as described in Ref. 49 by Ferraro and Ziomek. For two formula units of $TlPt(CN)_5$ in the cell, each with 12 atoms and the site symmetry C_{4v}, 60 internal or vibrational modes, $(3N-6)\cdot Z' = 60$, and 12 external or lattice modes (lattice translations and lattice rotations) are expected. The correlation between site symmetry and factor group symmetry (Scheme 3) shows that the internal modes belong to the following symmetry species in the factor group D_{4h}:

$$\Gamma(\text{internal}) = 7A_{1g} + A_{2g} + 4B_{1g} + 2B_{2g} + 8E_g + A_{1u} + 7A_{2u} + 2B_{1u} + 4B_{2u} + 8E_u.$$

$$\Gamma(\text{external}) = A_{1g} + A_{2g} + 2E_g + A_{1u} + A_{2u} + 2E_u.$$

The normal modes belonging to the A_{1g}, B_{1g}, B_{2g} and E_g symmetry species are Raman active, while only the A_{2u} and E_u species are IR active, and there are (in principle) no coincidences.

Scheme 3. Factor group analysis for $TlPt(CN)_5$. For details see ref. 49.

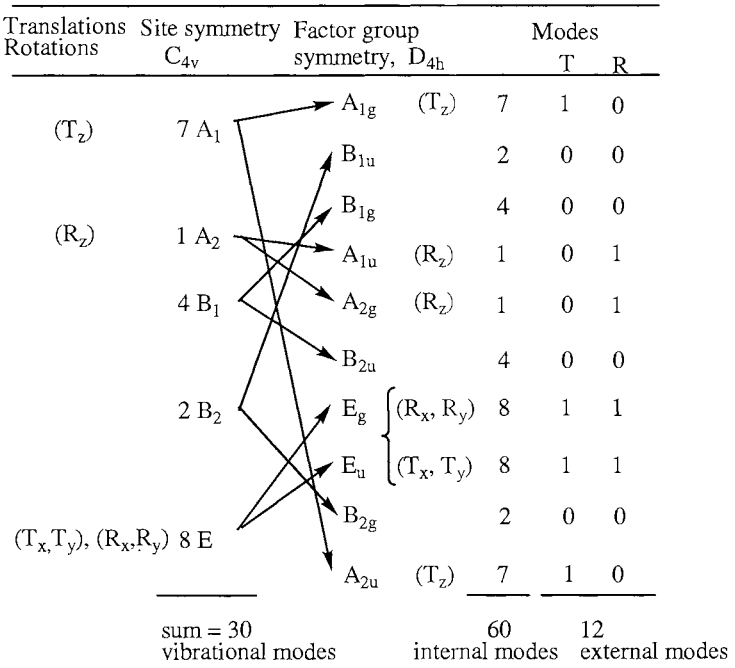

When applying the correlation method to find out how the stretching vibrations for the $Pt(CN)_5$ group will split, the following representations are obtained when correlating C_{4v} site symmetry with D_{4h} factor group symmetry:

$$\Gamma_{stretch}(C\text{-}N) = 2A_{1g} + B_{1g} + E_g + 2A_{2u} + B_{2u} + E_u$$

$$\Gamma_{stretch}(Pt\text{-}C) = 2A_{1g} + B_{1g} + E_g + 2A_{2u} + B_{2u} + E_u$$

The 4 Raman and 3 IR bands expected, are no longer coincident, as they would be for an isolated molecule (p.104; *cf.* Figure 42), because of the centrosymmetric arrangement of the two $TlPt(CN)_5$ entities (Figure 43c), but the displacement from the coincident positions of the modes $2A_1 + B_1 + E$ for an isolated $TlPt(CN)_5$ molecular entity should not be very large. Thus, from the correlation in Scheme 3, the splitting of the A_1 mode gives a Raman active (A_{1g}) and an IR active (A_{2u}) pair of vibrational modes. The B_1 mode splits into B_{1g} and B_{2u}, but B_{2u} is inactive so only one Raman active band (B_{1g}) is expected, and the E species gives an E_g (Raman) and E_u (IR) active pair (*cf.* Table 7).

The strongest bands in the cyanide stretching region of the spectra were then assigned to these 4 Raman ($2A_{1g} + B_{1g} + E_g$) and 3 infrared ($2A_{2u} + E_u$) modes, based on the following additional considerations:

The highest vibrational frequencies in the cyanide stretching region should belong to the bridging cyano ligands, since in an M-CN-M′ type of bridge, the ν(C-N) frequency shifts to higher wavenumbers with 40 cm^{-1} or more (see below).[11b,51a] The Raman vibrational spectrum (Figure 42a, Table 7) shows the highest frequency band in the C-N-stretching region at 2233 cm^{-1}. This can then be assigned to the symmetric stretching mode, A_{1g}, of the axial bridging cyano group of the linear ···Pt-Tl-N2≡C2-Pt··· chain (Figure 43). The IR band at slightly higher frequency, 2235 cm^{-1}, must then belong to the A_{2u} stretching mode of the axial cyano group. In a similar way, the next highest pair of frequencies, 2210 and 2219 cm^{-1} for the bands in the Raman and IR spectra, respectively, were assigned to the symmetry species A_{1g} and A_{2u} of the stretching frequencies of the (less strongly bridging) equatorial cyano groups. The stretching frequencies E_g (Raman) and E_u (IR) are found at 2205 and 2195 cm^{-1}, respectively, and the single Raman band of B_{1g} symmetry was ascribed to the weak band at 2153 cm^{-1}. The weak IR bands at 2170 and 2154 cm^{-1} correspond to the calculated E_u frequencies (using the same force constants as for the main isotopic species $^{12}C^{14}N$) for the minor isotopic species $^{12}C^{15}N$ and $^{13}C^{14}N$, with natural abundance 0.4 and 1.1 %, respectively. Because of the higher mass, this asymmetric stretching frequency (E_u) shifts toward lower wavenumber with about 40 cm^{-1}.

From measurements of other platinum-cyano complexes, the Pt-C stretching bands can be expected in the region from about 410 to 500 cm^{-1}.[52,53] It has been observed for bridging cyano groups, of the type M-CN-M′, that the metal-carbon stretching frequency generally shifts toward lower wavenumbers.[11b] The reason is, in the currently accepted view of the bonding, that formation of a σ-bond via the lone-pair on the nitrogen atom (N:→ M′) increases the polarization toward the more electronegative nitrogen atom in the cyano ligand and increases the π-bond strength (*cf.* Section *5.1*). This weakens simultaneously the Pt-C bond (the Pt-C frequency shifts to lower wavenumber) because it decreases the availability of the lone-pair on the carbon atom, which is used for the formation of a σ-bond to the platinum atom. However, if we assume that the 431 cm^{-1} (Raman) and 438 cm^{-1} (IR) bands are the downshifted PtC axial stretching modes, then the calculated stretching force constant for the axial Pt-C bonds would get an improbably low value (*cf.* Paper III), which would correspond to a much longer bond length. Therefore, a more realistic assignment is the one given in Table 7. Raman and IR bands in the region between 411 and 457 cm^{-1} can then be ascribed to the Pt-C stretching modes of the equatorial cyano ligands.

The bending modes of the linear Pt-C-N groups fall into the symmetry species $A_1 + A_2 + B_1 + B_2 + 3E$ for an isolated $Pt(CN)_5$ unit in the C_{4v} point group.[53] The A_1 and E modes are active, and A_2 is inactive, in both Raman and IR spectra, while the B_1 mode is only Raman active. Following the previous careful work by Jones et al. these linear Pt-C-N bendings are generally likely to occur at frequencies lower than the Pt-C stretchings.[53] However, for a bridging cyano group with a stronger C-N bond, it is likely that the frequencies shift toward higher wavenumbers. We therefore assigned the bands in the region from 490 down to 474 cm^{-1} to these bending modes of the axial linear Pt-CN group, and the 398 to 315 cm^{-1} bands to the bendings of the linear equatorial Pt-C-N groups. Because of the weak coupling between the interacting molecules for these types of modes, the splitting is small and the bands are not always resolved. In some cases, more than one vibrational mode has to be assigned to the same observed band (*cf.* Table 7).

These proposed assignments are aided by the results from the normal coordinate analysis in an trial and error procedure. It is in the nature of normal coordinate analyses, for which different solutions to the problem of assigning the bands always exist, that the most probable assignment should be selected by means of all criteria available.

However, there are some remaining problems with the description of the coupling of the vibrations. For the Pt-Tl bond only one Raman active, A_{1g}, and one IR active, A_{2u}, band would be expected for this factor group symmetry, D_{4h}. Instead, four Raman and two IR features were observed in the region 150-220 cm^{-1} (*cf.* Figure 42b). There can be two reasons for this: (1) lower site symmetry (lower than C_{4v}) for the Pt atom (a static effect), and/or (2) dynamical coupling between Pt-Tl groups in neighboring chains.

In both cases, in order to explain the experimental vibrational stretching features, an enlarged Bravais unit cell must be used.[49,50] This should mean, however, that the crystallographic unit cell has been chosen too small (and with too high symmetry), since its size is smaller than that necessary for interpreting the vibrational spectra. For this purpose, it was necessary to choose a structural entity containing at least eight formula units ($Z' = 8$) in four parallel neighboring chains (with the atoms oriented in opposite directions) connected by the bridging equatorial cyano groups (*cf.* Figure 43b). The eight interacting Pt-Tl stretching vibrations within this assumed entity, can then be assigned to the Raman active, $A_{1g} + B_{1g} + E_g$, and IR active, $A_{2u} + E_u$, species (see Paper III), using D_{4h} symmetry. The low frequency doublet (164 and 151 cm^{-1}) with almost equal intensity bands, can then originate from the doubly degenerate Eg mode split by a correlation splitting due to disturbed site symmetry.

The description of the crystal structure shows an apparent disorder, which may be caused by too high symmetry giving averaged positions of the light atoms. For example, the Pt-C distances appear too short from the powder diffraction determination of the crystal structure parameters (*cf.* Table S2, Paper III). Possibly, this effect can be caused by a slight twisting of neighboring $Pt(CN)_5$ groups relative to each other, because of the repulsion between the parallel cyano groups (*cf.* Figure 43 a and b). A positional disorder of the C-atom would give an apparently shorter Pt-C distance, as described in p. 68 (Scheme 2). Such a twist is common for the $Pt(CN)_4$ groups, which are stacked on top of each other in the partially oxidized platinum(II)tetracyano compounds (see Section *5.3*). If this proposed twisting occur in an ordered manner, it will give rise to a larger crystallographic unit cell than the one used. However, since such a disorder only affects some light atom positions, the effect is very difficult to detect in the x-ray powder diffraction data.

In this model, the main splitting of the Pt-Tl vibrational frequencies in the Raman spectrum of the $TlPt(CN)_5$ compound is considered to be caused by the *dynamic* movements of the atoms. This is because there is no indication of any large *static* distortion of the local coordination geometry, *i.e.*, with different Pt-Tl distances, neither in the powder diffraction determination of the crystal structure, nor in the EXAFS results for the local structure. The EXAFS data shows that the disorder (Debye-Waller) parameter σ^2 for the Pt-Tl distance is smaller in the solid $PtTl(CN)_5$ compound, 2.627(2) Å, than for the three solution complexes, $[(NC)_5Pt\text{-}Tl(CN)_n]^{n-}$, n = 1-3 (*cf.* Table 20). Also, it is evident for the solution complexes that the Pt-Tl stretching frequency shifts rather little for a change in the Pt-Tl distance. Therefore, it is unlikely that the large splitting observed here of the Pt-Tl stretching vibration frequency in the solid $(NC)_5Pt\text{-}Tl(s)$ compound could be caused by a static distribution of different Pt-Tl distances.

3.6 Experimental vibrational spectroscopy.[54a]

3.6.1 Infrared absorption measurements. Modern IR spectrometers are almost always equipped with interferometers and use the Fourier-transform (FT) technique, which has major optical advantages as compared to the dispersive instruments. However, with KBr beamsplitters or windows, the strong increase of the IR absorption of KBr in the far-IR region (below about 400 cm^{-1}) sets a lower wavelength limit at about 350-400 cm^{-1} for these instruments. Therefore, polyethylene windows and Mylar beamsplitters are often used for the far-IR region (Figure 44a).

For mid-IR measurements, traditionally 4000 - 400 cm^{-1}, finely ground solid samples are diluted with KBr in the form of a pressed disc (pellet). This method cannot be used for the compounds that are likely to undergo halide exchange. For far-IR measurements a polyethylene pellet can be used.

Liquid cells comprise two windows held apart by a spacer, which gives the path length through the cell (Figure 44b). The most common window materials are NaCl, KBr or CsI, which can be used down to 600, 350 or 200 cm^{-1}, respectively. All are water-soluble materials, and IR spectra of aqueous solutions must be measured with water-insoluble cell windows such as CaF_2 and BaF_2, for which the low limit of the usable range is cut already at 1100 and 870 cm^{-1}, respectively. When measuring samples in solution, it is often useful to subtract a background spectrum of the cell containing the pure solvent..

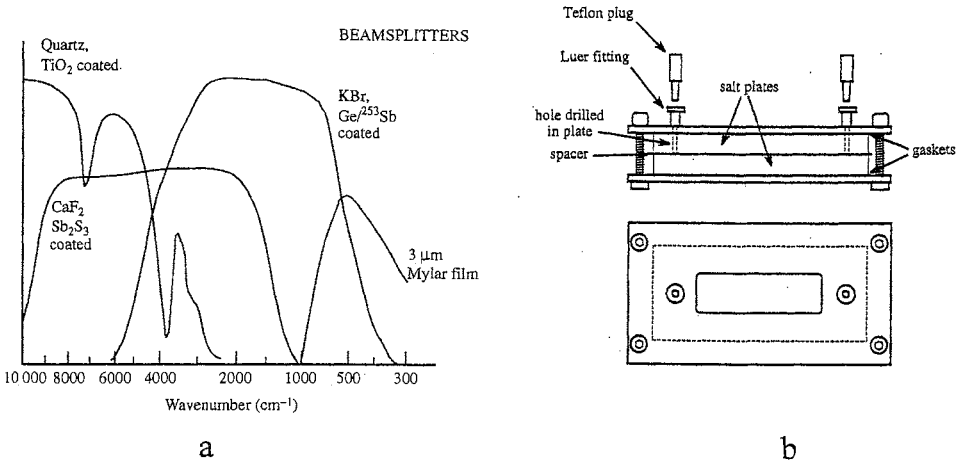

Figure 44. a) Transmission ranges for different material for beamsplitters and IR cell-windows, b) Liquid cell for IR spectroscopy (ref. 54a,b).

3.6.2 Raman spectroscopic measurements.[10] The experimental setup for a Raman experiment is very simple in principle. What is needed is a monochromatic light source to excite the molecular vibrations, a very sensitive detector to measure the weak Raman signals, and some means to prevent the strong Rayleigh scattering (without wavelength change) from reaching the detector. The light source for measuring Raman spectra is nowadays almost always a laser (Figure 45). Since water has very weak Raman scattering, Raman spectroscopy is very useful for the study of dissolved species in aqueous solutions, which is very resricted with IR spectroscopy due to the strong water absorption.

- *Monochannel dispersive instruments.* For optical reasons a visible laser line was mostly used previously. A usual setup was an effective monochromator with gratings to eliminate the Rayleigh scattering, and a mono-channel photomultiplicator detector for detection of the weak Raman lines. A selected wavenumber range was scanned for a fixed band width by tilting the gratings of the monochromator. Such an instrument, the DILOR Z24, which is a dispersive instrument with a triple monochromator and holographic gratings, was used for some preliminary measurements on the Pt-Tl bimetallic complexes and compounds. An argon ion laser giving a green 514.5 nm line with about 500 mW at the sample was used to get sufficient intensity. However, the solid $PtTl(CN)_5$ sample (Paper III) decomposed in the intense laser beam, and gave strong fluorescence with the green light. Also for the $[(NC)_5Pt\text{-}Tl(CN)_n]^{n-}$, n = 1 - 3, complexes in solution (Paper IV), partial decomposition took place and $[Pt(CN)_6]^{2-}$ complexes were formed. Thus, in order to obtain useful spectra of the present samples, which are light sensitive, more modern techniques had to be used. However, the optical instruments with visible light are still useful for special purposes, *e.g.* for solid samples in the low wavenumber region below 100 cm^{-1}, because the monochromator gives better discrimination of the Rayleigh line and no notch filter is used.

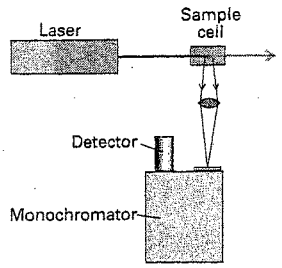

Figure 45. Principle of a monochannel Raman instrument

Raman microscope. A significant recent improvement of the technique came with the use of the very sensitive CCD (charged coupled device) multi-channel area detector. The quantum efficiency of modern CCD detectors can be over 50%, and thus requires rather weak exciting laser light, normally only a few mW. The photosensitive area is typically divided into small (30x30 μm) elements (pixels), composed of Si photodetectors. The width of the sensitive area allows a large part of the spectrum to be sampled at the same time. Diode lasers operating at 782 nm, which reduces fluorescence, are available at relatively low cost and can be used with the CCD detector. This has made Raman microscopy a useful method especially for solid samples, requiring a very small amount of the sample, which can be inspected visually (in the microscope) before and after the measurement. The laser light enters into the microscope and illuminates the sample through the objective. The back-scattered light goes via a beam-splitter to the detector. A notch filter blocking out the Rayleigh line (< ca. 100 cm^{-1}), is necessary to protect overloading of the sensitive detector at low wavenumbers. The Renishaw System 1000 spectrometer, equipped with a Leica DMLM microscope and a Peltier-cooled CCD detector, was used for measurements of most solid samples.

- *FT-Raman.* With the use of infrared lasers, mostly YAG lasers operating at 1024 nm, modern Fourier transform interferometers of the same type as for FT-IR instruments can be applied also for Raman spectrometers. The intense Rayleigh scattering has to be excluded from the interferometer by means of a notch filter, which prevents Raman spectra to be obtained below about 100 cm^{-1}. The Fourier transform technique has made Raman spectroscopy both easier to use and applicable to more samples, since fluorescence is less of a problem when infrared light is used for excitation. The entire spectral region is sampled in a very short time, and a large number of scans can be added to get good S/N ratio. A BioRAD FTS6000 instrument equipped with a Raman module was used for some of the aquoeus solutions and solid samples. However, aqueous solutions and glass cells absorb more with infrared light and the Raman intensities are weaker with the longer wavelength. Relatively high laser power (normally more than 50 mW) has to be used, which can damage sensitive samples.

Table 8. Comparison of experimental structural techniques used in the present work

Technique	Description of Effect	Structural information	Interaction time	Sample amount	Comments
X-ray crystallography	Diffraction by electrons, interference in 3-dimensional lattice	Electron density map giving precise positions of atoms in the unit cell of the crystal	~ 10^{-18} s with average over vibrational and static disorder	Single crystal ~ 10^{-2} mm^3	If there is static disorder in the structure, then systematic errors will occur in the distances
X-ray powder diffraction (XPD)	Diffraction at certain angles θ (given by Bragg's law) by the electrons within the planes of the crystals	Unit cell dimensions from the θ values; heavy atom positions from peak intensities	~ 10^{-18} s with average over all orientations of the crystal powder	Crystalline powder ~ 0.1 cm^3	The number and precision of the atomic positional parameters are limited, in particular for light atoms
X-ray scattering from amorphous samples (LAXS)	Scattering by electrons, interference between pairs of atoms	Radial distribution function (RDF) with interatomic distances between pairs of atoms	~ 10^{-18} s with average over vibrational and static disorder	Liquid or amorphous sample ~ 5 cm^3	One-dimensional modified RDF with peaks for *all* well-defined interatomic distances in molecular species or with heavy atoms in the sample
X-ray absorption fine-structure (XAFS) spectroscopy	Photoelectrons from central atom back-scattered by ligand atoms	Coordination distances, number and types of ligand atoms; central atom with Z > ~ 20	~ 10^{-17} s with average over vibrational and static disorder	Any state, solid samples ~ 0.1 cm^3, liquids ~ 1 cm^3	One-dimensional modified RDF with peaks only for short and well-defined distances to atoms around the central atom
Vibrational infrared (IR) absorption	Absorption of IR radiation giving vibrational transition due to dipole change during vibration	Symmetry information of molecular species, bonding information for small molecules	~ 10^{-13} s	Any state, solid samples ~ 0.01 cm^3, liquids ~0.1 cm^3	Characterization of solid samples; limited application for aqueous solutions
Vibrational Raman scattering	Scattering of intense monochromatic radiation; frequency change due to change of induced dipole during vibration	Symmetry information of molecular species, force constants giving bonding information for small molecules	~ 10^{-14} s	Any state, solid samples ~ 1 mm^3, liquids ~0.01 cm^3	Characterization of solid samples; favorable for aqueous solutions; different selection rules than for IR absorption
Nuclear magnetic resonance (NMR) spectroscopy	Transitions between nuclear spin energy levels in magnetic field	Number of magnetically equivalent nuclei in each environment	10^{-1} - 10^{-9} s	Preferably liquids, *ca* 2 cm^3	Characterization and structural information from the number and multiplicity of signals

Results and Discussion

4. Hydration of ions in aqueous solution

Water is the most important, and also, the most studied solvent. Still, there are a number of anomalous properties, which are difficult to explain on a molecular level. A unique property of the water molecule is its ability to accept and to donate two hydrogen bonds. In order to interpret the X-ray diffraction (LAXS) data on aqueous solutions, and for modelling the structure of the "bulk" water, it is useful to assume a small tetrahedrally hydrogen bonded ice-like aggregate as a dominant structural feature (*cf.* Figure 46a). Then one can imagine the structure of water as a network of flickering clusters held together by hydrogen bonds, which are continuously breaking and reforming. The hydrogen bonding in water, and how it is modified in the presence of ions, is of primary importance for an understanding of the properties of electrolyte solutions. Although intensively studied, because of its importance *e.g.* for the chemistry of biological systems, all aspects of the hydrogen-bonding network in solutions are not yet fully understood

In aqueous solution, all ions are hydrated to some extent. A large amount of experimental information is available on the structure and dynamics of hydrated ions, notably in the recent review by Ohtaki and Radnai,[42] and in the book by Richens.[55] Most of the information concerns the hydration of cations, but also the hydration of anions attracts increasing interest even though it is weak and structure studies are difficult. However, the neutron scattering properties of the different chlorine isotopes, ^{35}Cl and ^{37}Cl, has allowed the hydration of chloride ions in aqueous (D_2O) solution to be studied using isotopic substitution methods. The results show that $Cl^-\cdots$H-O-H hydrogen bonds are formed to about six water molecules around each free chloride ion.[39]

Cations are always bonded to the oxygen atom of a water molecule. The geometry of this arrangement M—O$\begin{smallmatrix}\nearrow H\\ \searrow H\end{smallmatrix}$ can be a planar trigonal, or with a tilted plane of the water molecule (Figure 46b). For a tetrahedral "lone-pair" coordination of the oxygen atom, the tilt angle $\theta \approx 56^\circ$ is expected. Neutron diffraction (isotopic substitution) experiments revealing hydrogen atom positions have been performed on concentrated aqueous (D_2O) solutions of calcium ions. The hydration number was reported to vary between 6 and 10.[40] From the Ca-O and Ca-D distances obtained, the coordinated water molecules were found to have a noticeable tilt angle, $\theta \approx 36^\circ$ (Figure 46b).

Highly charged metal ions form a tightly bonded first hydration shell of coordinated water molecules, which are polarised by the strong electrostatic field of the ion and form strong hydrogen bonds (stronger than in bulk water) with water molecules in a secondary hydration shell.

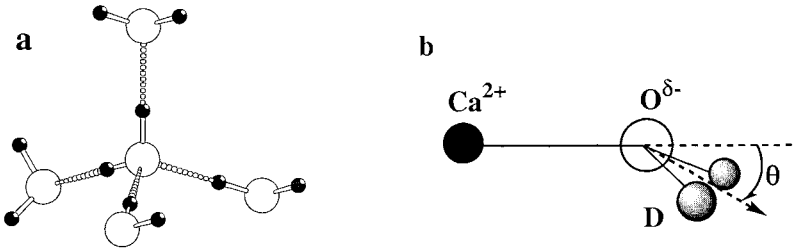

Figure 46. a) Fragment of ice-structure; b) Tilt angle of water coordinated to a calcium ion.

The structure, bonding and coordination geometry within these hydration spheres around the cations are important for an understanding of the water exchange rates and mechanisms, and also for complex formation with other ligands.

Another aspect is the increase in acidity for the coordinated water molecules, which is specially pronounced for highly charged ions such as U^{4+} and Th^{4+}, with a strong electrostatic field. The polarisation effect of these ions on the coordinated water molecules facilitates the loss and transfer of a proton from a water molecule in the first hydration shell to one in the second sphere. In order to suppress this so-called hydrolysis process and to ensure that no hydroxo complexes would form, very acidic solutions (1.5 M $HClO_4$) had to be used for the studies of the hydrated U^{4+} and Th^{4+} ions. In the case of the Ca^{2+} ion, its large size gives low acidity, and no additional acid is required to suppress the hydrolysis in an aqueous solution.

In general, for hydration studies using concentrated electrolyte solutions, the role and extent of the cation-anion interactions must be considered. In the present studies on aqueous solutions of Ca^{2+}, U^{4+} and Th^{4+} ions, it has been sufficient to assume the hydrated halide ion to be separated from the hydrated cations, or to be present in the second hydration sphere as an ion-pair sharing a solvent molecule with the metal ion. In the limit, the anion enters the first hydration sphere and forms a contact ion-pair or a complex. This is the case for the fluoride complexes of the U^{4+} and Th^{4+} ions, studied in Paper II. For understanding the properties of electrolyte solutions, it is important to distinguish between complex formation and solvent-shared ion pairing. Direct structural results about the coordination is one way of providing such information. A complication for the presently

studied ions is the less well-defined coordination geometry, which leads to a broad distribution of the metal-oxygen distances for the high coordination numbers and also often an asymmetry in the distribution.

EXAFS and LAXS are the experimental structural methods used in the present work for determining the hydration number of the above ions, *i.e.* the number of water molecules in the first hydration sphere. As described in Sections *1* and *2*, the accuracy of the coordination number derived from the amplitude of the scattering functions is often not better than ±1, or even ±2, in particular for the EXAFS method.

On the other hand, the accuracy of the metal-ion distances can be better than ± 0.01 - 0.02 Å. Therefore, for estimating the hydration number, it is often more reliable to use a correlation between the mean distances and the coordination numbers derived from crystal structures or ionic radii, since the effective ionic radius of an ion increases with increasing coordination number.[43] In the present study, comparisons of the experimental M-O(aq) distances for the hydrated ions have been made versus mean M-O distances from crystal structures. Another useful source of data for predicting bond distances is provided by Shannon´s effective ionic radii,[43] based on an ionic radius of 1.40 Å for the oxide ion. Values of interest for the ions in the current study are given in Table 9. However, we have to consider that the results from different sources and techniques are slightly different (*cf.* Section *1.7.4* and *2.1*), and care must always be taken to ensure that they are comparable.

Table 9. Comparisons between predicted Ca-O bond distances (as the sum of Shannon´s effective ionic radii),[43] with the experimentally obtained Ca-O(aq) values, assuming an ionic radius 1.40 Å for O^{2-}. Also three sets of correlations between coordination number (*N*) and Ca-O distances (*d*) are given, which are evaluated for crystal structures.

Coord. No. (*N*)	Effective ionic radius/ Å	Predicted M-O distance/ Å	1st set of *d* - *N* correlation[a]	2nd set of *d* - *N* correlation[b]	3rd set of *d* - *N* correlation[c]	Experimental Ca-O(aq) / Å in this study[d]
6	1.00	2.40	2.334(9)	2.35(1)	2.31-2.33	
7			2.403(5)	2.41(1)	2.40-2.41	
8	1.12	2.52	2.481(6)	2.45(1)	2.47-2.49	2.46±0.01
9			2.521(4)	2.48(4)	2.53 (2.55-2.57)[e]	
10	1.23	2.63				

[a] Reference 56. [b] Reference 57. [c] From hydrated Ca^{2+}(aq) ions in crystals (see text p. 121). [d] Present EXAFS and LAXS results. [e] 9-hydrates with bridging water

As can be seen in columns 4 to 6 of Table 9, the experimental mean Ca-O distance for a known coordination number is often shorter than the predicted Ca-O distances based on the effective ionic radius of the oxygen ion, 1.40 Å. The main reason for the shorter distance is probably an increase in covalency of the metal-oxygen bond and the polarization of the water molecule due to hydrogen bonding.

4.1 Calcium. The calcium(II) ion is of similar size as the U(IV) and Th(IV) ions (*cf.* Tables 9 and 12), but has a much smaller charge-to-radius ratio. Thus, the effect on the structure of its surrounding water molecules is less pronounced, and allows a flexible coordination geometry and fast kinetics in the first hydration sphere. The irregular coordination figure around the calcium ion is then strongly influenced by its second coordination sphere.[58] These coordination properties makes the calcium ion useful in the control of conformational changes in the biological functions of the cell. The hydrated calcium ion has a diversity of important roles in biochemical processes in the human body, *e.g.* in the control of metabolism, nerve impulse and muscle contraction, blood clotting, cell division, etc.[58] The great importance of the biochemical activities of the hydrated calcium ion has led to a number of structural studies in aqueous solution. However, the flexibility of the first coordination sphere makes it difficult to interpret the experimental data, which has given rise to large variations in the results.[42]

EXAFS studies. In the present study, the Ca K-edge EXAFS data were measured (*cf.* Figure34c) in fluorescence mode, using a Lytle detector without fluorescence filter. The experiment was set up in helium atmosphere in order to reduce air absorption and scattering. For energy calibration of the Ca K-edge EXAFS spectra, the CaO and $Ca(OH)_2$ solids with known structures were measured and analyzed. The same threshold energy, E_0, was used for the solutions as for the solid measured at the same occasion.

Assuming symmetric distribution of the Ca-O distances in the first coordination sphere of the hydrated calcium ion, resulted in a mean Ca-O bond distance of about 2.43 Å. The Debye-Waller factor, which corresponds to a root-mean-square (*r.m.s.*) displacement of 0.10(2) Å, shows a wide distribution of the Ca-O distances. Moreover, the phase shift of the EXAFS data at high *k*-values reveals that the distribution actually is asymmetric (Figure 22).

The cumulant expansion method was used to model this asymmetry (*cf.* Section *1.5.7*). When the 3rd phase-adjusting cumulant was included the value obtained for the centroid of the distribution of the Ca-O distances, shifted to about 2.46 Å for the three solutions

Table 10. EXAFS parameters for least-squares model fitting of the first hydration shell of the calcium(II) ion in aqueous solution from *k* and *r*-space fitting of Fourier-filtered k^3-weighted data, together with the solid calibration compounds used. The parameters are the coordination number (*N*), Ca-O bond distance *d*, mean-square amplitude of DW factor σ_e^2, third phase adjustment cumulant C_3 for asymmetric distance distribution, phase shift ΔE_0 from the calcium threshold energy 4038 eV, and residual.[b]

Sample	*k*-range (Å^{-1})	*N*[a]	*d* (Å)	σ_e^2 (Å^2)	C_3 (Å^3)	ΔE_0 (eV)	S_0^2	Residual
CaO(s)	2.7 – 9.9	6	2.398[a]	0.008(1)	-	6.0(1)	0.42(2)	20.5
$CaCl_2$ (1.5 mol dm^{-3})	3.4 – 9.6	8	2.435(6)	0.012(2)	-	6.0[a]	0.82(7)	14.2
	3.4 – 9.6	8	2.461(9)	0.011(1)	0.0011(3)	6.0[a]	0.81(7)	5.5
$Ca(OH)_2$(s)	3.4 – 11.4	6	2.374(8)	0.007(1)	-	5.0(8)	0.40(4)	17.8
$Ca(ClO_4)_2$ (1.88 mol dm^{-3})	2.5 – 10.0	8	2.426(4)	0.012(1)	-	5.0[a]	0.83(6)	20
	2.5 – 10.0	8	2.457(7)	0.011(1)	0.0013(3)	5.0[a]	0.83(5)	7.1
$Ca(ClO_4)_2$ (0.94 mol dm^{-3})	2.5 – 11.0	8	2.425(4)	0.012(1)	-	5.0[a]	0.89(6)	20.4
	2.5 – 11.0	8	2.453(8)	0.012(1)	0.0012(3)	5.0[a]	0.90(6)	9.3

[a] fixed parameter

[b] $$\text{Residual [\%]} = \frac{\sum_{i=1}^{N} [y_{exp}(i) - y_{theo}(i)]}{\sum_{i=1}^{N} [y_{exp}(i)]} \times 100$$

* Measurements at SSRL were performed at two different occasions using different standard compounds for energy calibration.

studied. The same value of ΔE_0 as for the Gaussian model was used in this refinement. The estimated uncertainty in ΔE_0 of ±1 eV increases the estimated error in the Ca-O mean bond distance to ± 0.02 Å.

The results evaluated for the Ca K-edge EXAFS data are summarized in Table 10.

LAXS studies. Several different calcium halide solutions were investigated by large angle x-ray scattering, since the distances for the hydrated halide ions X···(H)-O to some extent overlap the Ca-O distances (Table 11). A consistent value, 2.46(1) Å, was obtained for the mean Ca-O bond distance, although for the LAXS data only a Gaussian model could be applied to describe the distribution of the distances in the first shell (see Figure 36).

The mean Ca-O_{II} distance from the calcium ion to its rather diffuse second hydration sphere (see Figures 34b & 36a), can be determined from the LAXS data (Table 11). However, no features corresponding to the second hydration sphere could be seen in the EXAFS data (Figure 34d).

Correlation with crystal structures. Two separate surveys of Ca-O bond lengths have been made in order to correlate the bond distances d to the coordination number N. These include a large number of coordination compounds of calcium(II) with a wide range of organic ligands, in crystal structures of small molecules mostly from the Cambridge Structural Database.[56,57] The results are given in Table 9, shown as 1st and 2nd set of *d-N* correlation. Besides, a number of crystal structures can be separated out containing hydrated calcium(II) ions only surrounded by water molecules, with coordination numbers from 6 to 9. All these structures display a fairly wide distribution of the Ca-O_w distances. But, the arithmetic mean values are found to vary little for reasonably well-determined structures. The values are: Ca-6O_w 2.31-2.33 Å, Ca-7O_w 2.40 - 2.41 Å, Ca-8O_w 2.47-2.49 Å, and Ca-9O_w 2.53 Å (tricapped trigonal prism, 6x2.501, 3x2.579 Å), Ca-9O_w (with six bridging O_w) 2.55 – 2.57 Å, and are given as 3rd set of *d-N* correlation in Table 9.[59]

When comparing the mean Ca-O distance, *ca.* 2.46 Å, obtained from both the LAXS and EXAFS data in the present study, with the different correlations in Table 9, the probable coordination number for the Ca^{2+}(aq) ions in solution can be evaluated as 8.

There is an enhanced polarisation of the coordinated water molecules by the hydrogen bonding to the second hydration sphere in aqueous solution. This effect was found to shorten the Ca-O distances by 0.02 Å, based on results of high level density functional theory (DFT) calculations, for an isolated calcium ion surrounded by 6 water molecules

when 12 hydrogen bonded water molecules was added in a second sphere.[60] This DFT calculation also shows that six-coordination is definitively excluded for hydrated calcium ions in aqueous solution, since the calculated Ca-O bond distance was 2.35 Å for the hexahydrated Ca^{2+} ion with a hydrogen bonded second sphere of twelve water molecules, $[Ca(H_2O)_6](H_2O)_{12}^{2+}$. For an isolated $[Ca(H_2O)_8]^{2+}$ ion the calculated mean Ca-O bond distance was 2.48 Å.[60]

Table 11. LAXS parameters for pair functions (eqn. 45) used for modelling the experimental data for the calcium halide solutions. Parameter values are given for the distance *d*, the number of distances *N*, and the mean-square variation of the distance σ_i^2 in the Debye-Waller factor. The estimated standard deviations are given within brackets for refined parameters.

Sample	Distance	*N*	*d* (Å)	σ_i^2 (Å^2)
CaI_2(aq)	Ca-O	8	2.46(1)	0.007(1)
	Ca···O_{II}	13(2)	4.58(5)	0.04(1)
	Ca···I	2	5.25(10)	0.05(2)
	I···O	8	3.61(1)	0.016(2)
	O_w···O_w	2	2.93(2)	0.008(2)
$CaBr_2$(aq)	Ca-O	8	2.46(1)	0.006(1)
	Ca···O_{II}	13(2)	4.58(5)	0.04(1)
	Ca···Br	2	5.02(10)	0.05(2)
	Br···O	6	3.35(1)	0.012(1)
	O_w···O_w	2	2.89(1)	0.012(1)
$CaBr_2$(aq)	Ca-O	8	2.46(1)	0.006(1)
	Ca···O_{II}	11(2)	4.58(5)	0.04(1)
	Ca···Br	2	5.02(10)	0.05(2)
	Br···O	6	3.36(1)	0.011(1)
	O_w···O_w	2	2.87(2)	0.013(1)
$CaCl_2$(aq)	Ca-O	8	2.46(1)	0.006(1)
	Ca···O_{II}	11(2)	4.58(5)	0.04(1)
	Ca···Cl	2	4.90(10)	0.05(2)
	Cl···O	6	3.25(5)	0.009(1)
	O_w···O_w	2	2.89(1)	0.012(1)

4.2 Uranium(IV) and thorium(IV). These ions are important as models for other actinides with the same oxidation state, which have similar coordination properties, except for the size effects of the "actinide contraction" caused by the poor shielding of the increasing nuclear charge from the filling of the 5f shell. Uranium(IV) has a $5f^2$ electronic configuration while thorium(IV) has no 5f-electrons. Knowledge of the detailed coordination chemistry of the actinides is important because of the need for predictions of properties of actinide ions in nuclear waste storage and recovery processes, but investigations have been restricted mostly to uranium and thorium for practical and safety reasons.

Hydration. Very high hydration numbers can be expected for the U^{4+} and Th^{4+} ions in aqueous solution because of their large size and high charge. From previous LAXS studies, hydration numbers of about 8 were reported.[42,46] However, evidence from other sources suggests even higher hydration numbers.[55] According to the previous LAXS and the current EXAFS studies, the difference in the metal – oxygen bond lengths for these two ions is about 0.03-4 Å, close to their difference in effective ionic radii, about 0.04 Å (Table 12).[43] This indicates that the hydration number is similar for the two ions.

Table 12. Comparison between predicted M-O bond distances (as the sum of Shannon's effective ionic radii, ref. 43) with the experimentally obtained M-O(aq) values for some ions.

Ion	Coord. No.	Effective ionic radius / Å	Predicted M-O distance/ Å	Experimental M-O(aq) / Å in this study.[a]
Er^{3+}	6	0.89	2.29	
	8	1.004	2.40	2.35-6
	9 [b]	1.062	2.46	
U^{4+}	6	0.89	2.29	
	8 [c]	1.00	2.40	
	9	1.05	2.45	
	10			2.42±0.01
	12	1.17	2.57	
Th^{4+}	6	0.94	2.34	
	8	1.05	2.45	
	9	1.09	2.49	
	10	1.13	2.53	2.45±0.01
	11	1.18	2.58	
	12	1.21	2.61	

[a] Present EXAFS results. [b] For a hydrated Er^{3+} ion the average bond distance is M-9O_w 2.42 Å for a trigonal prism (6x2.37 + 3x2.52 Å); ref. 61. [c] For U(IV) oxide (Figure 47): U-8O 2.37 Å, ref. 62.

From the results of our present EXAFS measurements, we suggest that both the U^{4+} and Th^{4+} ions are 10-coordinated in aqueous solution. Also, we propose that nine water molecules are coordinated in the mono-fluoride complex, UF^{3+}, *i.e.* giving a $[UF(OH_2)_9]^{3+}$ species. However, the EXAFS technique does not provide precise values for the coordination number, and the conclusions were based on comparisons with other data (*cf.* Table 12 and Paper II).

Although the M-O bonding must be strong, the coordination geometry is probably somewhat irregular for such high hydration numbers. As discussed below (p.127), this could lead to a slightly asymmetric distribution of the individual metal-oxygen bond distances in the first hydration sphere.

A proper determination of the threshold energy, E_0, is important for obtaining accurate experimental distances, in particular in cases when the distribution of distances is wide and asymmetry can be expected. For the U L_{III}-edge EXAFS measurements performed at the SSRL, uranium(IV) oxide, UO_2, with eight oxygen atoms around each uranium (Figure 47), was used as standard compound for a calibration of this parameter.

The distances reported from the crystal structure determination of the uranium(IV) oxide are: U-O_I 2.37 Å; U-U 3.87 Å, and U-O_{II} 4.53 Å.[62] The agreement between the crystallographic distances and the EXAFS results (Table 13) seems sufficiently good to give confidence in the ΔE_0 values (and the accuracy of the distances), determined independently for the solution data which were measured at the same occasion at the SSRL.

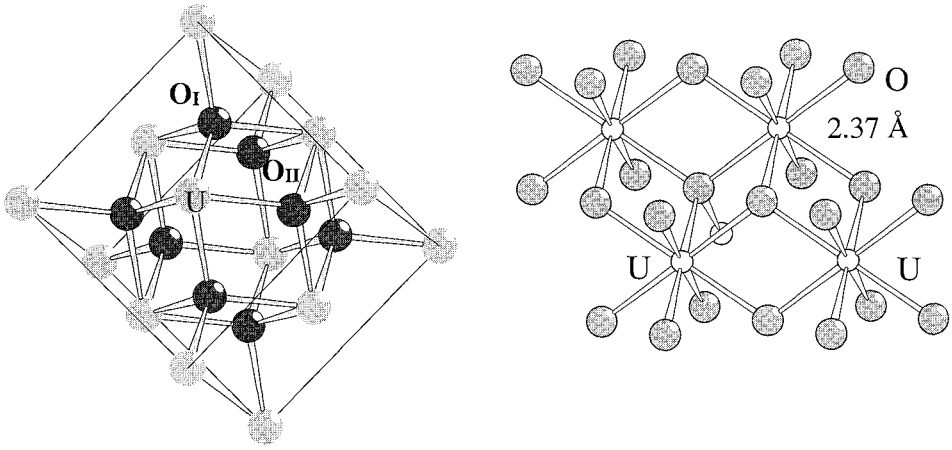

Figure 47. The crystal structure of uranium(IV) oxide.

However, UO_2 is not an ideal standard compound despite the high symmetry of the U-O_I first coordination shell (Figure 47), because:

(1) the U-U backscattering dominates the EXAFS oscillations of UO_2, in particular at high *k*-values;

(2) the results for U-O distances were sensitive to the spline removal procedure, and different ΔE_0 shift values were obtained during the refinement process;

(3) non-stoichiometric compositions,[63] UO_{2+x}, can occur for the oxide and may affect the crystallographic distances. It is, therefore, doubtful if a ΔE_0 value from the oxide can be applied for the U^{4+}(aq) solution data.

The improbably low value, ~0.5, of the amplitude reduction factor (S_0^2) for the known coordination number of the UO_2 oxide, shows that there are systematic errors in the EXAFS amplitude, probably due to experimental factors. Since there is a direct correlation between the amplitude reduction factor and coordination number (eqn. 14), it was not possible to use this S_0^2 value to estimate the coordination number for the U^{4+}(aq) ion in aqueous solution.

For energy calibration of the x-ray beam from the monochromator, the spectrum of an yttrium foil (K edge = 17038 eV) was recorded simultaneously during the EXAFS measurements at HASYLAB. The threshold energies, E_0, were arbitrarily defined as the inflection point of the uranium L_{III} edge spectra. The accuracy of the E_0 value (and the distances) was checked by measuring and evaluating the EXAFS spectrum of $Ba_2U(C_2O_4)_4 \cdot 8H_2O$. This gave a mean bond distance of 2.38 Å and coordination number of 9.0 ± 0.7 oxygen atoms for a fixed amplitude reduction factor $S_0^2 = 1.0$, to be compared with the crystal structure average, 2.407 Å, for nine coordinated oxygen atoms.[64]

Uranium L_{III}-edge EXAFS were measured for several solutions with the hydrated U^{4+} ion, and also with U-F complexes (Paper II). The Fourier-filtered data, which contain only the first shell contributions, were then used for the refinement procedure. Curve fitting was made with a model function assuming a Gaussian distribution of U-O bond distances described by a Debye-Waller factor (Table 13).

Table 13. EXAFS parameters for least-squares model fitting of the first hydration shell of the uranium(IV) ion in aqueous solution from *k* and *r*-space fitting of Fourier-filtered k^3-weighted data. The parameters are the coordination number (*N*), U-O, U-F and U-U distances *d*, mean-square displacement σ^2 of DW factor, third (phase adjustment) cumulant C_3 for asymmetric distance distribution, threshold energy shift ΔE_0, amplitude reduction factor S_o^2 and residual.

Sample	Comment	Assumed E_0 / eV	k_w	FT k-range / Å^{-1}	FT-Filter range *r*/ Å	Scattering Path	Coord. No.	Distance *R* / Å	DW factor σ^2 / Å^2	ΔE_0 / eV	S_o^2	3rd cumulant	Res.
A: UO_2 (solid)	SSRL	17160.7	2	3.07 – 15.04	1.37 – 4.74	U-O_I U-U U-O_{II}	8 f 12 f 24 f	2.360 (11) 3.872 (3) 4.435 (22)	0.0110 (18) 0.0054 (5) 0.0140 (37)	4.9 (7)	0.54 (5)	----------	18
B: U^{4+}(aq) 0.05 M	SSRL	17158.4	3	2.89 – 11.74	1.408 – 2.83	U-O U-O	10 f 10 f	2.401 (6) 2.421 (17)	0.0098 (9) 0.0099 (9)	4.2 (5) 5.0 (8)	0.86 (7) 0.89 (7)	---------- 0.0004	8.6 6.6
C: U^{4+}(aq) 0.05 M	HASYLAB	17166.0	3	2.89 – 14.13	1.42 – 2.72	U-O U-O	10 f 10 f	2.406 (5) 2.434 (12)	0.0083 (7) 0.0083 (7)	2.5 (5) 3.7 (7)	1.03 (7) 1.09 (8)	---------- 0.0004 (2)	12.6 7.2
D: U^{4+}(aq) 0.2 M	HASYLAB	17165.9	3	2.87 – 12.76	1.42 – 2.79	U-O U-O	10 f 10 f	2.406 (6) 2.423 (14)	0.0090 (8) 0.0090 (8)	3.4 (5) 4.1 (7)	1.12 (8) 1.15 (9)	---------- 0.0003	9.7 8.0
E: UF^{3+}(aq) (0.05 M U^{4+} + 0.06 M F^-)	SSRL	17160.3	3	2.93 – 12.47	1.54 – 2.48	U-F U-O	1.5 (4) 9 f	2.108 (18) 2.451 (8)	0.0030 (18) 0.0090 (17)	4.1(2.9)	0.9 (2)	----------	17
F: UF^{3+}(aq) (0.055M U^{4+} + 0.055M F^-)	HASYLAB	17166.0	3	2.88 – 14.01	1.56 – 2.56	U-F U-O	0.8 (1) 9 f	2.103 (8) 2.43 (2)	0.0022 f 0.0089 (9)	3.0 f	0.99 (8)	----------	9.6
G: UF^{3+}(aq) (0.055 M U^{4+}+ 0.09 M F^-)	HASYLAB	17166.0	3	2.88 – 14.10	1.59 – 2.53	U-F U-O	1.2 (2) 9 f	2.119 (5) 2.43 (2)	0.0022 (10) 0.0085 (8)	3.0 f	0.87 (7)	----------	19.3

For the EXAFS data with the largest *k*-range, some phase shift deviation was detected at high *k*-values (curve **a**, Figure 48), which indicated a slight asymmetry in the distribution of the U-O_I distances. Refinements were also made including the 3rd cumulant to account for the phase-shift caused by the asymmetry, which in all cases resulted in a slightly longer U-O mean bond distance. The ΔE_0 value was refined independently in the fitting procedure of the models, with and without the 3rd cumulant, since no reliable independent calibration of the ΔE_0 value could be made.

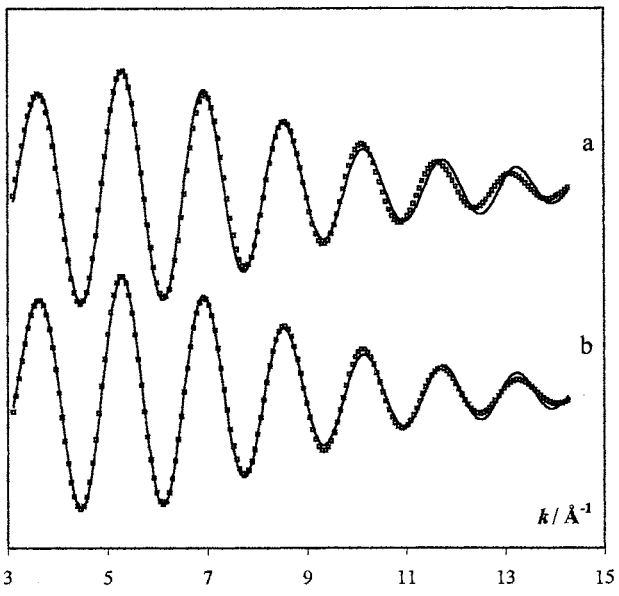

Figure 48. EXAFS curve fitting of Fourier-filtered data from HASYLAB (Table 13, row C). The solid line represents the experimental data and the dots (□□□□□) the model function. A model assuming symmetric (Gaussian) distribution of the U-O distances is used for curve **a**, and shows a phase shift at high *k*-values. The effect of including the 3rd cumulant in the model function to account for the phase-shift from an asymmetric distribution is shown in curve **b**.

Additional information on the hydration number of the U^{4+} ion was obtained from comparisons with the Er^{3+} ion, which has almost the same ionic radii as U^{4+} (see Table 12), but lower charge. In aqueous solution, the Er^{3+} ion has very probably the hydration number 8, and the Er-O mean distance 2.35-6 Å.[42] The average Er-O value from a crystal structure with a 9-hydrated erbium(III) ion in a trigonal tricapped prism is 2.42 Å,[62] similar to the

value obtained for the U^{4+} solution. Since the charge is higher, the hydration number of U^{4+}(aq) should then be higher than 8.

Another indication of a high coordination number was the comparison with the slightly shorter mean U-O distance 2.38 Å, for the 9-coordinated solid compound $Ba_2U(C_2O_4)_4{\cdot}8H_2O$,[64] as obtained from the EXAFS measurements. We therefore concluded that the coordination number 10 ± 1 is the most likely for both the U^{4+} and Th^{4+} ions in aqueous solution.

As was discussed for the calcium ion (p. 121), the mean M-O(aq) distances are often shorter for a known coordination number than the predicted M-O distances based on the effective ionic radii (mostly based on oxides).[43] The main reasons seem to be shortening due to the increased covalence in the bonding, connected to the strong polarisation of the coordinated and hydrogen-bonded water molecules in the first sphere.

To summarise, the mean U-O bond distance for the U^{4+} ion in aqueous solution is found to be 2.42 ± 0.02 Å, with a rather wide and slightly asymmetric distribution (*r.m.s* displacement 0.09 – 0.10 Å), of the U-O distances. The probable hydration number is 10 ± 1. The main source of error is the uncertainty in the threshold energy, which causes the estimated error limit of ± 0.02 Å in the determination of the U-O bond distance.

A similar data treatment was made for the thorium(IV) ions, using ThO_2 as a standard compound.[65] For the hydrated Th^{4+} ion in aqueous solution a mean distance of 2.45 ± 0.02 Å was obtained, and a probable hydration number of 10 ± 1 (Paper II).

Fluoro complexes in aqueous solution. In order to explain the different water exchange rates measured by ^{17}O NMR in a previous investigation,[66] for the UF^{3+} and ThF^{3+} complexes as compared to the U^{4+} and Th^{4+} ions in aqueous solution, EXAFS measurements were made on acidic solutions with added NaF. Strong complex formation is expected, and UF^{3+} and UF_2^{2+} complexes should form according to the equilibrium constants.

A comparison of the U L_{III} edge EXAFS data measured at two different sites, SSRL and HASYLAB, shows the same deviating feature at k = 10.55 $Å^{-1}$ (Figure 49). Thus, this feature cannot be a "glitch", *i.e.* caused by an imperfection in the monochromator crystal, but should rather be a result of a multi-electron excitation. These features were removed from the data and at the refinement stage, Fourier-filtered data were used.

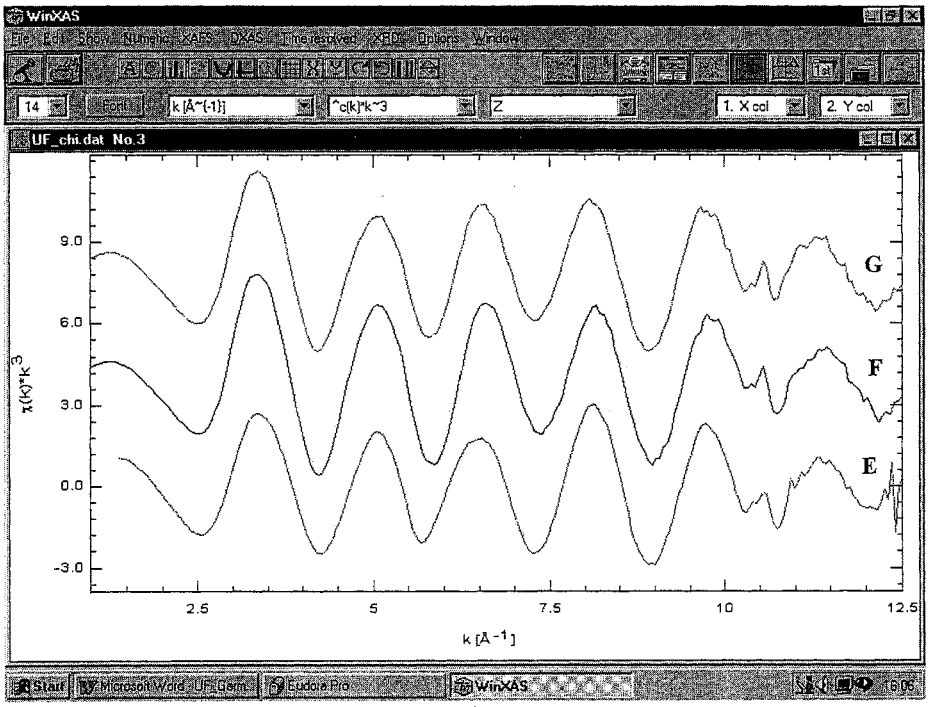

Figure 49. Comparison of different EXAFS data sets (from Table 13) for UF^{3+}(aq) solutions showing the multielectron excitation feature at $k = 10.55$ Å^{-1}: bottom) **E** (SSRL), middle) **F**, and top) **G** (HASYLAB).

When evaluating EXAFS spectra it is not possible to distinguish O and F as backscatterers, but if the difference between the U-O and U-F bond distances is large enough, they can be modelled separately. For two shells of backscatterers with similar atomic number, the effective k-range, Δk, is related to the resolution limit by: $\Delta R = \frac{\pi}{2\Delta k} =$ 0.16 Å for a Δk range of about 10 Å^{-1}, as in the spectra above. The results of the refinements (Table 13), gave U-F distances of about 2.11 Å and U-O of about 2.44 Å, with a separation clearly possible to resolve. The separate EXAFS contributions are shown in Figure 50, obtained both by k-space fitting of the EXAFS oscillations, and by r-space fitting of a filtered range in the Fourier transform.

In the refinements the coordination number of the U-O interaction was fixed to 9 in order to be able to refine the amplitude reduction factor (which can be influenced by systematic errors), and to estimate a coordination number for the U-F interaction (Table 13). The results indicate that most fluoride ions added to the solution forms inner-sphere complexes with the U(IV) ion, with a much smaller Debye-Waller factor (*r.m.s.* displacement ~0.05 Å) for the U-F bond than for the U-O shell.

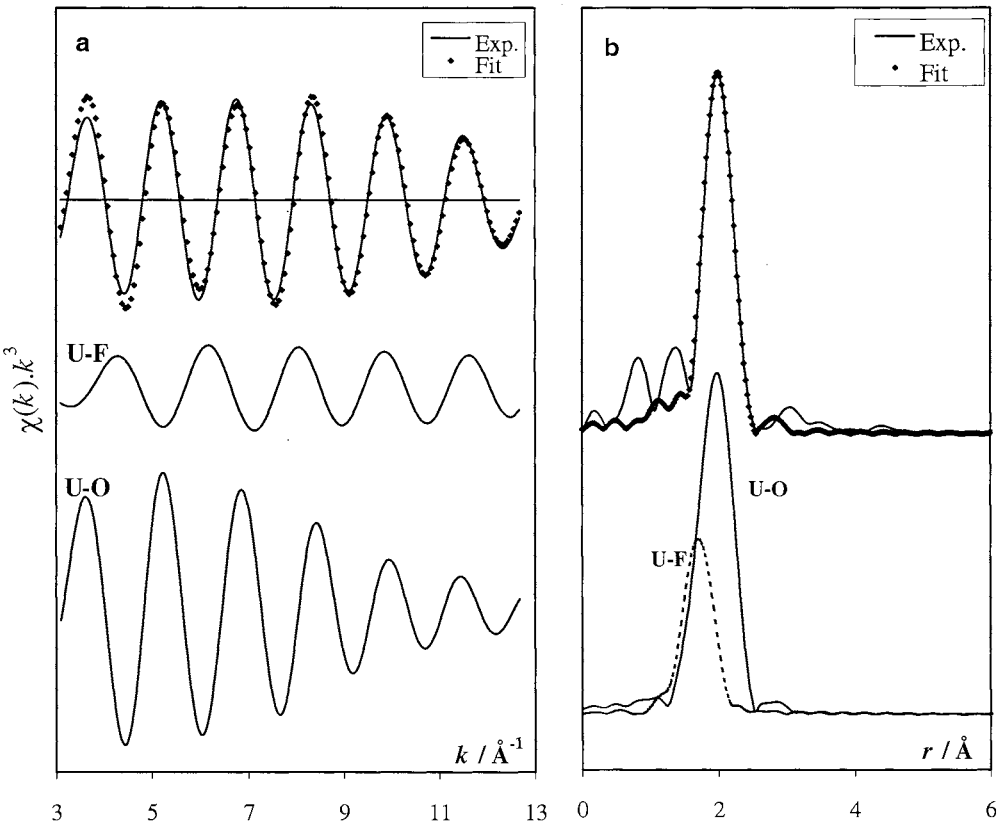

Figure 50. Fourier filtered uranium L_{III} EXAFS data for solution **G** in Table 13 (solid curve in the top figure **a**). The parameters for the model function fitted in *k*-space (dots) are given in Table 13, with the separate U-F and U-O contributions shown below; b) the result from *r*-space fitting of the U-O and U-F distances

4.3 Halide ions. Halide ions form a fairly well-defined first hydration shell in aqueous solution, as shown by the LAXS studies of the calcium halide solutions in Paper I (*cf.* Table 10 and Figure 36). For chloride solutions, neutron diffraction experiments with isotopic substitution of the chloride ion have shown that the bonding occurs *via* the hydrogen atom, *i.e.* with $Cl^-\cdots$H-O-H hydrogen bonding (Figure 51a).[39]

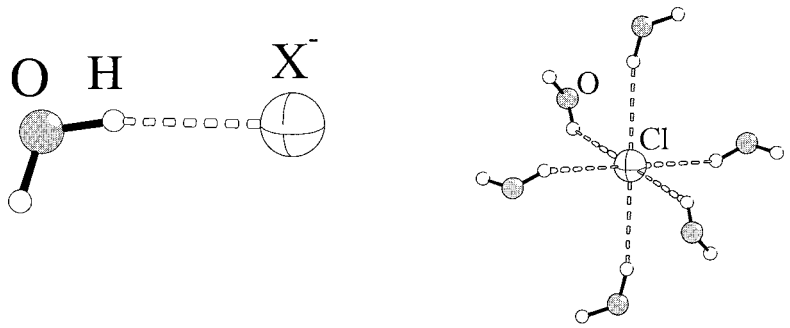

Figure 51. a) Hydrogen bond interaction between a water molecule and a halide ion. b) First hydration shell around a chloride ion from the crystal structure of $ScCl_3 \cdot 6H_2O$.[67]

The $X^-\cdots$O distances, X = Cl, Br or I, obtained from the LAXS studies (Paper I), are 3.25(5), 3.36(1) and 3.61(1) Å (Table 10), for assumed coordination numbers of 6, 6 and 8 water molecules, respectively. These distances correspond to the sum of the ionic or van der Waal's radii of the halide ion and the water oxygen atom (Table 14), and show that the hydrogen bond is weak. A change in the coordination number affects the Debye-Waller parameter (Table 10), but not the distance significantly.

Table 14. Comparisons between the sum of Shannon's effective ionic radii,[43] for halide ions (X) and oxygen atoms (1.40 Å), with the experimentally obtained hydrogen bond distances, X···(H)-O, for X = Cl, Br and I, from the current LAXS results.

Halide Ion	Coord. No.	Effective ionic radius / Å	Predicted X-O distance/ Å	Experimental X···(H)-O(aq) / Å in this study
Cl^-	6	1.81	3.21	3.25(5)
Br^-	6	1.96	3.36	3.36(1)
I^-	6	2.20	3.60	3.61(1)

The assumptions of the coordination numbers are based on previous results in the literature,[42] and on the following considerations. The $Cl^-\cdots O$ distance obtained for the chloride ion is somewhat longer than the mean value, 2.15 Å for a chloride ion octahedrally hydrogen bonded to six water molecules in the crystal structure of $[Sc(H_2O)_4Cl_2]Cl{\cdot}2H_2O$ (Figure 51b).[67] A recent MD simulation resulted in a hydration number of 7.9 for the iodide ion and the highest probability for the $I^-\cdots O$ distance at 3.60 Å.[68] In the crystal structure of calcium iodide 6.5-hydrate the average $I^-\cdots O$ distance to the eight closest surrounding water molecules, is about 3.7 Å, *cf.* Figure 52.[69] This structure also displays octahydrated calcium ions with the mean Ca-O distance 2.47 Å (three oxygen atoms shared between the calcium ions), and 11 second sphere $Ca\cdots I$ distances around each calcium ion in the range from 5.0 to 5.6 Å, mean value 5.30 Å.

It is clear from the LAXS modified radial distribution function (RDF) in Figure 53, that there are iodide ions in the second sphere around the calcium ion in approximately the stoichiometric ratio. For the calcium halide solutions there is no evidence of formation of a contact ion pair, even in concentrated solutions where solvent shared ion-pairs must form for stoichiometric reasons.

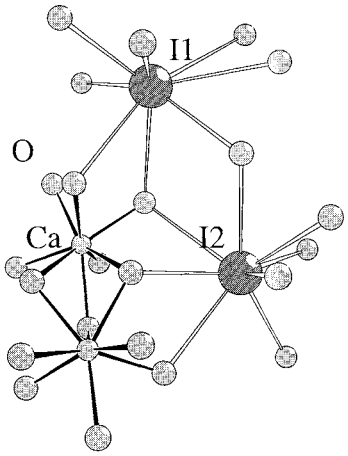

Figure 52. The crystal structure of $CaI_2{\cdot}6.5H_2O$, showing hydrated iodide ions and octahydrated calcium ions, sharing three water molecules (ref. 69).

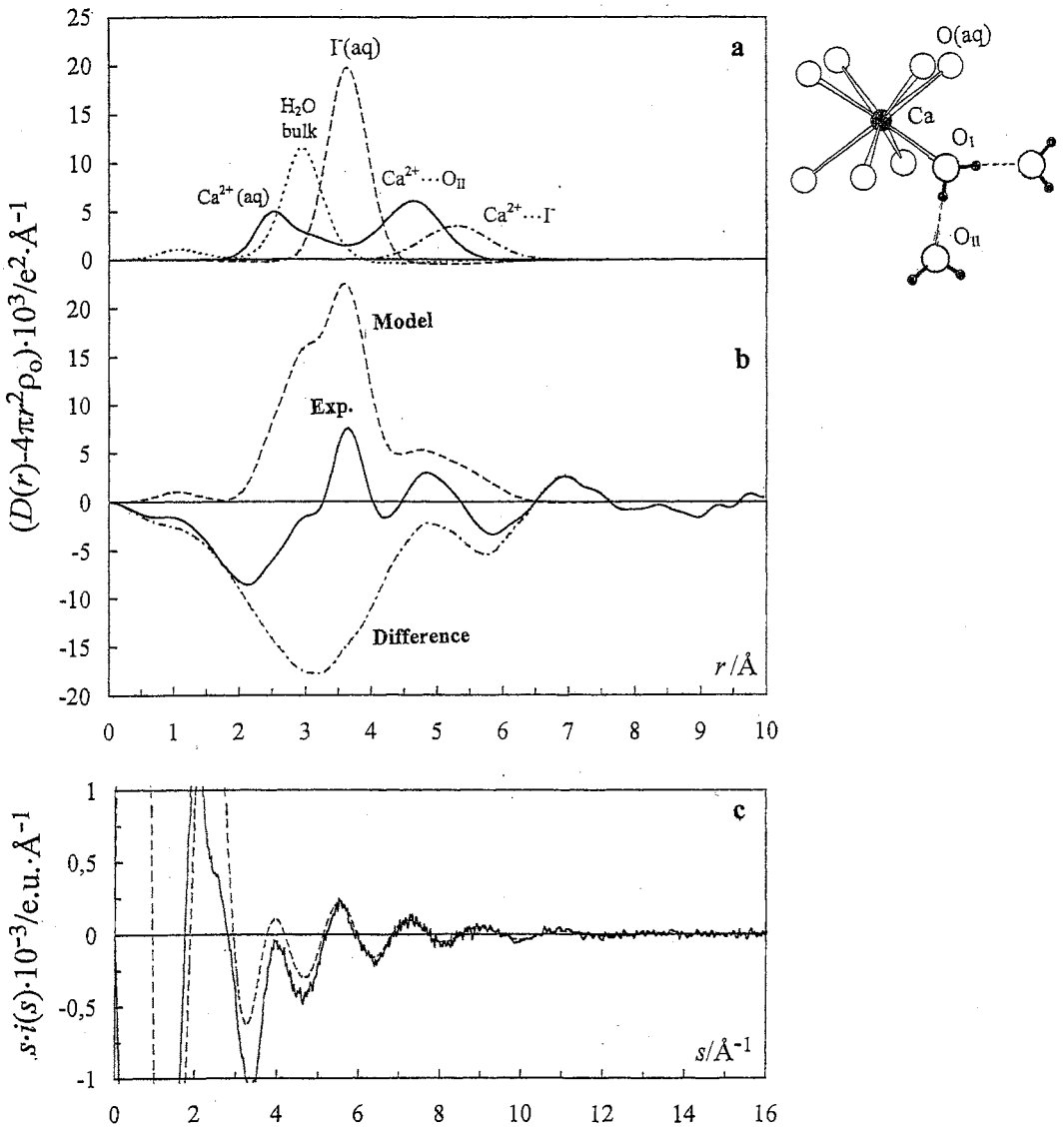

Figure 53. LAXS distributions (RDF) for a 1.5 M CaI_2 solution. a) Separate model peak shapes (according to pair functions in Table 11): the $[Ca(H_2O)_8]^{2+}$ ion with the first ($Ca\text{-}O_I$) and second ($Ca\text{-}O_{II}$) hydration sphere (solid line), the hydrated iodide ion (dashed line) and O···O interactions in bulk water (dotted line). The dash-dotted line represents contributions from 2 iodide ions in the second coordination sphere of calcium (~5.3 Å). b) Experimental RDF: $D(r)\text{-}4\pi r^2\rho_o$ (solid line); sum of model peak shapes in **a** (dashed line); difference: Exp. - Model (dash-dotted line). c) LAXS structure-dependent intensity functions $s\cdot i(s)$ (solid line); model $s\cdot i_{calc}(s)$ (dashed line).

5. Cyano complexes

5.1 Cyanide as ligand. The CN^- ion is isoelectronic with CO and NO^+, but is a stronger σ-donor because of its negative charge. The molecular orbital (MO) energy level diagram of the valence orbitals in Scheme 4a shows that there is a significant energy difference between the C and N orbitals forming the triple bond (the 3σ and the two 1π orbitals) in the cyanide ion. The highest occupied MO (HOMO) orbital is the bonding 3σ orbital. Because of the energy difference there is still some lone-pair character of this MO on the C and N atoms, which allows the formation of a σ-bond from the ligand to the metal ion: $M \overset{\sigma}{\leftarrow} C{\equiv}N$.[51b] The lowest unoccupied MOs (LUMO) are the two empty antibonding $2\pi^*$ orbitals, which can receive electron density from filled d_{xz} and d_{yz} orbitals on the metal and give rise to a π-bond: $M \overset{\pi}{\rightarrow} C{\equiv}N$. This is illustrated in the representation of the orbital overlaps in Scheme 4b.

Formation of a strong M←C≡N σ-bond will raise the stretching frequency of the C≡N bond.[11b] This is probably an effect of a reduced polarization toward the more electronegative nitrogen atom, making the C≡N bond more symmetrical and stronger.[52] Thus, the effect of an increase in the oxidation state of a metal ion is an increase in the vibration frequency of the C-N stretching toward higher wavenumbers.[11b,51a,52]

The cyano ligand also has a marked tendency to act as a π acceptor (NO^+ and CO are even better as π acceptors), which has an important influence on its behavior in complex formation. When π backbonding occurs the C-N stretching frequency decreases,[52] because the electron density increases in the antibonding π^*-orbitals of the cyano ligand. A lower positive charge on the metal ion will promote the π-bonding, as shown by comparing the $Hg^{II}(CN)_2$ complex with the isoelectronic $Au^{I}(CN)_2^-$ species with much stronger π backbonding.[52] Therefore, the position of the C-N stretching band in the spectra depends on the balance between these two effects, *i.e.* the σ-donation and the π backbonding.[51a]

Also the nitrogen atom can form σ–bonds, but only as a bridge between two metal atoms in linear M-C≡N-M′ groups.[51a,52] The vibrational C-N stretching frequency is found to shift toward higher wavenumbers at a M-C≡N-M′ bridge formation, and at the same time the M-C frequency usually becomes lower.[11b,52] It seems that the more symmetrical bonding arrangement not only will increase the C≡N bond strength, but also can increase the strength of the N→M′ bond at the same time as M←C decreases.[51a]

Thus, for cyano ligands in a series of related complexes, it is a sensitive probe of the change in the C-N bond character to compare the shifts of the C-N stretching vibration frequency, which is in a convenient range for vibration spectroscopy.[11b,52]

a.

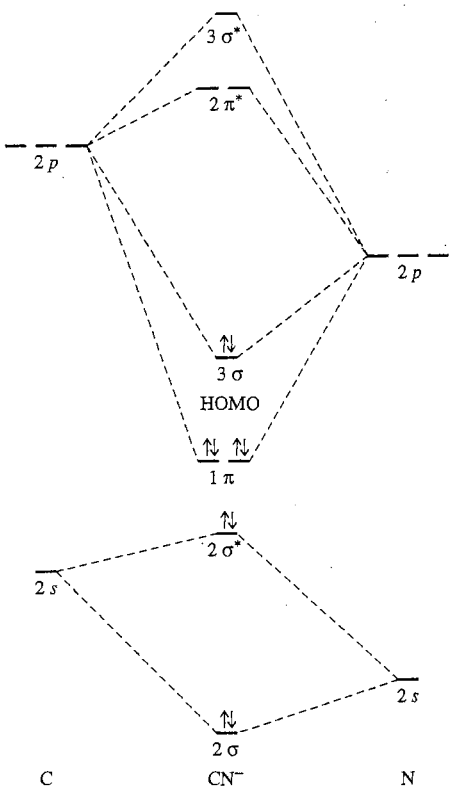

b.

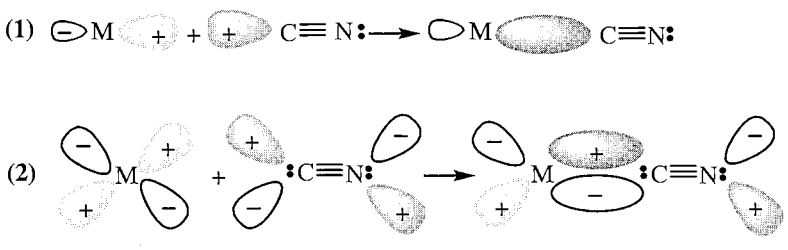

Scheme 4. a). Cyanide ion: Energy levels for molecular orbitals (adapted from ref. 51b, p. 328); b). Schematic representation of orbital overlap leading to metal M-CN bonding: (1) σ donation from the lone-pair (3σ HOMO, see text p. 134) on C into a vacant metal orbital to form a M←C σ–bond, (2) π donation from a filled d_{xz} or d_{yz} orbital on the metal M into the vacant anti-bonding 2π* LUMO orbitals on CN to form a π M→ C bond.(adapted from ref. 63, p. 927)

5.2 Thallium.

Oxidation states. Thallium(I), which has a lone-pair electron in its valence shell ($6s^2$), is the most stable oxidation state in aqueous solution. Thallium(II) is unstable, and disproportionates easily to thallium(I) and thallium(III):

$$2\ Tl_{aq}^{2+} \rightleftharpoons Tl_{aq}^{+} + Tl_{aq}^{3+} \qquad K = 6.2 \times 10^{31} \qquad (49)$$

The trivalent state, thallium(III), is strongly oxidizing, as shown by the reduction potential for the Tl_{aq}^{3+}/Tl_{aq}^{+} redox pair, E^0 = +1.25 V. Moreover, the hydrated Tl^{3+} ion is a strong Brønsted acid (pK_a = 1.14 in 3 M $NaClO_4$). Thus, in the absence of complexing ligands, thallium(III) is partially hydrolyzed even at pH = 0 (1 M $HClO_4$), and the hydrated oxide, Tl_2O_3, may precipitate from concentrated solutions. Strong complex formation is needed to stabilize the thallium(III) oxidation state.[70]

Cyano Complexes $Tl(CN)_n^{3-n}$. Thallium(III) forms very strong and kinetically stable complexes with cyanide ions in aqueous solution. With the use of ^{205}Tl and ^{13}C NMR spectroscopy, in combination with pH measurements, the stability constants have been determined for the four $Tl(CN)_n^{3-n}$ complexes (n = 1 - 4). The distribution of the monomeric cyano complexes $Tl(CN)_n^{3-n}$ as a function of the cyanide concentration is shown in Figure 54.[70]

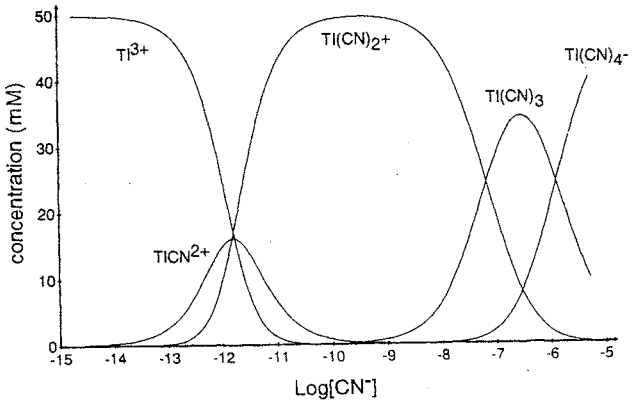

Figure 54. Distribution of the monomeric cyano complexes $[Tl(CN)_n]^{3-n}$ as a function of the free cyanide concentration. $[Tl(III)]_{tot}$= 50 mM (ref. 70).

The structure of the cyano complexes in aqueous solution has been studied previously by EXAFS, LAXS and vibrational spectroscopic methods.[71] Six-coordination was found for the $[Tl(OH_2)_6]^{3+}$, $[Tl(CN)(OH_2)_5]^{2+}$ and $[Tl(CN)_2(OH_2)_4]^{+}$ complexes, and four-coordination for the $[Tl(CN)_3(OH_2)]$ and the $[Tl(CN)_4]^{-}$ species.

However, the strong multiple scattering from the linearly coordinated cyano ligands could at that time not be handled properly, and the great enhancement of the "Tl-N peak" in the Fourier transform due to multiple scattering pathways, was modelled simply with one common empirical set of backscattering parameters for the amplitude and phase shift.

In the current work the model including multiple scattering that was tested out for other cyano complexes was applied on the previously obtained EXAFS data, introducing the dominant 3 and 4 leg multiple scattering pathways, see Scheme 5. The results are given in Table 15 for the $[Tl(CN)_2(OH_2)_4]^{+}$, $[Tl(CN)_3(OH_2)]$ and $[Tl(CN)_4]^{-}$ species.

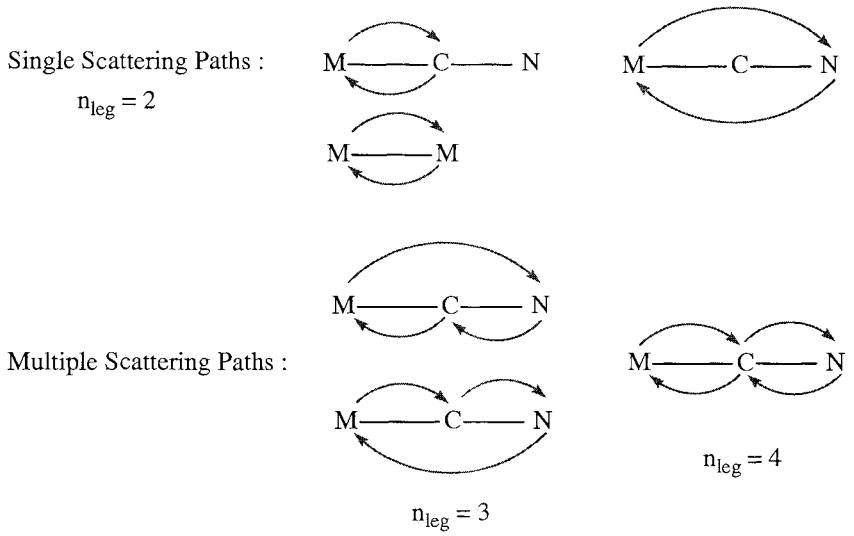

Scheme 5. EXAFS scattering pathways in the linear Tl-C-N units, M = Pt or Tl. The degeneracy of the triple scattering path ($n_{leg} = 3$) is twice of the other paths.

Table 15. Results of Tl L_{III}-edge EXAFS data analyses for thallium(III)-cyano complexes in aqueous solution. The estimated standard deviations for refined model parameters are given within brackets. Fourier-filtered, k^3-weighted EXAFS data were used.

Sample	E_0/eV	Fourier Transform k-range/Å^{-1}	FT-filter range [a] r / Å	Scattering Path [b]	Coor.No./ frequency	Distance R / Å	Debye-Waller parameter σ^2/ Å^2	ΔEo / eV	S_o^2	Residual
$[Tl(CN)_2(OH_2)_4]^+$	12650	3.061 – 13.353	1.301 – 7.996	Tl – C	2	2.092 (4)	0.0029 (3)	10.1 (7)	1.0	26.0
				Tl – O	4	2.429 (6)	0.0177 (11)			
				Tl – N	2	3.263	0.0055			
				Tl – C – N (3)	4	3.263 (3)	0.0055 (3)			
				Tl – C – N (4)	2	3.263	0.0055			
$[Tl(CN)_3(OH_2)]$	12653	2.953 – 13.667	1.217 – 7.996	Tl – C	3	2.133 (4)	0.0039 (3)	7.5 (7)	0.9	20.0
				Tl – O	1	2.422 (17)	0.0089 (23)			
				Tl – N	3	3.293	0.0056			
				Tl – C – N (3)	6	3.293 (3)	0.0056 (3)			
				Tl – C – N (4)	3	3.293	0.0056			
$[Tl(CN)_4]$ Solution	12653	2.93 – 13.66	1.217 – 7.996	Tl – C	4	2.176 (6)	0.0042 (4)	7.9 (9)	1.1	18.6
				Tl – N	4	3.322	0.0060			
				Tl – C – N (3)	8	3.322 (5)	0.0060 (6)			
				Tl – C – N (4)	4	3.322	0.0060			
$[Tl(CN)_4]$ Solid	12653	2.952 – 13.687	1.229 – 7.996	Tl – C	4	2.172 (5)	0.0043 (3)	8.1 (7)	1.1	15.7
				Tl – N	4	3.323	0.0060			
				Tl – C – N (3)	8	3.323 (4)	0.0060 (4)			
				Tl – C – N (4)	4	3.323	0.0060			

[a] The r-range used for the Fourier filtering is given without phase shift correction

[b] The distance and Debye-Waller parameter for Tl-N and C-Tl-C-N (4) are correlated to the dominant path Tl-C-N (3).

The difference between the Tl-C and Tl...N distances is in all cases between 1.15 to 1.17 Å, as expected for the C-N distance in a cyano ligand, and is consistent with a linear coordination geometry.[51a,72] The second cyano complex $[Tl(CN)_2]^+$ was found to have a Tl-C distance of 2.092(4) Å. The vibrational spectra indicate a linear *trans*-configuration, as for other d^{10} metal ions – *e.g.*, copper (I), silver (I), gold (I), and mercury (II), which also form linear dicyano complexes.[52] A Tl-O bond length of 2.43(1) Å was found for the hydrated $[Tl(CN)_2(OH_2)_4]^+$ complex (Table 15). Probably, there are four water molecules completing a pseudo-octahedral coordination around the linear NC-Tl-CN entity.

For the tricyano complex in solution, the Tl-C distance 2.133 (4) Å was obtained. The vibrational spectra indicated a pseudo-tetrahedral C_{3v} symmetry, $[Tl(CN)_3(OH_2)]$.[71] Although the model fitting for the EXAFS spectra could not distinguish between one and two water ligands, a distinct Tl-O bond distance, 2.42(2) Å, was obtained.

For the $[Tl(CN)_4]^-$ complex, tetrahedral symmetry was expected since tetrahedral $M(CN)_4$ complexes are formed by many other d^{10} ions, *e.g.*, copper (I), silver (I), zinc (II), cadmium (II), and mercury (II).[51a] The Tl-C distance was found to be 2.176(6) Å. For the solid compound $K[Tl(CN)_4]$, the Tl-C bond distance was found to be 2.172(5) Å.

The force constants of Tl-C and C-N, obtained from normal coordinate analyses of the vibrational spectra,[71] have been plotted versus the Tl-C distance (Figure 55a and b), and the proposed structures of the $[Tl(CN)_2(OH_2)_4]^+$, $[Tl(CN)_3(OH_2)]$ and $[Tl(CN)_4]^-$ complexes in aqueous solution are shown in Figure 55c. The Tl-C force constant decreases as expected with an increasing number of cyano ligands. With the use of the force constant determined previously for the $[TlCN(aq)]^{2+}$ complex in solution,[71] extrapolation of the trend in Figure 55a, indicates a Tl-C distance of about 2.085 Å in $[TlCN(aq)]^{2+}$. When the corresponding C-N stretching force constant is plotted against the Tl-C distance (*cf.* Figure 55b), the trend indicates an enhanced bond strength for the $[Tl(CN)_2(aq)]^+$ complex. Several of the cyanide complexes of d^{10} ions, such as copper(I), silver(I), gold(I), and mercury(II), show an increase in stability for the second complex, MX_2.[73]

A comparison of the bonding in the series of isoelectronic species, $[Au(CN)_2]^-$, $[Hg(CN)_2]$ and $[Tl(CN)_2]^+$, shows some interesting features with participation of the d_{z^2} orbital in the bonding orbitals. Even though the total bond energy is highest for Tl(III) because of the electrostatic attraction, the shortest M-C bond is found for the $[Au(CN)_2]^-$ complex (Tl-C 2.09 Å, Hg-C 2.04 Å, Au-C 1.97 Å).[73] The π back-bonding from the metal d_π to empty anti-bonding $\pi^*(CN^-)$ orbitals has important consequences for the bond

strength and the vibrational spectra of these cyano complexes. On the one hand, a highly charged metal ion, such as thallium(III), gives a strong σ-bond because of the ion – dipole attraction, but does not allow extensive back-bonding. On the other hand, for gold(I) with lower charge an increased amount of π back-bonding occurs, which weakens the C-N bonds.

This balance between the different effects from the bond character in the linear $[M(CN)_2]$ species, M = Au, Hg, and Tl, is reflected in the bond stretching force constants from their vibrational spectra. The values obtained for the M-C stretching vibrations are: f_r = 2.73, 2.52, and 2.38 N cm^{-1} and for the C-N stretching vibrations: f_R = 17.72, 18.20, and 17.76 N cm^{-1}, respectively.[71,73] The highest f_R value, *i.e.* the strongest C-N bond, is found for the $[Hg(CN)_2]$ complex, while the shortest M-C bond is found for the $[Au(CN)_2]^-$ complex (Tl-C 2.09 Å, Hg-C 2.04 Å, Au-C 1.97 Å).[71]

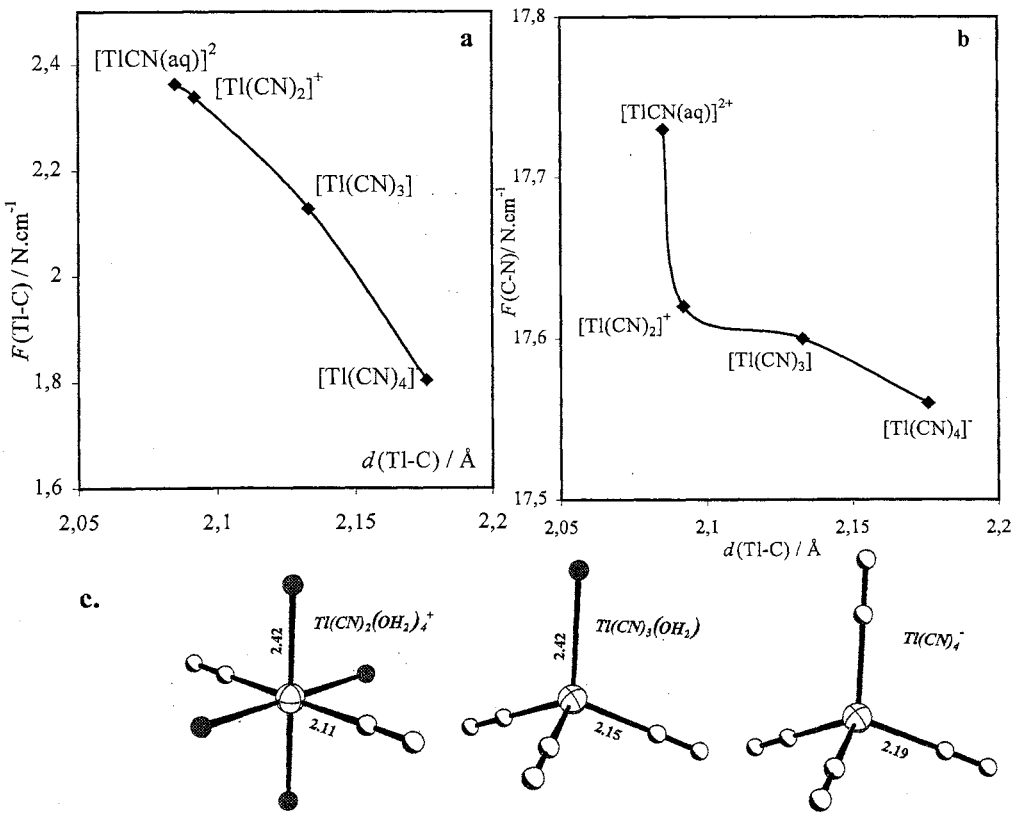

Figure 55. a) Tl-C and b) C-N stretching force constants *vs.* Tl-C bond distance in $[Tl(CN)_n]^{3-n}$ cyano complexes; c) The proposed structures for the $[Tl(CN)_2(OH_2)_4]^+$, $[Tl(CN)_3(OH_2)]$ and $[Tl(CN)_4]^-$ species.

5.3 Platinum

Oxidation states. Pt(II) and Pt(IV) are the common oxidation states for platinum. Pt(II), a d^8 ion, is almost always four-coordinated in square-planar geometry, because of the strong ligand field effect in complexes of the third-row transition elements. Pt(III) is mostly found in binuclear Pt compounds with a single Pt-Pt bond supported by bridging ligands.[74] Pt(IV) complexes are both thermodynamically stable and kinetically inert with a low-spin t_{2g}^6 electron configuration in octahedral coordination geometry.

Cyano complexes. Platinum(II) forms very stable complexes with cyano ligands. Reaction of $[PtCl_4]^{2-}$ with excess KCN gives $K_2[Pt(CN)_4]\cdot 3H_2O$. A neutron diffraction crystal structure determination of this compound shows that planar $Pt(CN)_4^{2-}$ groups are stacked to give linear Pt chains with a Pt-Pt separation of 3.478(1) Å.[75] Adjacent $Pt(CN)_4^{2-}$ groups in the chain are twisted about 16° from the fully eclipsed configuration (Figure 56).

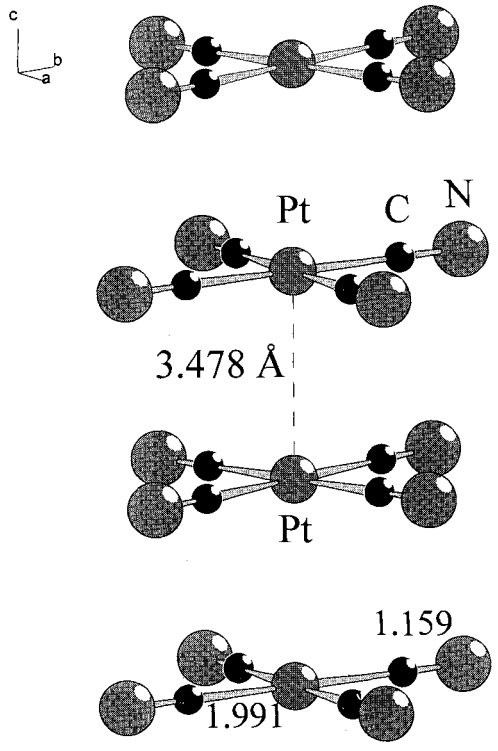

Figure 56. The stacking of $[Pt(CN)_4]^{2-}$ complexes in $K_2[Pt(CN)_4]\cdot 3H_2O$.

Monomeric platinum(IV) cyano complexes. X-ray crystallographic studies of $K_2[Pt(CN)_6]$ shows that the $[Pt(CN)_6]^{2-}$ ion is regular octahedral with linear Pt-C-N bonds.[76] The IR and Raman spectra of the $[Pt(CN)_6]^{2-}$ complex display C-N stretching vibrations at higher frequencies, 2211 cm^{-1}, and C-N force constants which are larger than for the corresponding divalent complex, $[Pt(CN)_4]^{2-}$, with 2143.5 cm^{-1} for the symmetric stretching.[77,78] The crystal structure values for the Pt-CN distances, however, are not significantly different for the two oxidation states, $K_2[Pt(CN)_4]\cdot 3H_2O$, Pt-C, 1.989 Å; Pt-N, 3.148 Å;[75] $K_2[Pt(CN)_6]$: Pt-C, 2.005 Å; Pt-N, 3.153 Å.[76] This is consistent with a higher degree of π back-donation from the metal to the empty π^* orbitals of the cyano ligands in the Pt^{II} complex.

These compounds have been used as standards for testing the multiple scattering models, which were derived for the platinum and thallium cyano complexes in Papers III-V. Our EXAFS values (Table 1 in Paper IV), actually shows that the corresponding distances are slightly shorter for the $[Pt^{II}(CN)_4]^{2-}$ complex, Pt-C 1.985(2) Å, Pt-N 3.149(2) Å, than for $[Pt^{IV}(CN)_6]^{4-}$, 2.004(2) and 3.155(2) Å. For the $[Pt(CN)_6]^{2-}$ complex a normal coordinate analysis has been performed (Table 6 in Paper IV) in order to compare the changes in force constants when replacing a cyano group with another ligand.

Pentacyano complexes of platinum(IV) are usually viewed as monosubstituted hexacyano species. Three compounds of this type, $[Pt^{IV}(CN)_5X]^{2-}$, X= Cl, Br, I, have been characterized with their Raman and IR spectra.[53] Halopentacyano complexes can be prepared by oxidative addition reaction of $[Pt^{II}(CN)_4]^{2-}$ with cyanogen iodide (ICN) or bromide, or by the action of Cl_2 or Br_2 on $[Pt^{IV}(CN)_5I]^{2-}$.[53] In the present work, all investigated compounds and solutions were obtained starting from the bimetallic $[(NC)_5Pt\text{-}Tl(CN)_n]^{n-}$ (n = 0 – 3) complexes.

An EXAFS study of the structure of the pentacyanoplatinum(IV) species $[Pt(CN)_5(OH)]^{2-}$, $[Pt(CN)_5(OH_2)]^{-}$ and $[Pt(CN)_5I]^{2-}$, in aqueous solution is reported in Paper V (Table 16, Figure 57). The mean Pt-C bond distance of the pentacyanoplatinum groups was found to increase slightly in the $[Pt(CN)_5X]^{n-}$ complexes with increasing donor ability of the ligand X = H_2O, OH and I, with very similar values for I and CN (Table 17).

The structures of the $[Pt(CN)_5(OH)]^{2-}$ and $[Pt(CN)_5I]^{2-}$ complexes in the solid state were determined by single crystal X-ray diffraction studies of the compounds $Tl_2[Pt(CN)_5(OH)]$ and $K_2[Pt(CN)_5I]\cdot 0.6H_2O$, and the distances used for comparisons with the EXAFS models (Paper V).

Table 16. Results of Pt L^{III}-edge EXAFS data analysis using k^3-weighting and Fourier-filtering. The estimated standard deviations for refined model parameters are given within brackets. The dominant Pt – C – N (3-leg) path gives the distances and Debye-Waller parameters σ^2 of all paths of the "Pt-N" peak.

Sample	E_0 / eV	Fourier transform (FT) k-range / Å^{-1}	FT-filter range[a] r/ Å	Scattering Path	Frequency	Distance R / Å	Debye-Waller parameter σ^2/ Å^2	ΔE_0 / eV	S_o^2	Residual [c]
$[PtOH(CN)_5]^{2-}$ 0.1 M	11568.6	2.6 – 14.1	1.10 – 8.00	Pt – C	5	1.996 (4)	0.0034 (1)	7.4 (3)	1.2	17.0
				Pt – O	1	2.028	0.0017 (1)			
				Pt – N	5	3.152	0.0043			
				Pt – C – N (3)	10	3.152 (1)	0.0043 (1)			
				Pt – C – N (4)	5	3.152	0.0043			
$Tl_2[PtOH(CN)_5]$ Solid	11566.8	2.6 – 14.0	1.07 – 8.00	Pt – C	5	1.986 (4)	0.0036 (2)	7.5 (4)	1.2	14.2
				Pt – O	1	2.028	0.0009 (6)			
				Pt – N	5	3.146	0.0049			
				Pt – C – N (3)	10	3.146 (2)	0.0049 (2)			
				Pt – C – N (4)	5	3.146	0.0049			
$[Pt(OH_2)(CN)_5]^-$ 0.1 M	11568.5	2.6 – 14.1	1.05 – 8.00	Pt – C	5	1.986 (2)	0.0040 (2)	7.2 (4)	1.2	16.0
				Pt – O	1	2.037	0.0025			
				Pt – N	5	3.144	0.0048			
				Pt – C – N (3)	10	3.144 (2)	0.0048 (2)			
				Pt – C – N (4)	5	3.144	0.0048			
$[PtI(CN)_5]^{2-}$ 0.1 M	11568.8	2.6 – 14.1	1.07 – 8.00	Pt – C	5	2.002 (2)	0.0029 (2)	7.1 (4)	1.2	14.2
				Pt – I	1	2.664 (2)	0.0039 (2)			
				Pt – N	5	3.154	0.0043			
				Pt – C – N (3)	10	3.154 (2)	0.0043 (2)			
				Pt – C – N (4)	5	3.154	0.0043			
$[Pt_2(CN)_{10}]^{4-}$ 0.035 M	11568.5	2.6 – 14.0	1.11 – 8.00	Pt – C	5	2.008 (2)	0.0033 (1)	7.1 (3)	1.2	16.0
				Pt – Pt	1	2.729 (3)	0.0045 (3)			
				Pt – N	5	3.160	0.0044			
				Pt – C – N (3)	10	3.160 (2)	0.0044 (2)			
				Pt – C – N (4)	5	3.160	0.0044			

[a] Fixed value estimated from the calibration compounds and from refinements on the actual complex which give S_o^2 values between 1.2 and 1.3.
[b] Fixed value estimated from crystal structures. [c] For definition, see text p. 66.

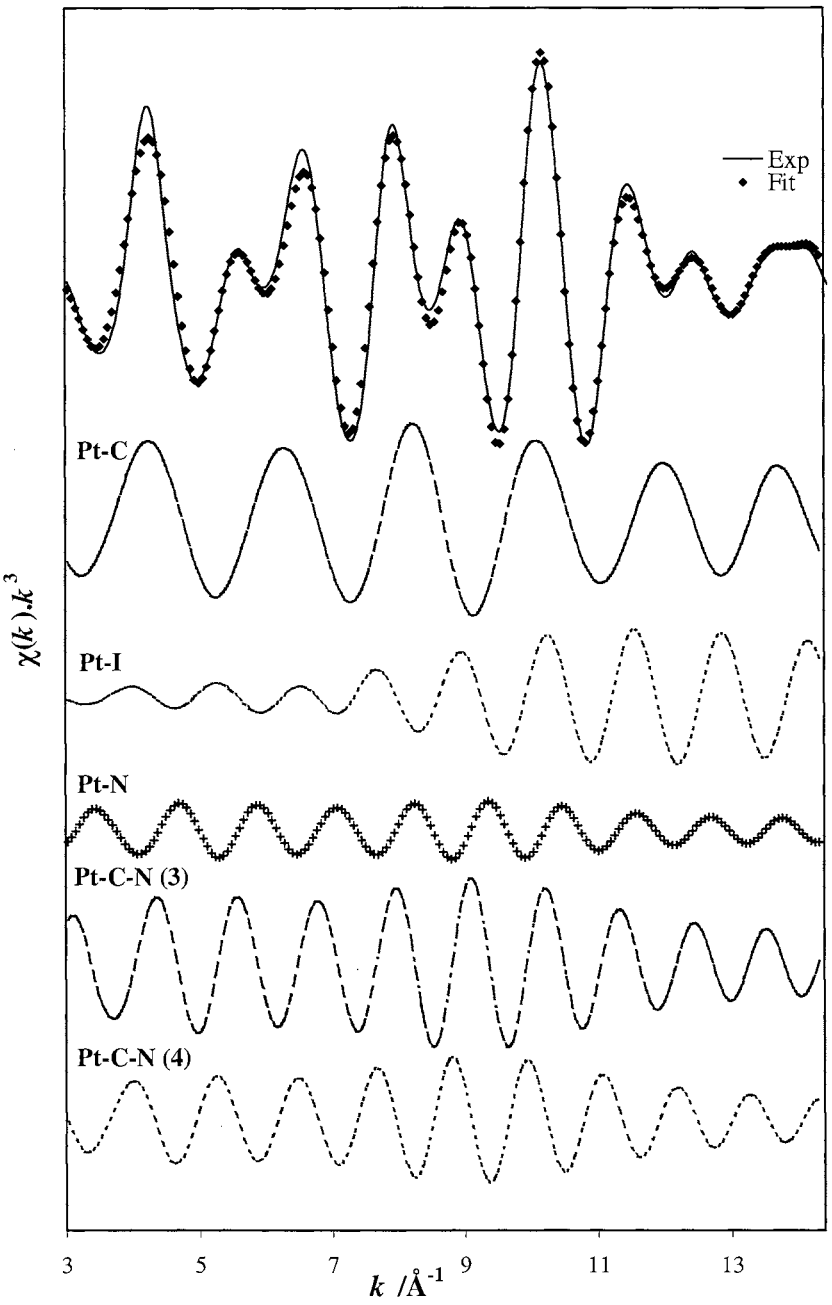

Figure 57. Pt L_{III} edge EXAFS of the 0.1 M $[PtI(CN)_5]^{2-}$ aqueous solution. Calculated (♦) and Fourier-filtered measured EXAFS functions (solid line) with individual contributions shown separately (*cf.* Table 16).

Both the $[Pt(CN)_5(OH_2)]^-$ and $[Pt(CN)_5(OH)]^{2-}$ complexes belong to the point group C_{4v}, like the previously studied $[Pt(CN)_5X]^{2-}$ (X= Cl^-, Br^-, I^-) complexes,[53] which leads to similar vibrational spectra. In the cyanide stretching region of $[Pt(CN)_5(OH_2)]^-$ and $[Pt(CN)_5(OH)]^{2-}$, only the stretching vibrations of the equatorial (but not for the axial) cyano ligands could be observed, as previously for the $[Pt(CN)_5Cl]^{2-}$ species (Table 17).[53]

The mean C-N symmetric stretching frequency decreases for X = CN > H_2O > OH ≈ Cl > Br > I (Table 17). This would correspond to an increasing π back-bonding, and seems to follow the expected order of increasing electron-releasing ability from CN to I, when replacing the CN group with a σ donor halide ligand.[53] The Pt-C symmetric stretching frequency is dominated by the equatorial ligands (for X = I, a weak Pt-C axial frequency can be seen at 432.9 cm^{-1}),[53] and is less sensitive with a slightly increasing trend.

Table 17. $[Pt^{IV}(CN)_5X]^{n-}$ complexes: distances (Å) and symmetric stretching frequencies (cm^{-1}).

Ligand X	Mean Pt-C bond distance	Mean Pt-N distance	Pt-C symmetric stretching frequency[a]	C-N symmetric stretching frequency[a]
OH_2	1.986 (2)	3.144 (2)	464	2207
OH	1.996 (2)	3.152 (2)	463	2202
Cl			462.9	2204.9
Br			465.8 (452.5)[b]	2203.0
I	2.002(2)	3.154 (2)	467 (432.9)[b]	2195.5
CN	2.004 (2)	3.155 (2)	469	2211

[a] Values for X = Cl, Br, I from ref. 53, for X = CN from ref. 76.
[b] Pt-C symmetric stretching of the axial ligand

Partially oxidized cyanide chain complexes. The cyano complexes of platinum(II) can be partially oxidized to give mixed-valence, one-dimensional metallic conductors such as $K_2Pt(CN)_4X_{0.3}\cdot 3H_2O$, X = Br^- or Cl^-.[74] The Pt-Pt distance then decreases to allow strong overlap of the d_{z^2} orbitals, which gives rise to metallic conductance along the chain direction. As a result of the partial oxidation of Pt^{2+} to an average oxidation state of $Pt^{2.3+}$, the Pt-Pt separation decreases from 3.478(1) Å in $K_2[Pt(CN)_4]\cdot 3H_2O$ to 2.890(1) Å in $K_2Pt(CN)_4X_{0.3}\cdot 3H_2O$,[74,75] while the stacked $Pt(CN)_4^{2-}$ groups twist from a nearly eclipsed (~16° torsion angle) to a staggered (45°) configuration, The increase in the torsion angle between the stacked planar $Pt(CN)_4$ groups with shorter Pt-Pt distance is a result of the increasing repulsion between the π-orbitals of the CN^- groups.[79] For large separations (over about 3.7 Å) an eclipsed conformation with parallel cyano ligands occurs, which gradually

transforms to completely staggered at about 2.9 Å.[79] The shortest Pt-Pt distance, 2.798(1) Å, is found for the $Rb_2[Pt(CN)_4](FHF)_{0.40}$ compound, for which the formal oxidation state of platinum is 2.4.[80] The shortened Pt-Pt separation has been explained to be due to a partial removal of d_{z2} electrons from Pt at the oxidation, which allows substantially improved d_{z2} orbital overlap and stronger metal-metal bonding.[74,79]

Binuclear platinum(III) cyano complex. In Paper V, an EXAFS study is reported of the structure of the platinum(III) complex $[Pt_2(CN)_{10}]^{4-}$ in aqueous solution (Table 16). A non-supported Pt-Pt bond, 2.729(3) Å, was found to connect two $Pt(CN)_5$ groups in the dimeric complex. From the correlation between the Pt-Pt distance and torsion angle in crystal structures discussed above,[79] it is obvious that the dimeric $[(NC)_5Pt\text{-}Pt(CN)_5]^{4-}$ complex must have a staggered conformation (*cf.* Figure 64).

However, for other symmetrically bridged diplatinum(III) complexes considerably shorter Pt^{III}-Pt^{III} distances can be found, in the range 2.47 to 2.58 Å.[81,82] The expected single bond distance for a Pt^{III}-Pt^{III} bond with bond order 1 is 2.59 Å, and has been successfully used in correlations between bond order *vs.* metal-metal distances based on Pauling's theory of the metal bond.[83] The longer Pt^{III}-Pt^{III} distance in $[Pt_2(CN)_{10}]^{4-}$ indicates that there evidently are interactions between the bulky ligands which increase the Pt-Pt separation, even in the staggered conformation.

5.4 Platinum-thallium cyano complexes. Both the redox couples Pt(II) to Pt(IV) and Tl(III) to Tl(I) have the unusual property of being capable of two-electron transfer. This makes Pt-Tl compounds with a metal-metal bond potentially interesting for photo-induced redox reactions. Absorbed light can be converted to chemical energy by the ability of the metal-metal bond to transfer electrons in a controlled multielectron redox process.

Such metal-metal bonded compounds are usually only stable in the solid state and not in solution, especially not in water. Maliarik et al. found that a new class of Pt-Tl cyano species was formed in aqueous solution by reaction between Pt^{II} and Tl^{III} complexes.[84-86] The composition of the complexes depend on the pH of the solution, and hence the amount of free CN^- since HCN dominates at low pH. The complexes formed were stable for a long time in the dark, and five different Pt-Tl cyanide species could be characterized by means of multinuclear NMR (^{195}Pt, ^{205}Tl, ^{13}C). The stability constants have been determined by means of multinuclear NMR (^{195}Pt, ^{205}Tl) methods.[86] A typical distribution of complexes is shown in Figure 58, which shows that the dominant bimetallic complex can be controlled

by the cyanide concentration and the pH. In solutions with pH ≈1 and a ratio CN : Pt : Tl = 7:1:1, up to about 90% of the total Pt and Tl content can be present as the complex $[(CN)_5Pt\text{-}Tl(CN)]^-$ (this is the case at low metal concentrations, which reduces the relative amount of the trimer, $[(NC)_5Pt\text{-}Tl\text{-}Pt(CN)_5]^{3-}$).

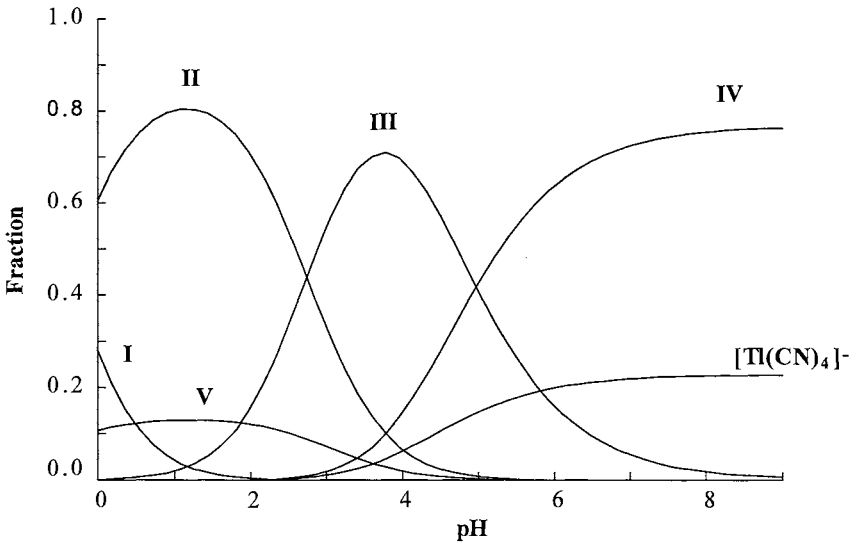

Figure 58. Typical distribution of Pt-Tl cyano species as a function of pH (increasing pH increases the free cyanide concentration) calculated from stability constants in ref. 86. Complex **I**: $[(CN)_5Pt\text{-}Tl(aq)]$; **II**: $[(CN)_5Pt\text{-}Tl(CN)]^-$; **III**: $[(NC)_5Pt\text{-}Tl(CN)_2]^{2-}$; **IV**: $[(NC)_5Pt\text{-}Tl(CN)_3]^{3-}$; and **V** is the trimer, $[(NC)_5Pt\text{-}Tl\text{-}Pt(CN)_5]^{3-}$. $[Pt]_{tot}$= 40 mM; $[Tl]_{tot}$= 30 mM; $[CN]_{tot}$= 280 mM.

The complexes were found to contain strong unsupported Pt-Tl metal-metal bonds with a stable $Pt(CN)_5$ group. The binuclear complexes could be represented by the formula $[(NC)_5Pt\text{-}Tl(CN)_n]^{n-}$ (n = 0-3). In the present study (Paper IV), the structure has been further characterized and bond lengths determined by means of the EXAFS technique for three of these complexes, and a complete analysis of their vibrational spectra has been performed.

These binuclear Pt-Tl species $[(NC)_5Pt\text{-}Tl(CN)_n]^{n-}$ (n= 0-3) can be viewed as metastable intermediate products of the electron-transfer reaction between Pt(II) and Tl(III) leading to Pt(IV) and Tl(I). When the number of cyano ligands increases the thallium atom becomes a less efficient acceptor of the electron pair donated from the platinum atom, resulting in a decreasing s-character of the Pt-Tl bond and a smoothly increasing electron density at the platinum atom. By interpolation between the values of the ^{195}Pt NMR chemical shift for the $[Pt(CN)_6]^{2-}$ and $[Pt(CN)_4]^{2-}$ cyano complexes (655 and –213 ppm,

respectively) and the ^{205}Tl NMR chemical shift for the $Tl^+(aq)$ and $Tl(CN)_3(aq)$ species (0 and 2842 ppm, respectively) with known oxidation states, "effective charges" could be estimated for the metal atoms in the binuclear complexes. The following charges were obtained: $Pt^{3.6}$-$Tl^{1.6}$ for $[(NC)_5Pt\text{-}Tl(aq)]$, $Pt^{3.4}$-$Tl^{2.0}$ for $[(NC)_5Pt\text{-}Tl(CN)]^-$, $Pt^{2.9}$-$Tl^{2.4}$ for $[(NC)_5Pt\text{-}Tl(CN_2)]^{2-}$, and $Pt^{2.7}$-$Tl^{2.6}$ for $[(NC)_5Pt\text{-}Tl(CN_3)]^{3-}$ (*cf.* Paper IV).

In solution, the binuclear complexes are stable toward redox decomposition in the dark at room temperature, but react when heated or exposed to visible light, except for the redox-inert $[(NC)_5Pt\text{-}Tl(CN)_3]^{3-}$ complex. The reaction product when thallium(III) is reduced is always Tl^+, while oxidation of platinum(II) gives different products under different conditions. Irradiation with light or heating of $[(NC)_5Pt\text{-}Tl(CN)_2]^{2-}$ gives $[Pt(CN)_6]^{2-}$ as decomposition product, and $[(NC)_5Pt\text{-}Tl]$ gives $[Pt(CN)_5(OH_2)]^-$ or $[Pt(CN)_5(OH)]^{2-}$ (depending on pH). The intermediate complex $[(NC)_5Pt\text{-}Tl(CN)]^-$ decomposes to both $[Pt(CN)_6]^{2-}$ and $[Pt(CN)_5(OH_2)]^-$. The complex $[(NC)_5Pt\text{-}Tl(aq)]$ decomposed in the synchrotron light during an EXAFS experiment, and its structure could not be determined (Paper IV).

$$(NC)_5Pt\text{-}Tl(aq) \xrightarrow[12\ \text{hours}]{80\,^{\circ}C,\ pH \sim 8} Tl^+ + [Pt^{IV}(CN)_5(H_2O)]^- \underset{+H^+}{\overset{-H^+}{\rightleftharpoons}} [Pt^{IV}(CN)_5(OH)]^{2-} \qquad (50)$$

However, for the other complexes the stability was sufficient to allow collection of EXAFS data without any noticeable change in the composition. This was checked by comparing repeated EXAFS scans, and also by NMR measurements a few days later.

The dominance of a single species (as shown in Figure 58) is necessary to allow a reliable analysis of the EXAFS data. The highest amount possible to obtain of the $[(NC)_5Pt\text{-}Tl(CN)_2]^{2-}$ species is only 75 %, which gives some additional uncertainty in the results, as discussed in Paper IV. A problem that had to be solved before the data could be analyzed properly, was how to handle the strong multiple scattering contribution from the linearly coordinated cyano ligands. This required that a suitable model was found which could adequately account for these contributions (see Scheme 5). A favorable circumstance is that two metal centers are available, although the EXAFS ranges both for the Pt and Tl L_{III} edges (11564 and 12658 eV, respectively) are limited by other absorption edges. For these bimetallic samples the usable EXAFS range of the Pt L_{III} edge is limited to $k < 15$ Å^{-1} by the Tl L_{III} edge, and the Tl L_{III} EXAFS range is limited to $k < 12$ Å^{-1} by the Pt L_{II} edge at 13273 eV.

The solid $TlPt(CN)_5$ compound. When acidifying an aqueous solution with the dominating complex $[(NC)_5Pt\text{-}Tl(CN)]^-$ (about 100 mM) with perchloric acid to a final free acid concentration of about 1.5 M, the neutral $[(NC)_5Pt\text{-}Tl(aq)]$ complex with low solubility (~3.7 mM) becomes dominant (Figure 58) and a white crystalline powder with the composition $TlPt(CN)_5$ slowly precipitates. Thus, the solid phase and the solution complex have the same stoichiometric composition (disregarding the hydration). Since no single crystals could be obtained the structure of the compound $TlPt(CN)_5$ was studied, by combining results from X-ray powder diffraction (XRD), EXAFS of the Pt and Tl L_{III} absorption edges, and vibrational spectroscopy by Raman scattering and IR absorption.

X-ray powder diffraction data were collected for the white powder contained in a 0.20 mm glass-capillary, which was rotated to minimize effects of preferred crystal orientation and radiation damage. The intensity were measured in symmetric transmission mode with a powder diffractometer (STOE STADI/P), in order to get symmetric profiles of the reflections. Monochromatic Cu $K_{\alpha 1}$ radiation was obtained by means of a germanium monochromator in the incident beam. The total data collection time was 45 hours. In Figure 59, the observed powder XRD profiles are presented.

From the accurately measured peak positions in the first part of the diffraction pattern, $2\Theta \leq 50°$, the unit cell was determined (see paper III). Of the two space groups, P4/*n* (No. 85) and P4/*nmm* (No. 129) which were possible from the reflection conditions (hk0: h+k = 2n and 0k0: k = 2n), P4/*nmm* could be used for a successful refinement of the structural parameters. The molecular structure was solved manually, by first locating the two heavy atoms by testing possible position in a trial and error procedure, combined with difference-Fourier maps to locate the positions of the carbon and nitrogen atoms.

However, there are some indications of irregularities in the model description of the structure. Firstly, the peak shapes are somewhat asymmetric, and the first peak in the diffraction pattern {001} is clearly much broader than the third one {110} (Figure 59). In the first part of the diffraction pattern some discrepancies can be seen in the plot of the difference between experimental and calculated intensities. Secondly, a common isotropic displacement (Debye-Waller) factor had to be used for all atoms, because refinement of individual atomic isotropic displacement parameters yielded very large values for the light atoms, without significantly improving the overall fit of the model. This indicates some disorder in the structure, as discussed in below (p. 151).

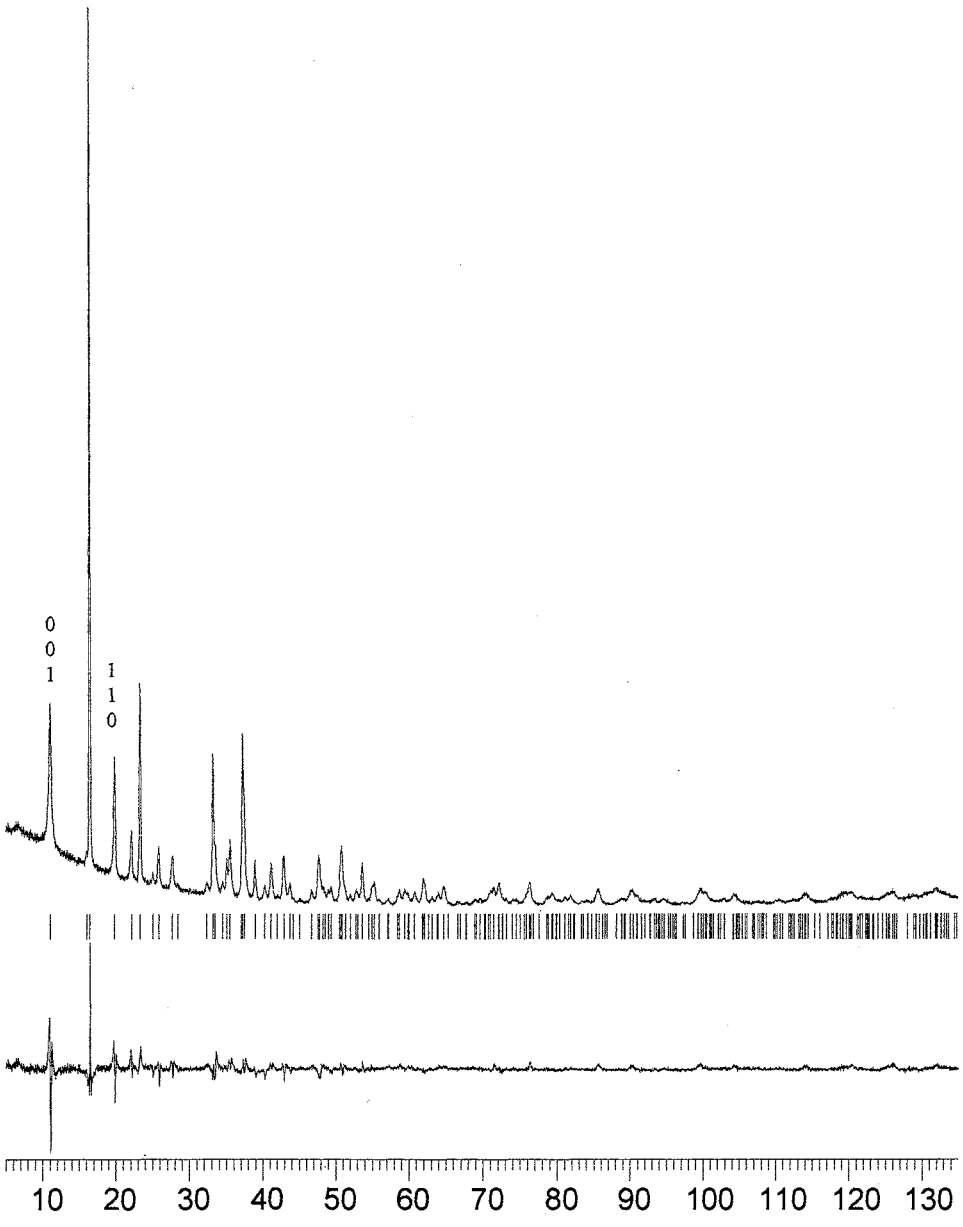

Figure 59. Powder X-ray diffraction intensities of $TlPt(CN)_5$ as a function of the scattering angle 2θ. *Upper trace:* Experimental intensity data, I_{obs}. *Lower trace:* I_{obs} - I_{calc}. The vertical markers show calculated peak positions.

The XRD positional parameters showed that the structure is composed of $TlPt(CN)_5$ entities linked together in linear -Tl···NC-Pt-Tl··· chains with the Pt-Tl bond distance 2.627(2) Å. The symmetry of the space group P4/*nmm* requires that the heavy metal atoms and one "axial" cyano group (C2-N2) are positioned on a four-fold axis along the c-axis of the unit cell (Figure 43), with four equivalent "equatorial" cyano ligands (C1-N1) around the platinum atom. A three-dimensional network is formed by the equatorial cyano ligands of the platinum atom, bridging to the thallium atoms of neighboring parallel chains (N1···Tl), which are oriented in the opposite direction. The nitrogen atom (N2) of the axial cyano ligand form a bridge with a short linear bond (Tl-N2 2.31 Å) to the thallium atom in the chain.

However, even though a precise value was obtained for the Pt-Tl distance from the x-ray powder diffraction (XRD) results, some of the distances for the light atoms were improbable. For example, the Pt-C1 distance appeared as 1.80(2) Å, while a value of 2.00 Å is expected for the four Pt-C distances in equatorial coordination, as *e.g.* in the standard compounds $K_2[Pt^{II}(CN)_4]\cdot 3H_2O$ and $K_2[Pt^{IV}(CN)_6]$.[75,76] In order to get a better description of the local structure around the Pt and Tl atoms, EXAFS data were recorded both at the Pt L_{III} and Tl L_{III} edges. The most important multiple scattering (MS) pathways, needed for a satisfactory description of the very large MS contributions to the EXAFS data, have been evaluated by means of the FEFF program (*cf.* Scheme 5). The results of the EXAFS analyses are given in Table 18.

Vibrational spectra were recorded by means of Raman and infrared absorption spectroscopy. The vibrational modes of the $TlPt(CN)_5$ entities are strongly coupled, in particular the metal-metal Pt-Tl bond stretching mode which is split into four Raman and two IR bands (see Figure 42). The assignments, which were made using factor group theory, show that a larger structural entity than the crystallographic unit cell must be used for the description of the vibrational coupling (see Section *3.5*). The force constant has been evaluated for the Pt-Tl bond and is compared with the correlation between the Pt-Tl force constants and bond length for the bimetallic solution complexes (*cf.* Figure 63 and Table 20).

The $[(NC)_5Pt\text{-}Tl(CN)_n]^{n-}$ (n = 1 - 3) complexes in aqueous solution. The structures of these complexes were deduced mainly from the Pt L_{III} and Tl L_{III} edge EXAFS spectra (Paper IV). The results from the data analyses of both the Pt and Tl L_{III} edges, are given in Tables 18 and 19, and the separate EXAFS contributions for the models used are shown in Figures 60 and 61 for the $[(NC)_5Pt\text{-}Tl(CN)(aq)]$ complex. The proposed structures of the hydrated binuclear Pt-Tl species $[(NC)_5Pt\text{-}Tl(CN)_n]^{n-}$ (n = 1- 3), together with the binuclear Pt-Pt complex $[(NC)_5Pt\text{-}Pt(CN)_5]^{4-}$ from Paper V, are shown in Figure 64.

For these complexes, the Raman and IR spectra have been obtained from aqueous solutions. This gives broad and overlapping bands, and large parts of the IR spectra are obscured by the water absorption (*cf.* Figure 62). On the other hand, there is no coupling of the vibrations between different molecular species. The point group symmetry of the complexes can be used: *i.e.* C_{4v} for the $[(NC)_5Pt\text{-}Tl(CN)]^-$ species, C_{2v} for $[(NC)_5Pt\text{-}Tl(CN_2)]^{2-}$, and C_s for $[(NC)_5Pt\text{-}Tl(CN_3)]^{3-}$. However, because of the few observed bands it is necessary to simplify the assignment by only considering the local group symmetries of the two parts of the complexes: the $-Pt(CN)_5$ group with C_{4v} local symmetry, and the $Tl(CN)_n$ group with local symmetry C_{2v} for $-Tl(CN)_2$, and C_{3v} for $-Tl(CN)_3$.

The general problem for the assignments is the lack of experimental fundamental frequencies. For example, for the $[(NC)_5Pt\text{-}Tl(CN)]^-$ complex we could only observe eight bands of 24 Raman active modes, predicted from Group theory. The Raman bandwidth of the CN stretching modes is about 8-13 cm^{-1}, and the three Raman bands observed at 2200.1, 2189.8 and 2177.6 cm^{-1} are strongly overlapping. Thus, these three bands must contain all four Raman active fundamental modes for the CN stretchings of the $Pt(CN)_5$ group, which belong to the symmetry species $2A_1 + B_1 + E$ of the point group C_{4v}.

In the region containing Pt-C and Tl-C stretchings, and bendings of the linear Pt-C-N entity,[11b,52,53] even less information is obtained from the Raman spectrum. Only three strongly overlapping bands at 468, 411 and 362 cm^{-1} were recorded, with the large band widths 55, 40 and 34 cm^{-1}, respectively. From previous studies of the $[Tl(CN)_n]^{3-n}$ complexes, it is clear that the band at 362 cm^{-1} belongs to the Tl-C stretching mode. Then all Pt-C stretchings ($2A_1 + B_1 + E$) and linear Pt-C-N bendings ($A_1 + B_1 + B_2 + 3E$),[53] must be contained in the remaining two Raman features.

However, for the normal coordinate calculations we need to estimate frequency values for all the possible vibrational modes. Therefore, for all those unresolved modes that are expected to be close in frequency, we assumed the same frequency as that of the observed broad band in the appropriate region (see Table 7 in Paper IV). Similar approximations were made for the complexes $[(NC)_5Pt\text{-}Tl(CN_2)]^{2-}$ and $[(NC)_5Pt\text{-}Tl(CN_3)]^{3-}$.

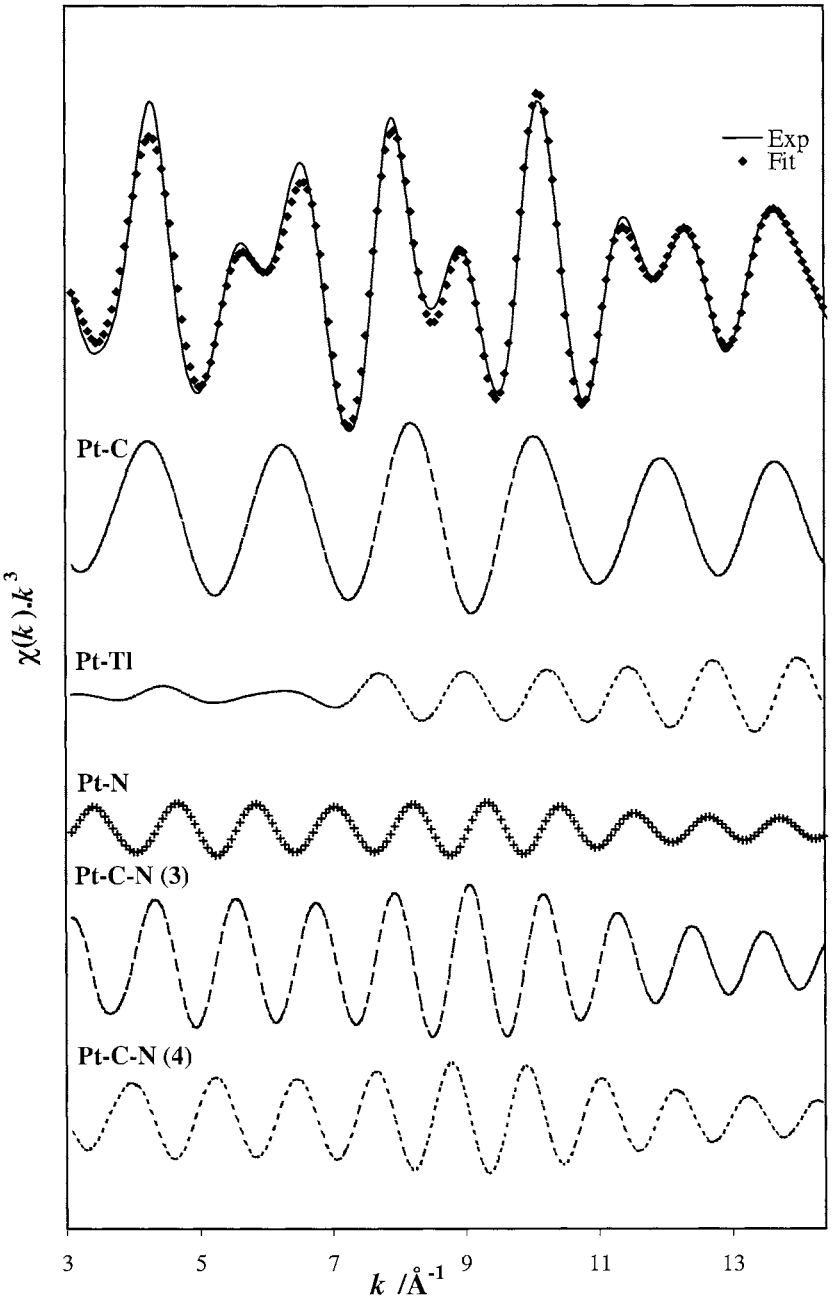

Figure 60. Pt L_{III} edge EXAFS for $[(NC)_5PtTl(CN)]^-$ in aqueous solution. Calculated (♦) and Fourier-filtered measured EXAFS functions (solid line) with individual contributions shown separately (*cf.* Table 18).

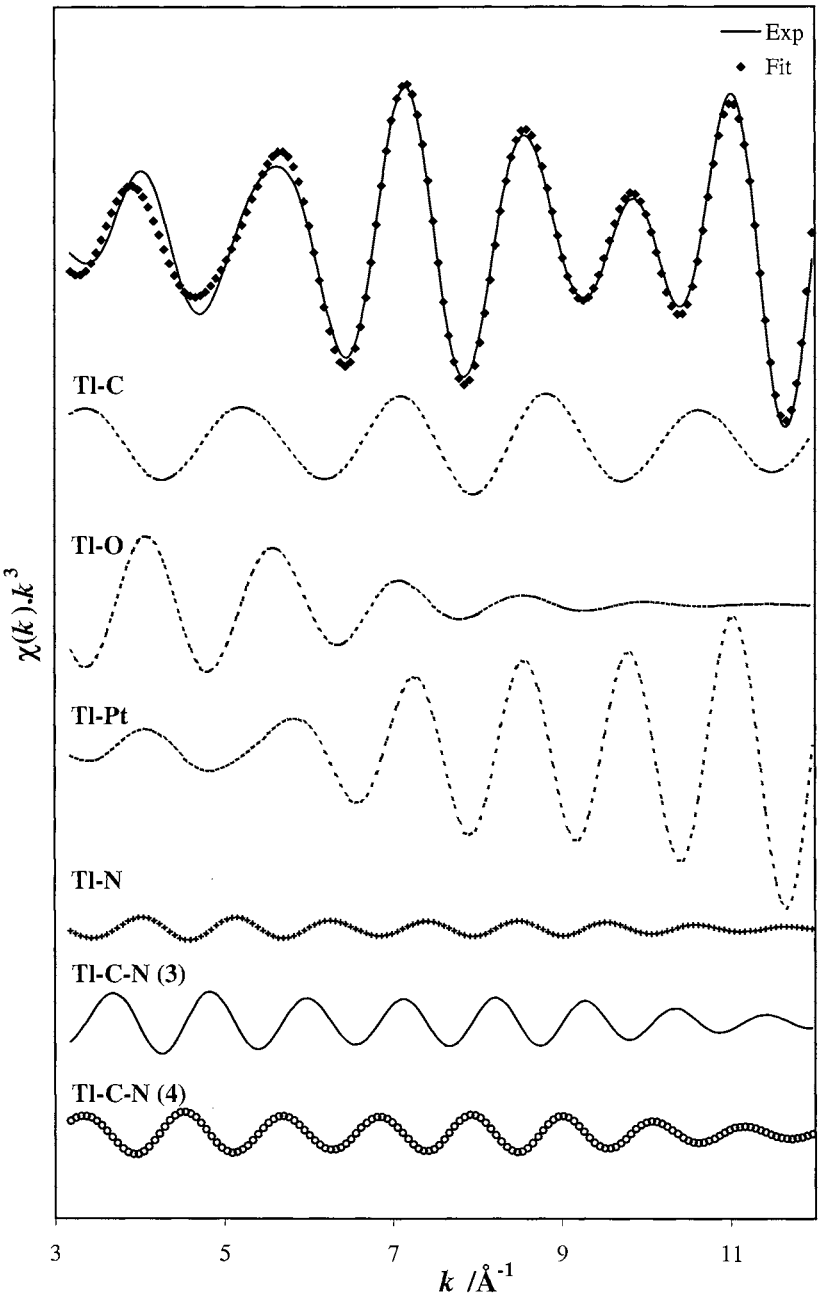

Figure 61. Tl L_{III} edge for $[(NC)_5PtTl(CN)]^-$ in aqueous solution. Calculated and Fourier-filtered experimental EXAFS functions (*cf.* Table 19) with individual contributions shown separately.

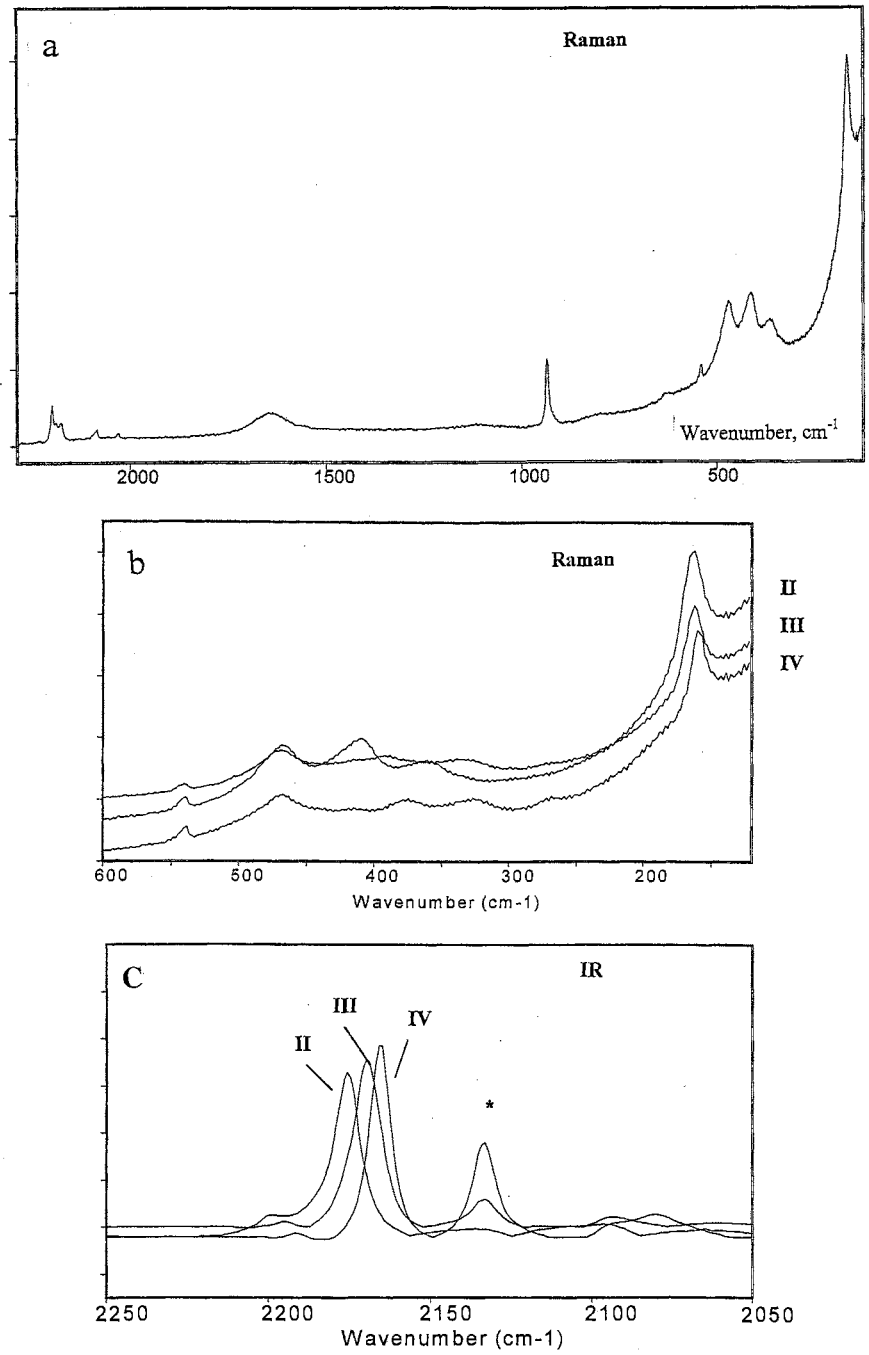

Figure 62. a) Raman spectrum of complex **II**: $[(NC)_5PtTl(CN)]^-$ in aqueous solution (~50 mM). b) Raman spectra in the low-frequency region of complexes $[(NC)_5PtTl(CN)_n]^{n-}$ n = 1, 2, 3 (complexes **II**, **III**, **IV**, respectively) in aqueous solution. c) IR spectra of the above complexes in the cyanide C≡N stretching region. * HCN band

Table 18. Results of Pt L_{III} edge EXAFS analysis. For refined model parameters estimated standard deviations are given within brackets.

Sample	E_0 / eV	*k*-range for Fourier transform / Å^{-1}	FT-filter range[a] *r* / Å	Scattering Path [b]	Frequency	Distance *R* / Å	Debye-Waller parameter σ^2/ Å^2	ΔE_0 / eV	S_o^2	Res.
$K_2[Pt(CN)_4].3H_2O$ Solid	11567.4	2.63 – 15.63	1.11 – 8.00	Pt – C	4	1.985 (2)	0.0029 (2)	6.6 (4)	1.15 (4)	17.9
				Pt – N	4	3.149	0.0046			
				Pt – C – N (3)	8	3.149 (2)	0.0046 (2)			
				Pt – C – N (4)	4	3.149	0.0046			
				Pt – Pt	2	3.53 (2)	0.0134 (20)			
$K_2[Pt(CN)_6]$ Solid	11567.7	2.66 – 14.81	1.11 – 8.00	Pt – C	6	2.004 (2)	0.0028 (1)	6.1 (3)	1.06 (3)	19.5
				Pt – N	6	3.155	0.0046			
				Pt – C – N (3)	12	3.155 (1)	0.0046 (1)			
				Pt – C – N (4)	6	3.155	0.0046			
$(NC)_5PtTl$ Solid	11567.9	2.68 – 14.55	1.10 – 8.00	Pt – C	5	2.003 (1)	0.0030 (1)	7.1 (2)	1.2	12.2
				Pt – Tl	1	2.627 (2)	0.0040 (1)			
				Pt – N	5	3.150	0.0044			
				Pt – C – N (3)	10	3.150 (2)	0.0044 (1)			
				Pt – C – N (4)	5	3.150	0.0044			
$[(NC)_5Pt\text{-}Tl(CN)]^-$ Solution	11569.0	2.63 – 14.71	1.12 – 8.00	Pt – C	5	2.009 (2)	0.0027 (1)	7.2 (3)	1.2	14.7
				Pt – Tl	1	2.602 (2)	0.0049 (2)			
				Pt – N	5	3.162	0.0047			
				Pt – C – N (3)	10	3.162 (2)	0.0047 (2)			
				Pt – C – N (4)	5	3.162	0.0047			
$[(NC)_5Pt\text{-}Tl(CN)_2]^{2-}$ Solution	11567.0	2.61 – 14.75	1.11 – 8.00	Pt – C	5	2.003 (2)	0.0032 (1)	7.3 (3)	1.2	13.7
				Pt – Tl	1	2.613 (3)	0.0055 (3)			
				Pt – N	5	3.151	0.0049			
				Pt – C – N (3)	10	3.151 (2)	0.0049 (2)			
				Pt – C – N (4)	5	3.151	0.0049			
$[(NC)_5Pt\text{-}Tl(CN)_3]^{3-}$ Solution	11568.3	2.66 – 14.69	1.15 – 8.00	Pt – C	5	2.008 (2)	0.0029 (1)	7.4 (3)	1.2	15.2
				Pt – Tl	1	2.637 (4)	0.0055 (3)			
				Pt – N	5	3.162	0.0048			
				Pt – C – N (3)	10	3.162 (2)	0.0048 (2)			
				Pt – C – N (4)	5	3.162	0.0048			

[a] The *r*-range used for the Fourier filtering is given without phase shift correction

[b] The distance and Debye-Waller parameter for Pt-N and Pt-C-N (4) are correlated to the dominant path Pt-C-N (3).

Table 19. Results of Tl L^{III}-edge EXAFS analysis. The estimated standard deviations for refined model parameters are given within brackets. Fourier-filtered, k^3-weighted EXAFS data were used.

Sample	E_0/eV	Fourier transform k-range / Å^{-1}	FT-filter range[a] r / Å	Scattering Path[b]	Frequency	Distance R / Å	Debye-Waller parameter σ^2/ Å^2	ΔE_0 / eV	S_o^2	Res.
$(NC)_5PtTl$ Solid	12654.8	3.13 – 11.80	1.36 – 3.48	Tl – N (ax)	1	2.31 (3)	0.0080	10.5 (4.2)	1.3 (3)	13.2
				Tl – N (eq)	4	2.50 (1)	0.014 (2)			
				Tl – Pt	1	2.627 (4)	0.006 (1)			
				Tl – N – C (3)	2	3.50 (2)	0.008 (2)			
$[(NC)_5Pt\text{-}Tl(CN)]^-$ Solution	12657.6	3.19 – 12.00	1.44 – 3.47	Tl – C	1	2.128 (6)	0.0027 (3)	7.4 (1.0)	0.9	12.5
				Tl – O	4	2.505 (5)	0.023 (1)			
				Tl – Pt	1	2.595 (1)	0.0030 (1)			
				Tl – N	1	3.284	0.0091			
				Tl – C – N (3)	2	3.284 (6)	0.0091 (8)			
				Tl – C – N (4)	1	3.284	0.0091			
$[(NC)_5Pt\text{-}Tl(CN)_2]^{2-}$ Solution	12661.9	2.91 – 11.92	1.40 – 3.49	Tl– C	2	2.206 (2)	0.0051 (2)	6.2 (2)	1.06 (2)	17.3
				Tl – Pt	1	2.622 (1)	0.0064 (2)			
				Tl – N	2	3.356	0.0073			
				Tl – C – N (3)	4	3.356 (1)	0.0073 (2)			
				Tl – C – N (4)	2	3.356	0.0073			
$[(NC)_5Pt\text{-}Tl(CN)_3]^{3-}$ Solution	12658.6	2.84 – 11.19	1.31 – 3.59	Tl– C	3	2.203 (6)	0.0069 (5)	6.2 (6)	1.25	15.2
				Tl – Pt	1	2.639 (8)	0.009 (1)			
				Tl – N	3	3.355	0.0100			
				Tl – C – N (3)	6	3.355 (5)	0.0100 (7)			
				Tl – C – N (4)	3	3.355	0.0100			

[a] The range of Fourier filtering is given without phase shift correction

[b] The distance and Debye-Waller parameter for Tl-N and Tl-C-N (4) are correlated to the dominant path Tl-C-N (3).

For the Pt-Tl stretching mode of the three $[(NC)_5Pt\text{-}Tl(CN)_n]^{n-}$ complexes with n = 1, 2 and 3, only one strong and polarized Raman band was obtained, at 163.7, 162.6 and 159.1 cm^{-1}, respectively,. The Pt-Pt stretch in the $[NC)_5Pt\text{-}Pt(CN)_5]^{4-}$ dimer (Figure 64) was observed rather close to these frequencies, namely at 140 cm^{-1}.

Figure 63 shows that there is a reasonably good correlation between Pt-Tl stretching force constants and bond distances for the three heterobimetallic PtTl cyano complexes and also for the solid compound. The force constants for the $[(NC)_5Pt\text{-}Tl(CN)_n]^{n-}$ complexes in Table 20 have been calculated including full cyano coordination in the complexes, according to Figure 64. The calculated force constants for the Pt-Tl frequencies without including any ligands, are also given. In Reference 11c, the following comment is made about the force constants calculated in various approximations for metal-metal bonds:

"It is noted that the metal-metal stretching force constants obtained by rigorous calculations are surprisingly close to those obtained by approximate calculations considering only metal atoms."

In the present case, however, the values differ substantially despite the very heavy metal atoms.

Table 20. Characteristics of the Pt-Tl bond in the solid $TlPt(CN)_5$ compound and in the binuclear $[(NC)_5Pt\text{-}Tl(CN)_n]^{n-}$ complexes in aqueous solution:,bond distance *d*, Debye-Waller (or disorder) parameter σ^2, NMR coupling constant ^1J, bond stretching frequency ν, and force constant *F*.

Species	*d* (Pt-Tl) Å	D-W parameter σ^2 / Å^2	$^1J(^{195}Pt\text{-}^{205}Tl)$ Hz	ν(Pt-Tl) cm^{-1}	*F*(Pt-Tl) N cm^{-1}
$[(NC)_5Pt\text{-}Tl]$ (aq)			71060		
$[(NC)_5Pt\text{-}Tl(CN)]^-$(aq)	2.598(3)	0.0049(2)	57020	163.7	1.736
$[(NC)_5Pt\text{-}Tl(CN)_2]^{2-}$ (aq)	2.618(4)	0.0055(3)	47260	162.6	1.693
$(CN)_5PtTl$ (s)	2.627(2)	0.0040(1)		[a]	1.648
$[(NC)_5Pt\text{-}Tl(CN)_3]^{3-}$ (aq)	2.638(4)	0.0055(3)	38760	159.1	1.563

[a] Splitted into four Raman bands: 211 s, 195 m, 164 s, 151 m (2 IR bands: 194 m, 150 m)

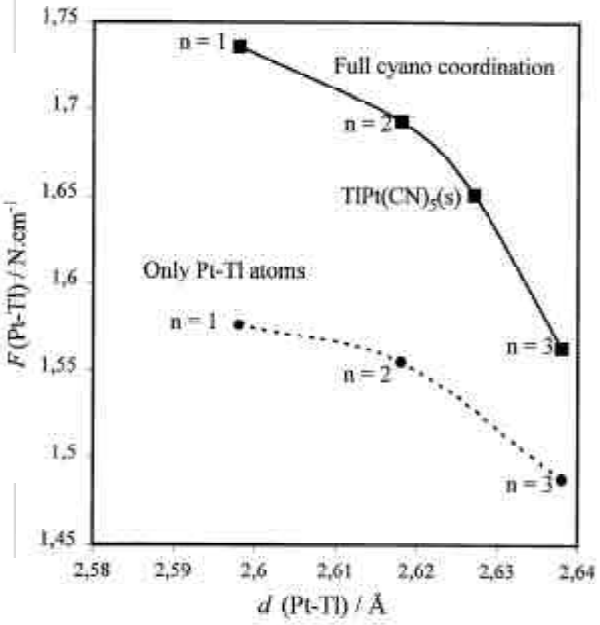

Figure 63. Correlation between the Pt-Tl stretching force constants and the bond distances for the aqueous solution complexes $[(NC)_5Pt\text{-}Tl(CN)_n]^{n-}$, with = 1, 2, and 3. The solid line represents the force constant calculated using the full cyano coordination, the dashes only including the two metal (Pt-Tl) atoms.

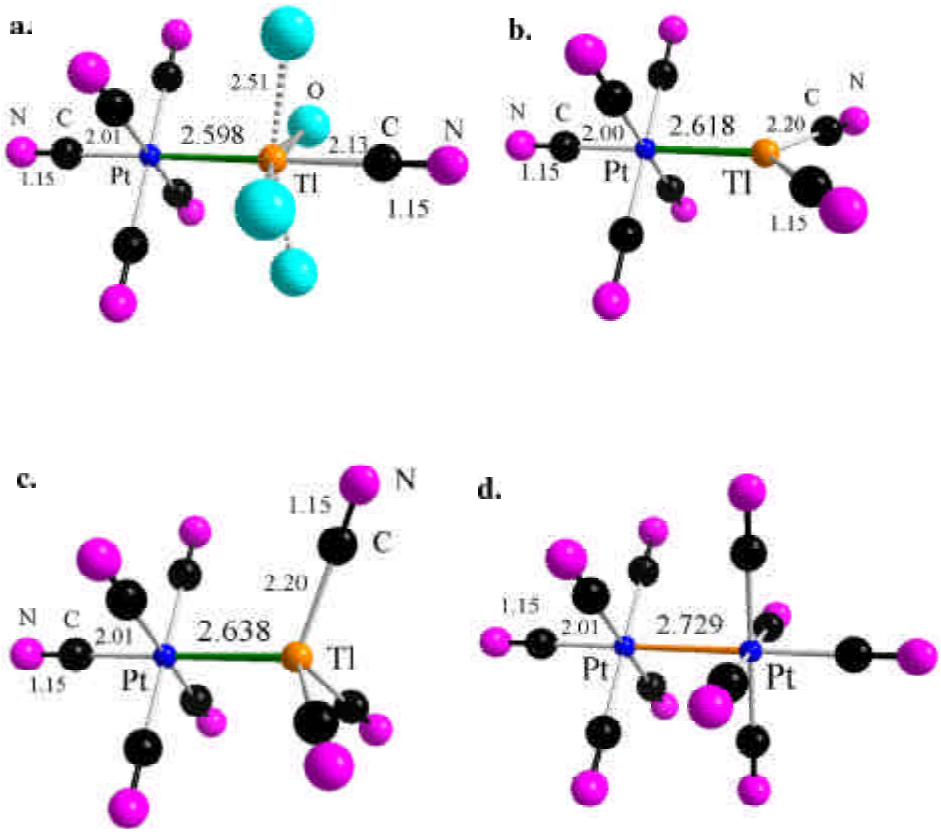

Figure 64. The structural models (distances in Å) proposed for the bimetallic complexes in aqueous solution. a) $[(NC)_5Pt\text{-}TlCN(aq)]^-$, b) $[(NC)_5Pt\text{-}Tl(CN)_2]^{2-}$, c) $[(NC)_5Pt\text{-}Tl(CN)_3]^{3-}$ (Paper IV) and d) $[(NC)_5Pt\text{-}Pt(CN)_5]^{4-}$ (Paper V). The Pt-Tl distance increases with the number of cyano ligands on the thallium atom.

Conclusions

The main results presented in this thesis concern the structure of hydrated metal ions and complexes in aqueous solution. This is a very important field of study, since most chemical processes in bio-inorganic and environmental systems depend on the hydration of the reacting species. However, such information is not easily available, and often requires a combination of methods, experimental as well as theoretical.

An example of this is the present study of the biochemically important calcium ion, which is relatively weakly hydrated (Paper I). The experimental structural information obtained by EXAFS and LAXS techniques was connected to a theoretical molecular dynamics simulation study. In this way the assumptions and approximations made in the MD study were checked, and the combined results could be used to gain detailed information on the structural aspects of the water molecules around the calcium ion. The new EXAFS data treatment programs could be used to show that the distribution of Ca-O bond distances around the hydrated ion not only is broad, but also asymmetric. This is in agreement with the MD simulations of the system.

EXAFS studies were also made of the hydration and fluoride complex formation of uranium(IV) and thorium(IV) ions (Paper II), which is of interest also for the aqueous chemistry of other actinide ions in connection with nuclear waste storage problems. The EXAFS technique permits structural studies for much lower concentration of the solutions than previously possible with the LAXS technique, and also higher resolution of the metal-oxygen bond distances. This allowed more reliable information to be obtained about the very high hydration numbers for the highly charged and large actinide ions.

The EXAFS technique also made it possible to study the structure of new bimetallic complexes in aqueous solution (Papers IV and V). The recently discovered platinum-thallium cyano complexes are of interest as model compounds for controlled reversible redox processes, converting solar to chemical energy. These species can be considered as intermediates in a two-electron transfer process via the metal-metal bond. The concentration and stability of these light-sensitive complexes was sufficient to allow EXAFS measurements. By means of a data treatment technique and computer programs based on new developments of the theory of the multiple scattering, it was possible to evaluate the Pt-Tl bond distance and to connect this information to results from vibrational and NMR spectroscopy.

Also for a solid compound with a similar Pt-Tl metal-metal bond, for which no single crystals could be obtained, the structure was evaluated. This time a combination of EXAFS, x-ray powder diffraction and vibrational spectroscopy was used, revealing a strong metal-metal bond and a three-dimensional network of bridging cyano ligands (Paper III).

The rapid development of EXAFS spectroscopy into a useful tool for structure studies of the coordination around atoms in solutions, in crystalline and amorphous solids, already allows many new applications in inorganic and also bio-inorganic chemistry. Experimentally, the data quality steadily improves, with synchrotrons specially built to give x-ray beams with even higher brightness and flux, and with improved instrumentation and detectors. Another important progress in the EXAFS method is the improvement of the scattering theory and in the data treatment, which now makes it possible to extract more reliable and detailed structural information from the collected data. This development will certainly continue, since many applications have become possible which allow new insight *e.g.* into the structural aspects of the chemical role of metal ions in biochemical and environmental systems.

References

1. Kronig, R. deL. *Z. Phys.* **1931**, *70*, 317
2. Teo, B.K. *EXAFS: Basic Principles and Data Analysis*; Springer-Verlag: New York, 1986.
3. *X-ray Absorption: Principles, Applications, Techniques of EXAFS, SEXAFS and XANES*; Koningsberger, D.C. and Prins, R., Eds.; John Wiley and Sons: New York, 1988.
4. *Inorganic Electronic Structure and Spectroscopy*, Eds., E.I. Solomon and A.B.P. Lever, John Wiley and Sons: New York, 1999; **a.** Zhang, H.H.; Hedman, B.; Hodgson, K.O. *X-ray Absorption Spectroscopy and EXAFS Analysis: The Multiple Scattering Method and Application in Inorganic and Bioinorganic Chemistry*, Chapter 9, Volume I; **b.** Solomon, E.I.; Hanson, M.A. *Bioinorganic Spectroscopy*, Chapter 1, Volume II.
5. Rehr, J.J.; Ankudinov, A.; Zabinsky, S.I. *Catal. Today*, **1998**, *39*, 263.
6. Klug, H.P.; Alexander, L.E.; *X-ray Diffraction Procedures*, John Wiley and Sons: New York, 1974, **a.** Chapter 12; **b.** Chapter 5.
7. Levy, H.A.; Danford, M.D.; Narten, A.H. *Data Collection and Evaluation with an X-ray Diffractometer Designed for the study of Liquid Structure*, Technical Report ORNL-3960, Oak Ridge National Laboratory, Oak Ridge, 1966.
8. Johansson, G.; Sandström, M. *Chem. Scr.* **1973**, *4*, 195.
9. Colthup, N.B.; Daley, L.H.; Wiberley, S.E. *Introduction to Infrared and Raman Spectroscopy*, 3rd ed.; Academic Press: New York, 1990.
10. Grasselli, J.; Bulkin, B.J. *Analytical Raman Spectroscopy*, John Wiley and Sons: New York, 1991.
11. Nakamoto, K. *Infrared and Raman Spectra of Inorganic and Coordination Compounds*, 5th ed., John Wiley and Sons: New York, 1997, **a**. Chapter I.; **b**. Chapter III-15, **c**. Chapter III-24.
12. Czernuszewics, R.S.; Spiro, T. *IR, Raman and Resonance Raman Spectroscopy*, Chapter 7 in: *Inorganic Electronic Structure and Spectroscopy*, Eds., E.I. Solomon and A.B.P. Lever, John Wiley and Sons: New York, 1999, Volume I.
13. Brown, G.E. Jr.; Calas, G.; Waychunas, G.A.; Petiau, J. In "*Spectroscopic Methods in Mineralogy and Geology*", Reviews in Mineralogy 18; Hawthorne, F., Ed.; Mineralogical Society of America, 1988, Chapter 11, pp 431-512.

References

14. **a.** Bunker, G. "*XAFS Class Notes*"; http://sparky.csrri.iit.edu/xafsdocs/.; **b.** Bunker, G. *Nucl. Instrum. Meth.* **1983**, *207*, 437.
15. Teo, B.K. *EXAFS- Basic Principles and Data Analysis*, Springer-Verlag: Berlin, 1986., **a.** Chapter 1; **b.** Chapter 4; **c.** Chapter 5; **d.** Chapter 7; **e.** Chapter 6.
16. *X-Ray Absorption; Principles, Applications, Techniques of EXAFS, SEXAFS and XANES*; Koningsberger, D.C.; Prins, R.; ., Eds.; John Wiley and Sons: New York, 1988, **a.** Bianconi, A. Chapter 11.5; **b.** Cramer, S.P. Chapter 4; **c.** Heald, S.M. Chapter 3.4; **d.** Sayers, D.E.; Bunker, B.A. Chapter 6.2, 6.3; **e.** Stern, E.A. Chapter 1; **f.** Crozier, E.D.; Rehr, J.J.; Ingalls, R. Chapter 9.
17. Stern, E.A.; Sayers, D.E.; Lytle, F.W. *Phys. Rev. B*, **1975**, *11*, 4836.
18. **a.** Rehr, J.J.; Zabinsky, S.I.; Ankudinov, A.L.; Albers, R.C. *Physica B,* **1995**, *208 & 209*, 23. **b.** Newville, M.; Ravel, B.; Haskel, D.; Rehr, J.J.; Stern, E.A.; Yacoby, Y. *Physica B* **1995,** *208 & 209*, 154.
19. Coppens, P. *Synchrotron Radiation Crystallography,* Academic Press: London: 1992, **a.** Chapter 6.4; **b.** Chapter 2; **c.** Chapter 3.2.
20. *FEFF code for ab initio calculations of XAFS:* **a.** Mustre de Leon, J.; Rehr, J.J.; Zabinsky, S.I.; Albers, R.C. *Phys. Rev. B* **1991,** *44*, 4146; **b.** Zabinsky, S.I.; Rehr, J. J.; Ankudinov, A.L.; Albers, R.C.; Eller, M.J. *Phys. Rev. B* **1995,** *52*, 2995; **c.** Ankudinov, A.L. *Ph. D. Thesis* (University of Washington 1996).
21. Stöhr; J. *NEXAFS Spectroscopy*; Springer: Berlin, 1996; Chapter 5.
22. Brown, G.E., Jr.; Waychunas, G. A. *X-Ray Absorption Spectroscopy: Introduction to Experimental Procedure*, http://www.ssrl.slac.stanford.edu/mes/XAFS/XAS_INTRO.html
23. Meitzner, G. *Catal. Today* **1998**, *39*, 282.
24. Lindquist-Reis, P.; Muñoz-Páez, A.; Díaz-Moreno, S.; Pattanaik, S.; Persson, I.; Sandström, M. *Inorg. Chem.* **1998**, *37,* 6675.
25. "Guide to XAFS Measurements at SSRL"; http://www-ssrl.slac.stanford.edu/mes/XAFS/main.html
26. George, G.N.; Pickering, I.J. *EXAFSPAK - A Suite of Computer Programs for Analysis of X-ray Absorption Spectra*, SSRL, Stanford University, CA., USA., 1993.
27. Ressler, T. *J. Phys. IV France* **1997**, *7*, C2-269.
28. Rehr, J.J.; Personal communication
29. Fay, M.J.; Proctor, A.; Hoffman, D.P.; Hercules, D.M. *Anal. Chem.* **1988**, *60*, 1225A.
30. Victoreen, J.A. *J. Appl. Phys.* **1948**, *19,* 855.

31. Roy, M; Gurman, S.J.; van Dorssen, G. *J. Phys. IV France* **1997,** *7*, C2-151.
32. ATOMS Manual, http://leonardo.phys.washington.edu/~ravel/atoms/
33. FEFF 8.0 Manual, http://Feff.phys.washington.edu/feff
34. Pickering, I.J. Stanford Synchrotron Radiation Laboratory, Workshop on X-ray Absorption Spectroscopy, July 8-12, 1993.
35. Trueblood, K.N. *In Accurate Molecular Structures, Their Determination and Importance*; Eds. A. Domenciano, I. Hargittai, IUCr; Oxford University Press: 1992, Chapter 8.
36. Villain, F.; Verdaguer, M.; Dromzee, Y. *J. Phys IV France* **1997**, *7*, C2-659.
37. Lindquist-Reis, P.; Lamble, K.; Pattanaik, S.; Persson, I.; Sandström, M. *J. Phys. Chem. B.* **2000,** *104,* 402.
38. Ultra-thin glass available from: DESAG, Postfach 80, D-3223 Grünenplan, Germany.
39. Howell, I; Neilson, G.W.; Chieux, P. *J. Mol. Struct.* **1991,** *250,* 281.
40. Enderby, J.E.; Cummings, S.; Herdman, G.J.; Neilson, G.W.; Salmon, P.S.; Skipper, N. *J. Phys. Chem.* **1987,** *91*, 5851.
41. Warren, B.E. *X-Ray Diffraction*, Addison-Wesley Publishing Co.: Reading, MA., 1969, Chapters 1 and 10.
42. Ohtaki, H.; Radnai, T. *Chem. Rev.* **1993**, *93*, 1157, and references therein.
43. Shannon, R.D. *Acta Crystallogr. Ser. A* **1976**, *32,* 751.
44. *International Tables for X-Ray Crystallography*; Wilson, A.J.C., Ed.; Kluwer Academic Publishers: Dordrecht, The Netherlands, 1995; Vol. C.
45. Debye, P. *Ann. Phys.* **1915,** 46, 809.
46. Johansson, G. *Acta Chem. Scand.* **1989**, *43*, 307; *Adv. Inorg. Chem.* **1992**, *39, 159.*
47. Molund, M.; Persson, I. *Chem. Scr.* **1985**, *25*, 197.
48. Kettle, S.F.A. *Physical Inorganic Chemistry, A Coordination Chemical Approach*, Spectrum Academic Publishers: Oxford, 1996, Chapter 12.2.
49. Ferraro, J.R.; Ziomek, J.S, *Introductory Group Theory*, Plenum Press: New York, 1975, 2nd ed.
50. Kettle, S.F.A. *Symmetry and Structure*, John Wiley and Sons: Chichester, 1995, 2nd ed., Chapter 13.
51. **a.** Golub, A.M.; Köhler, H.; Skopenko, V.V. *Chemistry of Pseudohalides*, Elsevier: Amsterdam, 1986, Chapter 3; **b.** Miessler, G.L.; Tarr, D.A. *Inorganic Chemistry*, 2nd Ed., Prentice Hall: Upper Saddle River, New Jersey, 1999, Chapter 10.3.4.

52. Jones, L.H. In *Inorganic Vibrational Spectroscopy*; Marcel Dekker: New York, 1971, Chapter 4.

53. Memering, M.N.; Jones, L.H.; Bailar, J.C. *Inorg. Chem.* **1973**, *12*, 2793-2801

54. **a.** Errington, R J. *Advanced Practical Inorganic and Metalorganic Chemistry*, Chapman & Hall, London, UK: 1997, Chapter 11; **b**. Duxbury, G. *Infrared Vibration-Rotation Spectroscopy*, John Wiley and Sons: Chichester, 2000, Chapter 5.2, p. 117.

55. Richens, D.T. *The Chemistry of Aqua Ions, Synthesis, structure and reactivity*, John Wiley and Sons: Chichester, 1997.

56. Carugo, O.; Djinovic´, K.; Rizzi, M. *J. Chem. Soc., Dalton Trans.* **1993**, 2127.

57. Katz Kaufmann, A.; Glusker, J.P.; Beebe, S.A.; Bock, C.W. *J. Amer. Chem. Soc.* **1996**, *118,* 5752.

58. Frausto da Silva, J. J. R.; Williams, R. P. J. *The Biological Chemistry of the Elements*, Clarendon: Oxford, 1991, Chapter 10.

59. For references, see Paper I.

60. Pavlov, M.; Siegbahn, P.E.M.; Sandström, M. *J. Phys. Chem. A* **1998**, *102*, 219.

61. Elding, I. *Structural Aspects of some Nine-coordinated Lanthanoid Complexes in the Solid State*, Ph. D. Thesis, University of Lund, Lund, Sweden, 1977.

62. Barrett, S. A.; Jacobson, A. J.; Tofield, B. C.; Fender, B. E. F. *Acta Crystallogr. Sect. B* **1982**, *38*, 2775.

63. Greenwood, N.N.; Earnshaw, A. *Chemistry of the Elements*, 2nd ed., Butterworth-Heinemann: Oxford, 1997, **a**. Chapter 14.2.5; **b**. Chapter 19.7.1.

64. Spirlet, M.R.; Rebizant, J.; Kanellakopulos, B.; Dornberger, E. *Acta Crystallogr., Sect. C*, **1987**, *43,* 19.

65. Hund, F.; Duerrwächter, W. *Z. Anorg. Allg. Chem.* **1951,** *265,* 67.

66. Farkas, I.; Grenthe, I.; Bányai, I. *J. Phys. Chem. A* **2000**, *104*, 1201.

67. Lindqvist-Reis, P.; Eriksson, L.; Sandström, M.; Lidin, S.; Persson, I. Unpublished results.

68. Thiele, G.; Putzas, D. *Z. Anorg. Allgem. Chem.* **1984**, *519*, 217.

69. Koneshan, S.; Rasaiah, J.C.; Lynden-Bell, R.M.; Lee, S.H. *J. Phys. Chem. B* **1998,** *102*, 4193.

70. Glaser, J. In *Advances in Inorganic Chemistry*; G. Sykes, Ed.; Academic Press: San Diego, CA, 1995; Vol. 43, pp 1-78.

71. Blixt, J.; Glaser, J.; Mink, J.; Persson, I.; Persson, P.; Sandström, M. *J. Am. Chem.*

Soc. **1995**, *117*, 5089-5104.

72. Britton, D. In *Perspectives in Structural Chemistry*; Eds. Dunitz, J. D., and Ibers, J. A.; John Wiley and Sons: New York, 1967, Vol. 1.
73. Åkesson, R.; Persson, I.; Sandström, M.; Wahlgren, U. *Inorg. Chem.* **1994**, *33*, 3715.
74. Wilkinson, G. *Comprehensive Coordination Chemistry* ; G. Wilkinson, Ed.; Pergamon Press: Oxford, 1987; Vol. 2, Chapter 52.4.2, pp 7-14.
75. Washecheck, D.M.; Peterson, S.W.; Reis, A.H.; Williams, J.M. *Inorg. Chem.* **1976**, *15*, 74.
76. Weiss, J.*Z. Naturforsch.* **1974**, *29b*, 119-120.
77. Kubas, G.J.; Jones, L.H. *Inorg. Chem.* **1974**, *13*, 2816-2819.
78. Siebert, H.; Siebert, A. *Z. Naturforsch.* **1967**, *22b*, 674.
79. Williams, J.M.; Keefer, K.D.; Washecheck, D.M.; Enright, N.P. *Inorg. Chem.* **1976**, *15*, 2446.
80. Schultz, A.J.; Coffey, C.C.; Lee, G.C.; Williams, J.M. *Inorg. Chem.* **1977**, *16*, 2129.
81. Hollis, L.S.; Roberts, M.M.; Lippard, S.J. *Inorg. Chem.* **1983**, *22*, 3637.
82. Cotton, F.A.; Walton, R.A. *Multiple bonds between Metal Atoms*, Clarendon Press: Oxford, 1993, Chapter 8.4, pp. 508-532.80.
83. Reis, A.H. Jr.; Peterson, S.W. *Inorg. Chem.* **1976**, *15*, 3186-3187.
84. Berg, K.E.; Glaser, J.; Read, M.C.; Tóth, I. *J. Am. Chem. Soc.* **1995**, *117*, 7550-7551.
85. Maliarik, M.; Berg, K.; Glaser, J.; Sandström, M.; Tóth, I. *Inorg. Chem.* **1998**, *37*, 2910.
85. Maliarik, M.; Glaser, J.; Tóth, I.; W. da Silva, M.; Zekany, L. *Eur. J. Inorg. Chem.* **1998**, 565.

Acknowledgment

At the time of printing this thesis it is almost three years since I entered to KTH in April 1997. The course on normal coordinate analysis by Prof. János Mink had just started, and from the first days of my stay, I felt a bit that it was a rather difficult start. Soon I got involved in different subjects from the normal coordinate analysis of DMPU (which has an awful smell, especially when it is mixed with acetone!) to EXAFS!

In mid June, I was going for my first visit to the synchrotron facilities in SSRL to measure new samples, but I had no idea what EXAFS was all about. I had not heard about it till that time. I remember that one of those early days, when I asked Prof. Magnus Sandström to introduce me to an understandable and easy-to-read reference for it, I was not even able to pronounce it, asking: "What do you call it? E-..X-..A-..F-..S ?!!"

Pt-Tl cyano complexes were among the samples, which we had to measure. In the beginning of June, before leaving for SSRL, a one day trip to Umeå was planned together with Professors Ingmar Persson and Magnus Sandström. This was one of the trips that I never will forget in my whole life! When we arrived to Umeå University, discussions started with Dr. Per Persson about all new progresses in EXAFS: from new FEFF codes to the WinXAS program. I really felt that I had come to a new planet, not a new country!!!... Then at that time when I was totally confused, discussions about multiple-scatterings in Pt-Tl complexes started, telling that Tl EXAFS data are not usable at all. Suddenly Per Persson turned to me and said: "Farideh, this is the problem which you have to solve"!!!

On the other hand, my knowledge about LAXS and even computer science (*e.g.* how to use Windows) was not better. Anyway, this was just a bit of history to show you what a long way I have come during the past three years.

All that I have achieved during this period, had not really been possible without the discussions, support and encouragement of my supervisor, Prof. Magnus Sandström. For the first time in my life, I met a chemist who was interested to discuss the physical aspects of phenomena with his student, such as thinking: "How can the photoelectron wave interfere with its own backscattered wave, before it even hits the backscattering atom?"

I never had such a possibility before, not in Iran and not even in Japan, to be able to have these type of discussions with my supervisors. I truly appreciate Magnus Sandström for all he taught me about science, helping me to believe in myself and to know my abilities better, and also how to look at life differently.

While we were working at KTH, the person who was pushing us to do our jobs more efficiently in a shorter time was Prof. Ingmar Persson in SLU (Uppsala). It is very interesting to see both Magnus and Ingmar during the EXAFS runs at SSRL. Even though Ingmar is quick, efficient and ignoring all details during measurements, all data collections are quite successful. However, when it is Magnus working shift, despite all precautions that he consider, there are always some problems waiting! Such as getting bubbles within the liquid sample cells in our last run (which finally we found out was just because we were using He around the sample chamber, to get a possibly better signal-to-noise ratio).

I really enjoyed very much this collaboration between Magnus and Ingmar. I don't think there are so many friends like them, with this much difference in character. They just simply complement each other and that is the secret of this successful collaboration. I also learned a lot from Ingmar, from how to use EXCEL and EXAFSPAK programs, up to LAXS measurements, which I appreciate very much.

I got the opportunity to meet Prof. John Rehr here at KTH, and since then he has always kindly answered all my questions about FEFF and EXAFS, and I wish to thank him very much for his help. Dr. Per Persson in Umeå University also has been one of my supports for learning about EXAFS. In fact, he was the one who at the beginning taught me how to use the WinXAS, FEFF and ATOMS programs. Also, I am also grateful to Prof. Lars Kloo for his help in handling these programs.

I appreciate the collaboration and interesting discussions which we had with Prof. Ingmar Grenthe and Dr. Henry Moll (KTH) for the EXAFS analysis of hydrated uranium(IV) ions in Paper II, and with Prof. Kersti Hermansson and Daniel Spångberg from Uppsala university for the Molecular Dynamics calculations for hydrated calcium ions in Paper I.

Prof. János Mink is another very nice person whom I got the opportunity to meet in Sweden and later during my visit in Hungary. I had the chance to attend to his lectures in Normal Coordinate Analysis and I wish to thank him for all his efforts with normal coordinate analyses on the complexes in Papers III & IV.

Besides János Mink, I had the opportunity of meeting other nice Hungarian researchers at KTH, such as Dr. Zoltán Szabó, Prof. István Bányai and especially Prof. Imre Tóth and his wonderful family, who were my neighbors at Wenner-Gren Center. They were really patient neighbors: they had to listen to my alarm ringing for two weeks, while I was at SSRL!!.... Prof. Imre Tóth kindly invited me to Hungary, to teach about EXAFS at the Lajos Kossuth University in Debrecen, which I appreciate very much.

ROYAL INSTITUTE OF TECHNOLOGY

Doctoral Thesis:
"Structure of Hydrated Ions and Cyanide Complexes by X-ray Absorption Spectroscopy"

Farideh Jalilehvand
Dept. of Chemistry, KTH, May 19th, 2000

Errata List

Summary. page 12: paragraph 3, line 6, $k = m / \eta \rightarrow k = mv / \eta$
page 65: paragraph 4, line 8, low S/N ratio → high S/N ratio
page 77: paragraph 2, $\mu \rightarrow \mu/\rho$
page 132: line 3, 2.15 Å → 3.15 Å

Paper I. page 6: $S_0^2 = 0.7 \rightarrow 0.8$
page 7: text in Table 2, eqn. 1 → eqn. 2; *k*- and *r*-space fitting → *k*-space fitting
page 18: 2.4 and 2.9 Å for Ca^{2+}-O and O_w-O_w, respectively
page 36: in Fig. S2.b, in the 2nd and 3rd curves, change: Shell II → Shell I,
and Shell I → Shell II, respectively
page 38: text in Fig. S4, Ca-O 2.37 Å → 2.47 Å; CĪ-O 2.15 Å → 3.15 Å

Paper III. page 9: line 4, Fig. 1b → 2b
page 14: text in Table 3, Table 6 → 4
page 20: subscript in Table 5, $* \rightarrow a$
page 15: paragraph 4, Table 7 → S3
page 33: text in Fig.S2, correct as: EXAFS data (solid line) for the compounds…;
eliminate: (dashes)

Paper IV. page 18: Table 6, first raw, correct: $[Pt(CN)_5Tl(CN)]^-$, $[Pt(CN)_5Tl(CN)_2]^{2-}$
page 21: paragraph 2, Fig. 7b → 7c
page 22: paragraph 1, (*cf*. Table 7) → Table 6
page 27: paragraph 1, line 8, increase → decrease
page 28, line 12: Table 6 → 7
page 29, paragraph 3: Table 6 → 7
page 30: paragraph 2, lowering of effective charge → increasing of …
page 36: (comment to table S3, S4) section must be eliminated

Paper V. page 1: in Title, eliminate "Vibrational Spectroscopy"
page 2: paragraph 3, $[Pt(CN)_5X]^{2-} \rightarrow [Pt(CN)_5X]^{n-}$
page 6: text in Scheme 1, Tl-C-N → M-C-N ; M = Pt
page 6: paragraph 1, (Fig. 13) → (Fig. 1)
page 8: line 8, Fig. 2 → Fig. 2a
page 10: paragraph 2, Fig. 4 → Fig. 3; last line, (*cf*. Fig. 5) → Fig. 4
page 11: Fig. 4 → Fig. 3; Fig. 5 → Fig. 4
page 12: paragraph 3, eliminate (Table 1)